

Post-mining water treatment: Nanofiltration of uranium-contaminated drainage – Experiments and modeling

vorgelegt von
Dipl.-Ing.
Michael Hoyer
geb. in Karl-Marx-Stadt

von der Fakultät III - Prozesswissenschaften
der Technischen Universität Berlin
zur Erlangung des akademischen Grades

Doktor der Ingenieurwissenschaften
– Dr.-Ing. –

genehmigte Dissertation

Promotionsausschuss:

Vorsitzende:	Prof. Dr.-Ing. Claudia Fleck
1. Gutachter:	Prof. Dr.-Ing. habil. Jens-Uwe Repke
2. Gutachter:	Prof. Dr.-Ing. Matthias Wessling
3. Gutachter:	Dr. Roland Haseneder

Tag der wissenschaftlichen Aussprache: 17. November 2016

Berlin 2017

List of contents

Glossary	7
1 Introduction	2
1.1 Uranium’s health effects	3
1.2 Uranium in the environment.....	4
1.3 Uranium mining in Saxony.....	7
1.4 Chemical speciation	10
1.5 Nanofiltration	11
1.6 Nanofiltration of uranium-contaminated water.....	13
2 Motivation and objectives.....	16
3 Mass transfer in NF membranes – existing modeling approaches	17
3.1 Irreversible Thermodynamics	18
3.1.1 The Kedem-Katchalsky model.....	19
3.1.2 The Spiegler-Kedem model.....	21
3.1.3 Extended Nernst-Planck equation (ENP).....	22
3.2 Mechanistic models.....	24
3.2.1 Space Charge (SC) model.....	24
3.2.2 Teorell-Meyer-Sievers (TMS) model	25
3.2.3 DSPM.....	25
3.2.4 Donnan-Steric Partitioning Pore Model incorporating Dielectric Exclusion - DSPM&DE.....	26
3.2.5 Other approaches	27
3.3 Model selection.....	28
4 Development of an adapted transport model	29
4.1 Model assumptions	30
4.2 Physical property data of the solution	32
4.3 Conservation equations.....	34
4.4 Electrical balance.....	35
4.5 Feed side mass transfer	36
4.6 Electrical double layer	40
4.7 Partitioning at the interfaces.....	41
4.7.1 Donnan exclusion.....	42
4.7.2 Steric exclusion	43

4.7.3	Dielectric exclusion due to image forces	44
4.7.4	Dielectric exclusion due to the Born effect.....	47
4.7.5	Activity exclusion.....	48
4.8	Transport through the membrane.....	49
4.8.1	Steric hindrance	49
4.8.2	Diffusion hindrance factor.....	50
4.8.3	Convection hindrance factor	52
4.9	Numerical solution.....	54
4.10	Parameter fitting.....	59
5	Materials and methods.....	60
5.1	Membranes.....	60
5.2	Membrane permeation experiments	63
5.3	Streaming potential measurements.....	66
5.4	Experimental procedure.....	68
5.5	Analytical methods.....	70
5.6	Predictive speciation modeling	70
5.7	Radius and diffusion coefficient of uranyl species	71
6	Experimental and modeling results	73
6.1	Feed side mass transfer	73
6.2	Membrane thickness	75
6.3	Membrane pore radius	82
6.4	Membrane charge density.....	85
6.5	Synthetic uranyl feed solutions	88
6.6	Nanofiltration of uranium-contaminated water – Case study at the Seelingstädt site of the Wismut GmbH 93	
7	Discussion of the experimental and modeling results.....	102
7.1	Experimental uncertainty assessment.....	102
7.2	Error analysis for Section 6.2.....	106
7.3	Error analysis for the experiments of Section 6.5.....	107
7.4	Model discretization	110
7.5	Model sensitivity.....	113
7.6	Simultaneously fitting multiple parameters.....	119
7.7	Linearity of the concentration gradient	121
7.8	Discussion of separation phenomena inside the membrane.....	121

8	Summary	124
9	Outlook.....	126
10	References	127
	Appendix A – Hagen Poiseuille for NF	138
	Appendix B – Friction coefficient.....	139
	Appendix C – Membrane data	140
	Appendix D – Model input data and testing.....	152
	Appendix E – Publications, conferences, and supervised theses	161

Declaration of academic honesty

With this statement I declare, that I have independently completed this PhD thesis entitled “Post-mining water treatment: Nanofiltration of uranium-contaminated drainage – Experiments and modeling”. The thoughts taken directly or indirectly from external sources are properly marked as such.

Munich,

Michael Hoyer

Acknowledgements

Over the past four years I have received support and encouragement from a great number of individuals; the most important contributions will be mentioned here. This dissertation would not have been possible without the hard work and dedication of Jens-Uwe Repke who supported me with great patience and an open ear for questions. I owe sincere and earnest thankfulness to Roland Haseneder who was always ready to help even on short notice and even when he was on the weekend or on vacation. I owe many thanks to André Rieger who spent hours to discuss my questions and motivated me with his fascination for science in general. His guidance has made this a thoughtful and rewarding journey. I am obliged to many of my colleagues who supported me, especially André, Daniel, Joachim, Rolf, and Dirk. I would like to show my gratitude to the students who inspired and motivated me with their curiosity and a fresh view.

I thank Andrea Kassahun for her dedication and perseverance to explore the potential of membrane filtration on real uranium-contaminated waters.

I owe many thanks to Vinzenz Brendler, Robin Steudtner, and Frank Bok for insights on the chemistry of uranium and speciation analysis.

For Membrane samples I would like to thank: Frank Lipnizki from Alfa Laval, Stephan Schütze from Desalogics GmbH, Pia Lippmann from the TZW Karlsruhe, Klaus Hagen from Veolia Water, Werner Ruppricht from Microdyn Nadir, Norman Bischofberger from Toray, Thorsten Hägert from InAqua Vertriebsgesellschaft mbH, Thilo Wüst from GE Water, Christian Konrad from Koch membrane systems.

I would like to thank Professor Ewald Schnug for the data on uranium in German tap water.

The author gratefully acknowledges the grant given by the European Social Fund which made this research and dissertation possible.

Glossary

Symbols

a_i	activity of ion i
α_i	Degree of dissociation
A_k	Membrane porosity (ratio of void fraction volume to total volume)
c_{ctr}	counter-ion (to the polarization charges of the membrane) concentration in mol/l
$c_i(0^{inside})$	i^{th} species' concentration at the membrane side of the feed/membrane interface, just inside the membrane, in mol/l
$c_{i,p}$	i^{th} species' permeate concentration in mol/l
CP	Concentration polarization index (Schäfer calls it M , Hwang calls it I)
c_x	membrane charge density in mol/l (i.e. same unit as concentration)
d_h	hydraulic diameter
$D_{i,\infty}$	i^{th} ion's bulk diffusion coefficient in solvent w , i.e. $D_{i,w}$ (values for D_∞ taken from [Lide2005], and [Nightingale1959])
η	bulk solvent dynamic viscosity
e_0	elementary charge
ε_0	vacuum permittivity
ENP	Extended Nernst-Planck equation (Section 3.1.3)
η_p	pore solvent dynamic viscosity
ε_r	relative permittivity
ε_b	relative permittivity of the bulk aqueous phase (around 80 for water)
ε_m	relative permittivity of the membrane phase
F	Faraday constant in C/mol
ϕ	dissipation function
φ	electric potential in V
F_i	external forces acting on a system

Φ_i	interfacial partitioning coefficient for species i
γ_i	activity coefficient of ion i
I	ionic strength in mol/l or current density in A/m ²
I_m	ionic strength in mol/kg
j_i	molar flux of solute i in mol/m ² /s
J_v	volumetric permeate flux in m/s
k	mass transfer coefficient
k_B	Boltzmann constant
$K_{i,c}$	convection hindrance factor
$K_{i,d}$	diffusion hindrance factor
λ	ionic radius/pore radius ratio
λ_D	Debye length
$L_{i,k}$	phenomenological coefficients connecting fluxes with driving forces
L_p	Permeability
μ	chemical potential
$\bar{\mu}$	electrochemical potential
N_A	Avogadro number 6.02283 [NIST2011]
N_{ions}	number of ions in the feed solution
N_n	number of mesh nodes for membrane discretization
$N_{positions}$	number of variables' positions. Each node is one position + the position outside the membrane feed surface and + 1 position outside the membrane permeate surface and the bulk of the permeate. The parameters of the bulk of the feed are not variables, i.e. concentrations are specified by the user and the electric potential is equal to 0.
ω	permeability per osmotic pressure difference at zero volume flux
p	pressure in bar
P_i	Spiegler-Kedem permeability
π	osmotic pressure in bar

Pe	Peclet number
Δp_e	effective pressure driving force in bar $\Delta p_e = \Delta p - \Delta \pi$
R	universal gas constant
ρ	mass density in kg/m ³
r_i	radius of ion i. In this work usually the Stokes radius, but depending on the physical meaning other size measures, e.g. cavity radius or hydrated radius could be more suitable
R_{int}	membrane intrinsic rejection
R_{obs}	apparent rejection
r_p	(mean) pore radius in m
S	entropy
σ	Staverman reflection coefficient
$S_{A,B}$	Selectivity of the membrane for ion A over B, defined as $S_{A,B} = \frac{1-R_B}{1-R_A}$
σ_x	membrane surface charge density
T	temperature in K
t	time
U_i	mobility of ion i
v_{cf}	cross-flow velocity
\bar{V}_i	molar volume of solute i
v_p	axial fluid velocity inside the membrane pores
$V_{s,i}$	specific volume of ion i
ΔW	dimensionless energy term. Difference in free energy.
x	axis normal to the membrane surface
Δx	Effective membrane thickness, equals pore length (equals membrane thickness times tortuosity)
Δx_e	Equivalent membrane thickness, equals effective thickness divided by porosity
z_i	i th ion's valence number

Indexes and exponents

<i>b</i>	<i>bulk</i>	bulk phase of the feed or the permeate
<i>Donnan</i>		electrical equilibrium at the membrane-solution interface (Donnan equilibrium)
<i>f</i>		feed
<i>in</i>		coinciding with the inside of the membrane-(feed/permeate)solution interface
<i>out</i>		coinciding with the outside of the membrane-(feed/permeate)solution interface
<i>p</i>		permeate
<i>s</i>		solute
<i>w</i>		water (as a representative solvent)

Abstract

Nanofiltration of real uranium-contaminated mine drainage was successfully discussed in experiments and modeling. For the simulation a renowned model was adapted that is capable of describing multi-component solutions. Although the description of synthetic multi-component solutions with a limited number of components was performed before ([Garcia-Aleman2004], [Gerald2006], [Bandini2003]) the results of this work show that the adapted model is capable of describing the very complex solution. The model developed here is based on:

- The Donnan-Steric Partitioning Pore Model incorporating Dielectric Exclusion – DSPM&DE ref. [Bowen1997], [Bandini2003], [Bowen2002], [Vezzani2002].
- The steric, electric, and dielectric exclusion model – SEDE ref. [Szymczyk2005].

The developed modeling approach is capable of describing multi-component transport, and is based on the pore radius, membrane thickness, and volumetric membrane charge density as physically relevant membrane parameters instead of mere fitting parameters which allows conclusions concerning membrane modification or process design.

The experiments involve typical commercially available membranes in combination with a water sample of industrial relevance in the mining sector.

Furthermore, it has been shown experimentally that uranium speciation influences its retention. Hence, all experiments consider the speciation of uranium when assessing its charge and size.

In the simulation 10 different ionic components have been taken into account. By freely fitting 4 parameters in parallel (pore radius, membrane thickness, membrane charge, relative permittivity of the oriented water layer at the pore wall) an excellent agreement between experiment and simulation was obtained. Moreover, the determined membrane thickness and pore radius is in close agreement with the values obtained by independent membrane characterization using pure water permeability and glucose retention. On the other hand, the fitted and the literature value of the relative permittivity differ by a factor of 2. This in turn has an influence on the membrane charge which is notably 60 times higher in order to compensate for the reduced contribution from the dielectric exclusion.

These results suggest that the developed model is capable of describing nanofiltration of concentrated, complex, real water samples to a high degree of precision. The way is thus paved for modeling and experiment, e.g. for nanofiltration of other complex mine waters.

I Introduction

Uranium is a hazardous substance due to its radiological and chemical toxicity. Uranium's radiotoxicity, originating from mainly alpha-decays, is low because all three major isotopes, ^{238}U (99.27% of U in the earth's crust, half-life $4.5 \cdot 10^9$ years), ^{235}U (0.72%, $7 \cdot 10^8$ years), and ^{234}U (0.0055%, $2.5 \cdot 10^5$ years), are relatively stable. Besides alpha decay which yields always the same products, an alpha particle and a nucleus with a mass number of four less, another path for the nuclear decay of uranium is fission which results in products in a certain distribution of mass and atomic numbers. In atomic energy production nuclear fission is industrially induced for energy production but it also occurs spontaneously in nature, however at a very low rate, e.g. for ^{238}U with a half-life of $8.1 \cdot 10^{15}$ years [Evans1955], [Siehl1996].

Nuclear radiation damages living tissue mainly by interactions with water molecules resulting in the formation of free oxygen radicals. This fact also explains the radioresistance of insects which is due to the low water content of their bodies (which would make them the major survivors of a worldwide nuclear holocaust) [Stabin2007].

A higher radiotoxic risk than that from uranium itself comes from its decay products, especially ^{230}Th (half-life $7.5 \cdot 10^4$ years) and ^{226}Ra ($1.6 \cdot 10^3$ years) [Siehl1996]. Radium poses an additional risk as it produces radon ^{222}Rn (3.8 days), an inert gas whose decay products can cause lung cancer [Merkel2006], an important fact that needs to be considered when working with uranium-contaminated water.

However, the hazards posed by uranium's chemotoxicity predominate its radiotoxic hazards [Merkel2013]. As described by [Busby2008] the chemotoxicity of uranium exhibits anomalous genotoxic effects. Generally, toxic elements bind strongly to biological molecules and cause, among others, enzyme poisoning, DNA deformation, and inflammation. As for other toxic elements, the affinity of uranium towards the phosphate groups of DNA is high, with a cell concentration as low as 23 ng l^{-1} reaching half saturation of the phosphate groups of chromosomal DNA (the half saturated DNA would contain 12 wt% U). For elements with high atomic number an additional effect plays an important role in DNA damage, the absorption of natural background radiation and re-emission as ionizing photoelectrons (beta radiation). Especially uranium, having an absorption cross section 500,000 times greater than that of water, shows high absorption of gamma and X-rays thereby focusing the energy into the DNA and causing increased genotoxicity. This means that ingestion of uranium is highly critical even at very low concentrations at which radiotoxicity would normally not be significant. The overall chemotoxicity of uranium in comparison to other toxic elements is illustrated in Table 1 by the occupational limits, a lower limit meaning higher toxicity.

Table 1: Occupational limits for heavy metals and their species, from [Busby2008].

	Cd	Cr	As, Co, Hg, Pb	U	Ni, Sb, V	Cu, Zn
Occupational limit (mg m^{-3})	0.015	0.05	0.1	0.25	0.5	1.0

1.1 Uranium's health effects

Despite its ubiquity in the environment uranium appears to have no metabolic function and is currently regarded as non-essential [Giddings2005]. As mentioned above, uranium possesses chemotoxicity, the mechanisms and effects of which should be described in more detail in this section.

A concise description of the mechanisms associated with uranium in the diet was given by [Bosshard1992] and compared to values for the amount of uranium humans typically take up. Actual daily intake via foodstuffs was in the range of 1 to 3 μg and for mining areas up to 9 μg per person per day, the data for different countries being in good agreement. Intake via drinking water showed much more variation depending on drinking habits and drinking water uranium concentrations, and can increase total intake to 100 μg per person per day, at the upper end.

A certain amount of the ingested uranium passes into the blood stream, gastrointestinal absorption of uranium being in the range of 0.5-5 % but even as high as 30 % of the ingested dose. Values differ depending on nutritional state, intestinal content and also age. For risk assessment an average absorption of 5 % is assumed.

Absorbed uranium leaves the body via the urinal tract. The chemical form in which uranium can pass through the glomeruli is a low molecular-weight uranyl bicarbonate complex. Once in the tubule the uranyl ion will partially dissociate from the bicarbonate, and may then be excreted or may react with the tubular cells. As physiological uranium concentrations are highest in kidney cells nephrotoxicity is the main symptom for uranium in the body. In human studies, the level of uranium kidney organ concentrations below which no nephrotoxic effects were observed, the no observable effect level (NOEL), was at 1 mg/kg. At an intake of 40 μg of uranium per person per day, which is the maximum estimated total daily intake in Switzerland, the steady-state kidney organ concentration would be 0.01 mg/kg, thus well below the NOEL. While kidney tubules are the most important site of the chemotoxic action of uranium, bone, in which uranium substitutes calcium and is deposited with a much longer biological half-life, is considered to be the critical organ for long-term radiation exposure to soluble uranium compounds.

Uranium excretion was studied in human trials of intravenous injection of uranium. Results showed that 95% of the injected uranium is cleared from the body through renal excretion with a biological half-life of 2 to 6 days. The remaining amount is lost with a half-life of 30 to 340 days. The 0.5% stored in the skeleton is lost with a half-life of 1500 days. [Busby2008] mentions that ingested uranium also targets lung, and, as recent evidence suggests, brain.

In the background document for the development of the World Health Organization's guideline for drinking-water quality [Giddings2005] health effects are thoroughly described. The primary effect of uranium's chemotoxicity to humans is nephritis. Three studies in Canada identified elevated urine albumin concentrations as an indicator for uranium induced nephritis. Tubular defects in the kidneys are the suggested explanation for the increase in urine albumin concentrations. One of these studies suggested that the uranium-induced tubular defect is rapidly reversible, as participants who have been informed of the situation and who have changed their water consumption, exhibited improved urine albumin concentrations.

Besides nephrotoxic effects uranium in the diet possesses reproductive and developmental toxicity, mutagenicity, and carcinogenicity, as investigated in animal studies [Giddings2005].

1.2 Uranium in the environment

Uranium is a ubiquitous lithophilic element with an average concentration in the continental crust of 1.7 mg/kg [Wedepohl1995]. Natural background levels in German soils (topsoil as well as subsoil) are typically in the range of < 0.5 mg/kg (sandy soils) to > 3 mg/kg (soils derived from magmatic and metamorphous rocks). Natural background levels for aquatic systems are dependent on the hydrogeologic source of the water. The mean uranium concentration in sea water is about 3.3 µg/l. Unaffected German groundwater has a uranium concentration in the range of 1 to > 100 µg/l. Due to erosion processes and the ubiquity of uranium also natural water sources contain measurable amounts of uranium. German stream concentrations vary from 1 to 3 µg/l [Merkel2012]. The Amazon bears 0.03 µg/l, while the Ganges contains 3.9 µg/l [Merkel2002].

The dissertation by Knolle [Knolle2009] gives the uranium contamination of 476 German tap water samples and 307 mineral water brands. In the context of his research the term “mineral water” refers to natural spa, mineral and table waters. The maximum observed concentrations were 8.54 µg/l and 474 µg/l for drinking water and mineral water, respectively. The average concentrations were 0.43 µg/l and 3.08 µg/l for tap and mineral water, respectively. Studies in other countries, as reported by the WHO [Giddings2005] yielded relatively low uranium concentrations as well. In a survey of 130 Canadian sites in Ontario, Canada concentrations were at an average of 0.4 µg/l. The mean uranium concentrations in New York ranged from 0.03 to 0.08 µg/l. The average uranium concentration for 978 sites in the USA was at 2.55 µg/l. The mean level in five Japanese cities was 0.9ng/l. The average uranium contamination of drinking water thus appears to be sufficiently low for human health. Uranium concentrations in 4097 German tap water samples are shown in Figure 1.

In Germany, mean uranium exposure is about twice as high for consumers of bottled water than for consumers of tap water [Hassoun2011] for both the regulatory limit is at 10 µg/l [TVO2011].

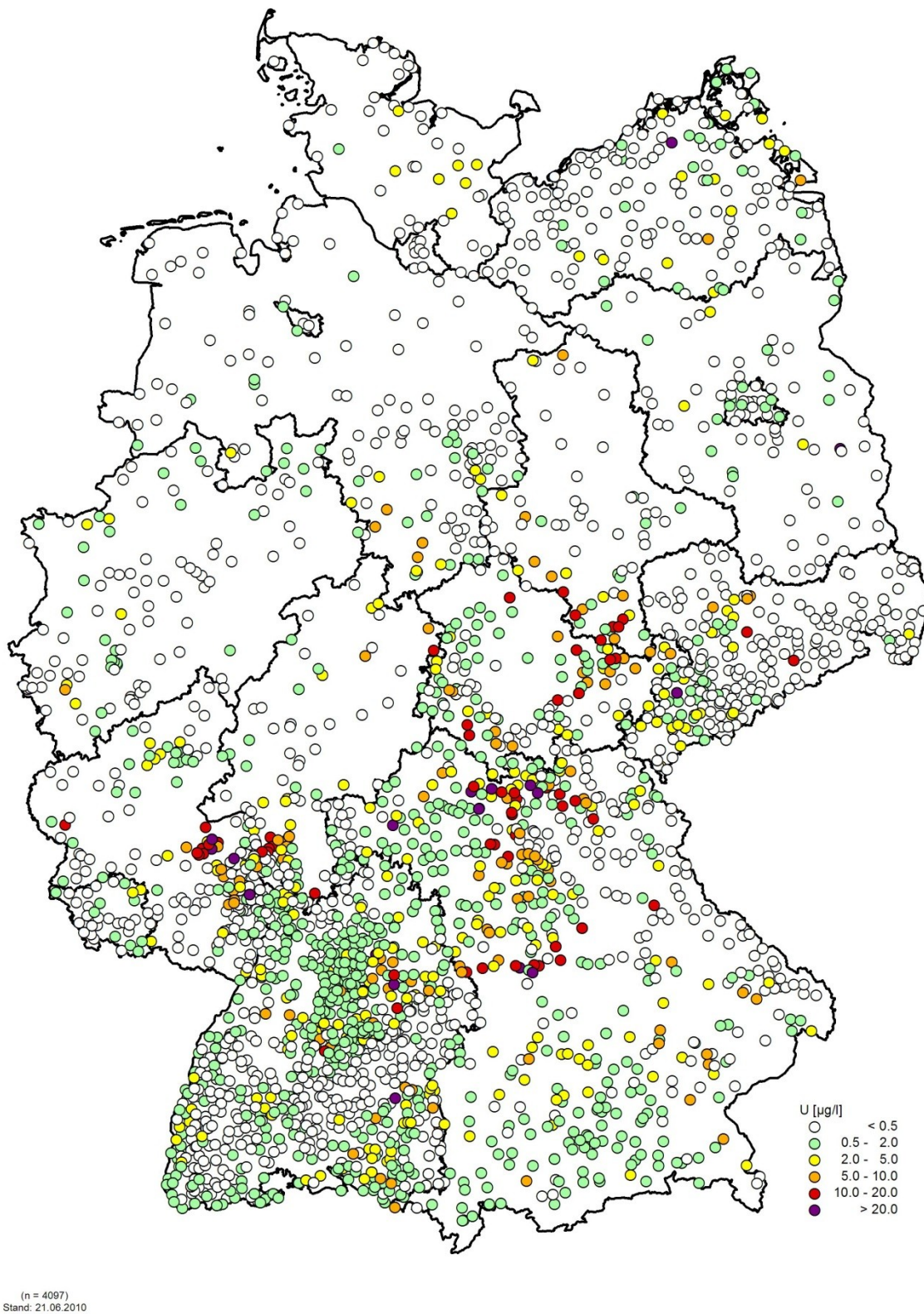


Figure 1: Regional distribution of U concentrations in German tap water (n= 4097), from [Hassoun2011].

However, maximum concentrations in drinking water can pose a considerable hazard to the local population. According to the WHO [Giddings2005], especially smaller supplies are at risk, also due to undermonitoring. Studies in Canada, Finland, and Norway discovered populations consuming drinking water with uranium concentrations of 700 µg/l, 28 µg/l, and >20 µg/l, respectively. Highest concentrations were found in well water near Helsinki with 14870 µg/l U [Knolle2009]. In Germany drinking water which exceeds the regulatory uranium concentration limit is also found in smaller supplies, as shown in Figure 2.

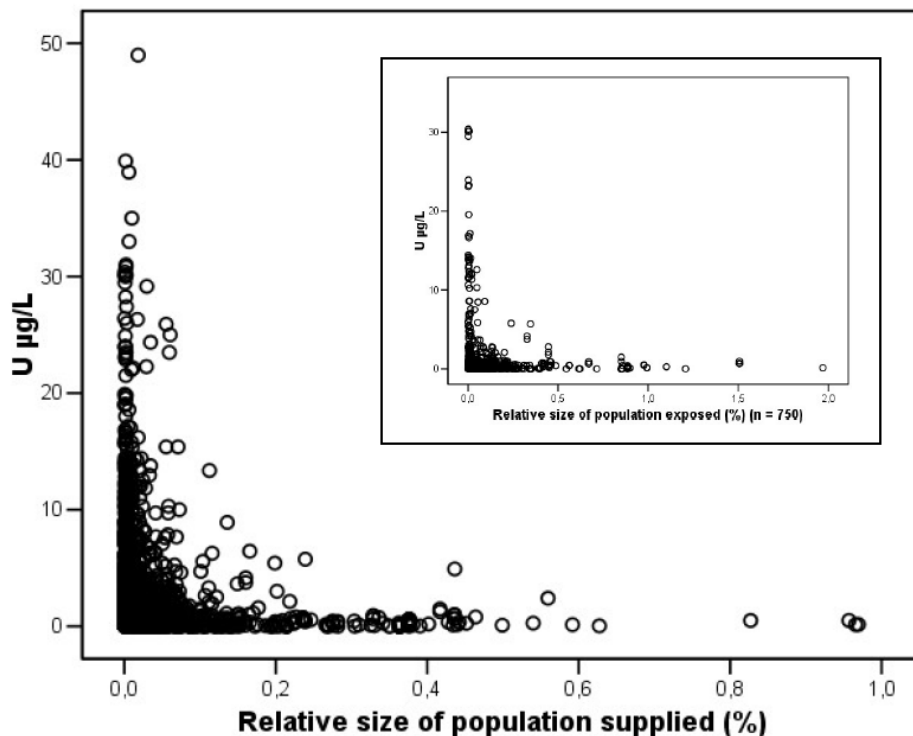


Figure 2: U concentration in 4095 German tap water samples and % of the population exposed of the total population observed (n = 60,354). Inlay graph: n = 750. Diagram from [Hassoun2011].

Regulatory limits for uranium concentrations are between the conflicting priorities of the clinical evidence and the best available technologies for treatment. This dilemma is intensified by uncertainties in clinical studies on the one hand and a general increase of uranium through non-point sources such as agriculture on the other hand [Hassoun2011]. The WHO recommends a provisional guideline value for uranium in drinking water of 15 µg/l [Giddings2005]. This value has been derived from a 91-day study in rats considering an intra- and interspecies variation uncertainty factor of 100 and assuming a 60 kg adult drinking 2 liters of drinking water per day and that an additional 20% of total daily uranium intake can be allocated to food. The study also acknowledges that treatment technology capable of reaching such low uranium concentrations is not always available. The WHO therefore concludes that a guideline value of 30 µg/l may be sufficient to prevent kidney toxicity regarding uncertainty in epidemiological studies. The limit for uranium in German drinking water has been set to 10 µg/l in November 2011 [TVO2011]. Requirements for waste water discharge into the receiving streams at an abandoned uranium mine in Germany was set to 500 µg/l [Metschies2013].

The natural valence states of uranium are +II, +III, +IV, +V, and +VI [Giddings2005]. Uranium exists in natural waters mainly in two oxidation states: In its hexavalent form U(+VI), and its tetravalent form U(+IV). In aquatic systems both oxidation states exist mainly as linear dioxocations UO_2^+ and UO_2^{2+} . Under reducing

conditions uranium in both oxidation states is virtually insoluble. Under oxidizing conditions U(+VI) is soluble even up to a pH as high as 7 in the range of several $\mu\text{g/l}$. Uranium readily forms complexes with inorganic ligands, such as carbonate, as well as with organic complexes. This formation of stable uranyl carbonato complexes translates into a positive statistical correlation between hydrogen carbonate concentrations and uranium contamination [Merkel2002].

In Germany, mineral phosphate fertilizer alone has contributed $14 \cdot 10^3$ t of uranium in the years from 1951 to 2011. This corresponds to 1 kg of uranium per hectare of agricultural area [Schnug2012]. The transfer coefficient of uranium from soil to crops is on average 0.05 (ratio of radioactivity in plant relative to soil [Frindrik1986]), comparable to As, Co, Hg, and Pb, no biomagnification effects being known, and thus, concerning human health risks, making the drinking water path more significant [Schnug2012]. Uranium intake via drinking water contributed 95 % of total intake [Schnug2012].

Another anthropogenic source of uranium is coal combustion. Although 99% of uranium is retained together with the fly ash during air pollution control there is no data available concerning the fate and proper disposal of the retained uranium. The amount of uranium from coal combustion can be calculated from available data on coal consumption and average uranium content and extrapolates to about 830,000 t over the years from 1937 to 2040 [Merkel2002].

The documented main influences on environmental uranium concentration are geology and phosphate fertilizer application. Only in special cases is the anthropogenic increase via mining the dominating factor for elevated uranium concentrations of a whole region [Merkel2002]. However, mining is a point source, producing high uranium concentrations in confined locations. Mining introduces oxygen into the natural mineral deposit, that way oxidize U(IV) to U(VI), thereby releasing considerable amounts of uranium into the environment that could be technologically avoided either by inhibiting water intrusion in order to eliminate the source of the contamination or by treatment of the polluted water, e.g. by nanofiltration.

1.3 Uranium mining in Saxony

Additional to geogenic uranium anthropogenic sources increase natural U concentrations on a local and global level. Global contamination can arise from use of uranium-contaminated phosphate fertilizer and burning of fossil fuels. Local anthropogenic sources are industry, nuclear energy, and uranium mining and ore processing [Knolle2009]. Of these local sources the high concentrations that can occur in mining effluent are within the focus of this work.

Between 1945 and 1989 more than 231,000 t of U were produced in the two East German Federal States Saxony and Thuringia [Merkel2006]. Figure 3 shows the locations of these uranium mining sites.

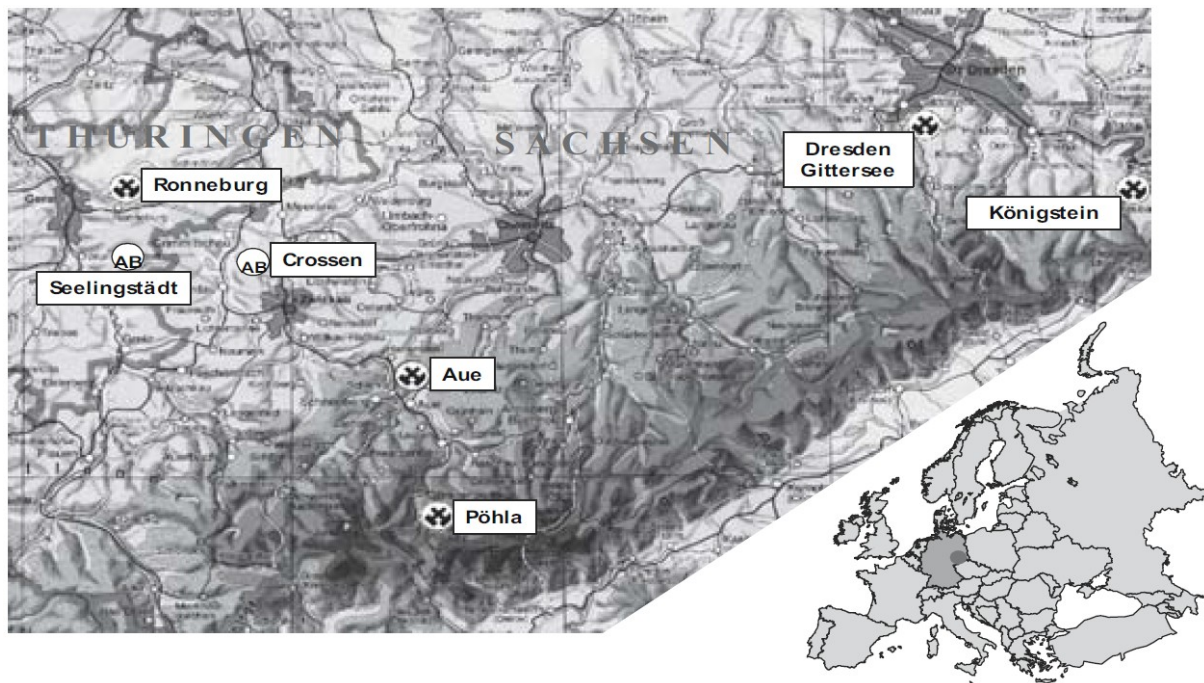


Figure 3: Mining and milling sites in eastern Germany of the Wismut SAG. (AB stands for milling site) [Wismut2014]

Uranium mining activities affected an area of approximately 100km² and left behind probably the “worst” uranium-mining legacy in the world [Merkel2006]. At the time of production closure in December 1990 the burden consisted of: Operations areas (37 km²), five large underground mines, and an open pit mine (84·10⁶ m³), mine tailings (311·10⁶ m³), and ponds filled with radioactive sludge (160·10⁶ m³) [Wismut2011].

In response to the environmental challenges a special “Wismut Act” was passed by the Federal Parliament, providing € 6.2 billion to the national corporation Wismut GmbH, an organization that was established for the purpose of the cleanup [Merkel2012]. By 2012, a total of € 5.65 billion were used for remediation, the remediation expenses in Saxony amounting to € 2.66 billion and in Thuringia to € 2.99 billion [Wismut2012].

The total amount of uranium that has been subject to remediation when production has been terminated in 1991 was in the order of 30,000 t [Merkel2012]. As a result of remedial actions considerable amounts of uranium have been already removed from soil and water, and discharges into the environment continuously decreased. Uranium is released via controlled and diffuse discharge. Controlled discharge is necessary as complete uranium removal is not feasible at all sites. In 1991 the controlled discharge of uranium to receiving streams totaled ca. 27 t and decreased to 4.4 t in 2010. However, diffuse discharge also contributes to total environmental burden, for example in Schlema (see Figure 3), where in 2010 controlled discharge amounted to 2.7 t of uranium, diffuse discharge is estimated to release an additional quantity of 20 % of the controlled discharge into the adjacent river, Zwickauer Mulde. This increases the river’s uranium concentration to an average of 8 µg/l in 2010 [Merkel2012].

As the uranium-contaminated drainage transports uranium into the environment the mine’s reserves of soluble uranium decrease over time. Figure 4 illustrates this concentration decline for the four major former uranium mines in Saxony.

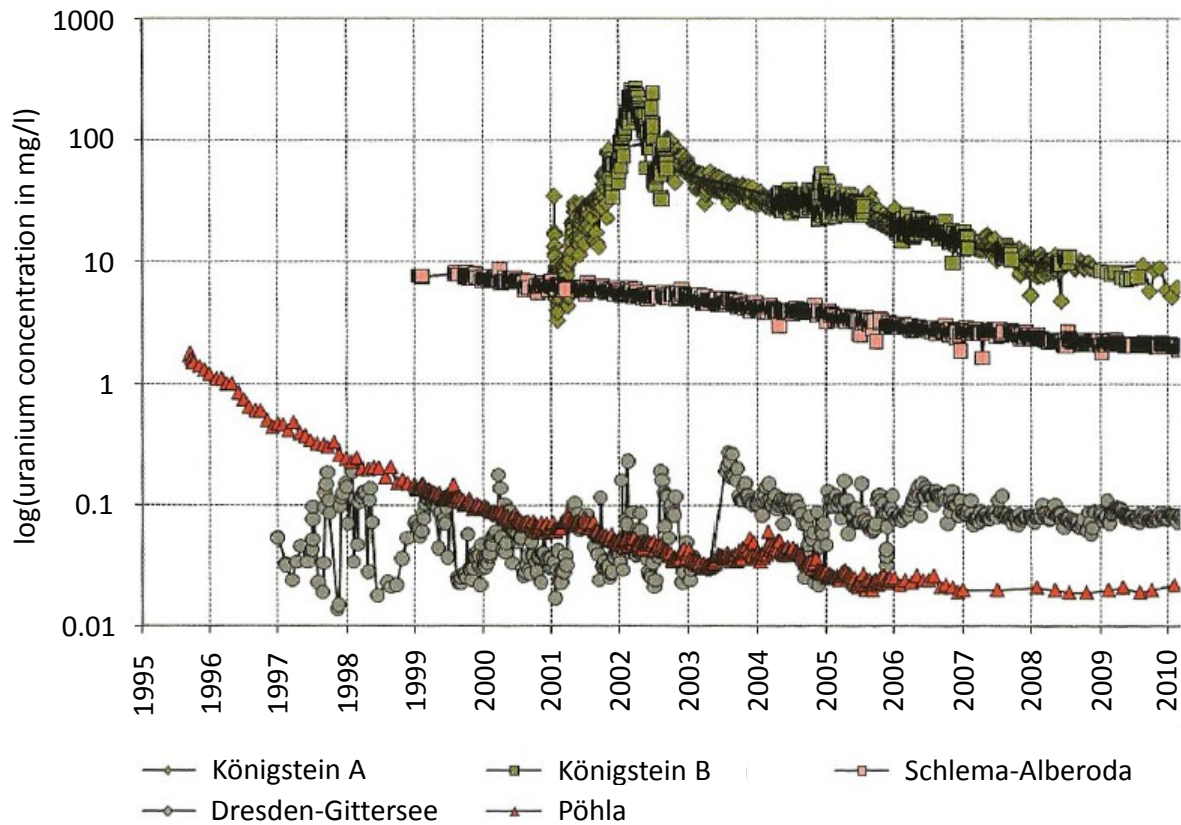


Figure 4: Development of effluent uranium concentrations at four Wismut locations [Paul2011].

This uranium concentration decline in the mines' effluent arises the need to adapt treatment technologies in order to meet the changing requirement. Process hybridization using membrane filtration could increase flexibility and adaptability of existing treatment technologies. Membrane filtration is currently not applied during treatment of the effluent from former uranium mines located in Saxony.

Uranium is a naturally occurring, ubiquitous element found in the environment, food, and also, at very low doses, in the body of healthy humans. Its toxicity is well researched and understood in order to release regulatory limits and safety standards for, e.g. the uranium concentration in drinking water (e.g. 10 µg/l) and mine water discharge (e.g. 500 µg/l). In those cases, however, where safe levels for uranium concentrations are being exceeded and where the safety of humans and the environment are at risk, reliable and efficient water treatment is necessary. Such cases include obvious examples such as abandoned uranium mine sites but also less expected and even more grave examples such as several sources for drinking water, also in Germany.

1.4 Chemical speciation

In aqueous solution a chemical element interacts, not only with water, but with all other elements in that solution forming certain chemical forms, the so called species. As a result a certain distribution of these chemical forms develops, called speciation. Influences on speciation include temperature, pH, concentration, and available ligands. The influence of the pH for an example uranium solution is shown in Figure 5.

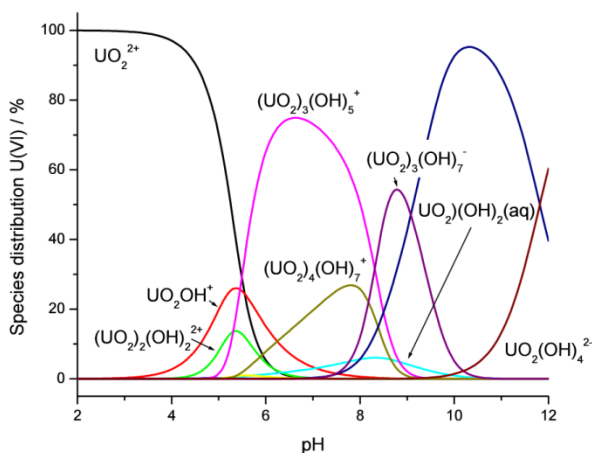


Figure 5: pH-dependence of uranium speciation [Bernhard2005].

As shown in Figure 6, knowing the speciation is important for feed ion characteristics, as it influences size, charge, mobility, and sorption behavior, etc. This makes speciation an important influencing factor for membrane separation.


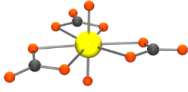
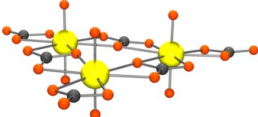
Steric model	Chemical equation	Size	Charge
	$[UO_2]^{2+}$	Small	+2
	$[UO_2(CO_3)_3]^{4-}$	Large	-4
	$[(UO_2)_3(CO_3)_6]$	Very large	0

Figure 6: Illustration on the speciation's influence on ion size and charge. Steric model adapted from [Graziani1972].

Numerous studies have focused on the influence of speciation on membrane filtration with a special focus on the interaction between the charge and size of the species and the observed membrane separation. Section 1.6 will focus on available literature on nanofiltration of uranium-contaminated water.

1.5 Nanofiltration

Membranes are thin layers that allow selective transport of permeable feed constituents and have some degree of rejection for the non-permeable constituents. Membrane processes are a separation technology of increasing importance in the process intensification strategies solving some of the major problems of our modern societies by decreasing raw materials utilization, energy consumption, equipment size, and waste generation [EMST2013 page 77]. Every year membranes and membrane processes are sold worth in excess of 1 billion Euros [Bowen2009].

A plethora of different membrane processes exists. Nanofiltration belongs to the pressure-driven membrane separation processes and has intermediate properties between ultrafiltration and reverse osmosis. Figure 7 shows the current classification of this membrane category. This classification has changed over time and the term “nanofiltration” was introduced well after such membranes were developed [EMST2013 page 1275]. Research on nanofiltration started in the 1970s when “low-pressure reverse osmosis membranes” were developed to reduce the energy consumption of sea water desalination. Drinking water softening was the second field where this newly developed membrane technology found an application and is still in use today [Bruggen2002].

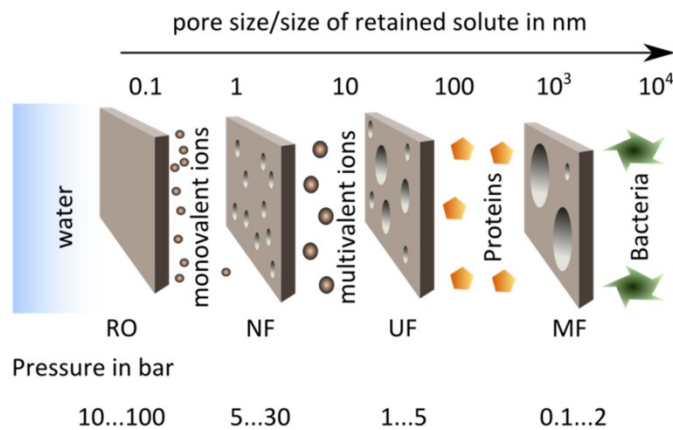


Figure 7: Classification of the pressure driven membrane processes reverse osmosis (RO), nanofiltration (NF), ultrafiltration (UF), and microfiltration (MF) [Melin2007].

In the second half of the 1980s nanofiltration emerged as a separate technology because the ability of selective separation of certain substances offered advantages for applications like, e.g. the removal of color, organic matter, and hardness from drinking water sources [EMST2013 page 1275]. The founding father of NF who introduced the term NF for this separate technology was [Eriksson1988]. This new terminology was necessary because previous distinctions between reverse osmosis and ultrafiltration became obsolete when “loose” or “low-pressure” reverse osmosis membranes were developed to have lower energy consumption than conventional RO. The name nanofiltration was based on the observation that these membranes reject molecules of the size of about one nanometer. Due to the lower energy requirements of this separation technology interest continues to grow, as visualized in Figure 8.

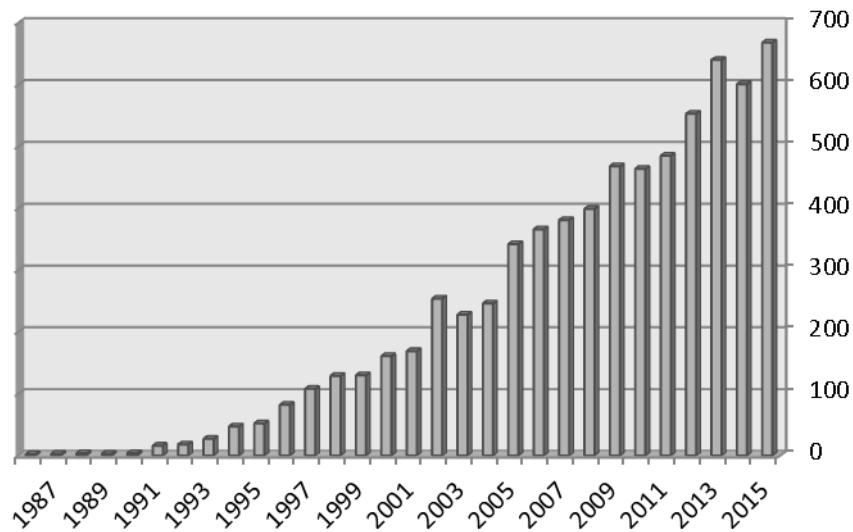




Figure 8: Research activity in nanofiltration continues to grow: Articles on Scopus that contain “nanofiltration” in their title, abstract, or key words. Retrieved on 2016/03/06.

Fields of application for nanofiltration are drinking water treatment, electroplating, the textile industry, and the food industry [Boussu2006]. The NF market is found 65% in water treatment, 25% in the food and dairy industry, and less than 10% in the chemical industry [Bessarabov2002]. But as mentioned earlier membrane operations find applications in various industries via process intensification as they offer several benefits, such as energy efficiency (no phase change required), environmentally friendly (limited or no addition of chemicals required), modularity, compactness [EMST2013 page 78].

Most commercial NF membranes are made of polymeric material, and have an asymmetric structure with a highly permeable support layer covered by a functionally active porous top layer at the feed side [Oatley2013]. They can further be categorized into two groups that are characterized by the employed material and synthesis as shown in Table 2.

Table 2: Characteristics of the two main categories of nanofiltration membranes, [EMST2013 page 1277].

	“tight” NF membranes	“loose” NF membranes
Properties close to	Reverse osmosis	Ultrafiltration
Typical materials	Made from different materials. Composite structure: 1) nonwoven support, 2) polysulfone sublayer, 3) top layer made of polyamide (mechanically resistant), or polyimide (high permeability) [Ekiner2006]	Made from one material. E.g. poly(ether)sulfones
MWCO	About 200 Da	500...1000 Da
Typical rejections	Ca ²⁺ , SO ₄ ²⁻ > 99 % Na ⁺ , Cl ⁻ 60...90 %	Ca ²⁺ , SO ₄ ²⁻ 90...99 % Na ⁺ , Cl ⁻ 10...60 %
Synthesis	Top layer formation by interfacial	Phase inversion via the following

	<p>polymerization by the following steps:</p> <ol style="list-style-type: none"> 1) Sublayer immersed in aqueous amine solution 2) Sublayer subsequently immersed in organic acyl chloride solution 3) amine and acyl chloride react to form top layer 	<p>alternatives:</p> <ol style="list-style-type: none"> a) immersion precipitation (immersion in a nonsolvent bath) b) controlled evaporation c) thermal precipitation (lowering the temperature) d) precipitation from vapor phase
Illustration from [Melin2007]	Asymmetric composite “Ward Riley” membrane	Integral asymmetric “Loeb Sourirajan” membrane
		

The separation mechanisms are sieving, electrostatic interactions between membrane and charged species, differences in diffusivity and solubility, differences in Born solvation energy, and dielectric exclusion [Labbez2003]. Additional phenomena that affect membrane performance are ion-membrane affinity, specific adsorption, reduced dielectric permittivity, and hydration [Garcia-Aleman2004]. Polarity also plays a role [EMST2013 page 1277]. [Yaroshchuk1998] gives a good overview of the interrelation between these mechanisms.

1.6 Nanofiltration of uranium-contaminated water

Nanofiltration is a proven technology for the treatment of uranium-contaminated water. Several studies are concerned with this topic motivated by different backgrounds, such as uranium fuel production and drinking water treatment. First studies investigated the influence of feed uranium concentration and pH on separation performance without taking into account that these are important parameters determining feed speciation.

Already in 1976 a study by [Sastri1976] using cellulose acetate membranes with uranyl sulfate solutions achieved uranium retentions in the range of 91 to 99.8 %. A main component of their research was to investigate the UO_2SO_4 concentration's influence on retention, increasing the concentration from 100 to 8000 mg/l (i.e. uranium concentration of 65 to 5200 mg/l). Up to a uranium concentration of about 650 mg/l the retention increases, whereas exceeding this concentration yielded a tendency of declining retentions. For uranium-phobic membranes, i.e. membranes with higher average uranium retentions, retention decreases at higher retentions. Nevertheless, for all 6 membranes in the study the lowest concentration yielded the lowest retention, indicating a positive correlation between uranium concentration and retention.

The work presented by [Chen1992] reports that the uranium conversion process during nuclear fuel production generates besides uranium nitrate effluent also uranium fluoride effluent. The scope of the study was to remove uranium in a selective fashion by taking the effect of the pH into account. The author shows that uranium retentions remained above 90 % for all values of pH. At the lowest pH (2.8) in the study, a very

high retention (100 %) was achieved and reproduced 3 times. The author does not give an explanation for the increased uranium retention at low pH. The applied polyamide membrane, Filmtec's FT-30 element SW30-2521, had low rejection for fluoride at acidic conditions and low rejections for ammonium at alkaline conditions, indicating an isoelectric point in the lower pH range. This could mean that the positively charged membrane (as the experiment is run at low pH) repels the positively charged uranium better or even that a new species formed.

Later studies increasingly took into account that uranium speciation has an influence on retention and the active separation mechanism. This idea was first mentioned by [Prabhakar1992] as a possible explanation for the unexpected positive correlation between uranium concentration and retention.

The effluent from nuclear fuel production, containing uranium mainly as uranium nitrate, was treated in a study by [Prabhakar1992] using cellulose acetate RO membranes. Concentrations that are normal for this effluent are in a range of up to 200 mg/l. The experiments were performed at 40bar. Retention increased with increasing feed uranium concentrations for all membranes and for all uranium concentrations, ranging from 20 to 200 mg/l. The relation was more pronounced at uranium concentrations below 100 mg/l. The authors also found that the relationship between feed uranium concentration and retention was highest for membranes with a pore size of about 25 Å and that the effect decreased for tighter and more open membranes. Such a concentration dependency is in disagreement with models for membrane separation. The authors hypothesize that this disagreement could be due to changes in the uranium speciation at increasing uranium concentration. The data presented did not show the same trend for the inflection point as in [Sastri1976] indicating an additional dependence besides uranium concentration, potentially the concentration of other elements involved in complex formation.

The promising results for the treatment of uranium nitrate effluents using cellulose acetate membranes motivated Prabhakar [Prabhakar1996] to use chemically and physically more resistant polyamide UF, NF, and RO membranes to investigate the effect of addition of sulfates, which are expected to enhance uranyl rejection. The positive correlation between uranium feed concentration and retention that was found for the cellulose acetate membranes could be replicated for NF. The study shows that the type of membrane is paramount as it determines the available separation mechanisms.

The first study specifically adjusting feed uranium speciation was performed by [Raff1999] who investigated the influence of uranium speciation on retention by five different NF membranes. Experiments were performed with four different artificial solutions with a uranium concentration of 1 mg/l. Solutions differed in carbonate content, starting from de-ionized water at pH 6.7, then increasing the pH by addition of NaHCO_3 to reach pH 8.3, 7.3, and 5.9. The carbonate concentration was increased in order to alter the speciation towards negatively charged uranyl carbonate complexes that way also increasing uranium retentions, which were above 95 % for the negatively charged complexes $\text{UO}_2(\text{CO}_3)_2^{2-}$ and $\text{UO}_2(\text{CO}_3)_3^{4-}$. The permeate quality was stable, high retentions, between 81 % and 99 %, were achieved during all experiments for all 5 different NF membranes, i.e. including the positively charged species $(\text{UO}_2)_3(\text{OH})_5^+$ and the uncharged complex UO_2CO_3^0 . The researchers proved that high uranium retentions are feasible with nanofiltration and a first step towards the influence of speciation on membrane separation performance was taken, pointing out the importance of charge effects for the retention of uranyl species. However, a separation between the effects of speciation and the effects of the membrane charge, which simultaneously influence retention, has not been achieved.

To take the uranium speciation into account also for more complex feed compositions numerical speciation calculation is necessary. Different speciation codes are available on a commercial and a freeware level.

In the study by [Favre-Réguillon2008] nanofiltration was used to selectively remove uranium from drinking water. The experiments were done for semi-real waters, using bottled mineral water with artificially increased uranium concentrations to 2 mg/l by addition of uranyl nitrate $\text{UO}_2(\text{NO}_3)_2 \cdot 6\text{H}_2\text{O}$. As for these waters no literature data exists concerning speciation, as opposed to the case for the artificial solutions used by [Raff1999], the species distribution needed to be determined using a speciation code, namely the code “Chess”. The solutions differed in their ionic strength, however, the main species was $\text{UO}_2(\text{CO}_3)_2^{2-}$ for all three waters. The performance of three different membranes was distinctly different, with uranium retentions of about 20 %, 90 %, and close to 100 %. The membrane with the highest selectivity for uranium against alkaline and alkaline-earth ions was then used at a lower uranium concentration. However, when decreasing the uranium concentration from 2 mg/l to 20 µg/l the retention remained at 95 % and the selectivity for uranium against sodium at about 16. Increasing the trans-membrane pressure from 1 bar to 4 bar increased the retention from 95 % to 98 %. The cross-flow velocity inside the plate module was kept at the relatively low value of 0.145 m/s and the influence of hydrodynamics has not been investigated. The authors concluded that nanofiltration is capable not only of high retentions but also of high selectivities and that charge effects determine the retention of uranium.

The review article by [Khedr2013] concluded that RO and NF are in certain aspects superior to the most common conventional methods of ion exchange resins, chemical precipitation, coagulation, and adsorption on surface active media. While RO and NF efficiently retained uranium and radium they cannot be used to remove gaseous pollutants such as radon. Thus an additional aeration step for membrane treatment of uranium-contaminated water is necessary. Nevertheless, the author emphasized the advantages of membrane processes: high retention of all isotopes, low vulnerability to interference with similar ions, regeneration-free operation, and reliability.

The full-scale plant study by [Montana2013] compares, with respect to the same feed stream, the performance of membrane filtration for uranium removal to ultrafiltration, sorption on activated carbon, ozonation, and sand bed filtration, showing that membrane filtration can reach a uranium radioactivity removal rate of 90 %, on average, where conventional treatment methods were not able to produce a significant decrease in radioactivity levels at all.

Nanofiltration attracts increasing attention and finds further applications in many different industries. Since the effects inside a nanofiltration membrane allow for a separation of differently sized and charged ions water treatment of uranium contaminated water is an obvious application. Several experimental studies approached the topic but a rigorous description of the separation process has not been approached yet. Such a description is complicated due to the complex interplay between chemical effects, such as altered uranium diffusivity by the speciation in which uranium is present, together with the nanoscale transport in nanofiltration membranes.

2 Motivation and objectives

Motivation to develop water treatment technologies for the removal of the toxic substance uranium is continuously amplified by current events and developments: wide-spread environmental pollution due to uranium in phosphate fertilizer, radioactive fallout after the disaster at the nuclear reactor at Fukushima, but also the stricter regulatory limit for uranium in drinking water which was enacted by German authorities in November 2011 which was set to 10 µg/l [TVO2011].

A growing number of models for nanofiltration of aqueous solutions are available for the advancement of membrane development and process design. To date, these models have been applied only to synthetic solutions with a limited number of ionic species, such as textile waste waters. The simulation of experiments involving real uranium-contaminated water samples and commercially available membranes has not been attempted yet. However, since membranes are mostly applied to multi-component solutions, e.g. sea water or waste water, it is of high importance to evaluate the capability of the currently available models to describe such complex separations.

Industrially relevant multi-component uranium-contaminated mine water was chosen as an example of a complex solution involving ions of strongly differing properties and including effects of chemical speciation. Among the models described in the literature some models will be most suitable for the here treated case of uranium mine water. The selection criteria are:

- The model must be capable of describing concentrated solutions, and multi-component transport,
- The model should be based on physically relevant parameters instead of mere fitting parameters (in order to derive statements concerning membrane modification or process design in order to improve the observed separation in future research),
- The model input constants and parameters need to be readily available.

Consequently, this thesis starts from the adaptation of a generally accepted model from the literature and then targets a case study of industrial relevance and properties comparable to other multi-component solutions. Furthermore, because uranium is characterized by complex speciation chemistry the question will be solved if uranium should be modeled as ion or as a complex for the description of its transport.

The membranes will be selected to represent a broad range of nanofiltration membranes. The prerequisites for such membrane research, e.g. the development of a state-of-the-art laboratory membrane test facility, are based on an intensive literature survey and will be presented only in brief.

This thesis is embedded within the framework of research targeting an optimized and environmentally friendly water treatment process for uranium-contaminated water. Considering the approach and outcomes of this study will thus benefit similar research efforts on e.g. nanofiltration of other complex mine waters.

3 Mass transfer in NF membranes – existing modeling approaches

Rigorous modeling of mass transfer through nanofiltration membranes needs to take electrostatic, dielectric, steric, and hydrodynamic effects into account. The fact that all these effects happen simultaneously and are thus all intertwined makes not just the mathematical description complicated but also a concise experimental investigation more laborious and time consuming. In addition, the pore of an NF-membrane is roughly within the range of the size of the molecular gap of the polymer of the membrane matrix and about 4 water molecules fit within such a pore when aligned along its diameter. Consequently, traditional methods used to describe transport at larger length scale start to break down at the scale of these nanometer structures.

The group of nanofiltration models that has been used to describe transport in the beginning of nanofiltration modeling overcame this complication by treating the membrane as a black box model. This group of phenomenological, i.e. mechanism-independent models, is based on irreversible thermodynamics, as shown in Figure 9, and will be described in more detail in Section 3.1.

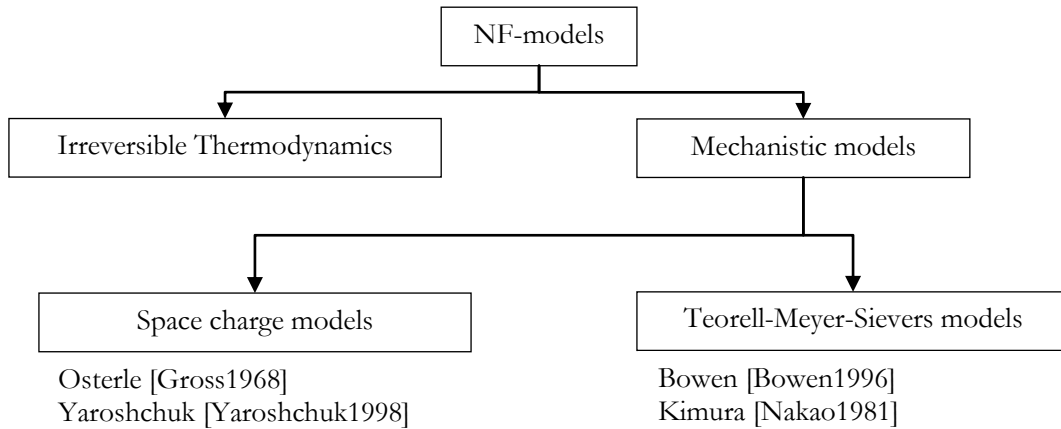


Figure 9: Modeling approaches for nanofiltration according to [GarciaAleman2004].

The second group, i.e. the mechanistic models, shown in Figure 9, consists of models that develop a model representation of the physical membrane structure, thereby accounting for the physical and chemical characteristics of membrane and surrounding solution. Although initially the mechanistic models require more assumptions, such as membrane thickness, pore size, and charge, they are much better suited to investigate the transport processes through the membrane in order to be able to make predictions.

Most mechanistic models fall in two categories [Fievet2002]:

- those based on the space-charge (SC) model proposed by Osterle
- the Teorell-Meyer-Sievers (TMS) model

The distinction between these two categories is sometimes difficult since they are similar and even hybrid models have been developed [Bowen1996], [Bowen1997], [Schaep1999], [Schaep2001]. Hence, the differences between the different approaches for mechanistic models will be reviewed together in Section 3.2.

3.1 Irreversible Thermodynamics

One of the two main groups shown in Figure 9 are models based on irreversible thermodynamics. Thermodynamic descriptions are applied when the structure of the membrane as well as the molecular mechanisms of transport within the membrane are not fully understood [Soltanieh1981]. Since membrane permeation is an irreversible process and entropy will increase, i.e. energy is dissipated which is reflected by the dissipation function, given by the equation [Sievertsen2001]:

$$\phi = T \frac{dS}{dt} = \sum_i j_i \cdot F_i \quad (3.1)$$

Where F_i are all forces that are acting on the system, represented often by the negative electrochemical potential gradients of the i components that the system consists of. One basic assumption of irreversible thermodynamics is already implemented in this expression, which is the division of the system into subsystems denoted by index i . Since the subsystems often correspond to the solution components (e.g. ions) the same index i is used for these two independent system variables, which is not strictly true. A second important assumption is local equilibrium. For systems close to equilibrium, which is assumed at the microscopic scale despite the obvious absence of an equilibrium at a macroscopic scale (i.e. between feed and permeate), a linear relationship between fluxes and forces can be assumed. The basis of the linear irreversible thermodynamics theory for transport through nanofiltration membranes is the Onsager theorem [Onsager1932] which expresses the diffusive fluxes in a multi-component system in terms of a linear matrix of phenomenological coefficients, L_{ik} , together with the respective driving forces, i.e. the gradients of the electrochemical potentials:

$$j_i = - \sum_{k=1}^s L_{ik} \nabla \bar{\mu}_k, \quad (i = 1, 2, \dots, s) \quad (3.2)$$

Where the electrochemical potential $\bar{\mu}_k$ depends on the chemical μ_k , and the electrical φ_k potential according to $\bar{\mu}_k = \mu_k + e \cdot \varphi_k$. The electrochemical potential is solely a characteristic of the surrounding feed and permeate solution and is not related to the physical measurable properties of the membrane material. In other words, the membrane is treated as a black box without a description of solute transport within the membrane matrix, which makes it impossible to include structural and electrical properties of the membrane [EMST2013 page 1858]. Onsager further proposes the reasonable assumption that molecular dynamical systems possess symmetry in past and future which consequently makes the matrix L_{ik} symmetrical, also called the Onsager Reciprocal Relationship (ORR):

$$L_{ik} = L_{ki} \quad (3.3)$$

The coefficients must also be larger or equal to zero, as well as limited in their magnitude because the dissipation of energy must be positive ($\phi > 0$):

$$L_{ii} \geq 0 \quad (3.4)$$

$$L_{ii} \cdot L_{kk} \geq L_{ik}^2 \quad (3.5)$$

The most important membrane models, based on irreversible thermodynamics, were developed by Kedem-Katchalsky [Kedem1958] and Spiegler-Kedem [Spiegler1966] which are given in the next paragraph. In these models the phenomenological coefficients L_{ik} are transformed to the less concentration dependent coefficients L_p , σ , and ω for Kedem-Katchalsky and the coefficients of Spiegler-Kedem P_s , and P_w which are even less concentration dependent as they have been derived on a local level inside the membrane.

When the membrane itself is considered as a thermodynamic component irreversible thermodynamics can be used to derive the Extended Nernst-Planck equation. Since the frame of reference, previously fixed with respect to water can now be fixed to the membrane, the water flux appears in the equation in the form of a convective transport term.

3.1.1 The Kedem-Katchalsky model

The first application of irreversible thermodynamics to membrane filtration consisting of an aqueous solution (index w) and a single electrolyte (index s) was implemented in the Kedem-Katchalsky model [Kedem1958]. A brief illustration is shown in Figure 10.

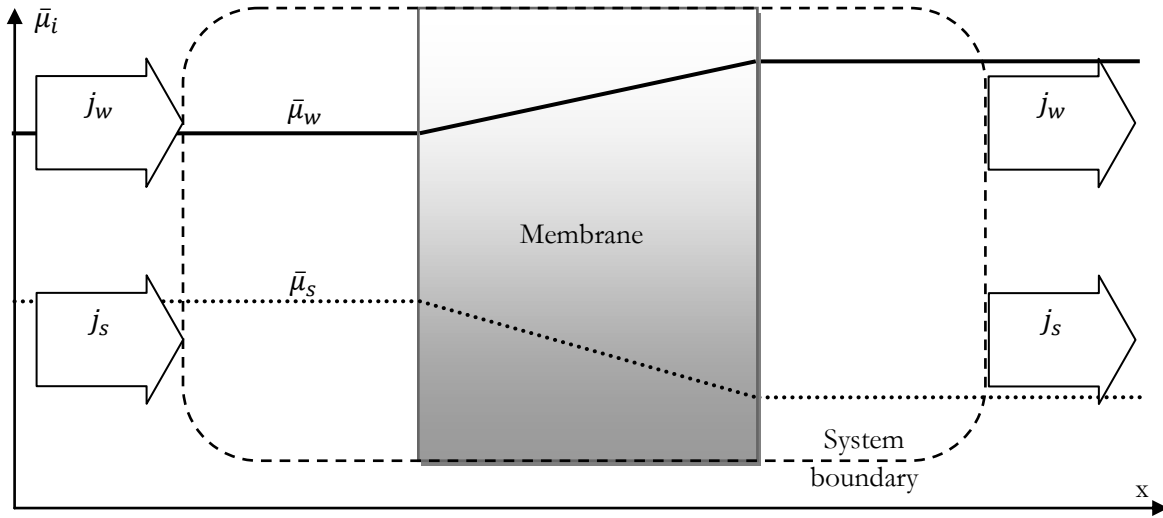


Figure 10: Schematic representation of the two component system of the Kedem-Katchalsky model.

For this simple system, the dissipation function ϕ of equation (3.1) reduces to:

$$\phi = T \frac{dS}{dt} = j_w \Delta \bar{\mu}_w + j_s \Delta \bar{\mu}_s \quad (3.6)$$

For uncharged membranes the electrical potential term of the electrochemical potential can be neglected:

$$\Delta \mu_w = \bar{V}_w (p_p - p_f) + RT (\ln a_{w,p} - \ln a_{w,f}) \quad (3.7)$$

$$\Delta \mu_s = \bar{V}_s (p_p - p_f) + RT (\ln a_{s,p} - \ln a_{s,f}) \quad (3.8)$$

Under the assumption of dilute solutions (which is already an assumption of the Onsager theorem) the activity of the salt component can be set to 1 and the van't Hoff equation can be used to simplify the potential terms to yield:

$$\Delta \mu_w = \bar{V}_w (\Delta p - \Delta \pi) \quad (3.9)$$

$$\Delta \mu_s \approx \bar{V}_s \Delta p + \Delta \pi / \bar{c}_s \quad (3.10)$$

Where the average membrane concentration is defined as:

$$\bar{c}_s = \frac{c_{s,f} - c_{s,p}}{\ln(c_{s,f}/c_{s,p})} \quad (3.11)$$

The dissipation function can now be written as:

$$\phi = (j_w \bar{V}_w + j_s \bar{V}_s) \Delta p + (j_s / \bar{c}_s - j_w \bar{V}_w) \Delta \pi \quad (3.12)$$

In this relationship the total volume flux J_v and the diffusive flux J_d can be defined by:

$$J_v = j_w \bar{V}_w + j_s \bar{V}_s \quad (3.13)$$

$$J_d \approx j_s / \bar{c}_s - j_w \bar{V}_w \quad (3.14)$$

In a similar fashion as for equation (3.2) the here defined fluxes and forces can be expressed as:

$$J_v = \mathcal{L}_{11} \Delta p + \mathcal{L}_{12} \Delta \pi \quad (3.15)$$

$$J_d = \mathcal{L}_{21} \Delta p + \mathcal{L}_{22} \Delta \pi \quad (3.16)$$

Here, the coefficient $\mathcal{L}_{11} \equiv L_p$ is called permeability of the membrane and the reflection coefficient, which corresponds to the solute fraction rejected by the membrane, is defined as:

$$\sigma = -\mathcal{L}_{12} / \mathcal{L}_{11} \quad (3.17)$$

Often the focus of a membrane separation is placed on the salt flux which can be obtained by rearranging equation (3.13) and (3.14) (under the assumption that $\bar{V}_s \bar{c}_s \ll 1$):

$$j_s = (J_v + J_d) \bar{c}_s \quad (3.18)$$

The Kedem-Katchalsky model as described in [EMST2013 page 1280 and 1859]: The volumetric flux J_v and the solute flux j_i can be described by:

$$J_v = L_p (\Delta p - \sigma \Delta \pi) \quad (3.19)$$

$$j_s = \bar{c}_s (1 - \sigma) J_v + \omega \Delta c_s \quad (3.20)$$

In which ω is the solute permeability per osmotic pressure difference at zero volume flux, defined by:

$$\omega = \frac{L_p \mathcal{L}_{22} - \mathcal{L}_{12}^2}{\mathcal{L}_{11}} \bar{c}_s = \left(\frac{j_s}{\Delta \pi} \right)_{J_v=0} \quad (3.21)$$

The solute permeability is always positive according to equation (3.5).

The advantage of this model is that many of the model parameters are accessible for experimental determination. For this, equation (3.20) can be rewritten as:

$$\frac{j_s}{\Delta c_s} = \omega_s + (1 - \sigma) J_v \frac{\bar{c}_s}{\Delta c_s} \quad (3.22)$$

By plotting this relationship, as shown in Figure 11, the membrane-solute specific parameters can be estimated.

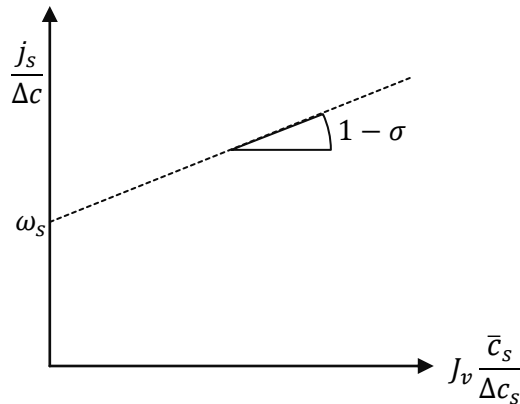


Figure 11: Graphical estimation of solute permeability and reflection coefficient, [EMST2013 page 1281].

3.1.2 The Spiegler-Kedem model

The Spiegler-Kedem model [Spiegler1966] is the differential analogous of the Kedem-Katchalsky model and the following equations are derived under the same assumptions including $\bar{V}_s \ll 1/c_s$:

$$\frac{d\mu_w}{dx} = \bar{V}_w \left(\frac{dp}{dx} - \frac{d\pi}{dx} \right) \quad (3.23)$$

$$\frac{d\mu_s}{dx} = \bar{V}_s \frac{dp}{dx} + \frac{1}{c_s} \frac{d\pi}{dx} \approx \frac{1}{c_s} \frac{d\pi}{dx} \quad (3.24)$$

Similarly, the solvent and solute flux equations can be calculated, assuming applicability of the van't Hoff equation, as:

$$j_w = L_{11} \left(-\frac{d\mu_w}{dx} \right) + L_{12} \left(-\frac{d\mu_s}{dx} \right) \quad (3.25)$$

$$j_s = L_{21} \left(-\frac{d\mu_w}{dx} \right) + L_{22} \left(-\frac{d\mu_s}{dx} \right) \quad (3.26)$$

Further assuming $\bar{V}_w \approx 1/c_w$, and $j_w \bar{V}_w \approx J_v$ the potential gradients can be substituted to yield:

$$J_v = -L_{11} \bar{V}_w^2 \left[\frac{dp}{dx} - \left(1 - \frac{L_{21} c_w}{L_{11} c_s} \right) \frac{d\pi}{dx} \right] \quad (3.27)$$

$$j_s = \left(\frac{L_{21}^2}{c_s L_{11}} - \frac{L_{22}}{c_s} \right) \frac{d\pi}{dx} + \frac{L_{21}}{L_{11} \bar{V}_w} J_v \quad (3.28)$$

Where the coefficients can be transformed to find an expression that resembles equation (3.19):

$$\sigma = 1 - \frac{L_{21} c_w}{L_{11} c_s} \quad (3.29)$$

$$P_w = -L_{11} \bar{V}_w^2 \quad (3.30)$$

$$P_s = \frac{RT}{c_s} \left(\frac{L_{22} - L_{21}^2}{L_{11}} \right) \quad (3.31)$$

Using these definitions along with the van't Hoff equation the following expressions are obtained:

$$J_v = P_w \left[\frac{dp}{dx} - \sigma \frac{d\pi}{dx} \right] \quad (3.32)$$

$$j_s = -P_s \frac{dc_s}{dx} + (1 - \sigma) c_s J_v \quad (3.33)$$

The thesis by [Sievertsen2001] relates the parameters of the Spiegler-Kedem model with those of the Kedem-Katchalsky model (where ν is the number of ions formed per solute molecule, and Δx is the membrane thickness):

$$L_p = \frac{P_w}{\Delta x} \quad (3.34)$$

$$\omega = -\frac{P_s}{\nu RT \Delta x} \quad (3.35)$$

These parameters can then be determined the same experimental method shown in Figure 11. Assuming constancy of the parameters P_s , and σ , the expression $j_s = J_v \cdot c_p$ can be used to calculate a relationship between retention and volumetric flux:

$$R = \frac{\sigma(1 - F)}{1 - \sigma F} \quad (3.36)$$

Where:

$$F = \exp\left(-\frac{1-\sigma}{P_s/\Delta x}J_v\right) \quad (3.37)$$

The rejection in Equation (3.36) reaches its limiting value, σ , at infinite volumetric flux, i.e. at pure convection. The reflection coefficient is a measure for the solute-water coupling while P_s is a measure for solute diffusion. The pore radius can be calculated from the reflection coefficient by:

$$\sigma = 1 - \left(1 + \frac{16r_s^2}{9r_p^2}\right) \left(1 - \frac{r_s}{r_p}\right)^2 \left[2 - \left(1 - \frac{r_s}{r_p}\right)^2\right] \quad (3.38)$$

This relationship is limited to solutes that do not dissociate into two separate ions of different radius, i.e. it can be used on organic molecules in order to determine the pore radius.

3.1.3 Extended Nernst-Planck equation (ENP)

The extended Nernst-Planck equation for the description of mass transfer in membranes has already been described more than 50 years ago by [Schlögel1964] and [Dresner1972ENP] and it is based on earlier work by Nernst and Planck on ion transport in dilute solutions. Yet, not until the 1990s has the ENP gained popularity as part of the Donnan-steric-pore model. Bowen and Mukhtar [Bowen1996] have chosen the ENP for the description of the transport inside the membrane as it best fulfills the requirements of being physically realistic, requiring a minimum number of assumptions, and having simple mathematics.

The starting point for a mathematical description of the flux of component i , j_i (in kg/m²/s), in all membranes is the simple equation [Wijmans2006]:

$$j_i = c_i \cdot v_i = -c_i \cdot U_i \cdot \frac{d\bar{\mu}_i}{dx} \quad (3.39)$$

with the concentration of component i c_i , the component's velocity v_i , and mobility (not necessarily constant) U_i , as well as the gradient of the electrochemical potential as the driving force $d\bar{\mu}_i/dx$.

The electrochemical potential is written as:

$$\bar{\mu}_i = \mu_i^0 + RT \ln(a_i) + \bar{V}_i(p - p_i^0) + z_i F \varphi \quad (3.40)$$

with the activity of component i , a_i , the component's valence, z_i , and the reference chemical potential of pure i , μ_i^0 , at its reference pressure, p_i^0 .

For incompressible liquids as well as the membrane phase Equation (3.40) can be rewritten as:

$$\bar{\mu}_i = \mu_i^0 + RT \ln(a_i) + \bar{V}_i(p - p_i^{sat}) + z_i F \varphi \quad (3.41)$$

with the saturation vapor pressure of pure component i , p_i^{sat} , as the reference pressure. In this way, the reference chemical potential is the same for the liquid and the gaseous state. In the pore-flow model the trans-membrane pressure difference produces a continuous chemical potential gradient according to Equation (3.41) and also a continuous pressure gradient through the membrane, as illustrated in Figure 13 on page 31.

The Nernst-Einstein equation can be used to express the mobility of component i as follows:

$$U_i = \frac{D_i}{RT} \quad (3.42)$$

Equations (3.39), (3.41), and (3.42) can be combined to yield:

$$j_i = -c_i \cdot \frac{D_i}{RT} \cdot \left(RT \cdot \frac{d \ln a_i}{dx} + \bar{V}_i \cdot \frac{dp}{dx} + z_i \cdot F \cdot \frac{d\varphi}{dx} \right) \quad (3.43)$$

Using the definition of the activity, $a_i = \gamma_i c_i$, and inserting in the above equation:

$$j_i = -c_i \cdot \frac{D_i}{RT} \cdot \left(\frac{RT}{c_i} \cdot \frac{dc_i}{dx} + RT \cdot \frac{d \ln \gamma_i}{dx} + \bar{V}_i \cdot \frac{dp}{dx} + z_i \cdot F \cdot \frac{d\varphi}{dx} \right) \quad (3.44)$$

Assuming a constant activity coefficient and negligible influence of pressure on the chemical potential the **Nernst-Planck equation** is obtained:

$$j_i = -D_i \cdot \frac{dc_i}{dx} - \frac{z_i \cdot F \cdot c_i \cdot D_i}{RT} \frac{d\varphi}{dx} \quad (3.45)$$

The classical Nernst-Planck equation can be extended to include the contribution of convective solute flux, which leads to the Extended Nernst-Planck equation (ENP). [Schlögel1964] included a convective term, however did neglect the full extent of interaction between solute and the membrane matrix. The membrane was considered thermodynamically inactive, merely acting as a frame of reference and keeping the fixed charges in their fixed positions. [Dresner1972] has added the membrane as a thermodynamic component, this way generating a steric hindrance factor multiplied to the convective transport term, as will be described below. The starting point of the derivation of the ENP is Equation (3.2) from irreversible thermodynamics. Previously, water was used as the component to which the frame of reference was fixed to. When the membrane is included and the frame of reference fixed with respect to the membrane, the thermodynamic component of water, indicated by the index w, appears in Equation (3.2):

$$j_i = -L_{iw} \frac{d\bar{\mu}_w}{dx} - \sum_{k=1}^n L_{ik} \frac{d\bar{\mu}_k}{dx} \quad i = w, 1, \dots, n \quad (3.46)$$

The electrochemical potential gradient for water can be eliminated by choosing $i=w$:

$$\frac{d\bar{\mu}_w}{dx} = - \frac{\left(j_w + \sum_{k=1}^n L_{wk} \frac{d\bar{\mu}_k}{dx} \right)}{L_{ww}} \quad (3.47)$$

Equation (3.46) can then be written as:

$$\begin{aligned} j_i &= L_{iw} \frac{\left(j_w + \sum_{k=1}^n L_{wk} \frac{d\bar{\mu}_k}{dx} \right)}{L_{ww}} - \sum_{k=1}^n L_{ik} \frac{d\bar{\mu}_k}{dx} = \frac{L_{iw}}{L_{ww}} j_w - \sum_{k=1}^n \left(L_{ik} - \frac{L_{iw} L_{wk}}{L_{ww}} \right) \frac{d\bar{\mu}_k}{dx} \\ &= K_{i,c} c_i J_v - \sum_{k=1}^n \mathcal{L}_{ik} \frac{d\bar{\mu}_k}{dx} \end{aligned} \quad (3.48)$$

Since the system is in mechanical equilibrium, the assumption proposed by [Onsager1932] $\mathcal{L}_{ik} = \mathcal{L}_{ki}$ (ORR) can be applied here. Further simplifications were proposed by [Schlögel1964], where interactions between ions are exclusively through the electrical field and not by collision or by interactions with water molecules. Neglecting such direct interactions eliminates all off-diagonal elements of the matrix, which means $\mathcal{L}_{ik} = 0$ for $i \neq k$. Furthermore, [Schlögel1964] compares the diagonal elements of matrix \mathcal{L}_{ik} , that describe diffusive flux, to Fick's first law:

$$\begin{aligned} j_i &= -\mathcal{L}_{ii} \frac{\Delta \bar{\mu}_i}{\Delta x} \approx - \frac{RT \cdot L_{ii}}{c_i} \cdot \frac{\Delta c_i}{\Delta x} \\ j_i &= -D_i \cdot \frac{\Delta c_i}{\Delta x} \end{aligned} \quad (3.49)$$

The diagonal elements of the phenomenological coefficient matrix can then be substituted by $\mathcal{L}_{ii} \approx \frac{D_i c_i}{RT}$. Inserting this approximate expression in Equation (3.48) leads to a similar approach as applied to Equation (3.43) and the sum term can be rewritten to yield **the Extended Nernst-Planck equation**:

$$j_i = K_{i,c} c_i J_v - D_i \frac{dc_i}{dx} - \frac{F z_i c_i D_i}{RT} \frac{d\phi}{dx} \quad (3.50)$$

Accounting for convection (caused by the pressure gradient), ionic diffusion (due to the concentration gradient), and electromigration (due to the electrical potential gradient) in the membrane pores. Here the above assumptions of negligible influence of pressure as well as constancy of ion activity along the pore's length have already been implemented.

Steric hindrance of the ions' fluxes are accounted for by means of two factors: Firstly, the hindered diffusivity $D_i = K_{i,d} \cdot D_{i,\infty}$ is calculated from literature values of pure solution limiting diffusion coefficients multiplied with the steric hindrance factor for diffusion. This factor accounts for the altered diffusion to the confinement within the nanosized pores. Secondly, the hindrance factor for convection inside the membrane $K_{i,c}$, which accounts for interactions between ions and the membrane that slow the ions compared to the velocity that they would possess if they would be swept along with the velocity of the permeating water. [Dresner1972] mentions the example that ions of type i could be bound by the fixed charges thus decreasing the concentration of mobile ions of type i , i.e. c_i . Consequently, $K_{i,c}$ for the ions of type i would be < 1 . A second illustration of such a hindrance effect could be caused by the electric double layer inside the membrane pores where counterions would accumulate close to the pore wall, where fluid velocity is lower and ions are thus transported at a lower rate. At the same time, coions will be repelled by the fixed charges and are at higher concentrations towards the center line of the pore where fluid velocity is higher. From the considerations for this second case [Dresner1972] derives that $K_{i,c}$ will be for < 1 counterions, and > 1 for coions. For details on the steric hindrance factors refer to Section 4.8.1.

It is important to keep mindful of the fact that this derivation leads to fluxes j_i and J_v that are based on total membrane area thus implying a perfectly porous membrane, i.e. a fractional porosity of 1.0 [Bowen1996].

3.2 Mechanistic models

Since the 1990's the focus of membrane models shifted from modeling using the phenomenological models of irreversible thermodynamics towards mechanistic models. Among these, models based on the extended Nernst Planck equation are now arguably the most commonly used type of model of current research [Oatley2014]. In later chapters a model will be developed that is based on similar approaches. This chapter is meant to show the historical development towards the commonly used type of nanofiltration model.

3.2.1 Space Charge (SC) model

In the late 1960s Osterle and his co-workers developed the space charge model, as described in [Morrison1965], [Gross1968], [Fair1971]. In this model, the membrane is assumed to have identical cylindrical pores. The membrane charges are homogeneously distributed on the inner wall of the membrane's pores. The resulting radial and axial distribution of the electrical potential and ion concentration is described on the basis

of the Poisson-Boltzmann equation. A separation of the electric potential φ into a radial term φ_{radial} , originating from the electrical boundary layer of the wall's surface charges, and an axial term φ_{axial} , due to electrokinetic effects of the electrolyte solution flowing across the charged surface, has been proposed by [Gross1968]:

$$\varphi = \varphi_{radial}(x, r) + \varphi_{axial}(x) \quad (3.51)$$

The Poisson equation relates the spacial distribution of charged ions to the spacial intensity of an electric field, as expressed in Equation (4.7).

The solution of the resulting equations has been attempted in the literature via several paths and can be roughly separated into two main approaches. The first approach is a rigorous solution involving numerical descriptions of the laws of Navier-Stokes, or Poiseuille for the transport of solute and the application of the extended Nernst-Planck equation for the transport of ions [EMST2013 page 79]. The second approach is the analytical solution by finding a physical interpretation of the phenomenological coefficients from the irreversible thermodynamics theories, e.g. of Spiegler-Kedem [Wang1995]. Both approaches are mathematically complex and simpler models found more widespread use, such as the TMS model, which is described in the next chapter.

3.2.2 Teorell-Meyer-Sievers (TMS) model

The TMS model, originally proposed by [Teorell1953] and Meyer and Sievers [Meyer1936], is also called the fixed charge model. Rightfully, the TMS model can be called a simplification of the SC model in that it is based on the same equations and approaches, however reduced to the special case of a homogeneous membrane which means that the electrical potential inside the pore is considered constant. In the words of [Wang1995] the TMS does not contain a structural representation of the membrane such as a pore radius and assumes a uniform distribution of the fixed charges and ions within the membrane matrix. For this, the surface charge density σ_x is transformed to the volume charge density c_x that has the unit of a concentration:

$$c_x = \frac{2 \cdot \sigma_x}{F \cdot r_p} \quad (3.52)$$

This membrane charge density is then used in the description of an instantaneous Donnan equilibrium for co-ions [Hoffer1972]. The ion mobility inside the membrane is assumed to be equal to that in the free volume, and ion transport is based on a force balance similar to the friction model, refer to Section 3.2.5. This assumption is especially problematic and lead to the development of a hybrid model that considers reduced ion mobility due to hindrance inside the membrane pores, the DSPM (see next chapter).

3.2.3 DSPM

The Donnan-steric partitioning pore model (DSPM) is an extension of the TMS model [Hussain2007]. In this model the membrane is considered as a charged porous layer and characterized by three adjustable parameters, the average pore radius, the volumetric charge density, and the effective membrane thickness. Its origins can be found in [Bowen1996] who first formulated this hybrid model in which the ENP was solved for a homogeneous non-porous membrane. The pore hindrance, i.e. the interaction between transported ions and the membrane material was then accounted for by hindrance factors for diffusion and convection which depend on the effective pore radius. The authors pointed out that this doesn't imply that geometrically well-

defined pores exist but rather that the observed effects were sufficiently well described with the pore radius as a fitting parameter. The hindrance factors used were taken from [Bowen1994] and further adapted to the nanofiltration case. The ENP considering steric diffusion for diffusion and convection was formulated as:

$$j_i = K_{i,c}c_iJ_v - K_{i,d}D_i\frac{dc_i}{dx} - K_{i,d}D_i\frac{Fz_ic_i}{RT}\frac{d\varphi}{dx} \quad (3.53)$$

Using the boundary condition $j_i = J_vc_{i,p}$ from the equation of continuity and rearranging yields the concentration gradient across the membrane:

$$\frac{dc_i}{dx} = \frac{J_v}{K_{i,d}D_i}(K_{i,c}c_i - c_{i,p}) - \frac{Fz_ic_i}{RT}\frac{d\varphi}{dx} \quad (3.54)$$

As the electrical balance, Equation (4.11), must be fulfilled the sum of the concentration gradients at all points within the membrane must equal null, i.e. $\sum dc_i/dx = dc_x/dx = 0$. Since the electrical potential gradient in Equation (3.53) is identical for all ion species, it can be expressed as:

$$\frac{d\varphi}{dx} = \frac{\sum_{i=1}^n \frac{z_iJ_v}{K_{i,d}D_i}(K_{i,c}c_i - c_{i,p})}{\frac{F}{RT}\sum_{i=1}^n z_i^2c_i} \quad (3.55)$$

At the two interfaces between the two surrounding solutions and the membrane Donnan-equilibrium is assumed to apply. In [Bowen1996] this equilibrium is described with the simple equation:

$$\frac{c_i^{in}}{c_i^{out}} = \exp\left(-\frac{z_iF}{RT}\Delta\varphi_D\right) \quad (3.56)$$

Here, effects of ion activity and steric partitioning at the interfaces were assumed to be not significant for the simple and dilute solutions targeted. In later publications, [Bowen1997], [Bowen1998a], [Bowen1998b], these steric effects were amended to the original formulation:

$$\frac{\gamma_i^{in}c_i^{in}}{\gamma_i^{out}c_i^{out}} = (1 - r_i/r_p)^2 \exp\left(-\frac{z_iF}{RT}\Delta\varphi_D\right) \quad (3.57)$$

While the effect of ion activity was formally acknowledged it has not been applied and later on the assumption of dilute solutions was made. Despite these assumptions the DSPM has successfully been applied to predict the separation of dye/salt mixtures [Bowen1998] and it realistically described the Donnan-effect in the separation of a NaCl/NaSO₄ mixture [Bowen1996]. However, for the DSPM discrepancies in rejection prediction of multivalent ions occurred. This was shown at the example of a CaCl₂ solution [Vezzani2002] where the observed rejection was above the predicted value. Discrepancies like this lead to the identification of an additional separation mechanism, dielectric exclusion, and the development of an adapted model, the DSPM&DE.

3.2.4 Donnan-Steric Partitioning Pore Model incorporating Dielectric Exclusion - DSPM&DE

As described above, the importance of electrostatic effects was early recognized and also mathematically described by the Donnan effect. Donnan exclusion alone however could not explain, e.g. high magnesium ion rejection by a negatively charged membrane. Actually, electrostatic interaction alone would suggest preferential partitioning in favor of the counter-ions. Also, transport through the membrane could not be described with the same equivalent membrane thickness for all electrolytes, which contradicts the notion that the membrane geometry is independent of the solution composition. Dielectric effects resolve this discrepancy as they are

dependent on the absolute value of the ion's charge and not the sign. This means dielectric exclusion increases the membrane's rejection for positively as well as negatively charged ions that possess high valence numbers.

The mechanism of dielectric exclusion was first described by E. Glueckauf in 1965 [Glueckauf1965] and later refined by [Hagmeyer1999], and [Bowen2002b]. Two mechanisms contribute to dielectric exclusion. The primary effect is ion exclusion due to electrostatic effects which are generated by the ions themselves, called the effect of image charges. The secondary effect is due to a difference in solvation energy of the membrane versus solution which is called the Born-effect. The mathematical details of this model will be described in later sections of this work.

3.2.5 Other approaches

The models in this section are not further described for reasons of space limitations, and a complete picture of existing modeling approaches is not attempted in any way. This section is merely meant as a reminder that a variety of other nanofiltration modeling approaches exists.

The sieve model [Banks1966] describes solvent flux using the Hagen-Poiseuille equation while solute retention is explained by the existence of two pore sizes, one that is large enough to let both solvent and solute pass, and a smaller class of pores that is only permeable for solvent.

The solution-diffusion model, developed by [Lonsdale1965], is best suited to describe dense membranes and consequently not the best description for nanofiltration. It has thus been upgraded to the solution-diffusion-imperfection model where the imperfections have no separation effect [Sherwood1967]. [Yaroshchuk2011] developed a solution diffusion model for the description of electrolyte mixtures. Such a model makes the description of multicomponent systems possible while intensive mathematics are avoided. However, the model requires the assumption that no convective coupling occurs between the flows of solutes and solvent inside the membrane. This translates to a reflection coefficient for all ions equal to one.

The friction model [Belfort1976] is based on the phenomenological coefficients of Equation (3.1) where the frictional forces are balanced by the driving forces. The law of friction yields an expression for the frictional forces by the relative velocity of the components together with a friction coefficient f_{ij} :

$$F_{ij} = f_{ij}(u_i - u_j) \quad (3.58)$$

The Maxwell-Stefan approach is the only model that does not assume dilute solutions and does consider interactions between solute molecules. Similar to the friction model it considers a force balance between the interacting components. [Krishna1997] shows that this approach is superior to descriptions using Fick's law of diffusion.

The charged capillary model was developed by [Jacazio1972] for the description of salt transport through porous material, e.g. through clay. The volume flow rate q through the clay membrane is described by a combination of Darcy's law, with the fluid viscosity η , the trans-membrane pressure Δp , and the membrane thickness Δx :

$$q = -\left(\frac{k}{\eta}\right)\left(\frac{\Delta p}{\Delta x}\right) \quad (3.59)$$

Together with the Kozeny-Karman correlation for the permeability coefficient k , with the membrane porosity A_k , and the specific surface of the membrane S_0 :

$$k = \frac{1}{5} \cdot (A_k^3/S_0^2[1 - A_k]^2) \quad (3.60)$$

The charge characteristics of the pore material are being related to the zeta potential. However, an important assumption of this model is that the pore size is large compared to the size of the permeating ions. This is in most cases not true for nanofiltration applications.

3.3 Model selection

The models presented above have all been successfully applied to the description of different nanofiltration systems. Consequently, all models have their specific justification and they will be useful for different purposes. This means that this section is not targeting the determination of the generally “best” model for nanofiltration but rather the identification of a model that is suitable to reach the objectives of this research. In brief the objectives for the model development are a mathematical description of multicomponent transport for solutions containing various chemical species and hence an improved understanding of the main separation mechanisms. The experiments will be performed at the example of a chemically complex mine water containing uranium species and several other ions.

One of the advantages of nanofiltration is that it allows selective retention of ions which means for our example that uranium can be separated from the main process stream and then be treated in an isolated manner. Models based on irreversible thermodynamics typically fail to predict membrane separations at low rejection [Hussain2007] which means that all ions will be retained at high rates. This makes models based exclusively on irreversible thermodynamics not suitable for the present research. Furthermore, while models based on the ENP can be adapted to high concentration applications the Spiegler-Kedem and Kedem-Katchalsky model assume an activity coefficient equal to one (ref. assumption leading to Equ. (3.9)) and that the Van’t Hoff equation is valid. An additional concern is the lack of options for physical parameter identification. The phenomenological coefficients of irreversible thermodynamics are determined using membrane filtration experiments. However, a conclusive model validation requires that the coefficients of the model can be tested in membrane-independent experiments. Examples for membrane-independent experiments include microscopy, porosimetry, impedance spectroscopy, titration, streaming potential measurement, and alike. In conclusion, irreversible thermodynamics are not suitable for the description of mine water nanofiltration.

From a practical perspective, the availability of physical property data for membrane and solution is also highly important. This means that a model that describes ion transport using standard bulk diffusivities will be preferred to a model that uses newly defined friction coefficients which would result in extensive experimental or modeling work.

The DSPM&DE proved to be capable of predicting retention for multicomponent systems [Fievet2002]. Since solution input parameters are readily available, such as the bulk diffusivity, and the viscosity, the DSPM&DE has greater predictive capability. The DSPM&DE has already been successfully applied to the description of multicomponent solutions ([Garcia-Aleman2004], [Gerald2006], [Bandini2003]) and it includes a physical representation of the separation mechanisms which can be tested membrane-independently and which could potentially also suggest measures for membrane enhancement. Models like the DSPM&DE or models similar to it, such as the SEDE (steric, electric, and dielectric exclusion model) model by [Szymczyk2005] are identified as a suitable basis for the model development in the present research.

Models for nanofiltration are based on a plethora of different approaches, all with their own assumptions and limitations. The objective of this research, to gain deeper understanding of the transport processes, favors the use of mechanistic models where model parameters possess a physical meaning which can (potentially) be determined by independent methods. The model developed here is based on models which consider phase equilibrium at both membrane/solution interfaces and transport inside the membrane described by the extended Nernst-Planck equation; examples are the DSPM and the SEDE model.

4 Development of an adapted transport model

A model for the mathematical description of nanofiltration of multi-ionic solutions is developed based on the DSPM&DE (ref. section 3.2.4) and the SEDE model [Szymczyk2005] described in the previous chapter. The model's equations are presented in order of the membrane's sections from upstream till downstream, as shown in Figure 12 where the relevant chapters for each layer of the membrane are shown in ellipses. The figure also shows the system boundaries for each layer along with the notation for the concentration and electrical potential profile. The mathematical expressions for each layer are based on the following approaches:

- Feed side transport and concentration polarization due to the limited mass transfer away from the membrane will be explained in Section 4.5. Furthermore, as an additional approach the concentration polarization due to the effects inside the electrical double layer are accounted for.
- Ion partitioning at the interfaces between the membrane and the surrounding solution will be explained in Section 4.7 based on the consideration of a membrane/solution phase equilibrium, i.e. a locally approximately equal electrochemical potential.
- The Extended Nernst-Planck equation inside the membrane will be described in Section 4.8.
- The concentration profile in the permeate is reduced to the effects inside the electrical double layer.

The numerical solution of all model equations will be presented in Section 4.9 along with the general properties of the model, such as input and output parameters, and a degree of freedom analysis.

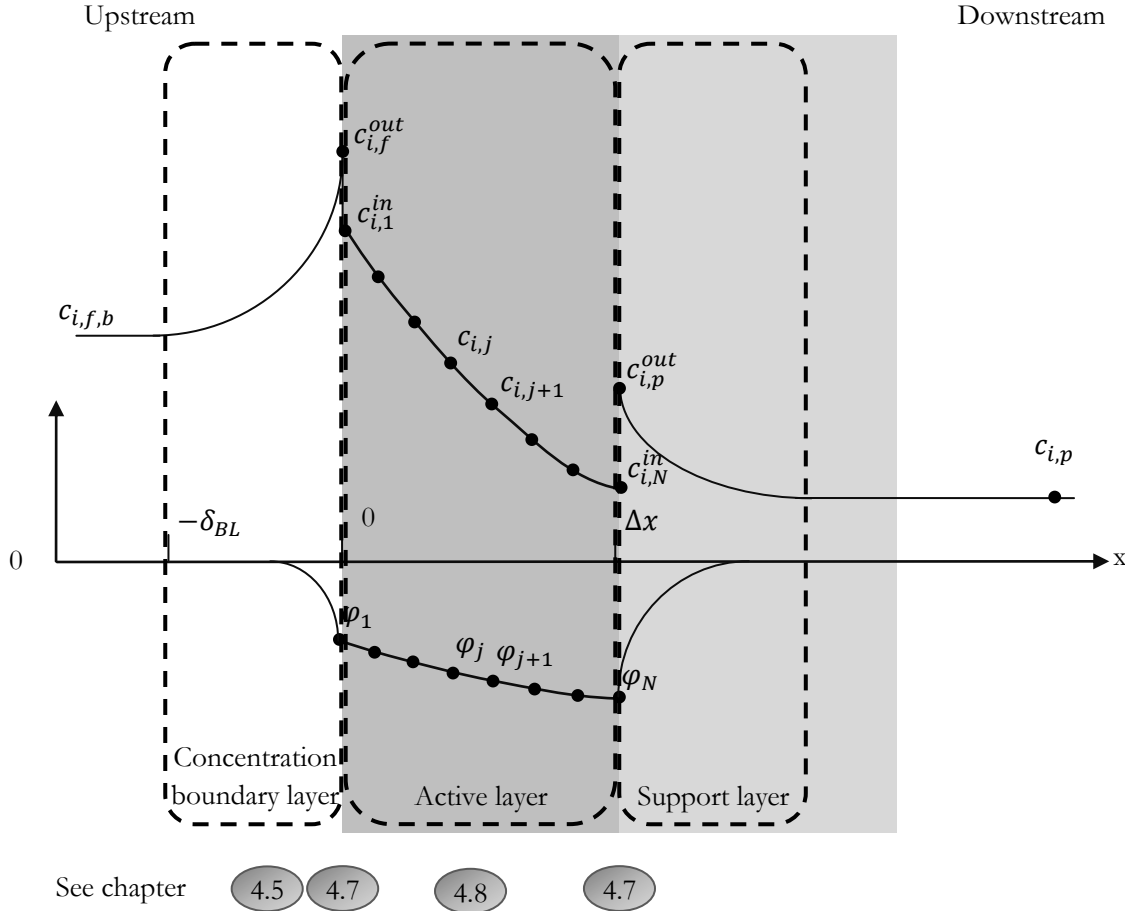


Figure 12: Notation for the concentration and electric potential profiles across the membrane for component i . The electrochemical potential is shown in Figure 13. The model assumes that the active layer (highlighted in dark grey) primarily determines the separation.

4.1 Model assumptions

In this section the assumptions of the here developed nanofiltration model are summarized in order to show limitations that need to be considered in the model's application.

Assumptions concerning the membrane: The structure of the membrane matrix has direct consequences for the model equations to be chosen. The most important decision concerning the membrane structure is whether pores exist in the active separation layer. This is shown at the example of an ideally porous and an ideally dense membrane. Assuming local equilibrium, the electrochemical potential gradient along the membrane thickness is a continuous function without gaps and leaps for both types of membrane. Figure 13 shows the electrochemical potential gradient for porous membranes (ultrafiltration, microfiltration) and dense membranes (reverse osmosis), respectively. While for dense membranes (solution-diffusion model) the pressure within the membrane is uniform and the chemical potential is represented by the concentration gradient, it is the opposite for porous membranes (pore-flow model) where the permeant concentration within the membrane is constant and the chemical potential gradient is determined only by the pressure gradient. The here developed model for application to nanofiltration assumes very fine pores and thus needs to consider

pore-flow (convection) together with a concentration gradient (diffusion), and electrical interactions between the solution components and the membrane's fixed charges (electromigration).

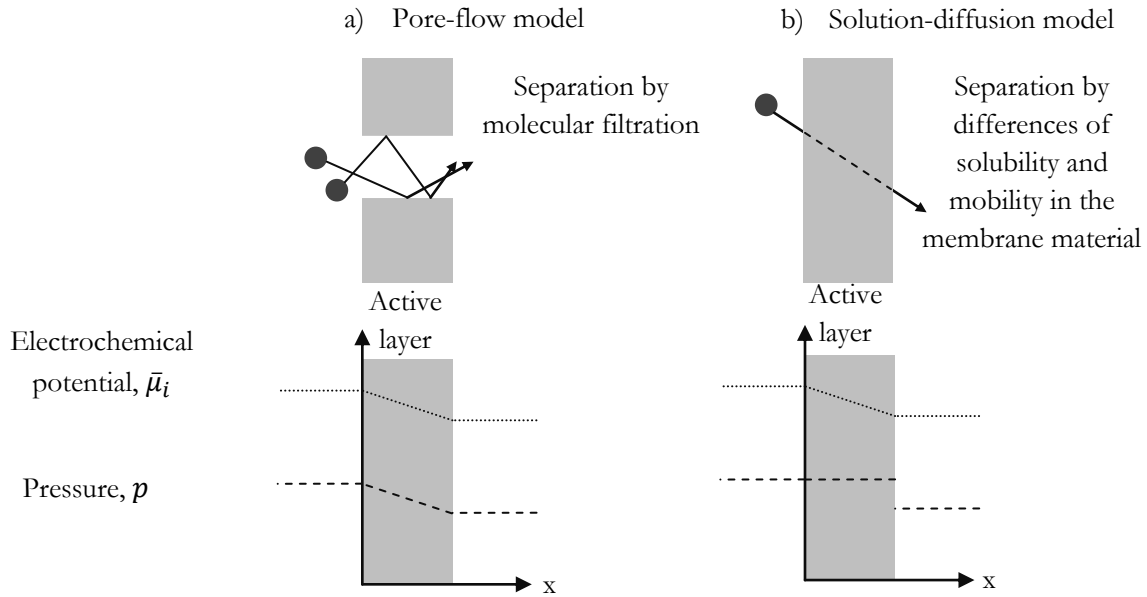


Figure 13: Driving force gradients for a one-component solution for porous membranes (left) and dense membranes (right) [Wijmans2006].

The existence of pores in nanofiltration membranes was subject to several studies and has to date not been resolved conclusively. A review of the porous nature of NF membranes is given in [Oatley2012]. In the book chapter on atomic force microscopy of membranes in [Bowen2009] surface pores were described to exist for different ultrafiltration membranes. Also a correlation between the surface pore dimensions from AFM and MWCO has been found for ultrafiltration membranes. The existence of pores in NF membranes is a much more delicate question with some evidence showing such surface structures. The authors acknowledge the higher risk for artifacts at the length scale of the nano-sized pores and the increased caution that is needed for proper imaging such as low surface roughness and the appropriate imaging force and electrolyte concentration. While some studies support the existence of pores, the shape of the pores is highly uncertain [Oatley2012]. AFM studies revealed that the pores appear to be rather slit like than circular in their cross-sectional shape at the pore entrance. In addition to this, SEM studies showed that the pores' pathway is quite convoluted. While independent methods were not able to determine the size and shape of the supposed nanopores the results from observed rejection of solute of well-known size strongly suggest the existence of pores. At a nominal molecular weight cut off in the range from 100 to 1000 Da which is typical for NF-membranes the corresponding pore diameter is about 1 nm [Oatley2013] and according to [Labbez2003] NF-membranes typically have pores of less than 2nm. Pores with diameters below 0.5 nm are not physically meaningful as pore models break down at length scales within the range of the thermal motion of the membrane matrix polymer chains [Wijmans2006].

Another important membrane characteristic besides the existence and size of pores is the surface charge of the membrane. Many models assume constant membrane charge density throughout the membrane, depending mainly on feed concentration [Labbez2003]. For the here developed model, the membrane charge density is also assumed to be homogeneously distributed and is a variable parameter.

The third assumption that needs to be made in order to reduce the description of the transport to a one dimensional form is that the membrane's thickness is homogeneous. Furthermore, the complex layered structure of typical nanofiltration membranes, as shown in Table 2, is reduced to a single layer, which is called the active layer. A model with more than one layer could still be reduced to one dimensional transport. The Influence of the membrane's support layer is investigated in Section 6.2.

Assumptions concerning the solution: As described above, the membrane pore radius is much smaller than the length of the pore. For such a pore geometry edge effects at the inlet and outlet of the pore as well as differences in the radial distribution across the pore's cross-section can be neglected and transport can be described in a one dimensional form with radially averaged ion flux j_i , concentration $c_{i,j}$, electrical potential ϕ , and volume flux J_v [Labbez2003], [Fievet2002], [EMST2013 page 101]. The permeate flow inside such a nano-pore is fully developed and of a Hagen-Poiseuille type [Labbez2003] [Fievet2002]. The solute is assumed to be a rigid sphere in ideal solution [Oatley2014].

An important assumption is that the fluids on either side of the membrane are in equilibrium with the membrane material at the interface (excluding effects of concentration polarization) [Wijmans2006]. This means that the chemical potential gradient is continuous. It also means that sorption and desorption is much faster than transport through the membrane. This assumption is necessary to derive the extended Nernst-Planck equation which requires application of the Onsager Reciprocal Relationship (ORR). The ORR is valid if ionic transport is a function of the chemical potential gradient only and the system is close to equilibrium. This assumption of linearity can be problematic at high pressure and concentration gradients which would render the local equilibrium condition questionable and the ORR would not be true. This can cause deviations between the model retention and experimental retention at high flux rates. The effect of pressure on the chemical potential is assumed to be negligible [Oatley2014].

A necessary assumption and at the same time the strongest limitation of the model is the assumption of low solute concentrations. In the derivation of the extended Nernst-Planck equation the assumption is made that the volumetric permeate flux equals the water flux and that the components don't interact directly, i.e. via collision, but indirectly through the electrical potential, as described in Section 3.1.3..

Assumptions made in the development of the model are that pores are straight and cylindrical and at a length much larger than their diameter. Furthermore, the membrane charge is assumed to be homogeneous throughout the thickness of the membrane. The model is reduced to one dimensional transport and for this the thickness of the membrane is assumed to be homogeneous. Hydrodynamics inside the nanopores of the membrane are simplified by assuming fully developed flow of a Hagen-Poiseuille type. Ion partitioning at the interfaces is derived from the assumption of interfacial equilibrium. The model is limited to the description at low ion concentrations.

4.2 Physical property data of the solution

Density, viscosity, and permittivity of pure water are temperature and pressure dependent parameters. In order to develop a flexible and modular program code, these dependencies are accounted for by using formulations available in the literature. The formulations for water density, and viscosity are taken from

[Tanaka2001], and [Huber2009] respectively. The relative permittivity ε of water is computed using the formulation proposed by [Fernández1997] based on the Harris and Alder equation:

$$\frac{(\varepsilon - 1)(2\varepsilon + 1)}{3\varepsilon} = \frac{n}{\varepsilon_0} \left(\frac{(2\varepsilon + 1)(\varepsilon + 2)}{9\varepsilon} \alpha_m + \frac{1}{3k_B T} g \mu_{di}^2 \right) \quad (4.1)$$

with the permittivity ε_0 of vacuum, the number density $n = N/V$, the dipole moment of the isolated molecule μ_{di} , and the molecular polarizability α_m .

The dielectric constant inside pores can be calculated based on the assumption that water molecules inside the pores have bulk properties except for a monolayer of oriented water molecules at the pore wall, as shown in Figure 14. This geometric correction of the pore relative permittivity as well as for the pore viscosity is commonly applied in the literature and shall be presented here.

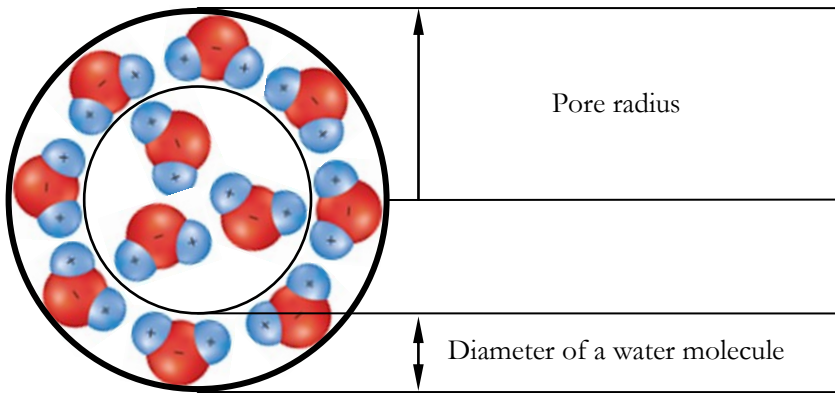


Figure 14: Hypothesis of a water monolayer at the pore surface proposed in [Oatley2012]; oriented water molecules with reduced dielectric constant and an inner annulus with bulk physical properties.

In [Schäfer2006 page 127] and [Bowen2002b] and [Oatley2012] the pore dielectric constant is calculated as:

$$\varepsilon_p = \varepsilon_b - 2(\varepsilon_b - \varepsilon^*) \left(\frac{d}{r_p} \right) + (\varepsilon_b - \varepsilon^*) \left(\frac{d}{r_p} \right)^2 \quad (4.2)$$

Where d is the diameter of a water molecule ($d = 0.28$ nm), and ε^* is the relative permittivity of the oriented water layer at the pore wall, which makes physical sense in the range between two extremes: a value of 80 would be applicable if there was no polarization and orientation of the water molecules, i.e. the bulk value and a value as low as 6 which corresponds to complete polarization which is known as the high frequency limit. The value used in the calculations in this work is 35 which is a value in agreement with the observations of [Bowen2002], and [Oatley2012] for a broad range of salts. However, as will briefly be described below, a more rigorous description will require further research on the exact value of the permittivity and the influence of the pore solution composition. This research exceeds the scope of this thesis and thus the relative permittivity will be set to a realistic value of 35 without adaptation to the solution composition for which currently no correlations exist.

[Bowen2002] determined $\varepsilon^* = 31$ by numerical fitting of model parameters. [Oatley2012] obtained $\varepsilon^* = 35$ for NaCl, KCl, and Na₂SO₄, however, for MgSO₄ a much higher dielectric constant was observed, 74, and 63 for NF99HF and NF270, respectively. This could be attributed to further effects that the Born model does not account for. [Oatley2012] mentions for example the effect of ion hydration, the extent of which is not clarified in the literature yet. Other authors also consider the physicochemical environment. The pore relative

permittivity is affected not only by confinement but also by the solution composition and membrane charge density [Szymczyk2005] [Szymczyk2006] [Escoda2011] [Silva2011]. As shown in Figure 91 on page 159, the dielectric constant for a typical nanofiltration membrane of radius 0.4 nm would yield a pore dielectric constant of around 40. [Szymczyk2005] showed that dielectric constants in the range of 60 to 70 are more realistic.

Values of the relative permittivity of the membrane polymer matrix, ϵ_m , are typically very low, in the range between 2 to 6 [EMST2013 page 98]. [Szymczyk2005] uses a membrane polymer dielectric constant of 3. According to the SEDE model a decreasing relative permittivity of the membrane polymer matrix would result in an increased rejection. Here, the dielectric constant of the membrane will not be considered in the partitioning.

In the same fashion as for the permittivity, the solvent viscosity is influenced by the confinement of the water molecules in the nanosized pores. In [Schäfer2006 page 124] the pore viscosity is calculated as (d is the diameter of a water molecule, $d = 0.28$ nm, and η_{bulk} is the bulk viscosity):

$$\frac{\eta_p}{\eta_{bulk}} = 1 + 18 \left(\frac{d}{r_p} \right) - 9 \left(\frac{d}{r_p} \right)^2 \quad (4.3)$$

This in turn influences the pore diffusivity (values for D_∞ taken from [Lide2005], and [Nightingale1959]):

$$D_p^* = D_p \frac{\eta_{bulk}}{\eta_p} = K_d D_\infty \frac{\eta_{bulk}}{\eta_p} \quad (4.4)$$

No correction of the viscosity was performed in this work however it is recommended to study the influence of such a correction in experiments with solvents of different viscosity and at different temperatures in more detail in later studies.

Physical property data, such as the permittivity, in the pores of nanofiltration membranes is different from their bulk values. This effect is due to the strong confinement within the nanoscale pores which results in an orientation of the water molecules. To account for this effect a correction for the solutions permittivity is introduced. However, other solution and ion characteristics could be influenced by this confinement as well, e.g. the viscosity, for which a correction is proposed in the literature, but also other ion characteristics (e.g. by sorption). This question is unresolved also in the literature.

4.3 Conservation equations

The individual physical expressions, e.g. the description of the Born effect or the steric hindrance factors, can be related by a framework of equations which are presented in this section. These equations appear throughout the derivation of transport equations along the membrane and cannot be assigned to one of the sections defined in Figure 12. For the understanding of the basic layout of the model these equations are very important.

Component's fluxes: The volumetric permeate flux, which can be calculated from the permeate volume that passes the membrane per unit time, and the membrane area, is an easily accessible parameter that can be determined with high precision. Here, the experimentally determined volumetric permeate flux serves as an

input parameter. The model can then be used to compute the fluxes of each dissolved ion. Hence the solution of the model derives the selective transport of each ion through the membrane for a given volumetric permeate flux.

For each component the continuity condition needs to be followed. The continuity equation for the steady state for all ion fluxes across the membrane can be expressed as:

$$\nabla j_i = 0 \quad (4.5)$$

Consequently the net flux for each component at each membrane section (a membrane section is a plane inside the membrane perpendicular to the direction in which the solution permeates) must be the same, independent of the location across the membrane's thickness. Hence the flux of the component that is leaving the system through the permeate, which can be easily and precisely determined, equals the component's flux through each membrane section. According to [Schlögell1964], the molar flux of a solute i can be calculated from the steady state volumetric flux by:

$$j_i = \left(c_{i,p} \cdot 1000 \frac{l}{m^3} \right) \cdot J_v \quad (4.6)$$

This condition will appear in the derivation of the extended Nernst-Planck equation where mass fluxes due to diffusion, convection and electromigration sum up to equal the mass flux through the permeate. It will also appear in the derivation of an expression for concentration polarization where convective transport towards the membrane minus the back transport into the bulk yields the component's flux leaving through the permeate.

4.4 Electrical balance

Charges of the same sign repel each other due to electrostatic forces which are stronger for multivalent ions. Figure 15 illustrates the distribution of ions according to their charge. The effects of the interactions between ions result in effects at the macroscopic scale. This notion is also the basis for the understanding of the relationship between Donnan exclusion and the Donnan effect.

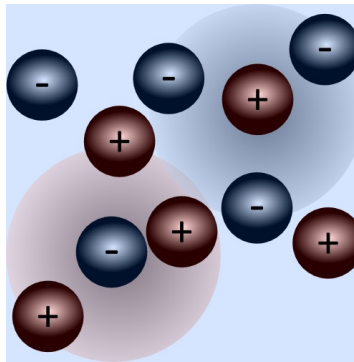


Figure 15: Like-charged ions exert repulsive force onto each other. The thickness of the ion cloud is referred to as Debye length as highlighted by the circular shade around two of the ions.

The Poisson equation which is employed in the expression for the boundary layer, the expression for the Donnan equilibrium and in the extended Nernst-Planck equation describes the dependence of ion concentration on the local electric potential:

$$\frac{\delta^2 \varphi}{\delta x^2} = \nabla^2 \varphi = -\frac{F}{\varepsilon_0 \varepsilon_r} \sum_i c_i z_i \quad (4.7)$$

The boundary conditions for the radial profile of the electrostatic potential inside a charged pore are [EMST2013 page 81]:

$$\left. \frac{\delta \varphi}{\delta r} \right|_{r=r_p} = \frac{\sigma}{\varepsilon_0 \varepsilon_r} \quad (4.8)$$

$$\left. \frac{\delta \varphi}{\delta r} \right|_{r=0} = 0 \quad (4.9)$$

Electroneutrality can be considered a special case of the Poisson equation which, according to [Bowen1996], can be calculated by:

$$-\frac{\delta^2 \varphi}{\delta x^2} = \frac{F}{\varepsilon_0 \varepsilon_r} \sum_{i=1}^{N_{ions}} z_i c_i = 0 \quad (4.10)$$

Inside pores the fixed charges need to be considered:

$$\sum_{i=1}^{N_{ions}} z_i c_i = -c_x \quad (4.11)$$

According to [Dresner1972] and [Bowen1996] no overall electrical current is passing through the membrane, when (the current density I expressed in A/m²):

$$I = \sum_{i=1}^{N_{ions}} F z_i j_i = 0 \quad (4.12)$$

Some studies suggest that the electroneutrality condition is not met inside nanopores [Lo1998] and [Lee1999]. However, [Siemer1998] develops two separate models where electroneutrality is assumed and where the Poisson equation is rigorously applied, respectively. He finds no significant difference in the modeling outcome and concludes that electroneutrality is a reasonable assumption to make inside the nanopores.

Conservation laws, such as the electrical balance and the continuity condition, are the boundary conditions which need to be fulfilled and can thus be used to relate the individual physical relationships. These expressions do not appear explicitly in the final model but will be used in the derivation of the model's equations.

4.5 Feed side mass transfer

A membrane is a semi-permeable separation layer. This means that some components can pass the membrane while others are retained. The retained components accumulate in the boundary layer close to the membrane surface, an effect that is referred to as concentration polarization. Thus, feed side hydrodynamics will have significant effects on overall membrane separation performance as the increased concentration can result, not only in an increased driving force for the mass transfer of the retained component, but also in the formation of additional mass transfer resistances, e.g. scaling or a gel layer.

As visualized in Figure 16, in a stationary process a balance between convection towards the membrane and back transport away from the membrane due to e.g. the concentration gradient will establish. Continuity requires that mass transfer due to convection and back transport at all points in the boundary layer sum up to the flux boundary condition, i.e. the mass transport of component i via the permeate. Back-transport mechanisms into the bulk of the feed are molecular diffusion, electro kinetic effects, and shear induced diffusion [Schäfer2006].

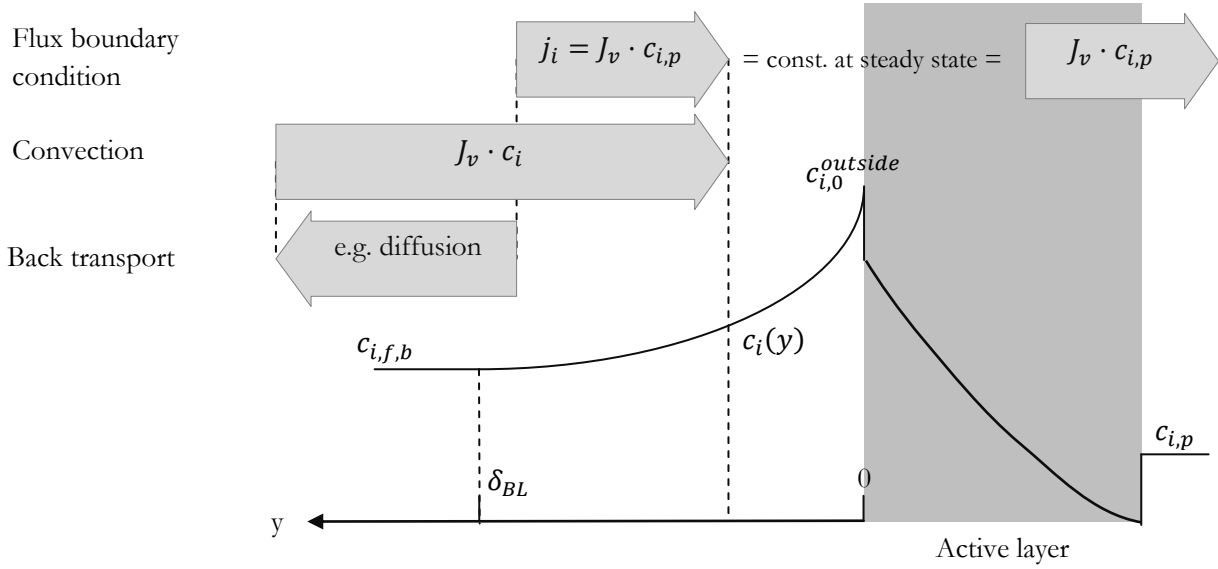


Figure 16: Notation for the relationships of feed-side mass transfer and concentration profile for solution component i , i.e. a retained species.

The well-known Film Model, as applied in [Bowen1996], [Fievet2002], [Kedem1958], [Lewis1924], [Malone1977], [Michaels1968], and [Nakao1981], develops a balance between net-convection and back-diffusion, which is the most important back-transport mechanism among the three and can be represented by the mass transfer coefficient in the following form:

$$k_i = \frac{D_i}{\delta} \quad (4.13)$$

At steady state the solute flux through the membrane will be independent of the perpendicular location and will be equal to the solute flux leaving the system through the permeate, which can be expressed by Equation (4.6). A simple mass balance thus yields [Mulder1996]:

$$j_i = J_v c_{i,p} = J_v c_i + D_{i,\infty} \frac{dc_i}{dx} \quad (4.14)$$

Where the back transport mechanism has been described by applying Fick's law for diffusion:

$$j_{i,diff} = -D_i \frac{dc_i}{dx} \quad (4.15)$$

Using the boundary conditions for the concentrations at the membrane surface and at the edge of the boundary layer where the bulk concentration has been reached:

$$x = 0 \Rightarrow c_i = c_{i,0}^{outside}$$

$$x = \delta_c \Rightarrow c_i = c_{i,f,b}$$

Rearranging and integration (for $x = 0 \dots \delta_c$ and $c_i = c_{i,0}^{outside} \dots c_{i,f,b}$) gives:

$$\ln \left[\frac{c_{i,0}^{outside} - c_{i,p}}{c_{i,f,b} - c_{i,p}} \right] = \frac{J_v \delta}{D_{i,\infty}} = \frac{J_v}{k} \quad (4.16)$$

The concentration polarization modulus, which describes the ratio of membrane surface concentration to feed bulk concentration, is then:

$$CP = \frac{c_{i,0}^{outside}}{c_{i,f,b}} = \frac{\exp\left(\frac{J_v}{k}\right)}{R_{int} + (1 - R_{int}) \exp\left(\frac{J_v}{k}\right)} \quad (4.17)$$

In this expression the mass transfer coefficient k is unknown, as the boundary layer thickness in Equation (4.13) cannot be determined directly. The velocity variation method, developed in [Berg1989] is an approach to determine k for membrane processes experimentally. For this, the relationship in Equation (4.16) can be combined with the definition of the apparent rejection:

$$R_{apparent} = 1 - \frac{c_{i,p}}{c_{i,f,b}} \quad (4.18)$$

and the definition of the membrane intrinsic rejection:

$$R_{intrinsic} = 1 - \frac{c_{i,p}}{c_{i,0}^{outside}} \quad (4.19)$$

to yield:

$$\frac{c_{i,m}}{c_{i,b}} = \frac{\exp\left(\frac{J_v}{k}\right)}{R_{int} + (1 - R_{int}) \exp\left(\frac{J_v}{k}\right)} \quad (4.20)$$

Linearization yields an expression which can be used to determine the mass transfer coefficient and the intrinsic rejection by interpolation:

$$\ln \left(\frac{1 - R_{obs}}{R_{obs}} \right) = \ln \left(\frac{1 - R_{int}}{R_{int}} \right) + \frac{J_v}{k}$$

This simple approach is well suited for single-salt solutions where the concentration boundary layer thickness for anions and cations is the same in order to fulfill the electroneutrality requirement. For mixtures of different anions and cations the electroneutrality requirement can be fulfilled notwithstanding the concentration boundary layer thickness is different for the individual species. At the multi-ionic level, which is within the scope of this work, the above described approach cannot be applied. Different alternatives are discussed in the following.

The above described Extended Nernst-Planck equation could be introduced to account for electromigration that way correcting the back transport for multi-ionic solutions. [Bowen2004] applied the Extended Nernst-Planck equation in the boundary layer and assumed the film layer thickness to be equal to the concentration boundary layer thickness of the ion with the lowest diffusion coefficient. The assumption that the concentration boundary layer thickness is the same for all ions is a strong limitation and other researchers found new approaches.

[Geraldes2007] modified the original film layer mass balance to include an electromigrative term and a diffusive term that considers that the concentration field is influenced by the mass transfer. Mass transport inside the film layer can then be described according to [Geraldes2007]:

$$j_i = -k_{J_v} \cdot (c_{i,0}^{outside} - c_{i,f,b}) - \frac{z_i F}{RT} c_{i,0}^{outside} D_{i,\infty} \frac{d\phi_f}{\delta} + c_{i,0}^{outside} J_v \quad (4.21)$$

Where the electrical potential gradient at the feed/membrane interface $\frac{d\phi_f}{\delta}$, which originates from the difference in mobilities for cations and anions, is accounted for. The corrected mass transfer coefficient k_{J_v} is modified to account for the effect of high mass transfer rates on the concentration field by the following semi-empirical correlation [Geraldes2006]:

$$k_{J_v} = k \cdot \left[\frac{J_v}{k} + \left(1 + 0.26 \cdot \left(\frac{J_v}{k} \right)^{1.4} \right)^{-1.7} \right] \quad (4.22)$$

The conventional mass transfer coefficient k is calculated using literature models [Bhattacharya1992], [Bird2002], [De1997], [Gekas1988], [Melin2007]. Here, the model for a flat channel with wall suction will be applied. The test cell of this work is described in Section 5.2. The hydraulic diameter of the rectangular feed channel can be calculated by its height (2 mm) and width (40 mm):

$$d_h = 4 \frac{\text{area}}{\text{wetted periphery}} = \frac{2 \cdot \text{height} \cdot \text{width}}{(\text{height} + \text{width})} \quad (4.23)$$

According to this, a hydraulic diameter of about 3.8 mm has been used. The Reynolds number can then be calculated as:

$$Re = \frac{d_h v_{cf} \rho}{\mu} \quad (4.24)$$

For a feed density of 1000 kg/m³ and a viscosity of 8.9 · 10⁻⁴ Pas the Reynolds number will be approximately in the range between 2159 (0.5 m/s) till 12954 (3 m/s) which means that the flow regime will be laminar and turbulent depending on the choice of the cross-flow velocity. All experiments in this work were performed at a cross-flow velocity of 1.3 m/s which corresponds to a Reynolds number of around 5500.

For each ion of the model the Schmidt number can be calculated:

$$Sc_i = \frac{\eta}{\rho D_i} \quad (4.25)$$

Mass transfer can be characterized by a Sherwood relationship:

$$Sh = a_1 Re^{a_2} Sc^{a_3} \left(\frac{d_h}{L} \right)^{a_4} \quad (4.26)$$

The coefficients of this equation are given in [Mulder1996], and have been used by many authors [Sievertsen2001]. For $Re \leq 4000$ the coefficients become:

$$Sh = 1.85 * \left(Re \cdot Sc \cdot \frac{d_h}{L} \right)^{0.33} \quad (4.27)$$

For $Re > 4000$ the coefficients become:

$$Sh = 0.04 * Re^{0.75} Sc^{0.33} \quad (4.28)$$

According to [EMST2013 page 1287] the so obtained Sherwood number can then be used to estimate the mass transfer coefficient in the feed channel:

$$Sh = k \cdot \frac{d_h}{D} \quad (4.29)$$

It should be mentioned here that several other approaches exist to describe mass transfer at the feed side of the membrane. The film model is the most common approach. It has been modified to include:

- Eddy-diffusion, as in [Afonso1998],
- shear induced diffusion [Foley2013 page 52]

However, for all modifications the basis for the description of the feed side mass transfer is a mass balance at steady state. The coordinate system, concentration profile, and fluxes are shown in Figure 16. An excellent review of the methods to determine the concentration polarization boundary layer thickness is given in [Gupta2007]. In concentrated solutions, more severe effects can occur which go beyond concentration polarization. Other models, besides the film model, are the gel model, the osmotic pressure model, different filtration models [Mulder 1996] and the boundary layer resistance model [Wijmans1985].

4.6 Electrical double layer

Concentration polarization at the membrane surface is also induced by the electrical interaction between dissolved ions and the fixed charges at the membrane surface.

[Kirby2010] presents a clear summary of the relationships which are necessary to derive the concentration profile through the electrical double layer. The electrical potential gradient around a charged surface can be described by the equation:

$$\varphi = \varphi_0 \cdot \exp\left(-\frac{y}{\lambda_D}\right) \quad (4.30)$$

Where y is the normal vector standing on the charged surface, φ_0 is the surface potential, and λ_D is the Debye length which can be expressed as:

$$\lambda_D = \sqrt{\frac{\varepsilon \cdot RT}{2F^2 I_c}} \Big|_{bulk} \quad (4.31)$$

Where I_c is the ionic strength in mol/m³, refer to Equation (4.60). The potential gradient directly influences the concentration gradient as described by the Poisson-Equation and the concentration profile can be described by:

$$c_i(y) = c_{i,f,b} \cdot \exp\left(-\frac{z_i F}{RT} \varphi_0 \cdot \exp\left(\frac{y}{\lambda_D}\right)\right) \quad (4.32)$$

The surface potential in this equation can be expressed by the membrane surface charge density and the ionic strength by the expression:

$$\varphi_0 = \frac{\sigma}{F \sqrt{\frac{2\varepsilon I_c}{RT}}} \quad (4.33)$$

The membrane surface charge density can be related to the volumetric membrane charge density by Equation (3.52). The advantage of this approach is that the concentration is directly related to the membrane charge density which is the same as inside the membrane pores. This increases the consistency of the modeling and brings it in line with the streaming potential measurements which are performed in tangential mode and are thus suitable to determine the surface charge.

For the concentration just outside the membrane surface Equation (4.32) reduces to

$$c_i^{out} = c_{i,f,b} \cdot \exp\left(-\frac{z_i F}{RT} \varphi_0\right) \quad (4.34)$$

Inserting the expression for the membrane surface potential in Equation (4.33) yields:

$$c_i^{out} = c_{i,f,b} \cdot \exp\left(-\sigma_x \cdot \frac{z_i F \cdot \lambda_D}{RT \cdot \varepsilon}\right) \quad (4.35)$$

The concentration just outside of the membrane is used as the reference concentration for the phase equilibrium for the concentration just inside the membrane. The phase equilibrium and concentration polarization due to the electrical double layer will be implemented at membrane/solution interfaces.

Concentration polarization can be calculated from a mass balance in the feed concentration boundary layer as the sum of convective transport, back transport into the bulk of the feed solution which has to yield the flux that leaves the membrane through the permeate (mass conservation). Back transport is determined by application of a Sherwood correlation.

A novel approach that is suggested here is the inclusion of an additional effect for concentration polarization which is based on the electrical double layer. Concentration polarization is calculated from the surface charge density by application of the Poisson equation.

4.7 Partitioning at the interfaces

The partitioning coefficients at the interfaces between the membrane and the external solutions take into account three separation mechanisms [Vezzani2002]: steric hindrance, Donnan equilibrium via the interfacial potential differences $\Delta\varphi_{Donnan}$, and dielectric exclusion. These three contributing effects will be considered in more detail in the following sections.

The partitioning at the interfaces serves as the boundary condition to solve the Extended Nernst Planck equation and is derived by assuming a local thermodynamic equilibrium at the interface between membrane and surrounding solution, i.e. equality at a nanoscopic scale of the electrochemical potential between the solution right before entry into the pores and immediately inside the pore. The derivation is given in [EMST2013 page 82] and [Szymczyk2005]:

$$\bar{\mu}_i^{in} = \bar{\mu}_i^{out} \quad (4.36)$$

The definition of the electrochemical potential includes the standard chemical potential of ion i μ_i^0 , a reference concentration of 1 mol/l c^0 , and the interaction free energy W_i . This interaction free energy accounts for the interactions between the surrounding medium and ion i which are not considered already by the mean field theory and can be described as an energy barrier to solvation:

$$\bar{\mu}_i = \mu_i^0 + RT \ln \left(\frac{c_i}{c^0} \right) + z_i F \varphi + W_i \quad (4.37)$$

The chemical potentials, the concentrations of the ions, and the electrical potential inside the membrane are radially averaged values. Using this expression in Equation (4.36) will lead to the partitioning coefficient, which is defined as the ratio of the concentrations just inside and just outside the membrane:

$$\Gamma_i = \frac{c_i^{in}}{c_i^{out}} = \exp \left(- \frac{z_i F \Delta \varphi_{Donnan} + \Delta W_i}{RT} \right) \quad (4.38)$$

Where $\Delta \varphi_{Donnan} = \varphi^{in} - \varphi^{out}$ is the Donnan potential and $\Delta W_i = W_i^{in} - W_i^{out}$, the difference in interaction free energy, can be described as an energy barrier to solvation. The total interaction free energy can be divided into a sum of four contributions:

$$\Delta W_i = \Delta W_{i,steric} + \Delta W_{i,Born} + \Delta W_{im} + \Delta W_{i,act} \quad (4.39)$$

The individual contributions to partitioning of the Donnan potential and the interaction free energy will be reviewed in the following sections.

Further reading: [Bandini2003], [Bowen1997], [Bowen1998a], [Bowen1998b], [Bowen2002], [Bowen2002b], [Oatley2014], [Vezzani2002], [Yaroshchuk1998], [Yaroshchuk2000]

4.7.1 Donnan exclusion

Charges of the same sign repel each other due to electrostatic forces which are stronger for multivalent ions. Figure 15 illustrates the distribution of ions according to their charge. The microscopic effects of the interactions between ions result in effects at the macroscopic scale. This notion is also the basis for the understanding of the relationship between Donnan exclusion and the Donnan effect.

The microscopic forces of electric repulsion and attraction influence the equilibrium that develops around a charged membrane, as described in [Donnan1995]. As an example, the retention of a sodium chloride feed solution by a negatively charged membrane is altered by adding sodium sulfate. As shown in Figure 17, when sodium sulfate is added to the feed solution then the negatively charged membrane will have high retention for the negatively charged sulfate while sodium is allowed to pass into the permeate. This will lead to an increased concentration of anions in the feed, i.e. the chloride ions and the additional sulfate ions. The electrostatic forces between these like-charged ions will cause the chloride to pass through the membrane even against its concentration gradient.

The chloride retention in this example reaches negative values when the feed has the same molar concentration of sulfate and chloride. This macroscopic effect is termed Donnan effect and its microscopic cause can be described by Donnan exclusion: co-ions are repelled and counterions are attracted by the electric field that develops at the surface of a charged membrane [EMST2013 page 1276].

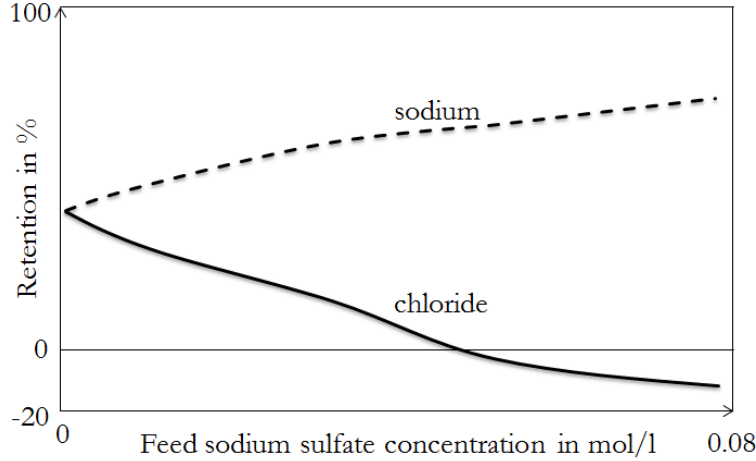


Figure 17: Donnan effect for NaCl (concentration of sodium chloride is 0.05 mol/l) with sodium sulfate from [Melin2007]. @ 25°C, 20 bar and a nanofiltration membrane.

The concentration inside the membrane will be different from the concentration just outside the membrane. The Donnan potential $\Delta\varphi_{Donnan}$ which is the potential difference between material just inside the membrane phase and the solution just outside the membrane surface will influence the partitioning, i.e. the two concentrations at the interface:

$$\Delta\varphi_{Donnan} = \varphi^{in} - \varphi^{out} = \frac{RT}{z_i F} \ln \frac{c_i^{out}}{c_i^{in}} \quad (4.40)$$

The basis for this relationship is the Poisson-Boltzmann theory in which the distribution of ions in an electric field is described. The expression for the Donnan potential can then easily be transformed to give the Donnan contribution to the interfacial partitioning:

$$\left(\frac{c_i^{in}}{c_i^{out}} \right)_{Donnan} = \exp \left(- \frac{z_i F}{RT} \Delta\varphi_{Donnan} \right) \quad (4.41)$$

As described by [Vezzani2002], a charged membrane gives favorable partitioning (i.e. the concentration inside the membrane is higher) for counter-ions (i.e. the Donnan potential has the same sign as the ion's charge) and unfavorable partitioning for co-ions. This contribution to partitioning is implemented in Equation (4.38).

4.7.2 Steric exclusion

According to [Deen1987], the steric partitioning coefficient reflects the ratio between the cross section actually available for the solute i to pass through the pore, to the full cross-sectional area of the pore, as illustrated by Figure 18. This ratio reflects the confinement due to the pores, i.e. the area available for the solute relative to the unconfined case. The expressions that can be developed for this type of exclusion depend on the shape of the pore, e.g. cylindrical or slit-like pores [Deen1987].

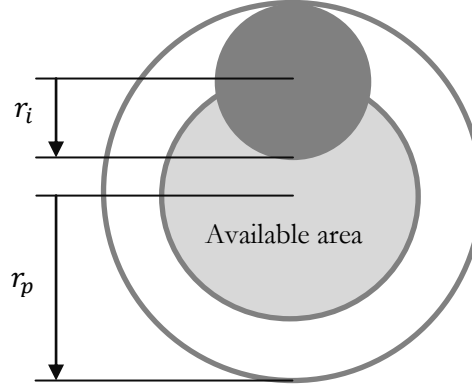


Figure 18: Available cross-sectional area for a spherical solute to pass through a cylindrical pore [EMST2013 page 83].

This coefficient varies in the range between 0 (for a solute larger than the pore radius) and 1 (for a point solute). For a pore of cylindrical cross section the steric partitioning coefficient is:

$$\Phi_{steric} = \left(1 - \frac{r_i}{r_p}\right)^2, \quad \Phi_i \in [0; 1] \quad (4.42)$$

Where the radius of the solute r_i can be expressed by different parameters, here the Stokes radius will be used as given by Equation (4.66).

The contribution of steric exclusion to the solvation energy barrier, as written in Equation (4.39), can be described as:

$$\Delta W_{i,steric} = -RT \cdot \ln \Phi_{steric} \quad (4.43)$$

4.7.3 Dielectric exclusion due to image forces

The mechanism of dielectric exclusion was first described by E. Glueckauf in 1965 [Glueckauf1965]. Ion partitioning due to dielectric effects is caused by a difference between dielectric properties inside the membrane pores and the dielectric properties in the bulk of the solution. The water molecules inside the pores become increasingly oriented because the pore radius is in the same order of magnitude as the size of the water molecules and owing to the polar nature of water [Bandini2003]. This higher degree of spatial and orientational order in small narrow pores makes the water molecules less able to respond to an applied electric field, and consequently the relative permittivity is lower compared to the bulk of the solution [Szymczyk2005].

The dielectric discontinuity surface is located in the boundary between the two dielectric media, feed phase and membrane phase. When this discontinuity surface is approached by a charged ion the surface will become polarized. The polarized layer then exerts a repulsive force on the ion which can formally be described as schematically shown in Figure 19: A mirror image of the ion (same charge and sign of charge and equal distance but opposite of the polarized layer) will cause electrostatic interactions with the approaching ion. Since the relative permittivity of the feed solution is always remarkably higher than that of the membrane matrix the polarization charges induced by the ions have the same sign as the ion charge itself. Thus, this primary mechanism always causes an additional rejection mechanism independent of the ion charge's sign [Bandini2003].

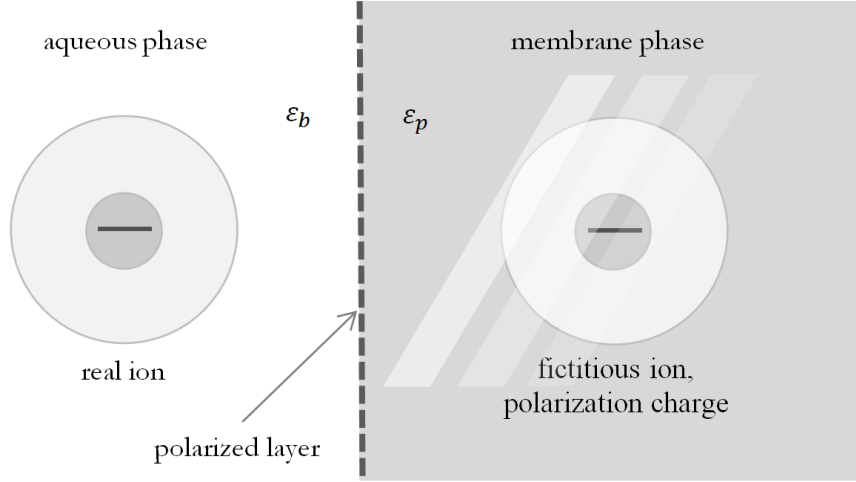


Figure 19: Image force exclusion mechanism at the example of an anion, from [Oatley2012].

Partitioning due to dielectric exclusion is effective for any charged ion independent of its charge's sign. This makes it effective to explain e.g. high magnesium ion retentions by negatively charged membranes where a mere Donnan exclusion would suggest too low retentions [Bandini2003]. For the description of the retention of uncharged membranes dielectric exclusion is of even higher importance as electric exclusion for this system would be equal to zero [Bandini2003].

The mechanism of dielectric exclusion due to image forces has been used in nanofiltration transport models. Two typical examples available in the literature are the DSPM&DE by [Vezzani2002] and the SEDE model by [Szymczyk2005].

[Vezzani2002] describes the electrostatic effects between the real and the fictitious ion based on the Debye-Hückel theory and a Boltzmann distribution type. This theoretical basis is easy to apply in the bulk solution, for the solution inside the pores, this is more complicated. The authors limited their description on the pore side to a partitioning between the bulk solution and the solution at the symmetry axis of the pore. Further, they assumed slit-like pores to yield the expression for the interaction energy:

$$\Delta W_{im} = r_B \{ \kappa^{out} - \kappa^{in} - \frac{1}{r_p} \ln [1 - \gamma \exp(-2r_p \kappa^{in})] \} \quad (4.44)$$

With the factors Bjerrum radius r_B :

$$r_B = \frac{F^2}{2\epsilon_S RT N_A} \quad (4.45)$$

and

$$\gamma = \frac{1 - \epsilon_M/\epsilon_S}{1 + \epsilon_M/\epsilon_S} \quad (4.46)$$

Non-ideality of the electrolyte solution is described through the classical Debye-Hückel theory:

$$(\kappa^{out})^{-1} = \frac{1}{F} \sqrt{\frac{\epsilon_S RT}{8\pi \cdot I^{out}}} \quad (4.47)$$

With the ionic strength defined in Equation (4.60), and $\epsilon_S = 4\pi\epsilon_0\epsilon_b$, $\epsilon_M = 4\pi\epsilon_0\epsilon_m$. Analogous relationships can be written at the membrane/permeate interface ($x = \Delta x$). These equations apply only for

slightly charged membranes with low dielectric constant values. As basic assumption, membrane and bulk aqueous phases are considered continuous media. The equations were developed for ions on the centerline of the pore and should thus only be applied if the product of pore radius and the Debye length is small [EMST2013 page 98]. In case the said product is not small or in the case of low electrolyte concentrations the mechanism of image charges will be negligible. The DSPM&DE model, proposed by [Vezzani2002], is physically inconsistent as it assumes cylindrical pores within the membrane but slit-like pores at the feed/membrane interface, where partitioning occurs.

The second approach that was implemented in the SEDE model by [Szymczyk2005] goes back to the work of [Yaroshchuk2000]. To be able to apply the theory to cylindrical pores approximations were necessary. Additionally, image-force-reducing screening effects were considered that result from the electric field of the fixed charges and the other ions. The image force interaction energy barrier, $\Delta W_{i,im}$, is the sum of two terms:

- One is dependent on the screening length and independent of the distance to the surface $\rightarrow \Delta W_{i,im}$ for an ion at the pore center
- Another one is independent of the screening length and dependent on the radial position.

Among these two terms, the one at the pore center is more important, as transport mainly occurs along the central parts of the pore. Based on this simplification [Yaroshchuk2000] derives for cylindrical pores:

$$\Delta W_{i,im} = \frac{2kT\alpha_i}{\pi} \int_0^\infty \frac{K_0(k)K_1(v) - \beta(k)K_0(v)K_1(k)}{I_1(v)K_0(k) + \beta(k)I_0(v)K_1(k)} dk \quad (4.48)$$

Where

$$\alpha_i = \frac{(z_i F)^2}{8\pi\epsilon_0\epsilon_p RT N_A r_p} \quad (4.49)$$

$$v = \sqrt{k^2 + \mu_{Ya}^2} \quad (4.50)$$

$$\mu_{Ya} = \kappa r_p \sqrt{\sum_i \frac{\left(z_i^2 c_i^b \Phi_i \left(\frac{\gamma_i^{out}}{\gamma_i^{in}} \right) \exp((-e z_i \Delta\phi - \Delta W_{i,Born} - \Delta W_{i,im})/kT) \right)}{2I}} \quad (4.51)$$

$$\kappa = \left(\frac{\epsilon_0 \epsilon_r RT}{2F^2 I^{out}} \right)^{-\frac{1}{2}} \quad (4.52)$$

$$\beta = \frac{k}{\sqrt{k^2 + \mu_{Ya}^2}} \left(\frac{\epsilon_p - \epsilon_m}{\epsilon_p + \epsilon_m} \right) \quad (4.53)$$

Where ϵ_m is the dielectric constant of the membrane, k the wave vector, I_0 , I_1 , K_0 , and K_1 the modified Bessel functions, μ_{Ya} is a factor that controls for the image force screening effect. [Szymczyk2005] modified μ_{Ya} derived by [Yaroshchuk2000] to include both steric and Born terms into the total interaction energy in order to create the SEDE model. The steric term could also be included by a reduced pore size in the (dimensionless) reciprocal internal screening length μ_{Ya} .

[Oatley2012] mentions that the fixed charges of charged membranes will result in a screening of the image charges. This is of especial concern at large Debye lengths. Furthermore, the ion exchange capacity of nanofiltration membranes will result in adsorbed ions which contribute to this screening effect. Even

[Yaroshchuk2000] and [Szymczyk2005] mention that under these conditions the effect of image charges will be negligible.

In the following section a second mechanism for dielectric exclusion will be presented. Simultaneously using both approaches to explain the dielectric mechanisms will result in overcompensation. Since the assumptions for the image force mechanism are much more severe only the Born mechanism will be considered in later sections of this work.

4.7.4 Dielectric exclusion due to the Born effect

The decreased dielectric constant of the solvent confined inside the nanosized pores, as described in Section 4.7.3, is also the starting point for the explanation of the Born effect.

The electrostatic free energy that an ion possesses in vacuum is called self energy. The ion possesses this energy even if it is not interacting with other ions. In any other medium this free energy is termed Born energy and is a measure for the work necessary to charge the ion in its particular environment. A mathematical description of this energy is developed in [Born1920]. In [EMST2013 page 94] the Born energy of an ion i in a medium of relative permittivity ϵ_r is given as:

$$W_{i,Born} = \frac{z_i^2 \cdot e_0^2}{8\pi\epsilon_0\epsilon_r r_i} \quad (4.54)$$

This equation shows that work is required if the dielectric constant of the medium around an ion of charge z_i is changed. Interestingly, the effect depends only on the magnitude of the charge and not its sign, i.e. the effect is the same for anions and cations of the same absolute value of charge. In membrane filtration this Born energy can be calculated for both the external solution, with a relative permittivity of ϵ_b , as well as for the solution inside the pores, with ϵ_p . The difference between these states is the Born energy barrier to solvation [EMST2013 page 94] and gives the work required for the transfer of a charge from a medium with relative permittivity ϵ_b to a medium of ϵ_p :

$$\Delta W_{i,Born} = \frac{z_i^2 \cdot e_0^2}{8\pi\epsilon_0 r_i} \left(\frac{1}{\epsilon_p} - \frac{1}{\epsilon_b} \right) \quad (4.55)$$

Using the atomic radius for r_i has been shown to result in an overestimation of the solvation enthalpies, especially for cations [Szymczyk2005]. Alternative measures are the Stokes radius and the highest accuracy is reached by using the cavity radius of the ions (which here is assumed to be independent of the medium's dielectric constant). The cavity radius can be defined as the distance from the center of the ion and the point where the dielectric constant becomes different from that of the vacuum, i.e. where the medium really begins [Szymczyk2005]. A method for the estimation of ion cavity size is given in [Rashin1985]. Based on empirical evidence, an increase of the so acquired cavity radius by 7% proved to reach best agreement with experimental observations [Szymczyk2005]. The correction has been explained by the dielectric saturation effect which assumes that the effect of the fixed charges is reduced in the vicinity of charged ions. However, the cavity radius is not available for uranium species and can thus not be used in the model. As a consequence, the question arises if other ions for which the cavity radius is known should be modeled using their cavity radius or their Stokes radius. The main function of modeling the ions with known cavity radius (e.g. Na^+ , K^+ , Cl^-) is a comparison with the behavior of the uranium species. Hence, the test ions should be described by the same variables as the uranium species: By their Stokes radius and not by their cavity radius. This way the stokes

radius for the uranium species can be derived from literature data of their diffusivity using the Stokes-Einstein equation.

The magnitude of the Born effect depends on the square of the ion's charge but it does not depend on the sign of the charge, as can be seen in Equation (4.55) [EMST2013 page 95]. Moreover, this effect could also occur for uncharged membranes as the effect depends on the charge of the ion and on a difference in dielectric properties only. Thus a determination of dielectric exclusion separate from Donnan exclusion could be performed at the isoelectric point of the membrane. Smaller values for the pore relative permittivity compared to the bulk relative permittivity will result in higher salt rejection.

Different approaches exist for the calculation of the relative permittivity inside the pores. Some authors assume that the water molecules inside the pores have bulk properties except for a monolayer of oriented water molecules at the pore wall. The mathematical relationship is given in Equation (4.2).

The Born energy will be included in the here developed model by the equation:

$$\Phi_{Born} = \exp\left(-\frac{\Delta W_{i,Born}}{k_B T}\right) \quad (4.56)$$

4.7.5 Activity exclusion

This contribution to ion partitioning at the solution/membrane interface originates from a difference in activity coefficients which is a description of the Coulombic forces between ions. For infinite dilution and under the assumption that the volume of the ions can be neglected the activity coefficients can be calculated according to the extended law of the Debye-Hückel theory [Luckas2001, page 141]:

$$\ln(\gamma_i) = -A_m \cdot z_i^2 \sqrt{I_m} \quad (4.57)$$

This equation has been modified by [Davies1962] in order to be applicable at higher ionic strengths. With the following equation the activity coefficient can be determined to about 2% accuracy for ionic strengths up to 0.1 mol/kg:

$$\log_{10}(\gamma_i) = -A_m \cdot z_i^2 \left(\frac{\sqrt{I_m}}{1 + \sqrt{I_m}} - 0.3 I_m \right) \quad (4.58)$$

where the interaction parameters and single ion contributions are:

$$A_m = \frac{1}{\ln(10)} \sqrt{2 \cdot 10^3 \pi N_A \rho_{solvent}} \left(\frac{e^2}{4\pi \epsilon_0 \epsilon k T} \right)^{\frac{3}{2}} \quad (4.59)$$

$$I_m = \frac{1}{2} \sum_i m_i z_i^2 \quad (4.60)$$

The advantage of the equations from the Debye-Hückel theory used here is that all required parameters are available and have already been used in other equations of the model, i.e. no new data is required. The Pitzer equation could be used at even higher concentrations but the necessary coefficients for the membrane phase need to be determined by extensive experimentation.

The contribution of activity exclusion to total ion partitioning at the interface between membrane and solution can be written as [Szymczyk2005]:

$$\Delta W_{i,act} = RT \cdot \ln(\gamma_i^{in} / \gamma_i^{out}) \quad (4.61)$$

Partitioning is based on the assumption of phase equilibrium at the membrane/solution interfaces at the feed and permeate side. The equilibrium is described by the electrochemical potential. Hence the distribution of each ion depends on the difference between the two phases (solution vs. membrane) in concentration, the electric potential, the activity coefficient, and the interaction free energy. The here employed form of interaction free energy includes steric and dielectric effects.

4.8 Transport through the membrane

Transport through the membrane is described by the extended Nernst-Planck equation accounting for convection, diffusion, and electromigration inside the membrane matrix, as derived in Section 3.1.3:

$$j_i = K_{i,c}c_iJ_v - K_{i,d}D_{i,\infty}\frac{dc_i}{dx} - \frac{Fz_i c_i K_{i,d} D_{i,\infty}}{RT} \frac{d\varphi}{dx} \quad (4.62)$$

The hindrance factors for convection $K_{i,c}$ and diffusion $K_{i,d}$, which gives the hindered diffusivity inside the membrane $D_{i,p} = K_{i,d}D_{i,\infty}$, will be discussed in the following sections.

A commonly applied simplification is linearization of the Extended Nernst Planck equation (ENP). The results obtained by this approximation have been shown to yield reasonable results [Sharma2008]. From Equation (3.50) in combination with Equation (4.6) the concentration gradient across the membrane pores can be expressed as:

$$\frac{dc_i}{dx} = \frac{J_v}{D_{i,p}} (K_{i,c}c_{i,j} - c_{i,p}) - \frac{z_i c_{i,j} F}{RT} \cdot \frac{d\varphi}{dx} \quad (4.63)$$

And thus the electric potential gradient across the pores [Schlög1972]:

$$\frac{d\varphi}{dx} = \frac{\sum_{i=1}^{N_n} \frac{z_i J_v}{D_{i,p}} (K_{i,c}c_i - c_{i,p})}{\frac{F}{RT} \sum_{i=1}^{N_n} (z_i^2 c_i)} \quad (4.64)$$

The pore inlet and outlet concentrations can quickly be calculated using the method described by [Oatley2014]. This method by itself is sufficient to solve the model equations, however, here a discretization of the membrane will be performed to calculate the concentration gradient across the membrane.

4.8.1 Steric hindrance

The hindrance factors account for the effects of the pore walls on the ions motion, as explained by [Vezzani2002]. There, these interactions are described as “sieve effect” due to the intrinsic porosity of the membrane. The correlations for the steric hindrance factors are usually expressed in terms of the ratio λ_i , where the radius of the solute, r_i , is compared to the pore radius, r_p :

$$\lambda_i = \frac{r_i}{r_p} \quad (4.65)$$

Different approaches exist for the solute radius, r_i . Often it is expressed as the Stokes radius which can be calculated from the solute’s diffusivity by the Stokes-Einstein equation [EMST2013 page 84], [Fievet2002], [Hussain2007], [Kerisit2010], [Labbez2003]:

$$r_{i,s} = \frac{k_B T}{6\pi\eta D_{i,\infty}} \quad (4.66)$$

The value below the fraction will be in the range between 4 and 6 which depends on the hydration of the ion. If the ion is stripped of its water shell (slip condition) the value is 4, and if the ion diffuses in its fully hydrated form (stick condition) the value is 6. As [Grathwohl1998] mentions, the Stokes-Einstein equation is valid only for spherical solutes which are much larger than the surrounding solvent molecules (here, water molecules). This means that the correlation should not be used when the transport of small ions, such as hydroxyl or hydronium ions, is considered.

The diffusion hindrance factor is the ratio of hindered diffusivity to bulk diffusivity, as defined by [Bowen1996]:

$$K_d = \frac{D_p}{D_\infty} \quad (4.67)$$

The convection hindrance factor is the ratio of solute velocity to solvent velocity [Bowen1996]:

$$K_c = \frac{u_s}{u_p} \quad (4.68)$$

Different formulations of the two hindrance factors have been developed in the literature based on theoretical consideration refined by experimental evidence. The following two sections will be dedicated to a review of the available correlations for the model development performed in this work.

4.8.2 Diffusion hindrance factor

Expressions for the hindrance factors have first been derived for the mathematically more accessible system of a symmetrically positioned ion, i.e. an ion located on the axis of the cylindrical pore. These correlations are termed centerline approaches. The much-quoted centerline approximation obtained by [Renkin1954] for $0 \leq \lambda_i < 0.4$, and used by many authors [Anderson1974], reads:

$$K_{i,d} = 1 - 2.1044\lambda_i + 2.089\lambda_i^3 - 0.948\lambda_i^5 \quad (4.69)$$

[Bungay1973] further optimized the centerline approximation, using asymptotic matching, to yield an accuracy of more than 1% for the range $0 \leq \lambda < 1$ [Dechadilok2006]. The obtained expression is used throughout the literature [EMST2013 page 101] and [Szymczyk2006]:

$$K_{i,d} = \frac{6\pi}{K_{i,t}} \quad (4.70)$$

Where the coefficient $K_{i,t}$ can be calculated with the factors $a_1 = -73/60$, $a_2 = 77.293/50.4$, $a_3 = -22.5083$, $a_4 = -5.6117$, $a_5 = -0.3363$, $a_6 = -1.216$, $a_7 = 1.647$ as:

$$K_{i,t} = \frac{9}{4}\pi^2\sqrt{2}(1-\lambda_i)^{-\frac{5}{2}} \left[1 + \sum_{n=1}^2 a_n(1-\lambda_i)^n \right] + \sum_{n=0}^4 a_{n+3}\lambda_i^n \quad (4.71)$$

Using the formulation by Bungay and Brenner offers the advantage of applicability over the entire range of solute-to-pore size ratio as shown in [Noordman2002]. Also, the expressions obtained by Bungay and Brenner were validated by more exact methods. [Bowen1994] used the finite element method to develop simpler equations. For the range $0 \leq \lambda_i \leq 0.8$ the equations are shown in [Bowen1997], and have been used by many authors, e.g. [Labbez2003], and [Noordman2002]:

$$K_{i,d} = 1.0 - 2.3\lambda_i + 1.154\lambda_i^2 + 0.224\lambda_i^3 \quad (4.72)$$

Instead of the center-line expression, an approach is desired that also takes off-diagonal ions into account. An analytical solution for the radial average of the hindrance factor was derived by [Brenner1977]. However, his result, that is considered accurate, is valid only for $\lambda_i \rightarrow 0$. Nevertheless, the expression can be used as a reference for comparing different approximate expressions (where the o in the equation denotes an error term proportional to λ_i):

$$K_{i,d} = 1/(1 - \lambda_i)^2 \left(1 - \left(\frac{9}{8}\right) \lambda_i \ln \frac{1}{\lambda_i} - 1.539\lambda_i - o(\lambda_i) \right) \quad (4.73)$$

[Nitsche1994] further modified the equation by [Brenner1977] to include wall curvature effects:

$$K_{i,d} = 1/(1 - \lambda_i)^2 \left(1 + \left(\frac{9}{8}\right) \lambda_i \ln \lambda_i - 1.539\lambda_i + 1.2\lambda_i^2 + o(\lambda_i^2) \right) \quad (4.74)$$

Asymptotic matching was also used for the upper end of λ_i . [Mavrovouniotis1986] yielded an expression for the radial average for $\lambda_i \rightarrow 1$:

$$K_{i,d} = \left[0.984 \cdot \left(\frac{1 - \lambda_i}{\lambda_i}\right)^{\frac{5}{2}} + o\left(\left(\frac{1 - \lambda_i}{\lambda_i}\right)^3\right) \right] \quad (4.75)$$

The radial average, i.e. off-axis expressions needed to be extended to the full range of λ_i . This was achieved by [Higdon1995] using a boundary element method to evaluate the hindrance factor at certain values of λ_i . This method yields accurate values for $K_{i,d}$ as a function of λ_i . A least-squares fit performed by [Dechadilok2006] on the full dataset of [Higdon1995] then yielded an expression that is valid for $0 \leq \lambda_i \leq 0.95$:

$$K_{i,d} = 1/(1 - \lambda_i)^2 \left(1 + \left(\frac{9}{8}\right) \lambda_i \ln \lambda_i - 1.56034\lambda_i + 0.528155\lambda_i^2 + 1.91521\lambda_i^3 - 2.81903\lambda_i^4 \right. \\ \left. + 0.270788\lambda_i^5 + 1.10115\lambda_i^6 - 0.435933\lambda_i^7 \right) \quad (4.76)$$

In the range $0 \leq \lambda_i \leq 0.95$ this correlation is about 2% accurate. If high precision is required for more closely fitting spheres, i.e. $0.95 \leq \lambda_i$, then the expression by [Mavrovouniotis1986] should be used.

However, also very rough methods have been employed in the literature, yielding sufficient results nevertheless, i.e. model dependence on the hindrance coefficients is not extremely sensitive. [Bowen1996] reduced the hindrance factor to a linear approximation for the range $0 \leq \lambda_i < 0.4$:

$$K_{i,d} = -1.705\lambda_i + 0.946 \quad (4.77)$$

The different correlations for the hindrance factors are shown in Figure 20.

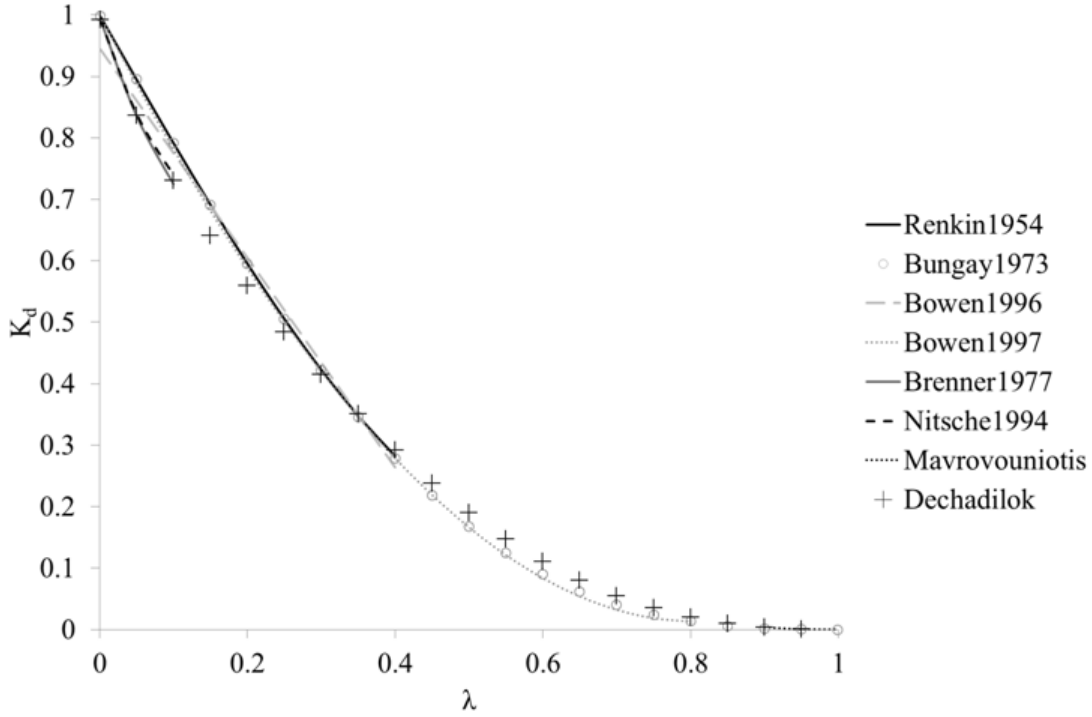


Figure 20: Comparison of different formulations for the diffusional hindrance factor.

Due to the advantages described in [Dechadilok2006] Equation (4.76) is used for the range $0 < \lambda_i \leq 0.95$ and above $\lambda_i > 0.95$ Equation (4.75) will be used to calculate $K_{i,d}$ in the model prepared here.

4.8.3 Convection hindrance factor

The centerline approximation approach has also been used in the development of hindrance factors for convection. [Bungay1973] developed an expression that is applicable to the full range of ion radii $0 \leq \lambda < 1$, and found widespread use in the literature [EMST2013 page 101]:

$$K_{i,c} = \frac{(2 - (1 - \lambda)^2)K_{i,s}}{2K_{i,t}} \quad (4.78)$$

with $K_{i,t}$ from Equation (4.71). With the factors $b_1 = 7/60$, $b_2 = -2.227/50.4$, $b_3 = 4.0180$, $b_4 = -3.9788$, $b_5 = -1.9215$, $b_6 = 4.392$, $b_7 = 5.006$ $K_{i,s}$ can be calculated as:

$$K_{i,s} = \frac{9}{4}\pi^2\sqrt{2}(1 - \lambda_i)^{-\frac{5}{2}} \left[1 + \sum_{n=1}^2 b_n(1 - \lambda_i)^n \right] + \sum_{n=0}^4 b_{n+3}\lambda_i^n \quad (4.79)$$

A centerline approximation for the range $0 \leq \lambda_i < 0.4$ is given in [Anderson1974]:

$$K_{i,c} = (2 - (1 - \lambda_i)^2) \left(1 - \frac{2}{3}\lambda_i^2 - 0.163\lambda_i^3 \right) \quad (4.80)$$

Using asymptotic matching to determine the radially averaged value of $K_{i,c}$ for $\lambda_i \rightarrow 0$, [Brenner1977] obtained:

$$K_{i,c} = 1 + 2\lambda_i - 4.9\lambda_i^2 + o(\lambda_i^2) \quad (4.81)$$

[Ennis1996] combined the exact results of [Brenner1977] with the centerline approximation of [Bungay1973] to yield:

$$K_{i,c} = \frac{1 + 3.867\lambda_i - 1.907\lambda_i^2 - 0.834\lambda_i^3}{1 + 1.867\lambda_i - 0.741\lambda_i^2} \quad (4.82)$$

[Bowen1996] reduced the hindrance factor to a linear approximation for the range $0 \leq \lambda_i < 0.4$:

$$K_{i,c} = -0.301\lambda_i + 1.022 \quad (4.83)$$

Using the finite element method [Bowen1997] developed a convection hindrance factor for the range $0 < \lambda_i < 0.8$ that has been used by [Labbez2003] and [Mohammad2003]:

$$K_{i,c} = (2 - (1 - \lambda_i)^2)(1.0 + 0.054\lambda_i - 0.998\lambda_i^2 + 0.441\lambda_i^3) \quad (4.84)$$

As can be seen in Figure 21, the centerline approximations consistently overestimate the hindrance factor, compared to the “exact” solutions by [Brenner1977] and [Ennis1996].

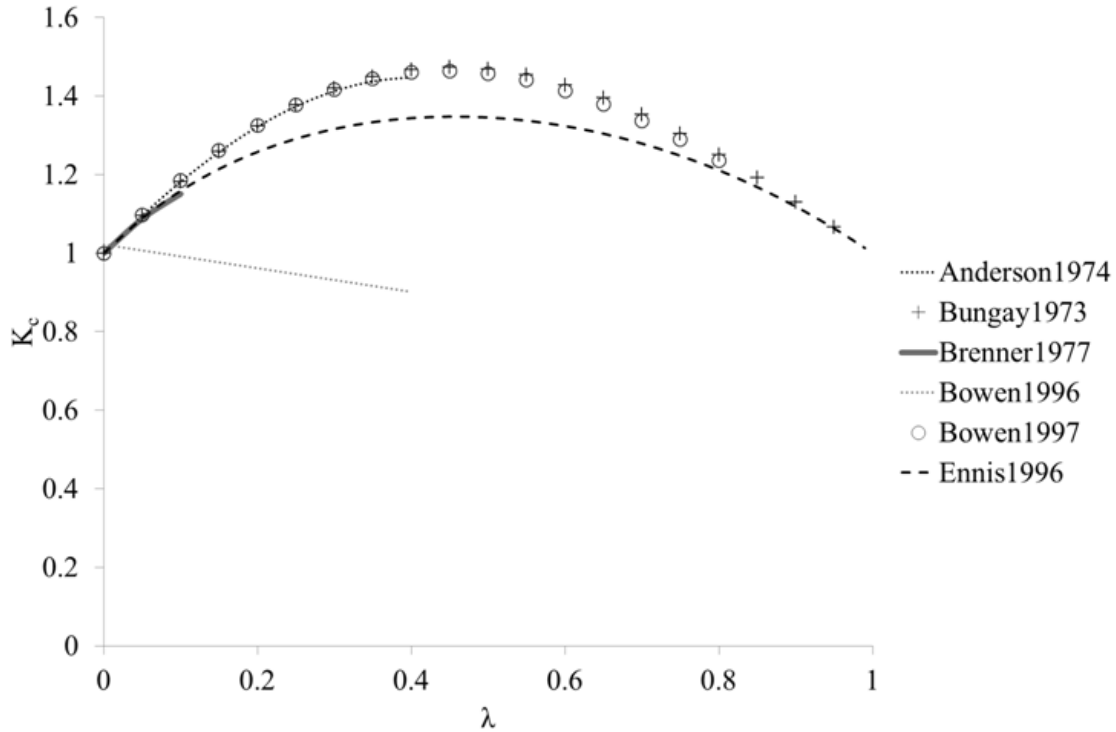


Figure 21: Comparison of different formulations for the convection hindrance factor.

The formulation developed by [Ennis1996], shown in Equation (4.82), offers both advantages of being precise, and applicable to the whole range of λ_i and will thus be implemented in the model developed in this work.

Transport inside the membrane is described by hindered convection, diffusion, and electromigration in the extended Nernst-Planck equation. The hindrance factors are based on theoretical considerations on the basis of the ratio between pore radius and solute radius. Different correlations which exist in the literature are reviewed and discussed here and suitable correlations for the hindrance factors were selected.

4.9 Numerical solution

The development of the program code will be presented in this section. The input parameters, constants, and model output parameters are summarized in Table 3. The numerical solution of the model is implemented in Matlab® and all input parameters will be defined by the user in an Excel spreadsheet and will then be imported into the Matlab® code automatically. The constants are defined within the Matlab® code as they need to be modified only if the model is meant to be changed and not for a regular model calculation. The concentration profiles are plotted automatically after the model is solved.

Table 3: Overview of the model parameters.

Model input parameters	Model constants	Model variables
Membrane pore radius r_p	Avogadro constant N_A $6.02214129 \cdot 10^{23}$ 1/mol	i × ion concentration at each point $c_{i,j}$
Membrane equivalent thickness Δx_e	Elementary charge e $1.602176565 \cdot 10^{-19}$ C	Electrical potential at each point φ_j
Membrane charge density c_x	Faraday constant F 96485.3365 C/mol	
i × Ion feed concentration $c_{i,f,b}$	Boltzmann constant k_B $1.3806488 \cdot 10^{-23}$ J/K	
i × Ion charge z_i	Molar gas constant R 8.3144621 J/mol/K	
i × Ion diffusivity $D_{i,\infty}$ (values for D_∞ taken from [Lide2005], and [Nightingale1959])	Vacuum permittivity ϵ_0 $8.8542 \cdot 10^{-12}$ F/m	
i × Ion Stokes radius r_i	Water density ρ_{H_2O}	
Volumetric permeate flux J_v	Water viscosity η_{H_2O}	
Test cell cross-sectional dimensions a , b , d_{hyd}	Water permittivity ϵ_b	
Test cell characteristic length L	Pore permittivity ϵ_p	
Number of nodes in the mesh that discretizes the membrane		

Before the development of a specific algorithm of the model computation, a degree of freedom analysis needs to be performed where the number of unknown variables is compared with the number of available equations. Since the membrane is discretized into a certain number of nodes the number of unknown variables and equations depend on the number of nodes. As shown in Figure 22, the number of “model positions” is the number of nodes plus 3 (for the feed and the permeate side of the membrane and for the permeate bulk solution): $N_{\text{positions}} = N_n + 3$. At each of these positions a certain number of variables and equations can be defined.

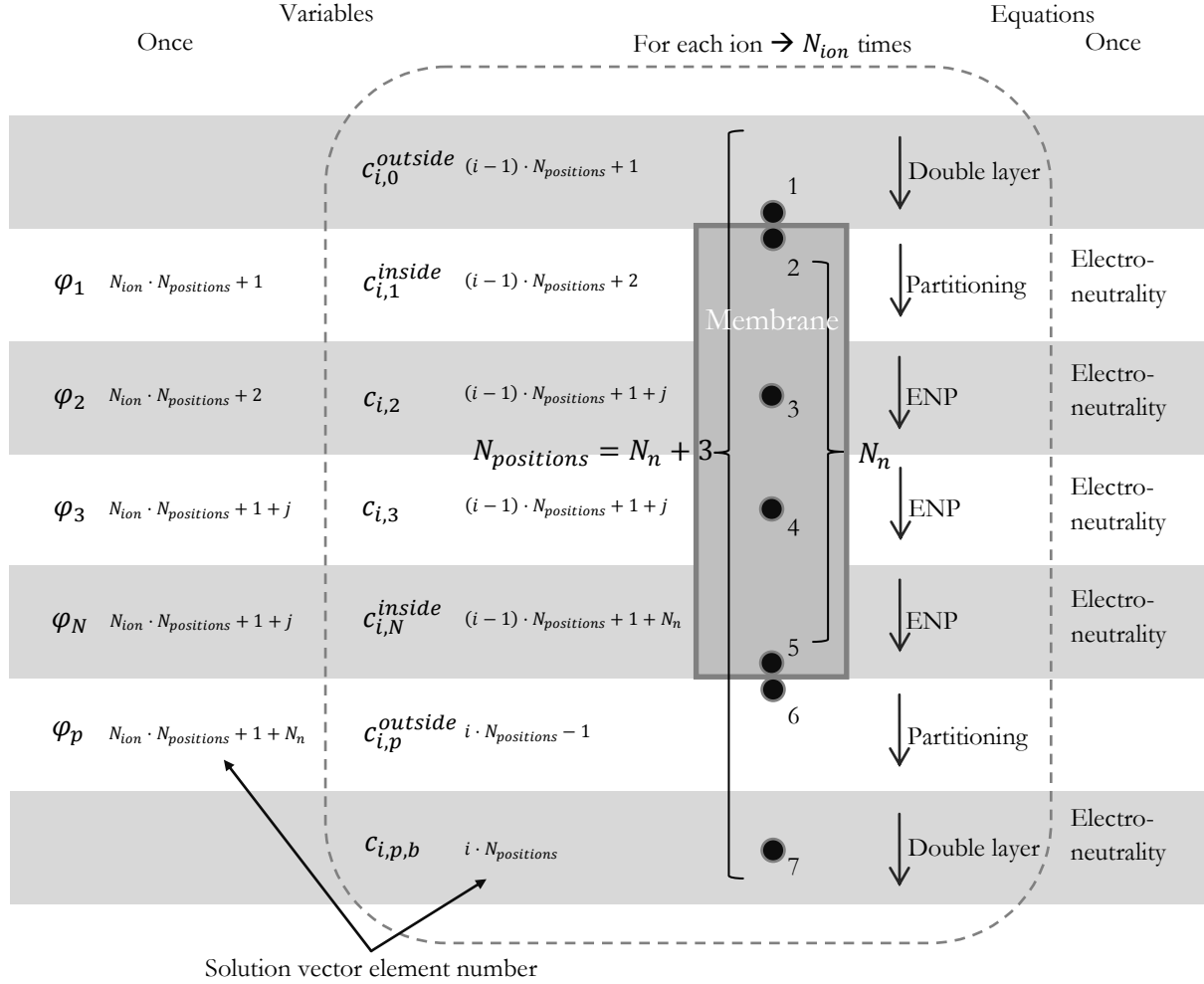


Figure 22: Degree of freedom analysis at the example of a membrane that is discretized into 4 points. The feed concentration is not listed because it is not variable and kept constant throughout the simulation (design parameter).

In a degree of freedom analysis the number of equations should be the same as the number of variables. Here, the number of variables concerning the electrical potential is balanced by the number of equations for the electroneutrality condition and the number of variables concerning concentrations is balanced by the number of transport equations. As summarized in Table 4 the model is well balanced and the number of unknown variables equals the number of equations.

Table 4: Degree of freedom analysis: The number of variables equals the number of equations.

Unknown model parameters:	
- Concentrations ($1 \times \text{feed}$, $2 \times \text{permeate}$, $N_n \times \text{membrane}$)	$N_{ion} \cdot N_{positions}$
- Potentials ($1 \times \text{permeate}$, $N_n \times \text{membrane}$)	$N_{positions} - 2$
- Total	$(N_{ion} + 1) \cdot N_{positions} - 2$
Model equations	
- Transport equations, i.e. (4.33), (4.39), (4.63)	$N_{ion} \cdot N_{positions}$
- Electroneutrality, i.e. (4.12)	$N_{positions} - 2$
- Total	$(N_{ion} + 1) \cdot N_{positions} - 2$

The model equations developed above are linearized and converted into a matrix operation of the type:

$$M \cdot x = v \quad (4.85)$$

This system is explicitly shown in Table 5 and the specific entries of the matrix are given in the equations below. The order of the entries in the solution vector x is given in Figure 22. This system is then solved using the Matlab® command `fsolve` and the Levenberg-Marquardt algorithm.

Table 5: Matrix operation of the type $M \cdot x = v$ that is at the core of the program for the numerical solution. (EDL=electrical double layer, ENP=extended Nernst-Planck equation)

M	$c_{i,0}^{out}$	$c_{i,1}^{in}$	$c_{i,j}$	$c_{i,j+1}$	$c_{i,N}$	$c_{i,p}^{out}$	$c_{i,p,b}$	φ_j	φ_{j+1}	φ_p	v
Feed EDL	(4.87)	0	0	0	0	0	0	0	0	0	$c_{i,f,b}$
Feed partition.	(4.90)	1	0	0	0	0	0	0	0	0	0
ENP	0	0	(4.93)	(4.94)	0	0	(4.97)	(4.95)	(4.96)	0	0
Permeate partition.	0	0	0	0	1	0	(4.99)	0	0	0	0
Permeate EDL	0	0	0	0	0	(4.87)	-1	0	0	0	0
Node elec.neutr.	0	0	z_i	0	0	0	0	0	0	0	$-c_x$
Permeate elec.neutr.	0	0	0	0	0	0	z_i	0	0	0	0

$\cdot x =$

Concentration polarization in the EDL:

In Sections 4.5 and 4.6 two different approaches for the description of concentration polarization are presented, due to feed hydrodynamics and due to the effects of the electrical double layer (EDL). At low cross flow velocities both effects need to be accounted for. At high cross flow velocities however, back transport into the bulk of the feed solution happens rapidly and concentration polarization can be described by the concentration distribution in the electrical double layer only. Hence, at low cross-flow velocity the system becomes more complex. Since a rigorous description of the hydrodynamic concentration polarization requires consideration of convective, electromigrative, and diffusive transport [Gerald2007], as well as Eddy diffusion, shear induced diffusion, formation of a gel layer etc. [Schäfer2006] the approach taken here is to increase the cross flow velocity sufficiently high and avoid hydrodynamic concentration polarization all together in order to reduce the model to concentration polarization due to effects of the electrical double layer.

The concentration just outside the membrane surface can be related to the bulk value by rearranging Equation (4.32):

$$c_{i,b} = c_i^{out} \cdot \exp\left(\sigma_x \cdot \frac{z_i F \cdot \lambda_D}{RT \cdot \varepsilon}\right) \quad (4.86)$$

The coefficient for c_i^{out} thus reads:

$$\exp\left(\sigma_x \cdot \frac{z_i F \cdot \lambda_D}{RT \cdot \varepsilon}\right) \quad (4.87)$$

This expression describes the concentration polarization at the feed and permeate side.

Ion partitioning at the feed solution/membrane interface:

Equation (4.38), describing ion partitioning at the interfaces between membrane and solution, can be transformed to yield:

$$\begin{aligned} \Gamma_i &= \frac{c_i^{in}}{c_i^{out}} = \exp\left(-\frac{z_i F \Delta \varphi_{Donnan} + \Delta W_i}{RT}\right) \\ &= \exp\left(-\frac{z_i F \Delta \varphi_{Donnan} + \Delta W_{i,steric} + \Delta W_{i,Born} + \Delta W_{i,mem} + \Delta W_{i,act}}{RT}\right) \\ &= \exp\left(\ln(\Phi_{steric}) - \frac{z_i F \Delta \varphi_{Donnan} + \Delta W_{i,Born} + \Delta W_{i,act}}{RT}\right) \\ &= \Phi_{steric} \exp\left(-\frac{z_i F \Delta \varphi_{Donnan} + \Delta W_{i,Born}}{RT} - \ln\left(\frac{\gamma_i^{in}}{\gamma_i^{out}}\right)\right) \\ \frac{\gamma_i^{in} c_i^{in}}{\gamma_i^{out} c_i^{out}} &= \Phi_{steric} \exp\left(-\frac{z_i F \Delta \varphi_{Donnan} + \Delta W_{i,Born}}{RT}\right) = \Phi_{steric} \Phi_{Born} \exp\left(-\frac{z_i F \Delta \varphi_{Donnan}}{RT}\right) \\ &\quad - \frac{\gamma_i^{out}}{\gamma_i^{in}} c_i^{out} \Phi_{steric} \Phi_{Born} \exp\left(-\frac{z_i F \Delta \varphi_{Donnan}}{RT}\right) + c_i^{in} = 0 \end{aligned} \quad (4.88)$$

For feed side partitioning this specifically translates to the following expression:

$$c_{i,0}^{out} \left[-\frac{\gamma_{i,0}^{out}}{\gamma_{i,1}^{in}} \Phi_{steric,i} \Phi_{Born,i} \exp\left(-\frac{z_i F (\varphi_1 - \varphi_0)}{RT}\right) \right] + c_{i,1}^{in} = 0 \quad (4.89)$$

Where the electric potential outside the membrane is set to be equal to zero, i.e. the frame of reference for all other potentials. The coefficient for $c_{i,0}^{out}$ thus reads:

$$-\frac{\gamma_{i,0}^{out}}{\gamma_{i,1}^{in}} \Phi_{steric,i} \Phi_{Born,i} \exp\left(-\frac{z_i F (\varphi_1 - \varphi_0)}{RT}\right) \quad (4.90)$$

For $c_{i,1}^{in}$ the coefficient is equal to one and the constant term is equal to zero.

Transport through the membrane pores described by the extended Nernst-Planck equation:

The extended Nernst-Planck equation, from Equation (4.62), can be transformed for the finite difference between each node and its subsequent node, to yield:

$$\begin{aligned} c_{i,p} J_v &= j_i = \frac{1}{2} K_{i,c} (c_{i,j} + c_{i,j+1}) J_v - D_{i,p} \frac{c_{i,j+1} - c_{i,j}}{\delta x} - \frac{F z_i (c_{i,j} + c_{i,j+1}) D_{i,p}}{2RT} \frac{\varphi_{j+1} - \varphi_j}{\delta x} \\ &= c_{i,j} \cdot \left(\frac{D_{i,p}}{\delta x} + \frac{1}{2} K_{i,c} J_v \right) + c_{i,j+1} \cdot \left(-\frac{D_{i,p}}{\delta x} + \frac{1}{2} K_{i,c} J_v \right) + \varphi_j \\ &\quad \cdot \left(\frac{F z_i D_{i,p}}{2RT} \frac{c_{i,j} + c_{i,j+1}}{\delta x} \right) - \varphi_{j+1} \cdot \left(\frac{F z_i D_{i,p}}{2RT} \frac{c_{i,j} + c_{i,j+1}}{\delta x} \right) \end{aligned} \quad (4.91)$$

The ENP will now be expressed in the form:

$$c_{i,j} \cdot A_{i,j} + c_{i,j+1} B_{i,j} + \varphi_j \cdot C_{i,j} + \varphi_{j+1} \cdot D_{i,j} + c_{i,p} E = 0 \quad (4.92)$$

With the coefficients being:

$$A_{i,j} = \frac{D_{i,p}}{\delta x} + \frac{1}{2} K_{i,c} J_v \quad (4.93)$$

$$B_{i,j} = -\frac{D_{i,p}}{\delta x} + \frac{1}{2} K_{i,c} J_v \quad (4.94)$$

$$C_{i,j} = \frac{F z_i D_{i,p} c_{i,j} + c_{i,j+1}}{2RT} \quad (4.95)$$

$$D_{i,j} = -\frac{F z_i D_{i,p} c_{i,j} + c_{i,j+1}}{2RT} \quad (4.96)$$

$$E = -J_v \quad (4.97)$$

Ion partitioning at the permeate solution/membrane interface:

The equations for ion partitioning at the permeate side of the membrane Equation (4.88):

$$c_{i,p} \left[-\frac{\gamma_{i,p}^{out}}{\gamma_{i,N}^{in}} \Phi_{steric} \Phi_{Born} \exp \left(-\frac{z_i F (\varphi_N - \varphi_p)}{RT} \right) \right] + c_{i,N}^{in} = 0 \quad (4.98)$$

The choice for the electric potential gradient of the Donnan equilibrium, i.e. whether it should be $\varphi_N - \varphi_p$ or $\varphi_p - \varphi_N$, needs to assume that the ion goes from outside into the membrane, also at the permeate side. The effect is already reversed by the concentrations used. Reversing the potential gradient would thus negate the choice of concentrations. The coefficient for $c_{i,N}^{inside}$ is equal to one and the coefficient for $c_{i,p}$ reads:

$$-\frac{\gamma_{i,p}^{out}}{\gamma_{i,N}^{in}} \Phi_{steric} \Phi_{Born} \exp \left(-\frac{z_i F (\varphi_N - \varphi_p)}{RT} \right) \quad (4.99)$$

The last series of equations take the ion balance into account. The equations for the electroneutrality condition in feed, permeate, and at each node can directly be used from the respective chapter, Section 4.4. The initial point for the vector x will be calculated by setting all concentrations to the feed concentration and setting the potential to zero at all positions. This system is then solved numerically using `fsolve` with the Levenberg-Marquardt algorithm.

The here developed model is based on the extended Nernst-Planck equation for the description of hindered transport inside the membrane pores and the equality of the electrochemical potential at the solution/membrane interfaces (equilibrium) as well as concentration polarization in the electrical double layer. Assumptions which are representative of the real mine water nanofiltration are low concentration and a homogenous membrane structure. These need to be considered when the limitations of the model are of relevance.

4.10 Parameter fitting

The membrane parameters pore radius, volumetric charge density were determined by fitting the model developed in the previous section to experimental data. An overview of the fitting operations is given in the following Table 6.

Table 6: Overview of the fitting operations in this thesis.

System	Chapter	Experimental input data	Fitted parameters	Sum of square error
Glucose solution	6.3	Glucose retention over permeate flux	• Pore radius	1.5E-5
KCl solution	6.4	KCl retention over permeate flux	• Membrane volume charge density	3.6E-3
Mine drainage	6.6	Component retention for 10 components	• Membrane volume charge density	1.4E-1
KCl solution	7.6	KCl retention over permeate flux	• Membrane volume charge density • thickness	1.3E-4
Mine drainage	7.6	Component retention for 10 components	• Membrane volume charge density • pore radius • thickness • permittivity	1.4E-2

The sum of squared error between experimental ($R_{experiment}$) and simulated ($R_{simulation}$) retention was divided by the number of measured retentions, n :

$$SSE = \frac{\sum_{n=1}^n (R_{experiment,n} - R_{simulation,n})^2}{n} \quad (4.100)$$

Where the retentions can take values of below 1, i.e. the retentions are not converted to percent. The resulting sum is smallest for the glucose retention and highest for the single parameter fit of the mine drainage. Excluding the large error for nitrate from the calculation of the sum of square errors for the 4-parameter fit of the mine drainage will reduce the error to 3E-3.

5 Materials and methods

In this section materials and methods are presented starting from the employed nanofiltration membranes, the laboratory equipment for the membrane experiments and characterization by streaming potential measurements towards the chemical characteristics of the uranium-contaminated solutions and methods that were used to evaluate the experiments.

5.1 Membranes

In this work the 18 membranes shown in Table 7 were chosen according to recommendations by the membrane manufacturers and from a literature study of similar studies. In the following section, existing information on these membranes is gathered; further membrane characterization will be presented in the experimental sections.

Table 7: List of the membranes, and their respective abbreviations used in this work.

Manufacturer	Membrane name	Type	Abbr.
Alfa Laval Corporate AB	Alfa Laval NF99 HF	NF	HF99
	Alfa Laval NF99	NF	ALNF
	Alfa Laval RO90	RO	RO90
	Alfa Laval RO99	RO	RO99
DOW Water and Process Solutions	Filmtec™ NF270	NF	NF270
	Filmtec™ NF90	NF	NF90
GE Power and Water	HL-Series	NF	HL
	DL- Industrial High Flow NF	NF	DL
	DK-Series	NF	DK
	SG-Industrial High Rejection Brackish Water RO	RO	SG
Koch Membrane Systems, Inc.	SR100-Low pressure selective rejection NF	NF	SR100
	SELRO® MPF36, pH stable	NF	MP36
	SELRO® MPF34, pH stable	NF	MP34
Microdyn-Nadir GmbH	Nadir® NP010	NF	NP10
	Nadir® NP030	NF	NP30
Toray Industries, Inc.	UTC-70 HF	RO	UHF70
	UTC-70	RO	UTC70
	UTC-60	NF	UTC60

Asymmetric membranes have a layered structure, similar to the one shown in Figure 23. All the membranes used in this work have a reinforcing fabric which is added to increase mechanical stability. Typical fabric materials are polyester or cellulose acetate.

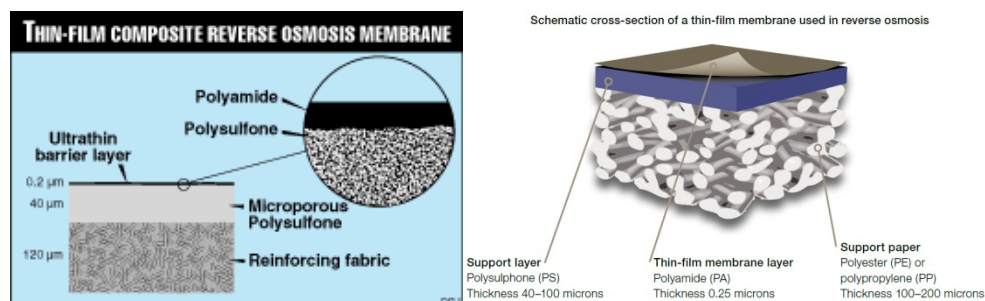


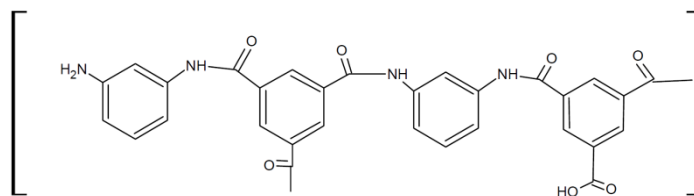
Figure 23: Layered structure of thin-film composite membranes [AlfaLaval] [FilmTec].

The intermediate microporous support layer is typically made of polysulfone. The most important layer with respect to the separation characteristics is the active layer. Phase inversion membranes (refer to Table 2) are homogeneous, which means that support layer and active layer materials are the same. Interfacial polymerization membranes have an additional layer added which is typically made of polyamide [DOW1]. More specifically, the polyamide active layer can consist of an aromatic polyamide (e.g. for NF90) or a mixed aromatic, aliphatic polyamide, referred to as polypiperazine (e.g. for NF270). These are the membrane polymers for the membranes used here. Their chemical structure is shown in Table 8.

Table 8: Chemical structure of membrane polymers.

Material name	Structure	Source
Polyethersulfone		[Melin2007]
Polysulfone		[Melin2007]
Polypiperazine		[DOW1]
	Free Amine Carboxylate	

Aromatic polyamide



[DOW1]

Free Amine

Carboxylate

The exact composition of membrane polymers is most of the time proprietary and often not included in datasheets by the manufacturer. Sometimes information about membrane material in the literature can even be contradictory. This could be due to process alterations by the manufacturer without reflecting this in the brand name. Table 9 can thus only be seen as an orientation for which membranes possess which active layer polymer structure.

Table 9: Active layer polymers of the membranes used here and the respective literature references.

Polysulfone	Polyethersulfone	Piperazine	Polyamide
MP34 [Matsumoto2005]	NP10 [Nadir1]	NF270 [Kim2007]	NF90 [DOW2]
	NP30 [Nadir1]	UTC60 [Kim2007]	ALNF [ALaval1]
		UTC70 [Ahmed2010]	ALHF [ALaval1]
			DK [Othman2010]
			DL [Othman2010]

Another important set of criteria that needs to be considered when selecting a membrane for a certain process is chemical and physical stability. Table 10 shows stability data that are important for acid mine waters that require high mechanical and thermal strength. These information will be important when selecting appropriate membranes as well as appropriate experimental conditions in later sections.

Table 10: Various process stabilities of the considered membranes with the respective literature references. Membranes in the order of their pH stability with higher pH-stability towards the end of the table.

Membrane and reference	Operating pH-range	Max. pressure in bar	Max. temperature in °C
SR100 [Koch3]	4-10	41.4	50
UTC60 [Bruggen2001]	3-9	15	35
HL [Dow4]	3-9	40	50
RO99 [ALaval2]	3-10	55	50
RO90 [ALaval2]	3-10	55	50
NF270 [Dow3]	3-10	41	45
NF90 [Dow2]	3-10	41	45
ALNF [ALaval1]	3-10	55	50
HF99 [ALaval1]	3-10	55	50

DL [Dow4]	2-10	40	80
DK [Dow4]	2-10	40	80
SG [Dow4]	1-11	40	80
MP36 [Koch2]	1-13	35	50
MP34 [Koch1]	0-14	35	50
NP30 [Nadir1]	0-14	40	95
NP10 [Nadir1]	0-14	40	95

5.2 Membrane permeation experiments

Laboratory membrane experiments are performed either in dead-end mode or in cross-flow mode. Here, experiments were performed in cross-flow mode due to several advantages, most importantly because process conditions, such as concentration and hydrodynamics on the feed side, can be kept at a stable level over an extended period of time. This is of significance since effects at the beginning of an experiment such as membrane compaction, sorption, and formation of concentration polarization change over the duration of the experiment and experimental reproducibility can be improved by process stabilization in cross-flow mode. Hence, all membrane experiments in this work were performed in cross-flow mode in the membrane module shown in Figure 24.

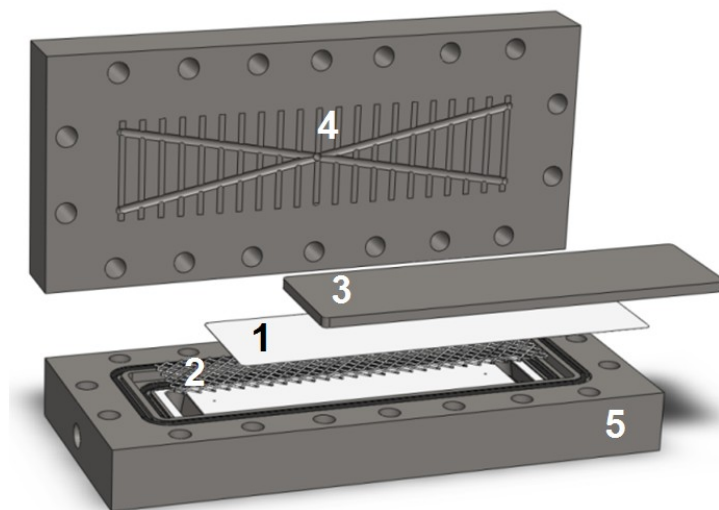


Figure 24: Exploded view of the cross-flow membrane module. 1: Membrane, 2: Feed-spacer, 3: Sinter-metal membrane support, 4: Permeate outlet, 5: Feed-channel and sealing.

A flowchart of the membrane lab facility in which the cross-flow module is embedded is shown in Figure 25. The cross-flow membrane module as well as all components of the cross-flow unit which are in contact with the process medium are made from stainless steel, EPDM, and PE.

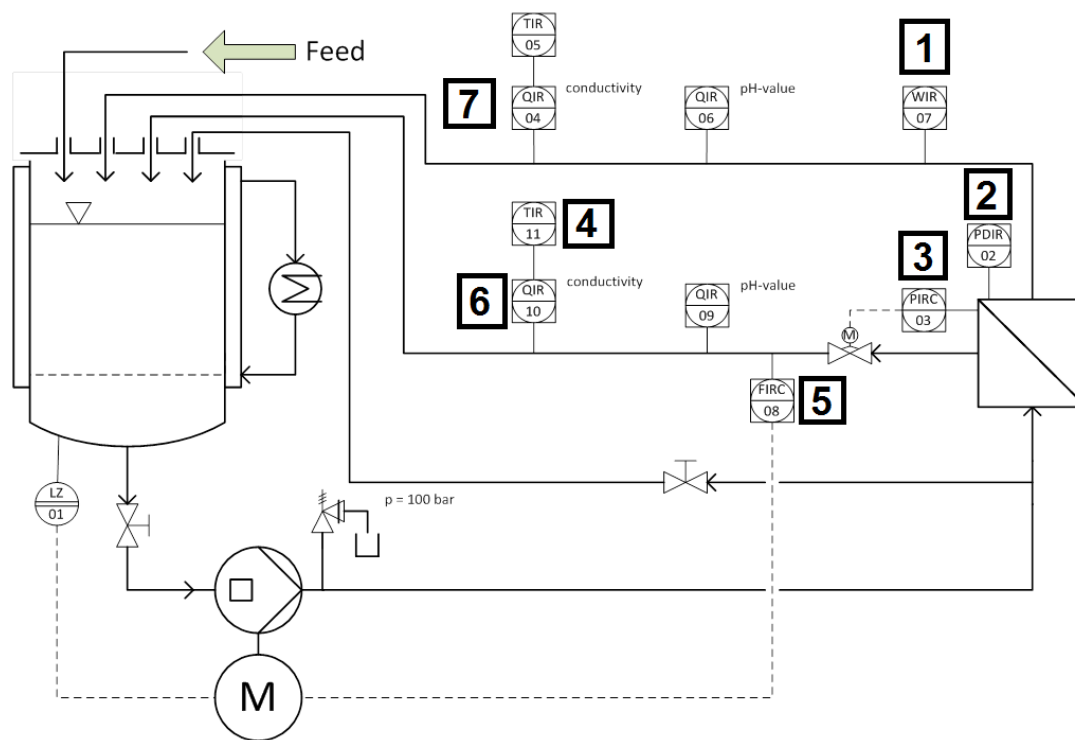


Figure 25: Flowchart of the cross-flow membrane unit.

From the feed tank which is wrapped by a heating jacket which is connected to a polystat the feed flows into the high-pressure plunger pump. To protect the pump a sieve collects all particles that might accidentally enter the tank and a limit level sensor turns off the pump when the liquid level decreases below a certain level which is detected by a change in electrical conductivity. Furthermore, if the pressure at the pump outlet increases above 100 bar a mechanical safety valve opens and releases the process medium in a collection vessel. An additional circuit turns off the pump in case of no pressure build up despite a running pump, which would be the case if a major spillage occurs and the pump runs dry.

The high-pressure plunger pump transports the process medium through a high pressure hose and through the lab membrane module to an automated electric valve. Hence, the cross-flow velocity is controlled by the revolutions per minute of the pump and the pressure is controlled by the valve.

Inside the membrane module the feed is separated into a permeate and a retentate stream. The permeate is collected and weighed to determine the permeate flux. The recovery of the lab unit is very low and hence most of the feed leaves the module as the retentate stream, which is then recycled into the feed tank.

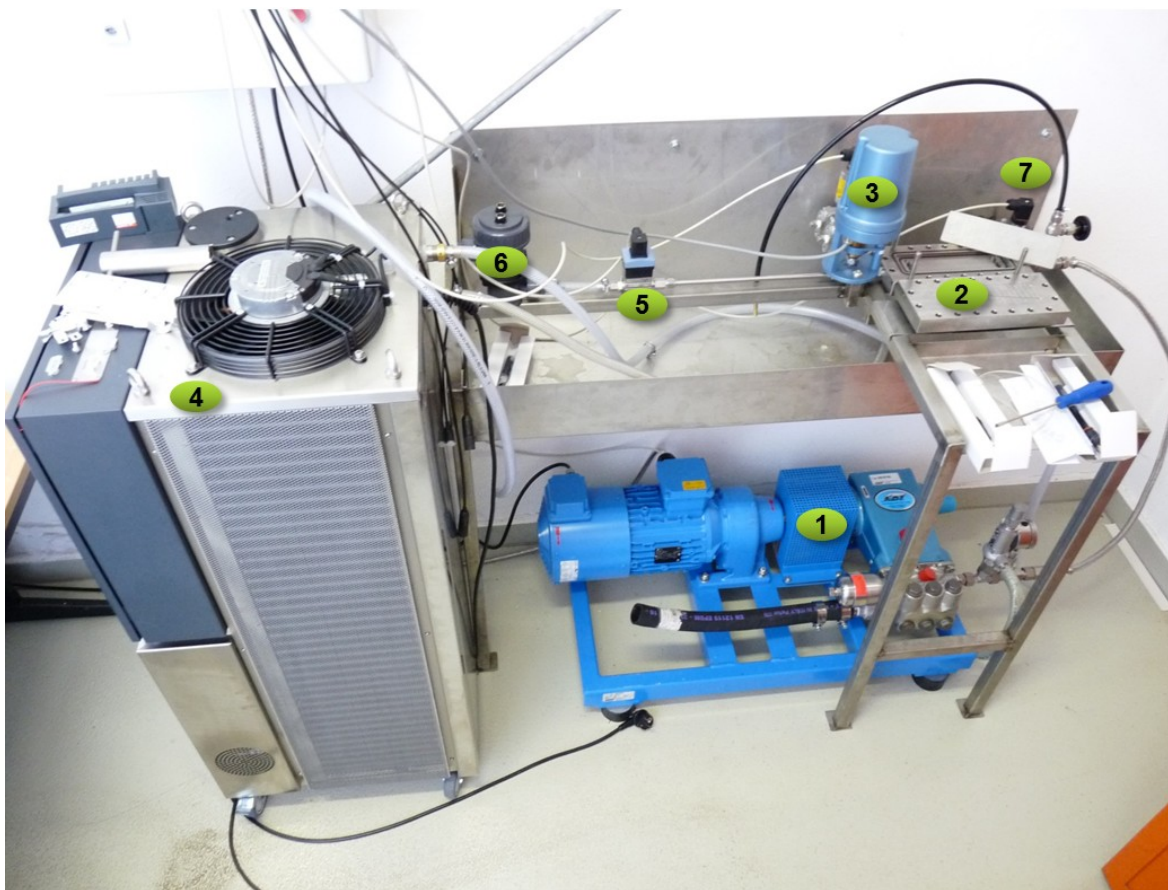


Figure 26: Photograph of the lab facility. 1. High-pressure plunger pump, 2. Laboratory membrane module, 3. Electric valve for pressure control, 4. Thermostat, 5. Turbine flow meter, 6. Feed conductivity electrode, 7. Gauge pressure sensor. Feed tank removed for this photograph.

The process is monitored by several instruments: pressure is measured by a gauge pressure sensor, the pressure loss across the membrane by a differential pressure sensor, conductivity, pH and temperature of the permeate and the retentate by the respective electrodes, a balance is used to weigh the permeate, and the cross-flow velocity is measured by a turbine flow meter. LabVIEW is used for process control as well as data acquisition and storage.

The feed channel height of the cross-flow test cell is 2 mm. The characteristic length L of the feed channel is 170 mm, i.e. the distance between the center of the inlet and outlet. The membrane surface area, of 0.009665159 m^2 , was calculated inside the inner o-ring, with a $49 \times 199 \text{ mm}^2$ rectangle with the cut-off corner area of $[(20 \text{ mm})^2 - \pi (10 \text{ mm})^2]$ being subtracted.

Cross-flow experiments were conducted in an adapted facility for retention measurement at constant pressure, cross-flow velocity, temperature, and concentration. Hence all major influence factors on membrane filtration can be controlled for and the performance of different membranes can be compared.

5.3 Streaming potential measurements

Streaming potential measurements were performed using the SurPASS by Anton Paar, Austria. A schematic of the streaming potential measurement unit is shown in Figure 27, where the main component is the tangential streaming potential cell with the membrane sample.

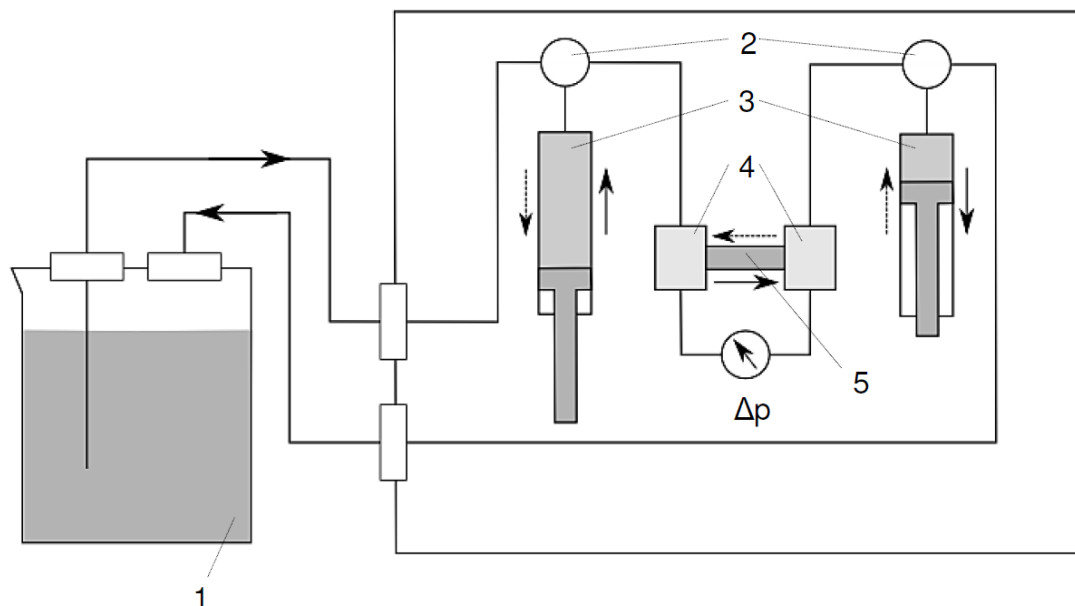


Figure 27: Schematic of the SurPASS by Anton Paar: (1) glass beaker with electrolyte solution (KCl), (2) three-way valve, (3) dual syringe pump, (4) electrodes and pressure sensor units, (4) tangential streaming potential cell with membrane sample [Bernhardt2015].

The kind of streaming potential cell used is the adjustable gap cell with disk shaped samples, as shown schematically in Figure 28. Electrolyte is pumped through the adjustable gap cell by the syringes and a streaming potential is induced due to the microscopic channel height. A system of two syringe pumps is used in order to avoid polarization by changing the direction of the electrolyte flow. Pressure loss inside the channel as well as the induced streaming potential are measured by the respective sensors and recorded.

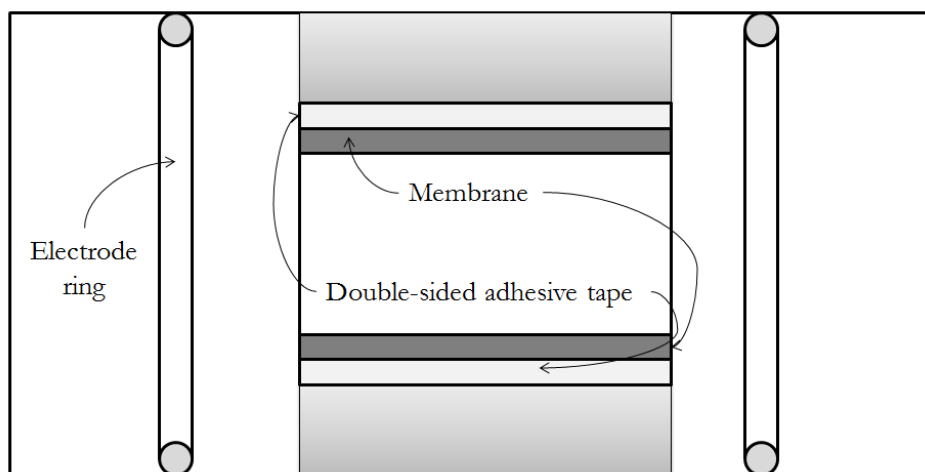


Figure 28: Schematic of the adjustable gap cell from Anton Paar, Austria [Bernhardt2015].

Continuously increasing the pressure difference across the channel due to a larger electrolyte flow rate results in an increase in the absolute value of the measured streaming potential. This way, the gradient of the streaming potential by the pressure difference is determined for pressure differences ranging from 0 to 300 mbar. Measured pressure loss and streaming potential are then used to evaluate the membrane charge. The zeta potential is calculated using the streaming potential coefficient dU/dp and the approximated Helmholtz-Smoluchowski approach:

$$\zeta = \frac{dU}{dp} \cdot \frac{\eta \cdot \kappa_{bulk}}{\varepsilon_r \varepsilon_0} \quad (5.1)$$

Where κ_{bulk} is the specific conductivity of the bulk electrolyte solution. This simplified approach assumes that only the electrolyte solution contributes to overall conductivity and the surface conductivity is assumed to be negligible. Consequently the measured zeta potentials are underestimated.

The commercial facility, described above, automatically performs the calculation of the zeta potential and adjusts the pH with an integrated titration unit. Zeta potentials calculated from the streaming potential can further be used in the Gouy-Chapman theory to derive membrane surface charge densities σ using the following equation:

$$\sigma_x = \left(2\varepsilon_0 \varepsilon_r k_B T \sum_i c_i N_A \left(\exp\left(-\frac{z_i e \cdot \zeta}{k_B T}\right) - 1 \right) \right)^{0.5} \quad (5.2)$$

The index i in this equation refers to the ions which are present in the solution. The so obtained surface charge density is then converted to a volumetric charge density c_x by using Equation (3.52).

Streaming potential measurement allows for the characterization of arbitrary surfaces' charge characteristics by using hydrodynamic effects. A voltage is induced by the shear movement of an electrolyte solution which flows along the surface, here the membrane. Characterization of the membrane surface is thus performed independently from the membrane's function as separation medium and is thus an independent characterization method for the membrane charge density which is important for modeling nanofiltration.

5.4 Experimental procedure

In this section conditions and execution of the experiments are summarized. An overview of the experiments in this work is given in Table 11.

Table 11: Overview of the performed experiments.

Experiment	Objectives	Process parameters	Membrane
Pure water permeability (ref. Section 6.2)	Determination of the membrane thickness	Pressure 3...40 bar Temperature 25° C Cross-flow 1.3 m/s	19 membranes
KCl retention (ref. Section 6.4)	Rating of the membranes' retention capabilities	Pressure 3...40 bar Temperature 25° C Cross-flow 1.3 m/s	8 membranes
Glucose retention (ref. Section 6.3)	Membrane pore radius	Pressure 3...40 bar Temperature 25° C Cross-flow 1.3 m/s	DK NP10
Uranyl pH variation (ref. Section 6.5)	Influence of membrane charge on uranyl retention	Pressure 15 bar Temperature 25° C Cross-flow 1.3 m/s	DK NP10
Uranyl phosphate variation (ref. Section 6.5)	Influence of uranyl speciation on uranyl retention	Pressure 15 bar Temperature 25° C Cross-flow 1.3 m/s	DK NP10
Mine water (ref. Section 6.6)	Transport mechanisms	Pressure 15 bar Temperature 25° C Cross-flow 1.3 m/s	DK NP10
Streaming potential measurements (ref. Section 6.4)	Membrane charge characteristics	Pressure loss 0...300mbar Temperature 25° C Gap height 123 µm	DK NP10

Preparatory steps

Prior to a set of experiments the cross-flow unit was cleaned with alkaline membrane cleaner (Wigol Microl liquid, 2wt%) and subsequently with an acidic membrane cleaner based on sulfuric acid and then flushed with deionized water until the conductivity of the water does not increase anymore during recirculation.

Membranes were firstly immersed in deionized water to induce swelling and secondly in the water sample for which they will be employed for 24 hours prior to the experiment. During the experiment the process conditions were kept stable for at least 1 hour or as long as the permeate conductivity is not stable.

Synthetic solutions were prepared using analytical grade chemicals and deionized water. Mine water was pre-conditioned using pleated filters. Microfiltration was investigated but no influence on retention was observed.

Experimental parameters:

Experiments were performed at conditions which are typical for nanofiltration, as shown in Table 12. These conditions apply to all experiments in this work unless otherwise stated. Such exceptions are, e.g. studying the influence of temperature on pure water flux for verification of the applicability of the Hagen-Poiseuille equation or studying the influence of the cross-flow velocity on concentration polarization.

Table 12: Selection of the experimental conditions for nanofiltration.

Parameter	Value	Explanation
Trans membrane pressure	15 bar	Pressure range which is typical for NF is 3 to 30 bar, according to [Melin2007], and [Baker2004 page 209]. Within this range 15 bar is an intermediate pressure.
Feed temperature	25° C	Standard temperature for membrane characterization, data sheets of manufacturers, streaming potential measurements, and available diffusion coefficient data (ref. Section 5.7)
Cross-flow velocity	1.3 m/s	Typical value for nanofiltration; avoiding concentration polarization (ref. Section 6.1) (equal to a Reynolds number of 5538)
Feed volume	30 l	Volume large enough to ensure constant concentration during sampling

Solution composition

Concentrations of the synthetic solutions were generally kept low which is required by the models assumption of having near infinite dilution. Assumptions are listed in Section 4.1. Studies in the literature which apply models with the same assumption use concentrations between 1 mol/m³ [Fievet2002], and 50 mol/m³ [Mohammad2003]. Modeling of the mine water cannot obey this assumption and the experiment can thus be seen as an exploration of the model's capabilities. Concentrations of typically 200-1000 mg/l are used to minimize the influence of solute-solute interactions [EMST2013 page 1035]. For the experiments in this work a glucose concentration of 1 mol/m³, 180 mg/l, was used to account for the assumption of infinite dilution.

Table 13: Composition of the employed solutions.

Experiment	Feed concentrations
Pure water permeability	Deionized water at 6 µS/cm conductivity
KCl retention	Deionized water with 1 mol/m ³ KCl
Glucose retention	Deionized water with 1 mol/m ³ glucose
Uranyl pH variation	Deionized water with 1 mol/m ³ KCl, and 1 mmol/m ³ UO ₂ (NO ₃) ₂ ; addition of HCl for pH-adjustment
Uranyl phosphate variation	Deionized water with 10 mol/m ³ KCl, and 1 mmol/m ³ UO ₂ (NO ₃) ₂ ; addition of K ₂ HPO ₄ for speciation adjustment
Mine water	Real mine water (refer to Section 6.6)
Streaming potential measurements	Deionized water with 1 mol/m ³ KCl

For purposes of consistency KCl was chosen as the major electrolyte in the experiments involving synthetic solutions. Potassium chloride exhibits a high degree of dissociation and low affinity for sorption which is also why KCl is typically used for conductivity electrode calibration. In this work feed and permeate concentrations were determined by conductivity measurement. Consequently KCl was used in the characterization of the membranes in order to increase accuracy of the conductivity measurements. Additionally, some samples were analyzed by ion chromatography to validate the result obtained by conductivity measurement.

5.5 Analytical methods

Single salt experiments were performed with a solution of KCl. The advantage of nanofiltration experiments of a single dissolved salt lies in the ease and rapidness of the analysis which is possible by conductivity measurement. The electrode for the concentrate conductivity is the LTC 1/23 SMEK and for the permeate the EGA 133 I. The conductivity measurements were verified using ion chromatography with the 850 Professional IC by Metrohm, Germany.

The samples of permeate and concentrate in the experiments involving glucose were analyzed using the multi N/C® 2100S TOC analyzer, Analytik Jena Analytical Instrumentation.

Concentrations of uranium, lithium, potassium, and phosphate were analyzed by ICP-MS using the Thermo X-Series II. The limit of determination of this method is: U – 0.001 ppb, Li – 0.1 ppb, K – 20 ppb, and P – 10 ppb. Before analysis the samples were diluted 1:10.

For the thickness determination membranes were sectioned with a scalpel and then measured optically. Membrane cross sections were captured with the optical microscope “Stereo discovery V12” from Carl Zeiss Microscopy GmbH.

5.6 Predictive speciation modeling

As introduced in Section 1.4, chemical elements associate in solution forming so called chemical species. Since the chemical speciation strongly influences on such properties as diffusivity, size, and sorption behavior it needs to be considered in modeling nanofiltration. Here, speciation is determined using the predictive speciation modeling code PHREEQC, version 3, and the database llnl.dat [Parkhurst1999].

In PHREEQC aqueous geochemical calculations are based on an ion-association model with the following mathematical equations:

- A mass balance for each element.
- The law of mass action for each element which takes all reactions into account that are listed in the database (dissociation reactions and association with water).
- Electrical neutrality of the solution.
- Phase equilibria (returning saturation indices for each species).
- Conservation of electrons.

Unknowns for each species are the species' activity, activity coefficient, molality, and moles in solution. Firstly, the mass action equations are rewritten in terms of the master species which are by default one for each element and valence state, e.g. Fe^{+3} , Fe^{+2} , U^{+2} , U^{+6} . Secondly, the compacted mass action equations are inserted into the equations for the mass and charge balance. The functions are then differentiated with respect to each master species thereby generating a Jacobian matrix and then solved numerically. Obviously, the quality of the results from such predictive speciation modeling is determined by the quality of the database.

The here employed database *lnl.dat* was developed at the Lawrence Livermore National Laboratory (LLNL) which is a United States Department of Energy national Laboratory located in Livermore. This database with thermodynamic data compiled by Jim Johnson (who created the database 'thermo.com.V8.R6.230') and converted to PHREEQC format by Greg Anderson with help from David Parkhurst includes many elements not available in any other PHREEQC database. Using this database returns results which are essentially equivalent to commercial programs such as Geochemist's Workbench.

Based on the analysis of the uranium-contaminated solutions PHREEQC has been used in this work to determine the species in which uranium is present in order to determine the size and diffusivity of the uranium species.

5.7 Radius and diffusion coefficient of uranyl species

In a later section, Section 6.6, the modeling of a uranium-contaminated water of complex composition will be approached. For this, the size and diffusivity of the uranium species is required. Although the species in which uranium exists in the bulk of the solution can be determined by predictive speciation modeling, the state in which uranium is present inside the membrane pores is uncertain. The question remains whether uranium passes the membrane in its ionic form or as a complex. Hence, two uranium species are of concern in this thesis: UO_2^{2+} (ref. Figure 42 on page 89) which corresponds to the uncomplexed, i.e. ionic form, and the calcium carbonate complex $[\text{Ca}_2\text{UO}_2(\text{CO}_3)_3]^0$ (ref. Table 20 on page 100). Data on diffusion coefficients and radii of the ionic and the complex uranium species is based on the literature presented in this section.

The diffusion coefficient of $[\text{Ca}_2\text{UO}_2(\text{CO}_3)_3]^0$ has been determined by [Bai2009] in experiments using the inward-flux diffusion shown in Figure 29.

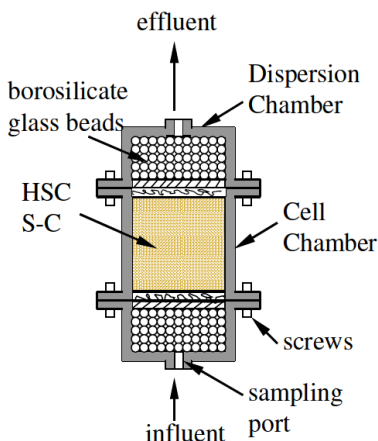


Figure 29: Schematic illustration of the diffusion cell as used by [Bai2009].

The chemical composition has been adjusted in order to ensure the prevalence of the calcium carbonate species. This has been accomplished by addition of calcite and equilibrium with atmospheric CO_2 ($p_{\text{CO}_2} = 10^{-3.5} \text{ atm}$) in order to reach saturation with respect to CaCO_3 . Solution properties, i.e. pH and ionic strength, were fixed at pH 8.0 (± 0.1), and an ionic strength of 0.02 M using a Na_2CO_3 - NaHCO_3 -buffer, and NaNO_3 as a support electrolyte, respectively. The speciation calculation performed by the authors at 22.5 °C obtained the following dominant U(VI) species: 68.3% in $[\text{Ca}_2\text{UO}_2(\text{CO}_3)_3]^0$, 30.8% in $[\text{CaUO}_2(\text{CO}_3)_3]^{2-}$, 0.5% in $[\text{UO}_2(\text{CO}_3)_2]^{2-}$, 0.4% in $[\text{UO}_2(\text{CO}_3)_3]^{4-}$. This dominance of $[\text{Ca}_2\text{UO}_2(\text{CO}_3)_3]^0$ was confirmed in own PhreeqC calculations. The authors obtain an “apparent” D_0 value in the range from 3.9 to $4.9 \cdot 10^{-10} \text{ m}^2/\text{s}$ for the diffusion of total U(VI) under the applied experimental conditions.

[Bai2009] also determined the size of $[\text{Ca}_2\text{UO}_2(\text{CO}_3)_3]^0$ based on the bond lengths determined by spectroscopy as published in the literature: the U-Ca bond distance is estimated to be 4.1 Å, and the U-C-O distance bond distance to be 4.2 Å. Based on such bond distance data and theoretical considerations on the structure of the complex the unhydrated radius has been estimated to be 5.24 Å.

The diffusion coefficient of the uranyl ion has been determined by [Marx1976] using the radioisotope method which is a variation of the moving-boundary method. In this method the boundary layer between radioactive and inactive solution is detected using a radiation sensor. The solutions were prepared using uranyl nitrate and nitric acid. Despite nitrate in the solution the predominant species is the uranyl ion. The speciation, as calculated by PhreeqC was at about 100% for the free uranyl ion. The authors determine a limiting ionic conductance, Λ_{meq}^0 , of $57 \text{ S cm}^2/\text{moleq}$. This conductance can be transformed to a diffusivity of $7.59 \cdot 10^{-10} \text{ m}^2/\text{s}$ using the Nernst-Einstein equation [Barthel1998].

In the publication by [Persson2010] spectroscopic data has been evaluated along with theoretical considerations and the U=O distance has been determined to be 2.42 Å. Since the shape of the uranyl ion is assumed to be linear, i.e. of the kind $\text{O}=\text{U}=\text{O}$, this bond distance is representative of the species’ radius.

A summary of the data on the size and diffusivity of the two species, the ionic species, i.e. UO_2^{2+} , and the complex species, i.e. $[\text{Ca}_2\text{UO}_2(\text{CO}_3)_3]^0$, is shown in Table 14.

Table 14: Literature sources for diffusion coefficient and unhydrated radius of the two uranyl species.

Species	Characteristic data	Determination method	Source
Experimentally obtained diffusivities			
UO_2^{2+}	$7.59 \cdot 10^{-10} \frac{\text{m}^2}{\text{s}}$	Radioisotope method	[Marx1976]
$[\text{Ca}_2\text{UO}_2(\text{CO}_3)_3]^0$	$4.4 \cdot 10^{-10} \text{ m}^2/\text{s}$	inward-flux diffusion cell	[Bai2009]
Theoretically derived unhydrated radius			
$[\text{Ca}_2\text{UO}_2(\text{CO}_3)_3]^0$	0.524 nm	Theoretical considerations based on spectroscopic data	[Bai2009]
UO_2^{2+}	0.242 nm	Theoretical considerations based on spectroscopic data	[Persson2010]

6 Experimental and modeling results

In order to obtain the data necessary for the simulation of the observed separation the experiments in this work followed two objectives: membrane characterization and filtration experiments of uranium-contaminated water. These two sections will be brought together in Section 6.6, where the membrane parameters obtained in the characterization will be used to model the experimental membrane performance and to explain the observed separation at the microscopic level.

Different approaches exist for the determination of the membrane characteristics thickness, pore size, and charge. Electron microscopy is the most commonly used method for the determination of the membrane thickness. However, membranes should be characterized in the state in which they are applied because swelling effects can alter membrane morphology [Schäfer2006 page 90]. The membrane samples should thus be immersed in the feed solution for characterization to include swelling effects. This condition can be fulfilled by applying the Hagen-Poiseuille equation to derive the thickness from the membrane's permeability.

Pore size is usually determined from the retention of uncharged solutes which is also related to the MWCO which is an important membrane characteristic for industrial practitioners. Other approaches do exist, such as AFM [Bowen1997], or slow positron beam techniques. However AFM only determines the size of surface pores and cannot determine whether these pores are “dead-end” pores that do not lead all the way through the membrane and can thus not contribute to mass transfer in the same way as an open pore. Slow positron beam techniques for pore size analysis are a novel approach that requires adequate equipment [De-Baerdemaker2007].

Characterization using filtration experiments can be performed with uncharged solutes, but also with single-salt solutions [Bason2010]. [Bowen1996] used retention over flux curves to fit the membrane charge using the DSPM model. The approach to fit missing membrane parameters to experimental data is highly dependent on the model that is employed for the fitting. Consequently, as an independent method, streaming potential measurement will be employed to verify the fitted membrane charge.

6.1 Feed side mass transfer

As described in Section 4.5 feed side mass transfer is described by diffusion, convection, electromigration, and at the microscopic level also by the ion distribution in the electrical double layer. The approach taken in this work is to increase the cross flow velocity and thereby the Reynolds number to induce sufficient back mixing from the membrane surface into the bulk of the feed solution. This approach reduces concentration polarization to the microscopic level at which only the electrical double layer is of concern. The reduced complexity of the experimental setup contributes to rigorous modeling of transport through the NF membrane: The number of unknown parameters in the experiment is reduced.

The question remains as to what constitutes a sufficiently high cross flow velocity in order to avoid concentration polarization. Numbers given in the literature differ depending on the type of module, the surface roughness of the membrane and the module, employed spacers, permeate flux so much that a critical Reynolds number cannot be of general nature but rather a benchmark. According to [EMST2013 page 1287] concentration polarization is minimized by increasing the cross-flow velocity above 1 m/s. This is the benchmark value which serves as the baseline in this work for the experimental determination of turbulence.

The approach taken here is to determine the pressure loss inside the module with a differential pressure sensor and each one drill hole at the inlet and the outlet of the module, as shown in Figure 30.

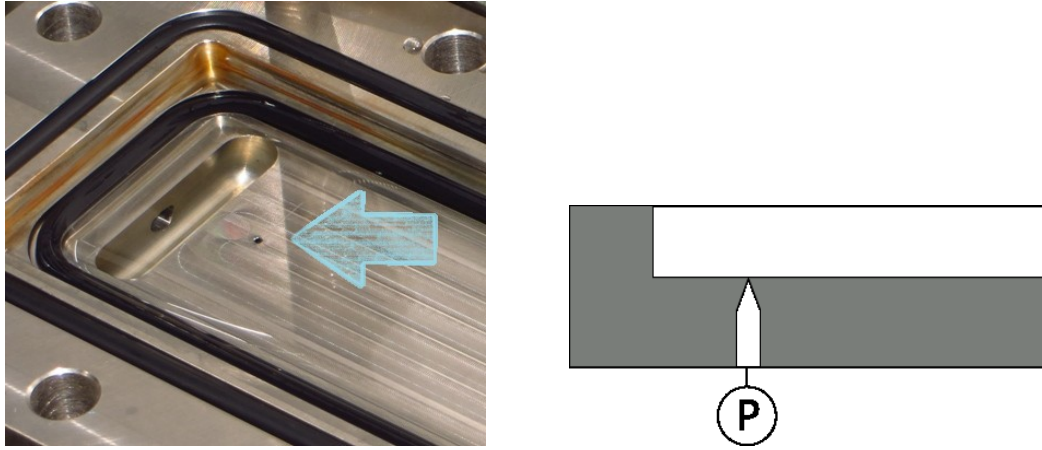


Figure 30: Drill hole for pressure loss measurements (left: photograph; right: illustration/side view); diameter 1mm; in this picture only the hole at the module inlet can be seen; an identical hole is at the module outlet; distance between the two holes is 12 cm, effectively covering the full undisturbed length of the channel.

The pressure loss across the channel Δp together with the cross-flow velocity v_{cf} and the density of the liquid ρ can be used to calculate the pressure coefficient. Furthermore, the pressure coefficient can be used together with the length $L_{channel}$ and hydraulic diameter d_{hyd} of the feed channel to calculate the friction coefficient f_{turb} :

$$f_{turb} = 2 \cdot \Delta p \cdot \frac{d_{hyd}}{\rho \cdot L_{channel} \cdot v_{cf}^2} \quad (6.1)$$

This approach has been taken for the experimental system of a 10 mM KCl solution at 25°C and the ALNF membrane. The friction coefficient for different cross-flow velocities is shown in Figure 31.

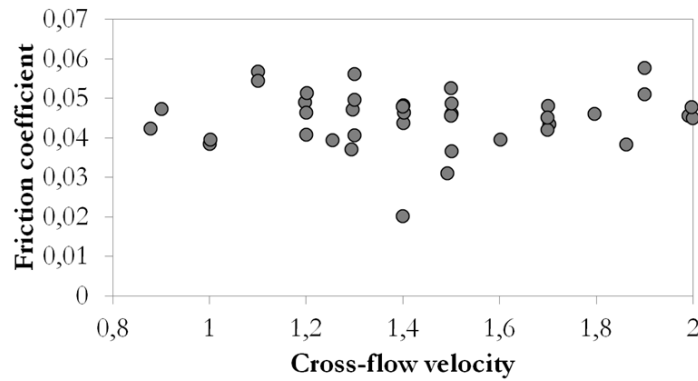


Figure 31: Friction coefficient as a function of cross-flow velocity. The usual representation as a function of Reynolds number is shown in Appendix B.

Over the whole observed range the friction coefficient does not change significantly which suggests that the transition from laminar to turbulent flow happens at an even lower cross-flow velocity which was experimentally not accessible. All further experiments in this work were conducted at 1.3 m/s cross-flow

velocity which is sufficiently high to avoid hydrodynamic concentration polarization and not beyond cross-flow velocities which are used in the industrial practice.

Cross-flow velocities high enough to avoid hydrodynamic concentration polarization are already reached at 1 m/s. The cross-flow velocity chosen in this work, of 1.3 m/s is thus high enough to ensure back-mixing into the feed and is thus suitable to reduce the number of unknown variables of the system that is modeled in further sections of this work. Precisely speaking this means that it is sufficient to consider concentration polarization due to the electrical double layer only.

6.2 Membrane thickness

The application of the Extended Nernst-Planck equation, which is at the core of the NF model developed in this work, requires at least knowledge of the membrane charge and the membrane thickness [Bowen1996]. This section is dedicated to an experimental determination of the membrane thickness that is independent of the final model in order to prove that the parameter, membrane thickness (i.e. thickness of the active separation layer), chosen possesses physical meaning and is not just a mathematical fitting parameter.

As shown in Section 5.1, the thickness of a thin film composite membrane can be divided into three distinct layers: The active layer (also referred to as skin layer or barrier layer), the support layer, and a nonwoven fabric layer. In mathematical descriptions, the membrane is commonly reduced to its active layer. At least for the retention of ions this assumption can be accepted as a reasonable approximation. The so called macrovoids of the support and fabric layer are not likely to separate ions from water molecules or ions from each other and so the assumption that all separation happens in the nanopores of the active layer appears justified. However, the assumption that the flux is independent of the thickness of the support and fabric layer requires some attention. Especially since the total membrane thickness is, depending on the membrane, more than 100 times larger than the active layer's thickness. So it seems likely that the total membrane thickness could have an influence on permeate flux. However, as will be shown in the following, it does not have a significant influence and will thus not need to be considered in the model.

For this question, samples of 20 membranes have been cleaned and soaked in water, in the same fashion as for the membranes used in all other experiments in this work. The samples have been sectioned and their thickness determined using an optical microscope as shown for the HF99 membrane in Figure 32. The active separation layer which is in the range of a few micrometers or even in the range of nanometers cannot be seen in this image.

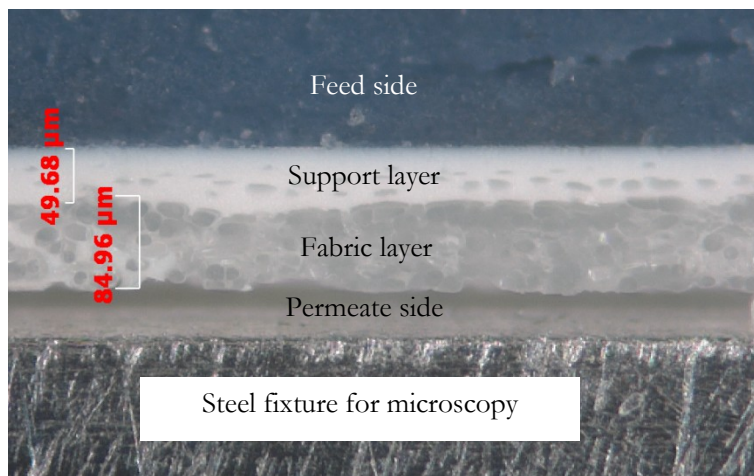


Figure 32: Cross-sectional image of the HF99 membrane. Two layers, the support and fabric layer, can be distinguished optically. The active layer is indistinguishable from the support layer and its relatively small thickness will be included in the support layer in the following analysis.

For all 20 membranes, four such images as shown in Figure 32 were taken and analyzed for the two layers' thicknesses. Figure 33 shows the obtained thicknesses together with the error of the measurement which is low enough to allow the comparison with the observed pure water permeabilities. The permeabilities and thicknesses were determined for samples from the same batch which proved to be important because variation within one batch was considerably smaller than between two batches. This could be due to advances and further progress on the side of the membrane manufacturer but to some extent also due to storage conditions.

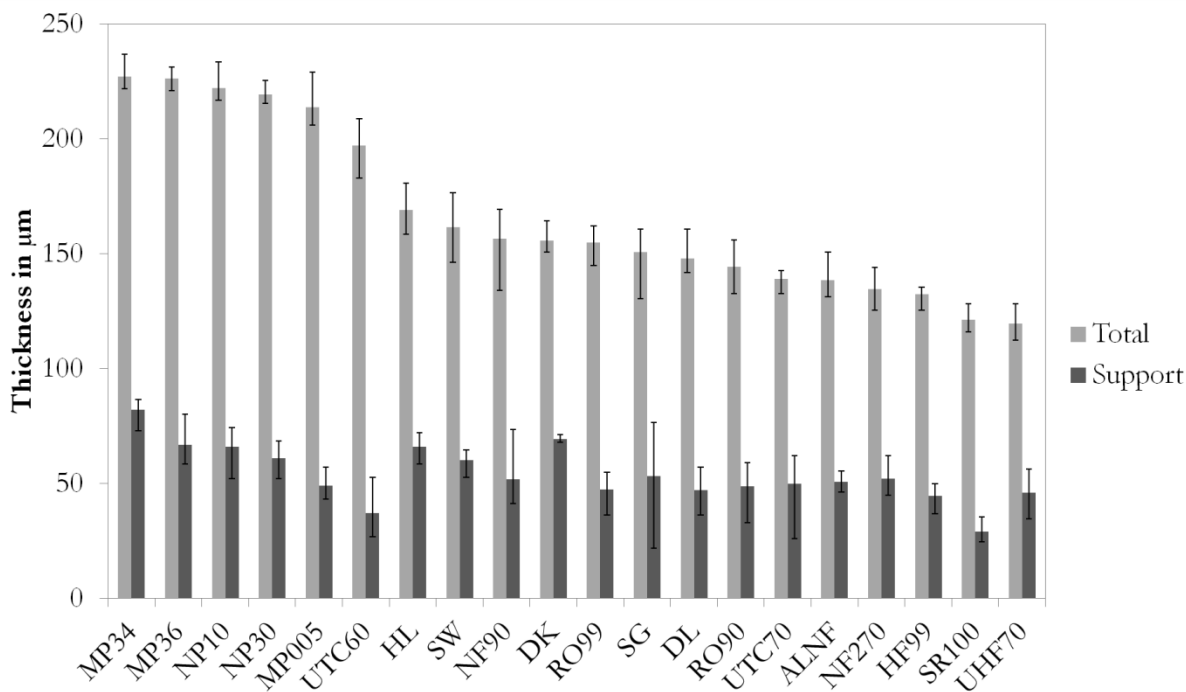


Figure 33: Membrane thickness measured by optical microscopy. Bars show the average from 4 samples (of the same batch), error bars indicate maximum and minimum thickness.

Experimentally determined membrane pure water permeabilities and the respective literature references are shown in Figure 34. The experiments were conducted using the facility described in Section 5.2, i.e. in filtration mode. All membranes were cleaned and soaked in water prior to the experiments at 25°C, a cross flow velocity of 1.3 m/s, and deionized water with conductivity below 6 $\mu\text{S}/\text{cm}$. The large error that characterizes some of the literature data shows once again that huge differences exist between membrane batches. The literature data stretches over many years and certainly membrane manufacturers further developed the membranes without changing the brand.

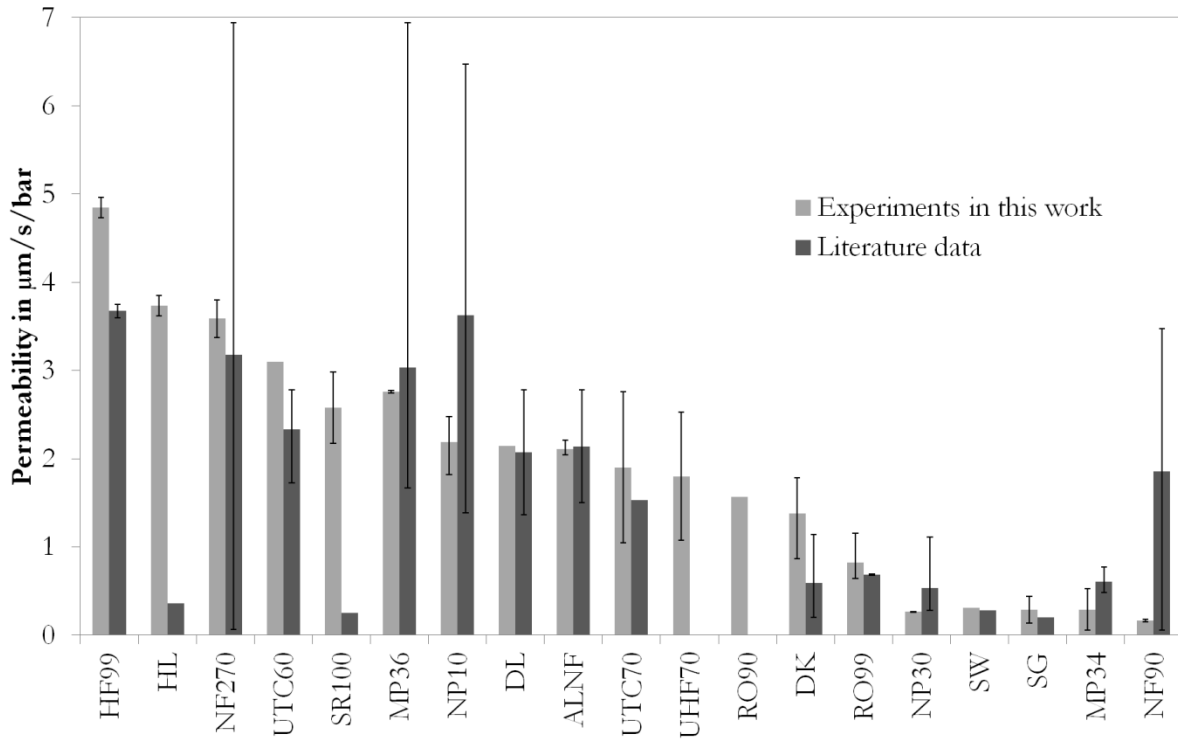


Figure 34: Comparison of experimental pure water permeabilities with literature data. Error bars indicate maximum and minimum values. Literature sources are given in Appendix C. Experiments at 25° C, with pure water at an electrical conductivity below 10 $\mu\text{S}/\text{cm}$, cross flow velocity of 1.3 m/s.

Now, membrane thicknesses and permeabilities can be compared, as shown in Figure 35. The diagram shows no correlation between permeability and membrane thickness, neither for the total membrane thickness nor for the thickness of the support layer. This result supports the assumption that the magnitude of the permeate flux is determined by the thickness of the active layer, primarily. The influence of the downstream layers is small, not only on retention but, as shown here, also on permeate flux.

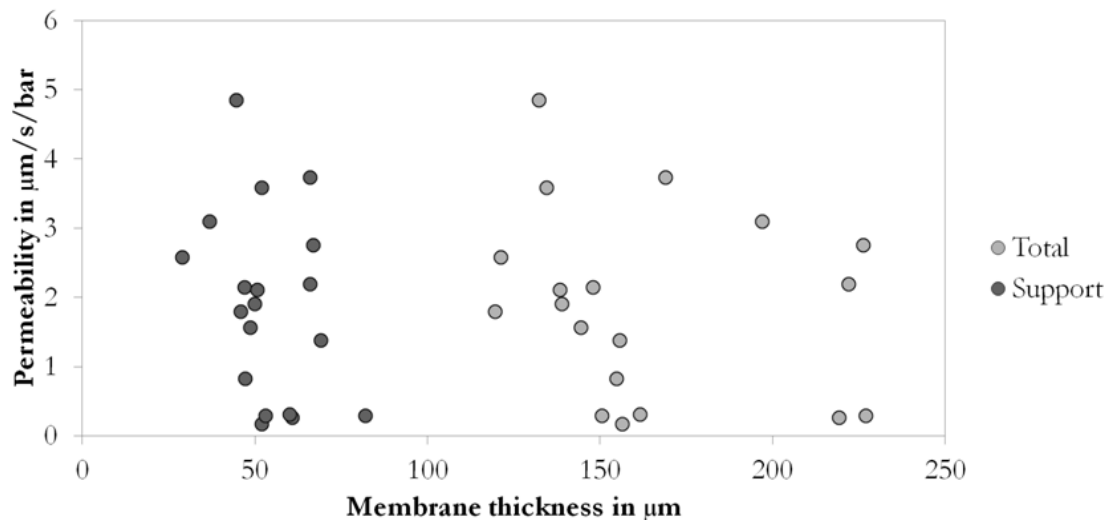


Figure 35: Pure water permeability versus total and support layer membrane thickness for 19 different membranes. No correlation observed.

The conclusion that can be drawn for membrane modeling is that only the active layer thickness needs to be accounted for. Since this thickness is rather small, more advanced characterization methods are necessary. A very common approach is imaging using Scanning Electron Microscopy (SEM) [EMST2013 page 1135] which was also used here.

The SEM image given in Figure 36 shows the area where the active layer is to be expected. However, the quality of the membrane preparation does not allow an estimation of the active layer thickness. As another preparation method immersion of the membrane and cracking was tested but the membrane fabric layer did not crack into a clean section and removing the fabric layer resulted in a deformation of the membrane.

Other researchers have reported SEM of the active layer not only of ceramic membranes, which are more resistant to the vacuum and to charging by the electrons, but also for the relatively fragile polymeric membranes. Pictures of a quality that is comparable to these publications could not be obtained here which could at least partially be attributed to a lack of expertise in the field of electron microscopy of polymers.

Furthermore, SEM suffers from the draw-back that the membrane is imaged in vacuum and needs to be dry. Hence, the requirement for optimal membrane characterization, that the membrane is characterized under the same conditions as in the actual experiments, is not fulfilled.

As a consequence SEM was not used in this work to determine the active layer thickness and the Hagen-Poiseuille equation was applied exclusively.

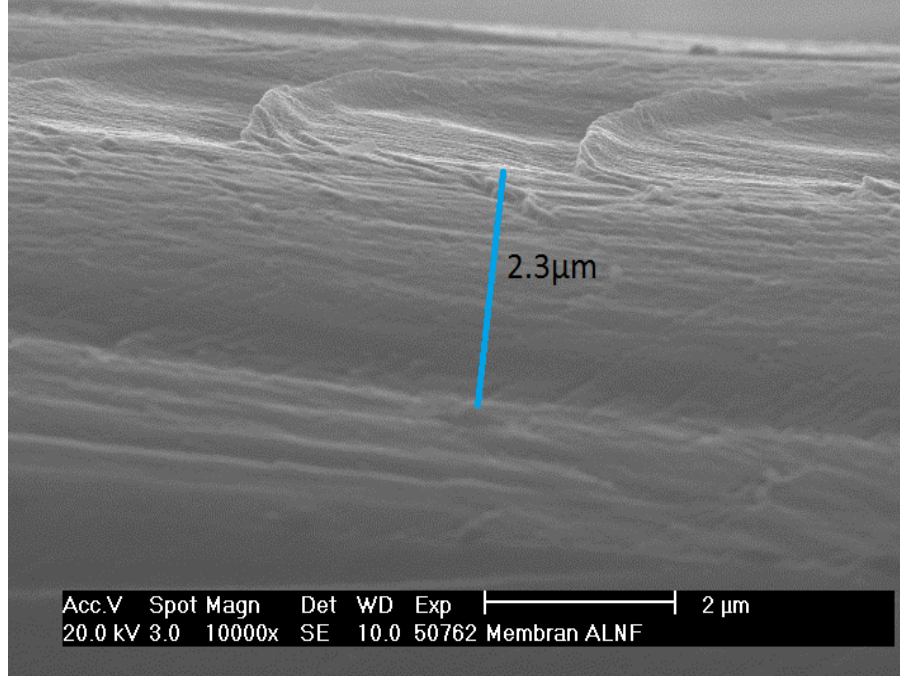


Figure 36: SEM image of the membrane ALNF. Membrane cleaned and then dried at room temperature. Sectioned using a scalpel. Determination of the active layer thickness not possible. Measuring bar shown for reference purposes only.

The derivation of the Hagen-Poiseuille equation is shown in Appendix A. [Mason&Lonsdale1990] presented it in the following form [Bandini2003] [Mohammad2003]:

$$J_v = \frac{r_p^2(\Delta p - \Delta \pi)}{8\eta\Delta x_e} = \frac{r_p^2\Delta p_e}{8\eta\Delta x_e} \quad (6.2)$$

For pure water this expression reduces to:

$$8\eta L_p = (r_p^2)/(\Delta x_e) \quad (6.3)$$

With the permeability L_p defined as:

$$L_p = (dJ_v)/(dp) \quad (6.4)$$

Where Δx_e is the equivalent membrane thickness:

$$\Delta x_e = (\Delta x_{eff})/(A_k) = (\Delta x \cdot \tau)/(A_k) \approx (\Delta x)/(A_k^2) \quad (6.5)$$

The factors membrane porosity A_k and membrane tortuosity τ should find a special mention here. Experimentally these factors are difficult to determine for the nanostructures that are found in nanofiltration. Typical values are:

- Tortuosity: According to [EMST2013 page 41] tortuosity is approximately the reciprocal of porosity. [Melin2007, page 38] gives a typical value of 25/12. [EMST2013 page 1035] in the range between 1.5 to 5.
- Porosity: Around 0.3 [EMST2013 page 43]. Random packings of spheres have a porosity of about 0.4 (0.38 to 0.43) [EMST2013 page 71]. Inorganic membranes in the range 0.3 to 0.4 [EMST2013 page 59].

However, the mathematical model for the transport of solute through the membrane developed in Section 4.8 requires knowledge of both parameters. Fortunately, as will be shown now, the Δx_e , as given in Equation (6.5) is an expression that is very suitable for use in the Extended Nernst-Planck equation. The equivalent membrane thickness Δx_e is the membrane thickness when taking account of tortuosity and porosity and thus reflects the stretched unconstrained membrane length. Firstly, the tortuosity is accounted for in the Δx_{eff} , mathematically converting the tortuous pores to straight pores.

Secondly, the porosity is included in the Δx_e , which relates the flux terms for diffusion and electromigration which are gradients over the membrane thickness to the same membrane area as the flux terms for convection and the ion flux. So, the macroscopically measured fluxes J_v and j_i need to be related to the open membrane area by dividing them by the membrane's porosity. Equation (4.62) would then need to be written as:

$$j_i/A_k = K_{i,c}c_iJ_v/A_k - K_{i,d}D_{i,\infty}\frac{dc_i}{dx_{eff}} - \frac{Fz_ic_iK_{i,d}D_{i,\infty}}{RT}\frac{d\phi}{dx_{eff}} \quad (6.6)$$

By multiplying this expression with the membrane porosity A_k the effective membrane thickness x_{eff} can be written as the equivalent membrane thickness x_e . Thus the Δx in Equation (4.62) uses the values for Δx_e as determined by the Hagen-Poiseuille equation.

That tortuosity and porosity are accounted for is a further advantage of the Hagen-Poiseuille equation compared to microscopic determination of the membrane thickness. Resulting membrane thicknesses are shown in Table 15.

Table 15: Membrane thicknesses relative to square of pore radius as determined by the Hagen-Poiseuille equation. Right column and the diagram show the membrane thickness under the assumption that all membranes have a pore radius of 0.5 nm, for illustration purposes.

Membrane	$\Delta x_e / r_p^2$	$\Delta x_{e, r_p=0.5nm}$	
	in $10^{12} \cdot 1/m$	in μm	
HF99	2.90	0.72	HF99
HL	3.76	0.94	HL
NF270	3.92	0.98	NF270
UTC60	4.53	1.13	UTC60
SR100	5.45	1.36	SR100
MP36	5.09	1.27	MP36
NP10	6.41	1.60	NP10
DL	6.56	1.64	DL
ALNF	6.67	1.67	ALNF
UTC70	7.38	1.85	UTC70
UTC70HF	7.81	1.95	UTC70HF
RO90	8.98	2.25	RO90
DK	10.16	2.54	DK
RO99	17.08	4.27	RO99
NP30	53.02	13.26	NP30
TFCSW	45.15	11.29	TFCSW
SG	48.47	12.12	SG
MP34	48.52	12.13	MP34
NF90	83.69	20.92	NF90

Typical membrane thicknesses given in the literature are obtained by microscopy analysis. The membrane manufacturer DOW gives a value of 200 nm as a typical membrane thickness for NF and RO membranes [DOW1]. According to [EMST2013 page 1040] thicknesses can be in the range from 15 to 300 nm thickness. A thickness of 200 nm converted by Equation (6.5) and assuming a porosity of 0.3 yields an equivalent thickness of 2.2 μm which is in agreement with the thicknesses obtained here by the Hagen-Poiseuille equation. A nanofiltration modeling study using the DSPM model obtained an equivalent thickness of 1 μm [Mohammad2003] further supporting the results obtained here. The thickness of the membranes NF90, MP34, SG or TFCSW which are relatively large when assuming a pore radius of 0.5 nm could be attributed to

a pore radius which is actually smaller, as will be explored in the next section which is dedicated to the determination of the pore radius by fitting to experimental rejection data.

Permeability is influenced by water purity, membrane batch, and temperature. Nevertheless, flux and pressure show a clearly linear relationship with a coefficient of determination of more than 0.95. Hence pure water permeability is a very reliable parameter to characterize membrane properties. Here, pure water permeability was used to determine the ratio of membrane thickness to pore size as a structural parameter of the investigated membranes.

6.3 Membrane pore radius

Nanofiltration membranes are often characterized by their retention of differently sized neutral solute. Such a criterion is the MWCO which is in the range of 150 to 3000 Da, where most nanofiltration membranes can be found at the lower end of this range [EMST2013 page 1277]. The MWCO is derived from the retention of uncharged solute, such as glucose.

While the retention of uncharged solute is an experimentally accessible parameter, the parameter which is necessary for the modeling in this work, the pore radius, is not directly accessible and will be obtained by fitting the model retention to the experimental retention. The relationship between uncharged solute retention and pore radius is not straightforward but rather highly dependent on the employed model.

Furthermore, due to the fact that nanofiltration membranes are prepared via interfacial polymerization their structure is expected to be highly irregular even down to the nanoscale [EMST2013 page 1040]. The meaning of pore radius is thus highly abstract considering that the pores of the membrane have a variety of individual pore sizes.

Additionally, the radius of a pore will vary considerably along the pore's length, having "bottlenecks" that significantly influence size exclusion within that pore. Furthermore, nanofiltration membranes are at the transition between dense and porous membranes. A pore diameter of 2 nm has been proposed for the distinction between porous and dense membranes [EMST2013 page 1063]. Strictly speaking, smaller pores are considered molecular gaps.

Consequently, the complexity of the membrane structure will make modeling difficult and the obtained fit is highly model dependent. Therefore, the approach taken here is to use the model developed in this work to fit the pore radius although many well established approaches are available in the literature [Schaep1999], [Szymczyk2005], [Oatley2014], [EMST2013 page 1071].

Another important question is which solute should be used and which solute size should be attributed. For solutes of unknown size a correlation exists to determine the Stokes diameter from the molecular weight which is a readily accessible parameter [EMST2013 page 1283]:

$$d_s = 0.065 \cdot (MW)^{0.438} \quad (6.7)$$

This makes sense, e.g. when the retention of a novel pharmaceutical compound should be modeled. In the here contemplated case a solute of known size shall be chosen which has been used already in many studies. Table 16 shows a list of some non-ionic solutes typically used in nanofiltration pore size studies.

Table 16: List of uncharged solutes used in nanofiltration studies targeting a pore size determination.

Reference	Solute
[Bowen1997]	Glucose, raffinose, sucrose, glycerin, vitamin B12
[Bruggen1999]	Xylose, Maltose, Toluene, Ethanol, Congo red and 20 other solutes
[Bruggen2002]	Maltose
[Labbez2002]	PEG
[Otero2008]	Ethanol, cyclohexanone, galactose, maltose, lactose, raffinose and α -cyclodextrine
[Silva2011]	Xylose, glycerin
[Oatley2012]	Glucose, glycerol
[EMST2013 page 1035]	Dextran, poly(ethylene glycol) (PEG)

This list shows that a variety of substances have been used in the literature and many chemicals appear to be suitable for pore size determination as long as the solute size is known. Adding to this, [Bruggen1999] has found that even polarity of the solute has a minimal effect on retention. In conclusion, no neutral compound of known molecular size can be excluded which makes it difficult to decide for a certain compound.

The compound chosen in this work is glucose as it is a typical substance of well known size and also often used for membrane characterization by membrane manufacturers. A conclusive choice will certainly also involve aspects of pore size and membrane homogeneity in order to determine a pore size distribution which is not the aim of this work.

Fitting of the pore size was performed as described in Section 4.10. The experimental glucose retention along with the modeled fit is shown for two membranes in Figure 37. The membrane choice will be explained in the next section. The fit was obtained by variation of the membrane pore size only; the membrane thickness as determined in the previous section was used.

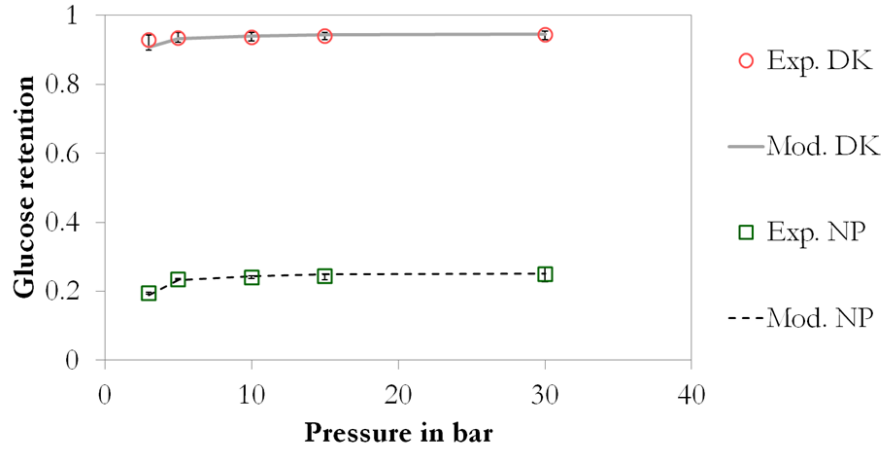


Figure 37: Experimental and modeled retentions (best fitting pore radius) for the two membranes DK, and NP.

The fitted pore radius is shown in Table 17 along with the membrane characteristics obtained so far.

Table 17: Membrane parameters for the two membranes, DK and NP, as determined up to this section. Thickness Δx_e calculated using the results shown in Table 15.

Characteristic	DK	NP
Relative Thickness $\Delta x_e / r_p^2$	$10.16 \cdot 10^{12} \cdot 1/m$	$6.41 \cdot 10^{12} \cdot 1/m$
Pore radius r_p	0.463 nm	1.543 nm
Thickness Δx_e	2.18 μm	15.26 μm

The pore radius for the DK membrane of 0.463 nm is close to the Stokes radius of glucose of 0.365 nm. This pore size is thus very close to the lower limit of a physically meaningful pore size, considering the model assumption of uniform pore size. However, other authors who used similar models also obtained similar results and this extremely small pore size can thus be attributed to the model's assumption. A pore radius for the DK membrane of 0.45 nm has been proposed by [Oatley2013]. For the NF membrane a pore radius of 1.4 nm has been determined by fitting it to experimental glucose retention [Wang2005b]. Hence, the here obtained results are very close to published data in the literature.

Pore sizes of two nanofiltration membranes were determined by fitting to experimental retentions of glucose. The fit was obtained by variation of the pore size only and consequently the pore size was determined isolated from membrane charge and interactions between ionic components. Furthermore, the determination method employs a membrane in its natural habitat; the obtained pore radius includes effects such as swelling and membrane compaction. Pore size determination using neutral solutes is an independent method at realistic conditions.

6.4 Membrane charge density

Membranes were screened for their KCl retention (ref. Figure 38) in order to select two membranes for the experiments involving uranium-contaminated water. To cover a broad range of nanofiltration membranes the membrane with the highest and the membrane with the lowest retention were selected.

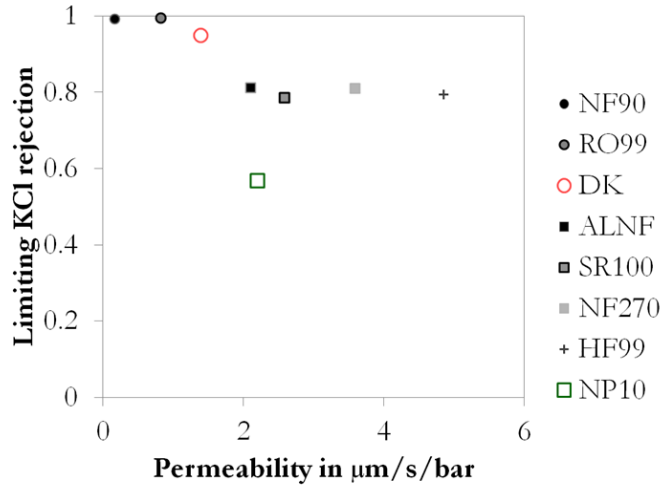


Figure 38: Limiting KCl-retention and permeability for 8 different membranes.

Membrane RO99 and NF90 were not selected because they possess RO-membrane-like properties, i.e. high rejection and low flux. They were not chosen because the properties of an RO membrane are in conflict with the model's assumptions.

Fitting of the membrane charge density was performed as described in Section 4.10. During the fitting, membrane pore radius and thickness were kept constant as determined in the previous sections. The fitting result is shown in Figure 39: While the experimental retention data for the DK membrane could be fitted well by the model the fit for the NP membrane is not in agreement with the experimental data. This difference will be further discussed in the chapter on the discussion, and there in Section 7.6.

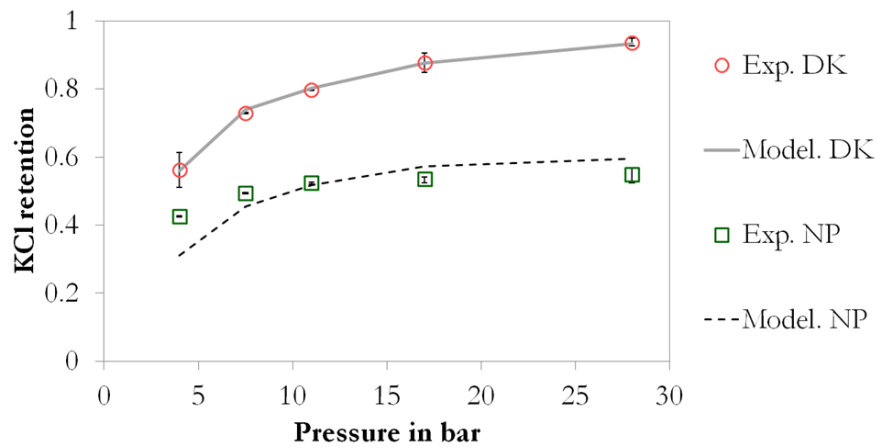


Figure 39: Experimental and modeled retentions (best fitting charge density) for the two membranes DK, and NP. Fitting of the membrane charge density was performed as described in Section 4.10.

With the fitting of the membrane charge density the determination of the membrane parameters which are necessary for the modeling of the complex uranium-contaminated mine water is completed. The resulting membrane properties are summarized in Table 18.

Table 18: Complete overview of the membrane parameters for the two selected membranes, DK and NP.

Characteristic	DK	NP
Relative Thickness $\Delta x_e / r_p^2$	$10.16 \cdot 10^{12} \cdot 1/m$	$6.41 \cdot 10^{12} \cdot 1/m$
Pore radius r_p	0.463 nm	1.543 nm
Thickness Δx_e	2.18 μm	15.26 μm
Volume charge density c_x	-0.33 mol/m^3	-0.98 mol/m^3

The membrane volume charge density is difficult to verify as it cannot be measured directly but only by indirect methods. Here, a method is presented by which the fitted membrane charge for the two membranes is compared. The result is not an absolute value but a value relative to the other membrane. Rearrangement of Equation (3.52) yields an expression for the membrane surface charge density σ_x , relative to the volumetric charge density c_x :

$$\sigma_x = \frac{F \cdot r_p \cdot c_x}{2} \quad (6.8)$$

The surface charge density is a parameter which is experimentally accessible, by streaming potential measurements. The results of the zeta potential, which can be derived from streaming potential measurement, for the two membranes are shown in Figure 40. This result is in accordance with the general observation that typical NF-membranes are negatively charged at neutral pH [EMST2013 page 1276]. The zeta potential is identical for the two membranes even over a broad pH range. Consequently, the surface charge properties of the two membranes are identical which implies that the expression in Equation (6.8) should be very similar for the two membranes.

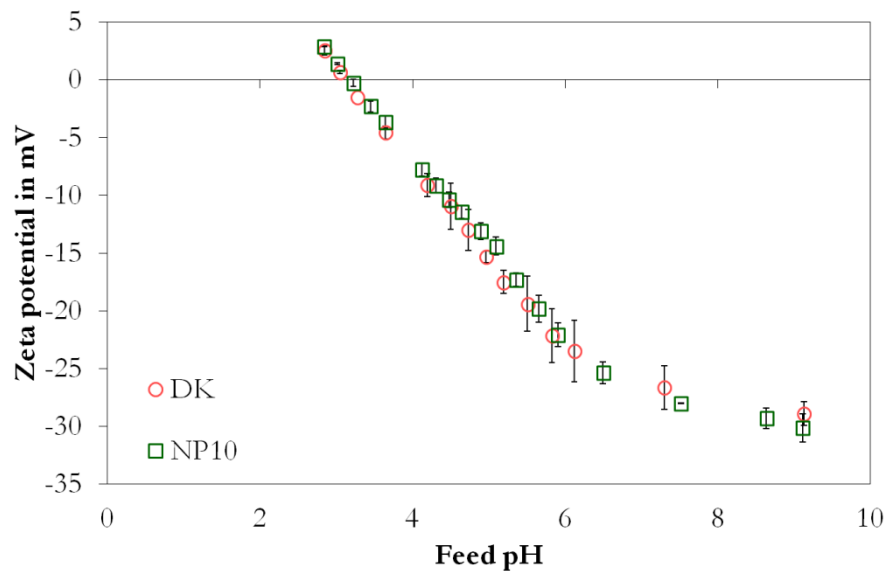


Figure 40: Zeta potential versus pH for a 1 mM KCl solution for the two selected membranes.

Equating the surface charge of the two membranes yields an expression which contains only the pore radius and the volume charge density:

$$\frac{r_{p,DK}}{r_{p,NP}} = \frac{0.463}{1.543} \approx 0.3 \neq 3 \approx \frac{0.98}{0.33} = \frac{c_{x,NP}}{c_{x,DK}} \quad (6.9)$$

Since the difference between the fitted and the measured membrane charge is relatively high streaming potential measurement for charge characterization appears not suitable for the determination of the membrane charge in this thesis. Furthermore, at high concentrations streaming potential measurements are complicated by the reduced streaming potentials. Hence, Section 6.6 uses another approach to determine the membrane charge density.

The volume charge density of two nanofiltration membranes was determined by fitting to experimental retention vs. flux data for a KCl solution. The result obtained by fitting was then compared to streaming potential measurement and the two approaches were in disagreement. As a consequence, the membrane charge in Section 6.6 (complex mine water) will be determined by fitting to the retention of other solution components.

6.5 Synthetic uranyl feed solutions

Section 1.4 introduced the concept of chemical speciation which influences the transport properties of uranium in aqueous solutions. This section is dedicated to the effects of uranyl speciation on uranyl retention by nanofiltration membranes. In this section, synthetic uranyl solutions were used to reduce the number of possible interactions that complicate the understanding of complex solutions. Section 6.6 is then dedicated to real mine waters for which the results from this section are applied.

In order to change the species in which uranium is present, the solution composition needs to be changed. Figure 41 shows the two pathways which were employed here in order to modify the uranium speciation. As shown in this figure, the uranium species, in which uranium exists initially, is a hydroxide species. This speciation is ensured by adjusting neutral pH in a KCl solution. The first pathway is titration with a HCl solution in order to obtain the free uranyl ion. The second pathway to change the speciation is to add a phosphate salt to the initial solution. Phosphate is especially suitable since it has a high complex forming constant \log_k with uranium as shown in Equation (6.10):



In the experiments phosphate has been added as K_2HPO_4 in order to target specifically the dissolved uranium thereby changing the prevalent speciation.

Analysis of the thermodynamic database lnl.dat, which contains data on most known uranium species, showed was used in order to find a suitable ligand for the selective complex formation of uranium. Uranium possesses a strong affinity towards phosphate which renders phosphate highly effective in changing the speciation of the uranium present in solution. Remarkably, already very low phosphate concentrations will be sufficient to change the speciation, which is an important consideration in order to keep the overall process unchanged. For other ions, such as lithium, the complex forming constant \log_k is much lower and therefore the speciation remains relatively unchanged by the addition of small amounts of phosphate salts. The chemical reaction for the complex formation of lithium is shown in Equation (6.11):

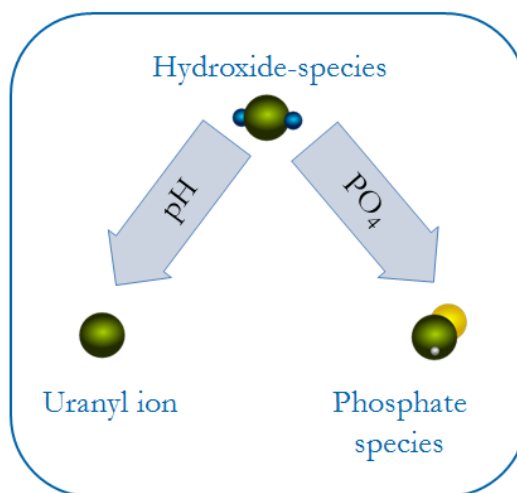
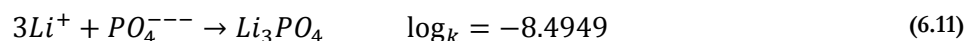


Figure 41: Principle of concept for selectively changing the uranium speciation and thereby also transport properties.

An overview of the experiments performed in this section is given in Table 19. The experiments were performed in identical manner in order to compare the behavior of a membrane with fine pores and large pores respectively.

Table 19: Overview of the experimental procedure for the uranyl speciation experiments.

Membrane	DK	NP
First pathway: Decreasing the solution's pH		
Principal approach	Addition of HCl to convert all uranium species to the free uranyl ion	
Side effect	The membrane surface charge will also be altered, as indicated by the streaming potential measurements in Section 5.3	
Replications	Two experiments for each membrane (at several values of pH)	
Second pathway: Addition of phosphate salt		
Principal approach	Addition of K ₂ HPO ₄ to convert all uranium species to phosphate species	
Side effect	No side effects expected. Monitoring of the separation using lithium ions by addition of lithium nitrate	
Replications	One experiment for each membrane (at several phosphate concentrations)	

Pathway 1: Changing the solution's pH value

The effect on speciation was assessed by predictive modeling using the software Phreeqc and the database llnl.dat, as described in Section 5.6. As can be seen in Figure 42 a lower pH will create uranium in the form of the uranyl ion which has a relatively low molecular weight.

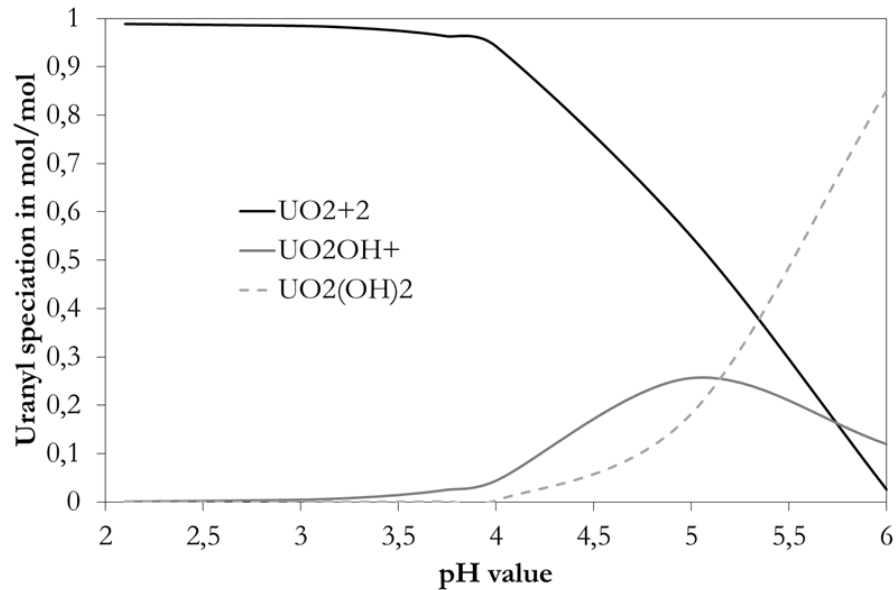


Figure 42: Uranyl speciation as a function of pH value as determined using Phreeqc (ref. Section 5.6).

Figure 43 shows the effects on species' size and charge properties more clearly by averaging these properties per mol of uranium. According to these calculations the size and charge of the species change drastically between pH 6 and 4. This effect can thus be compared to the streaming potential measurement in Section 6.4 which showed that the charge properties changed most significantly around the isoelectric point which lies at around pH 3.

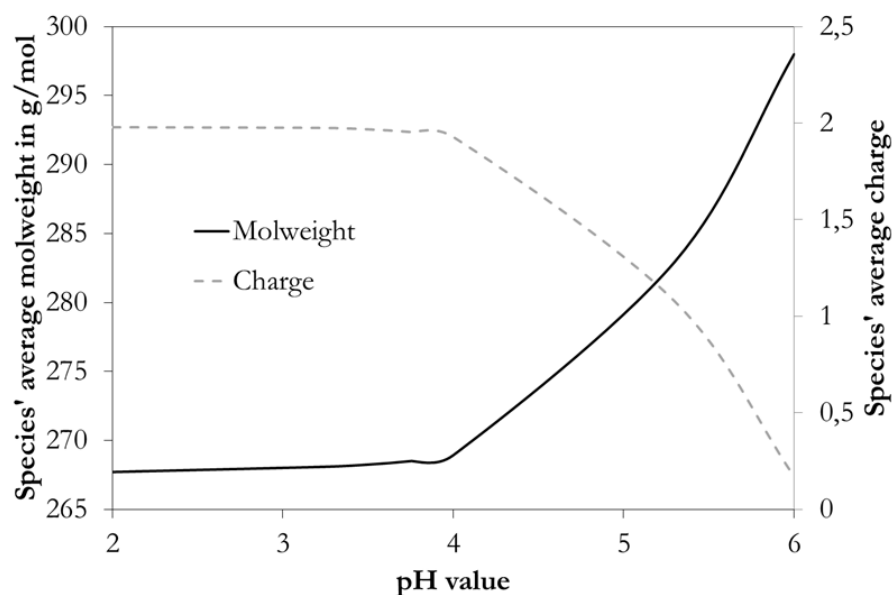


Figure 43: Uranyl species' average molar weight and charge as a function of pH value (determined using PhreeqC, ref. Section 5.6).

In response to the altered speciation, the measured changes in retention for the two membranes are shown in Figure 44. While no changes were observed in case of the finely porous membrane, the retention for NP10 decreased by more than 60 percent. The strongest decrease was observed between pH 7 and pH 3.5.

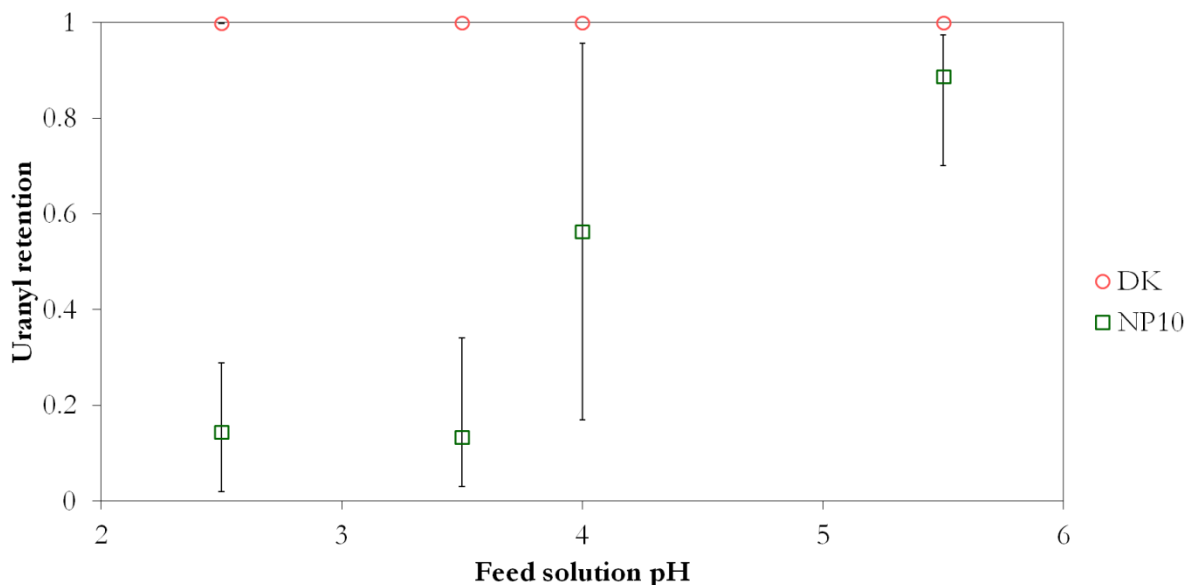


Figure 44: Measured uranium retention for the two membranes at different values of pH of the feed solution.

This observation suggests that speciation effects on uranium transport across the membrane are more pronounced at lower retention. The uranium retention of the finely porous membrane does not respond at all despite the fact that the membrane's charge changed its sign from negative to positive, according to the streaming potential measurements. Hence, size effects appear more pronounced and the fact that uranium passes the DK membrane at all could be attributed to defects in the membrane active layer.

Pathway 2: Addition of phosphate salt

Increasing the phosphate concentration results in high molecular weight phosphate species, as suggested by predictive speciation modeling, ref. Figure 45. Since several phosphate species exist averaging their size and charge properties will improve clarity.

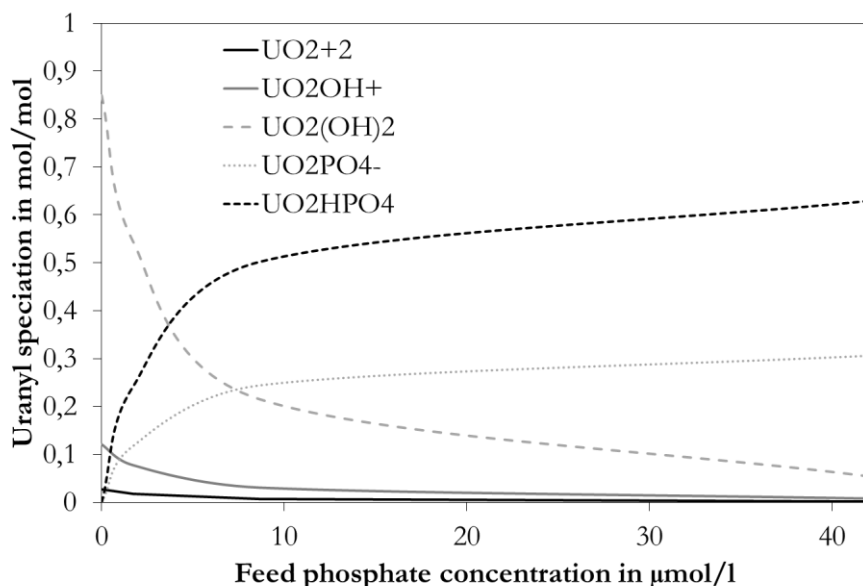


Figure 45: Uranyl speciation as a function of phosphate concentration in the feed solution (determined using PhreeqC, ref. Section 5.6).

The averaged molar weight (as a measure of size) and charge of the uranyl species is shown below in Figure 46. Significant changes occur already at extremely low phosphate concentrations. The influence of such low phosphate concentrations on membrane charge is here considered negligible, keeping in mind that the solution's electrical properties are governed by KCl which is present at a concentration of 10 000 μmol/l.

Further increasing the phosphate concentration did not significantly influence the uranyl speciation and above a phosphate concentration of 10 μmol/l molar weight and charge of the species increased insignificantly. The fact that most of the speciation conversion is completed at very low phosphate concentrations renders the employed method still more suitable to selectively target the uranyl speciation, i.e. isolated from the membrane charge which will remain relatively unimpaired.

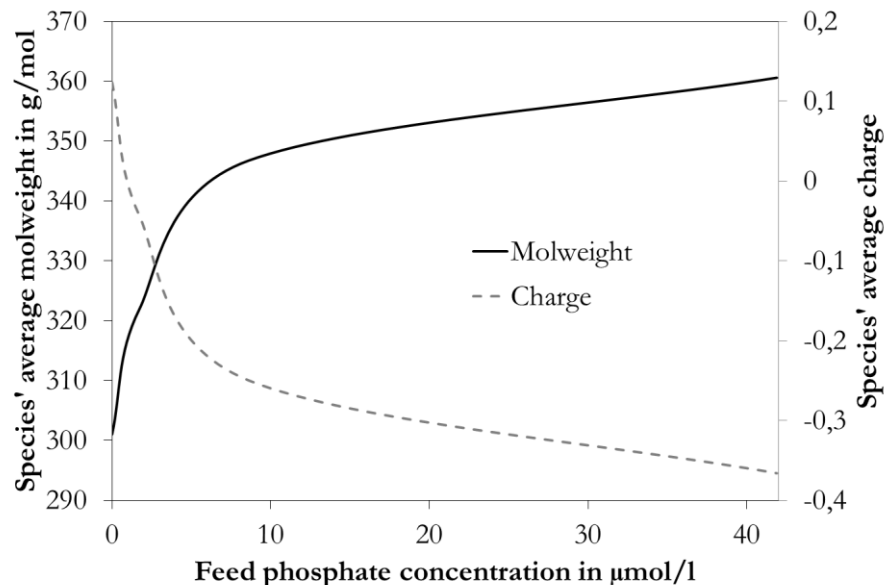


Figure 46: Uranyl species' average molweight and charge as a function of phosphate concentration (diagram is virtually the same for both membranes).

The result for the variation of phosphate concentration on the uranium retention is shown in Figure 47. As expected, the retention of the finely porous membrane stays at the same high level, although the species mol-averaged charge decreases from 0.15 to -0.4 thus further supporting the hypothesis that size effects are more important than charge effects for the DK membrane. Uranyl retention of the NP membrane changes most significantly below 40 $\mu\text{mol/l}$. However, the effects are much less clear than for the experiments involving pH adjustment. Before discussing this finding in too much detail it should be mentioned that replication of the experiment is necessary especially to investigate the delayed effect of phosphate addition. Nonetheless, addition of phosphate lacks a similarly remarkable effect as the one seen in the pH experiments. This could be explained by the fact that by altering the pH the surface charge is also influenced and this effect amplifies the effect of the new speciation. Moreover, the change in charge is more pronounced for the pH-experiment. These observations suggest that for the membrane with large pores charge effects matter.

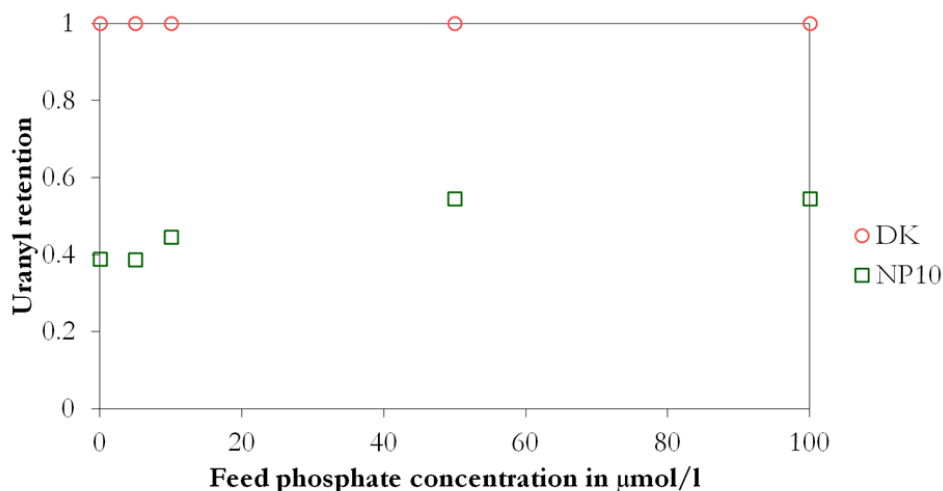


Figure 47: Measured uranium retention for the two membranes at different feed phosphate concentrations.

As mentioned above, the change in uranium retention is due to the sum of changes in the system when phosphate is added or the pH is reduced. Unfortunately, variation of pH and ion concentrations will inevitably influence the charge of the membrane as it is the result of dissociated functional groups and adsorbed ions on the membrane surface, the so called fixed charges which are highly pH sensitive as shown by the streaming potential measurements in Section 6.4.

In the variation of the phosphate concentration the effect of uranyl speciation is isolated by keeping the membrane charge stable. This is accomplished by a background electrolyte which is at a high concentration compared to the concentration of uranyl and phosphate. Here, potassium chloride was used as a background electrolyte. To ensure that the membrane charge and the membrane's separation behavior are stable lithium ions are added to the solution. The retention of the lithium ions indicates changes in the membrane charge. Changes in the lithium ion retention when phosphate is added make evident that the separation behavior of the membrane changed and that the effect of uranyl speciation could not be isolated. Lithium was chosen because it exhibits low retentions and because its tendency to form complexes with phosphate is low, as shown by a database analysis. The validation of the here observed phenomena will be presented in Section 7.2 of the discussion. For now, the result of this section is that speciation has a considerable influence on the nanofiltration of uranium-contaminated water.

The influence of uranyl speciation due to changes in the size and charge of the uranyl species was evaluated via two pathways: addition of HCl and addition of phosphate. The retention of the open membrane changed in both cases in response to the altered speciation and as a result, in Section 6.6 speciation needs to be considered in order to model the observed separation of the complex uranium- contaminated water sample.

6.6 Nanofiltration of uranium-contaminated water — Case study at the Seelingstädt site of the Wismut GmbH

The results from the speciation experiments with pure uranyl solutions and the numerical model are applied to a real water sample with its treatment being of industrial relevance. The example chosen here is a water sample from the tailings storage facilities at the former uranium milling site in Seelingstädt, in Thuringia, Germany. The history of these tailings is presented here because it directly influences the water composition and offers insight into future treatment challenges and the extent of the treatment problem.

Mined out material was processed at the Seelingstädt milling site leaving tailings storage facilities with a total volume of more than 100 million m³ of stored tailings material [Metschies2013]. The milling and processing facilities in Seelingstädt were put in operation in 1960. In the time up to 1990 more than about 109 Mio t uranium ore from the mineral deposits in Ronneburg, Culmitzsch, Dresden-Gittersee, Aue, and Königstein were processed at the Seelingstädt site via chemical extraction in order to produce concentrates which were then further processed in the former Soviet Union [Chronik2.3.1-20]. The concentrates were in the chemical form of ammonium diuranate (yellow cake) and had a uranium content of 60% [Chronik2.3.1-5]. Uranium was extracted from these ores by leaching using an alkaline process for uranium-poor and lime-rich ores, and an acidic leaching process for uranium-rich and lime-poor ores. In the early years the ores were primarily processed in the acidic process in later years the ores coming from Ronneburg shifted from the

siliceous rock type more to the carbonaceous rock type and the alkaline treatment scheme gained in importance [Chronik2.3.1-3]. The scheme of the alkaline process is shown in Figure 48. The acidic leaching process, used in parallel to the alkaline process, was similarly structured into comminution, leaching, ion exchange and precipitation, however, the leaching of the ore and the regeneration of the ion exchange resin being performed with sulphuric acid instead of natron. The leaching schemes are presented in more detail in the following.

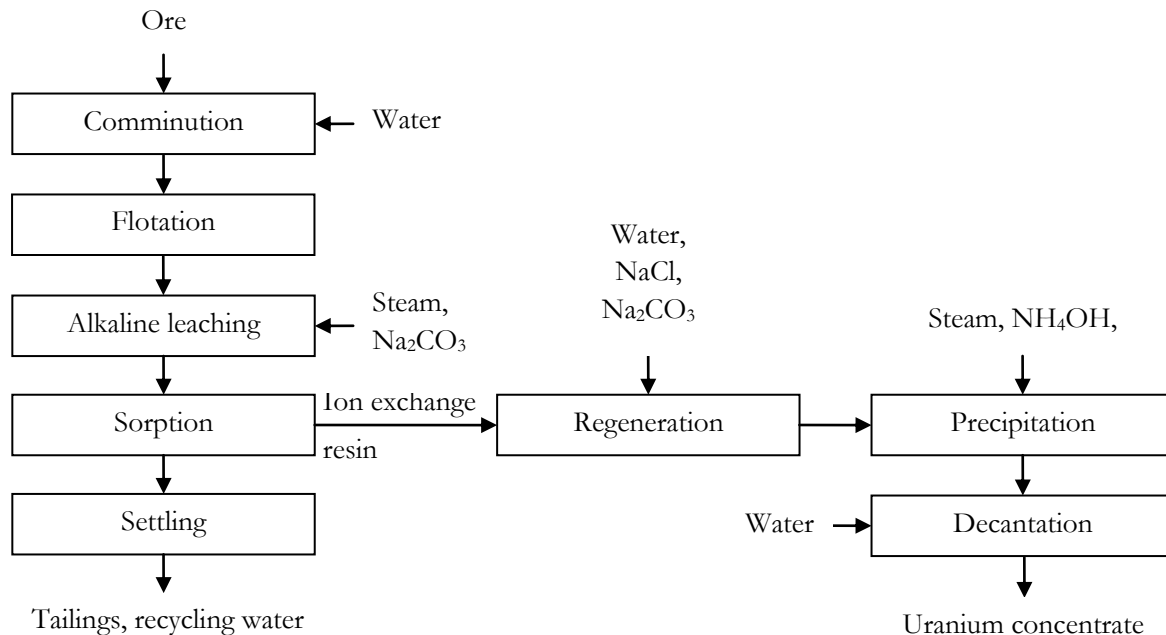


Figure 48: Schematic of the alkaline leaching process which was used predominantly in the last years of operation at the Seelingstädt milling site [Chronik].

Alkaline leaching process:

The first step is comminution using autogenous mills and water from pond B Culmützsch ([Chronik2.3.1-6]). The ore leaves the comminution in two fractions, a uranium rich fraction with a uranium content of 0.1% (constituting 20% of the uranium) and a uranium poor fraction with a uranium content of 0.055% (80% of the uranium). The two fractions were leached with natron separate from each other and the uranium rich fraction was pre-treated with flotation in order to remove pyrite. The pyrite consumes part of the natron during leaching and is therefore undesirable in the alkaline process but can be sent to the acidic leaching process where it is chemically inert.

After flotation the uranium rich fraction was sent to pressure leaching in autoclaves, at 15bar pressure at 120° C. The uranium rich slurry was pumped into autoclaves using piston pumps and heated in plate heat exchangers with steam. The grain size in leaching should be small but for flotation a too fine grain size reduces pyrite removal efficiency and thus only 30-40% of the pyrite could be removed. In order to mix and to oxidize the tetravalent uranium into the more soluble hexavalent uranium air was introduced at high pressure. The non-dissolved slurry leaving the autoclaves was depleted in uranium but left the process at a

high temperature and with a high natron content and could thus be reused in the leaching process for the uranium poor fraction.

The uranium poor fraction was leached at ambient pressure at 75-80° C inside reinforced concrete tanks. The leaching slurry inside the reinforced concrete tanks was transported, oxidized, and mixed using air which was recycled from the autoclaves. Oxygen was necessary to oxidize the tetravalent uranium into hexavalent uranium which has a higher solubility.

The uranium bearing solutions after leaching were sent through hydrocyclones to remove, e.g. sand and then mixed to be processed in the ion exchange unit.

In ion exchange the uranium bearing solution is directed in countercurrent flow with the ion exchange resin named Wofatit SBT. Due to the advantageous property of uranium to form anionic complexes with natron it is possible to separate uranium from other metals. Consequently most of the uranium is adsorbed to the ion exchange resin and the solution's uranium concentration was reduced to about 2-3 mg/l which was then sent to the tailings.

The ion exchange resin underwent regeneration in three steps. In the first two steps it was regenerated with process water of low uranium concentration and in the last step with uranium free water, natron, and sodium chloride. The process stream from alkaline leaching was mixed with the stream from acidic leaching.

Acidic leaching process:

Two different ore fractions were processed in the acidic treatment scheme: a coal based uranium ore and a pyrite or silicate ore. The two ores were kept separate from each other because the coal required more intensive leaching [Chronik2.3.1-13]. The comminution was performed separately in cone crushers and ball mills.

The aggressive solutions required acid proof coated steel tanks with a rubber layer. The pyrite slurry was first mixed with sulphuric acid and in a further step with sodium chlorate in order to oxidize the tetravalent uranium into the hexavalent uranium in order to increase solubility. The coal slurry was leached with sulphuric acid alone but at higher temperatures using steam. The coal and pyrite slurry was then mixed.

Before ion exchange, particles were removed from the produced solution by sieves and screw conveyors in countercurrent flow. Furthermore, the pH was increased from below 1 to 1.8 in order to improve uranium extraction in the ion exchange step. The ion exchange was performed in countercurrent flow of resin and solution. After ion exchange the solution was led along sieves in order to separate resin from the remaining slurry. The uranium depleted solution was then neutralized using lime treatment (to pH 6-7) and pumped into the tailings of Trünzig A or Culmitzsch A.

Regeneration of the ion exchange resin was performed using acidified sodium chloride solution in three steps. In the first steps uranium poor solutions were used and in the third step fresh acidic salt solution was added.

Concentrate winning

The product stream from the alkaline and the acidic extraction scheme were then mixed and sent to concentrate winning. The mixed product solution after uranium extraction contained 5-8 g/l uranium. Both streams were mixed and heated using steam and a pH below 2.5 was reached thus destroying the carbonate complex. This decomplexation was essential for the efficiency of the precipitation. The precipitate contained high concentrations of sodium chloride and had thus to be rinsed. The rinsing water was pumped to the tailings. The concentrate (yellow cake), after an dewatering step was then dried in a rotating thin film evaporator.

Tailings storage facilities (TSF)

Uranium recoveries of around 92% were reached and the uranium could be sent to further processing in the form of yellow cake. Tailings from the leaching processes containing the remaining 8% of the uranium as well as process water were then stored in tailings storage facilities (TSF) which were developed in mined out open cast uranium mines operated between 1949 and 1967 [Chronik2.3.1-23]. As can be seen in Figure 49, the tailings as well as process water were discharged into two separate TSF. These TSF were designed for deposition of residues from the alkaline and the acidic leaching process, respectively. At deposition the tailings in TSF A were partially neutralized in order to stabilize and contain contaminants. Today, the pore water in both TSF is slightly alkaline (around pH 7 to 9) [Chronik2.3.1-26]. During operation of the mill from 1961 till 1991 a total of 124.89 million m³ of process water was discharged into an adjacent river. Along with this discharge also 264.84 t of uranium were released.



Figure 49: Tailings storage facilities at the Seelingstädt site (1991) [Chronik 3.3.4 page 8].

The remediation scheme that was determined to be most suitable for the TSF is dry in-situ deposition. This requires removal of supernatant water in a first step. For this an external water treatment plant with a design capacity of 300 m³/h was put in operation in 2001 [Metschies2013].

As a pre-treatment, acid is added to destroy the uranyl complexes and free CO₂ is removed in stripping columns. The de-complexation improves the efficiency of the precipitation by lime treatment [Metschies2013]. The scheme of the treatment process is shown in Figure 50. The precipitate which contains

uranium, arsenic, and radium is filtered, dewatered, and then immobilized in concrete. The treated water is discharged into the adjacent river.

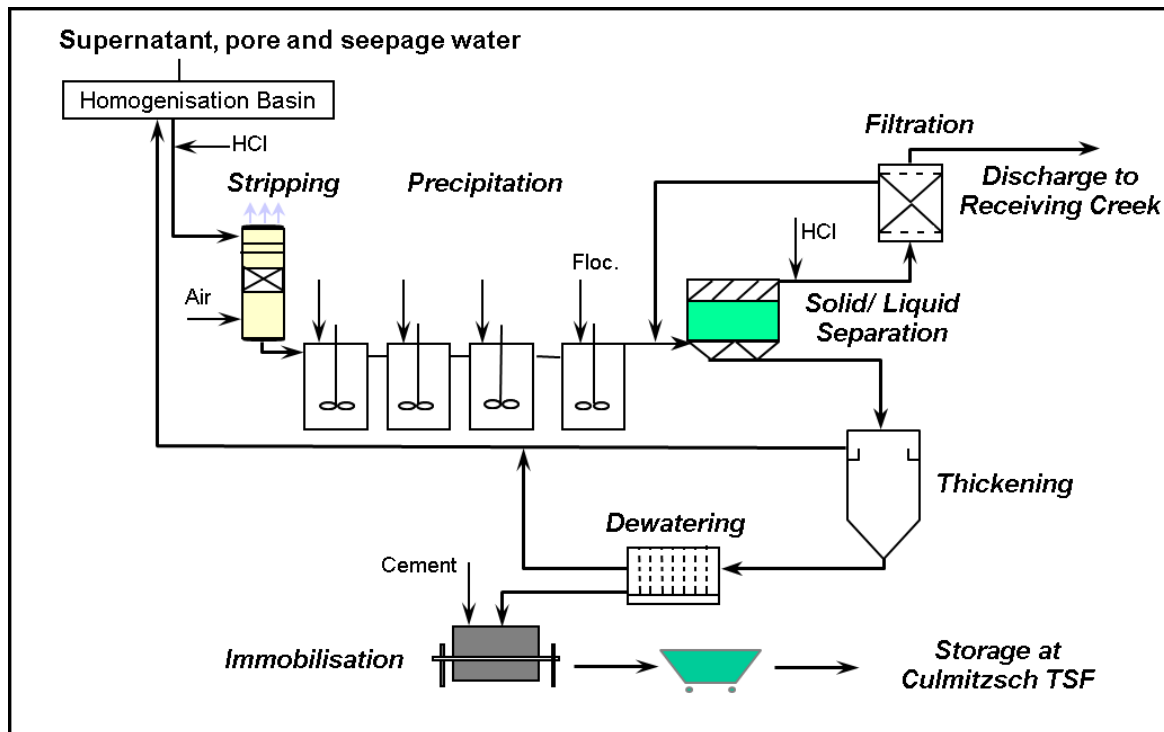


Figure 50: Layout of the precipitation stages of the current water treatment process at the Seelingstädt site [Wismut2014].

The progress of the remediation of the TSF is shown in Figure 51. Only a small fraction of the supernatant water remains on TSF A and TSF B is already completely dewatered. The water treatment facility is located left of the two ponds. Most of the tailings surface is sealed with an interim cover layer of 1 m thickness to reduce radiological impacts and erosion. The pond on TSF A was used as a reservoir where seepage from both, TSF A and B, but also pore water that is released from compaction, as well as rainwater catchment from buildings and structures of the Seelingstädt site.

The composition of the pond on TSF A differs over time, depending on precipitation and processes in the tailings but generally the water, which is further treated by the precipitation process shown in Figure 50, contains high concentrations of sodium, magnesium, sulphate, chloride, uranium, and hydrogen carbonate.



Figure 51: Aerial photograph of the tailings during remediation in 2012. Supernatant water only on TSF A. The total amount of uranium which is contained in the tailings is about 7,000 t [Metschies2013].

The current treatment process can reliably reduce concentrations of U, and As in the treated water below the required limits whereas the concentration of sulphate and chloride can be problematic when the adjacent river does not carry sufficient water to dilute the salt influx [Metschies2012].

A treatment process which is capable of reducing salt concentration even for high and low feed salt concentrations in times of low and high precipitation, respectively needs to be found before the end of the area's remediation which is projected till 2022 [Metschies2013].

The seepage that will emerge from the TSF could be treated in a membrane process, e.g. nanofiltration. Membrane technology is capable of reducing the salt content and could assist in finalizing the remediation process by ensuring the water quality of the river and thus avoiding surplus water storage. Water treatment will continue to be necessary after finalizing the dry in-situ deposition of the TSF. The pH of the ponds is around 8.0 and 8.3 for pond A and B, respectively [Metschies2013] which is an acceptable range for membrane processes. The influence of the high concentrations of sulphate, chloride, and ammonium on the membrane process will here be investigated experimentally.

The composition of the water sample to be treated is given in Figure 52. Each experiment was run with a fresh membrane sample but also with a fresh water sample and in total 8 individual experiments were performed. The variation between the individual feed water compositions is shown in the diagram with error bars indicating the maximum and minimum value for each concentration.

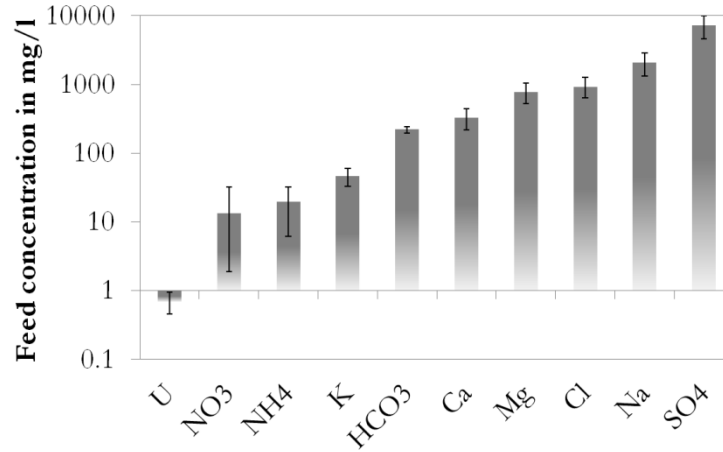


Figure 52: Composition of the mine water, average of all 8 experiments with independent sampling at pH 8.3.

For each of the water samples a separate experiment (trans-membrane pressure 15 bar, temperature 25° C, cross-flow velocity 1.3 m/s) was performed using a fresh sample of the membranes DK and NP. The obtained retentions were then averaged and the result is shown in Figure 53. The retentions of the smaller solution components, such as chloride and nitrate is for both membranes in a comparable range. For the large components, e.g. sulfate and uranium, the retentions divide and the DK membrane achieves a much better separation.

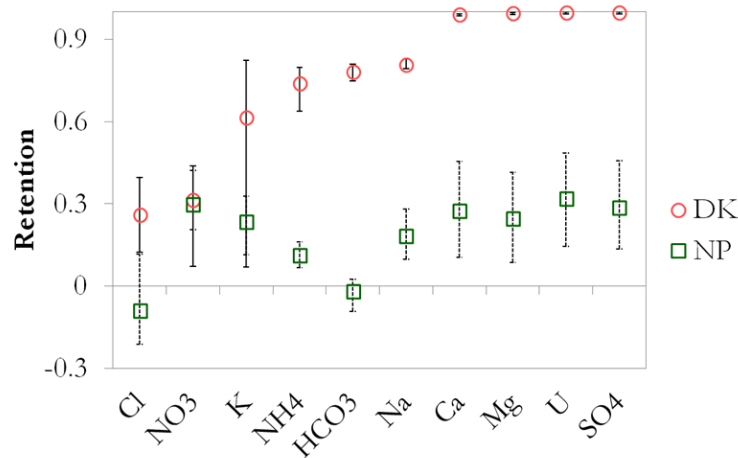


Figure 53: Average retention of each solution component by the two membranes, DK and NP.

The focus of this work however, is not to assess the practical applicability of each membrane but rather to use the observed retentions as a comparison for the modeled retentions of such a complex water with a special focus on uranium and its speciation.

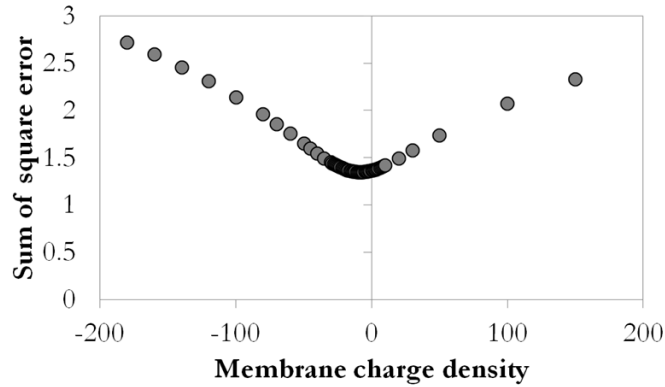
The solution is dominated by sulphate, sodium, and chloride at an average pH of 8.3. The composition of this complex water determines the speciation in which uranium is present. Separate speciation calculations were performed for each individual solution and the average speciation was determined using PhreeqC and the database lnl.dat. The average speciation, as shown in Table 20, is dominated by the calcium carbonate species described in Section 5.7. Thus, data on charge, diffusion coefficient, and size is known and can be applied to the modeling of the separation of the two membranes.

Table 20: Average uranium speciation of the feed solution averaged from the individual speciation of 8 experiments as determined using PhreeqC (ref. Section 5.6).

Species	Speciation in mol-%
$[Ca_2UO_2(CO_3)_3]^0$	76
$[MgUO_2(CO_3)_3]^{-2}$	18
$[UO_2(CO_3)_3]^{-4}$	5

However, the size of the calcium carbonate species of uranium is larger than the pore size of the DK membrane. The membrane pore radius of the DK membrane is 0.463 nm and the radius of the uranyl complex is 0.524 nm. Modeling with the assumptions of the molecule being a rigid sphere and the pore being an ideal cylinder with a certain radius is not possible since under these conditions retention will always be 100 %. Therefore, the experiments involving the DK membrane are omitted from the modeling.

Fitting of the membrane charge was performed according to the procedure described in Section 4.10. The fitting procedure for the NP membrane involves one single parameter, the membrane charge density. A visualization of the fitting is presented in Figure 54. The best fitting membrane charge density is -8 mol/m³.

**Figure 54: Fitting for the NP membrane charge density. The square error between modeled and experimental retention is summed up for all 10 solution components. Fitting was performed as described in Section 4.10.**

The thus obtained best fitting membrane charge density is physically realistic, as the NP membrane is expected to be negatively charged and as the volume charge density is below the sum of all ion equivalent concentrations which is 178 mol/m³. Nevertheless, as shown in Figure 55, a mere variation of the membrane charge density is not capable of obtaining a satisfying fit. Even the best fitting membrane charge density is overestimating retentions of the small solution components.

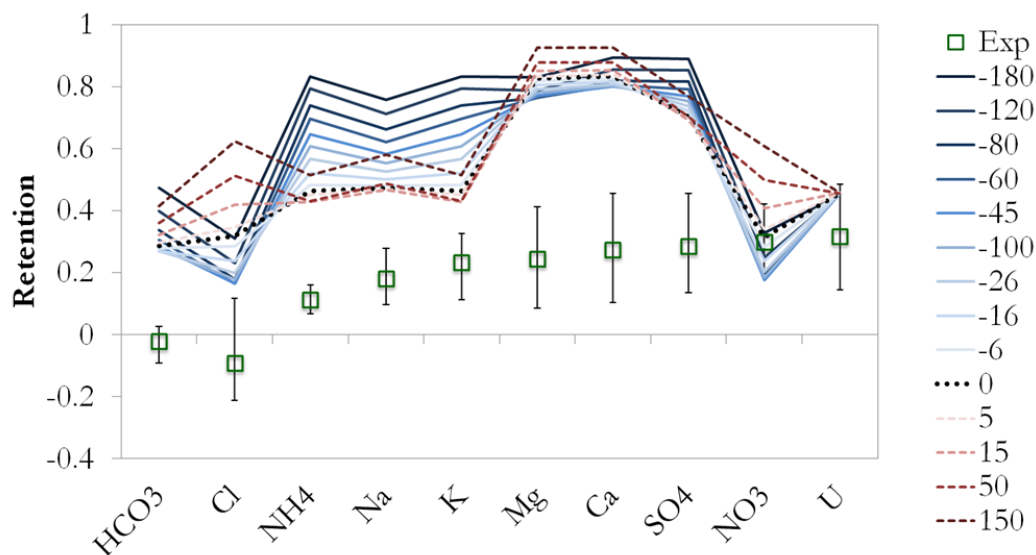


Figure 55: Comparison of modeled (lines) and experimental (points) retentions for the NP membrane. Modeled retentions at different membrane charge densities (legend shows charge in mol/m^3).

Nanofiltration of a complex uranium-contaminated water sample was performed for two membranes. Modeling the retention of 10 components was approached by using the membrane thickness and pore radius as determined in the membrane characterization, which means that the membrane charge density was the single fitting parameter. The obtained result was dissatisfying for both membranes: The pore sizes of the DK and the NP membrane were too small to permit the observed retentions. The repercussions will be discussed in Section 6.6.

7 Discussion of the experimental and modeling results

In this section an error analysis and an analysis of the assumptions of the model are discussed in more detail.

7.1 Experimental uncertainty assessment

Experimental errors can occur for measured data (concentration, flux) and for those parameters which should be at a stable level (temperature, membrane properties). An overview of the instruments accuracy as supplied by the respective manufacturer is listed in Table 21.

Table 21: Accuracy of the employed instruments as stated by the manufacturer. The numbers given in the first column refer to the P&I diagram in Figure 25.

Nr.	Sensor	Accuracy	Measure for accuracy
1	Permeate weight	$\pm 0.01\text{g}$	Value applies to all measured permeate weights.
2	Differential pressure	$\pm 0.1 \%$	Percentage of calibrated range (1 bar), i.e. an effective accuracy of $\pm 1 \text{ mbar}$.
3	Absolute pressure	$\pm 0.16 \%$	Percentage of measuring range (100 bar), i.e. an effective accuracy of $\pm 0.16 \text{ bar}$.
4	Temperature	$\pm 0.3^\circ \text{K}$	Value applies to the whole temperature range of interest in this work.
5	Cross-flow velocity	$\pm 3.75 \%$	Value calculated for the specific cross flow velocity used here, i.e. 1.3 m/s . The accuracy of this sensor is calculated as 0.5% of measuring range (3.25 m/s) plus 2.5% of measured value. In this specific case (1.3 m/s) the effective accuracy is $\pm 0.05 \text{ m/s}$.
6	Retentate conductivity	$\pm 5 \%$	Percentage of measured value.
7	Permeate conductivity	$\pm 20 \%$	Percentage of measured value.
	IC	$\pm 12 \%$	Empirical value. Including dilution of the samples.
	ICPMS	$\pm 15 \%$	Empirical value. Including dilution of the samples.

The uranium concentration was measured using ICPMS analysis which is capable of measuring at very low concentrations ($> 0.001 \text{ ppb}$). The accuracy given in Table 21 was verified in a separate experiment. The result of this analysis is shown in Figure 56.

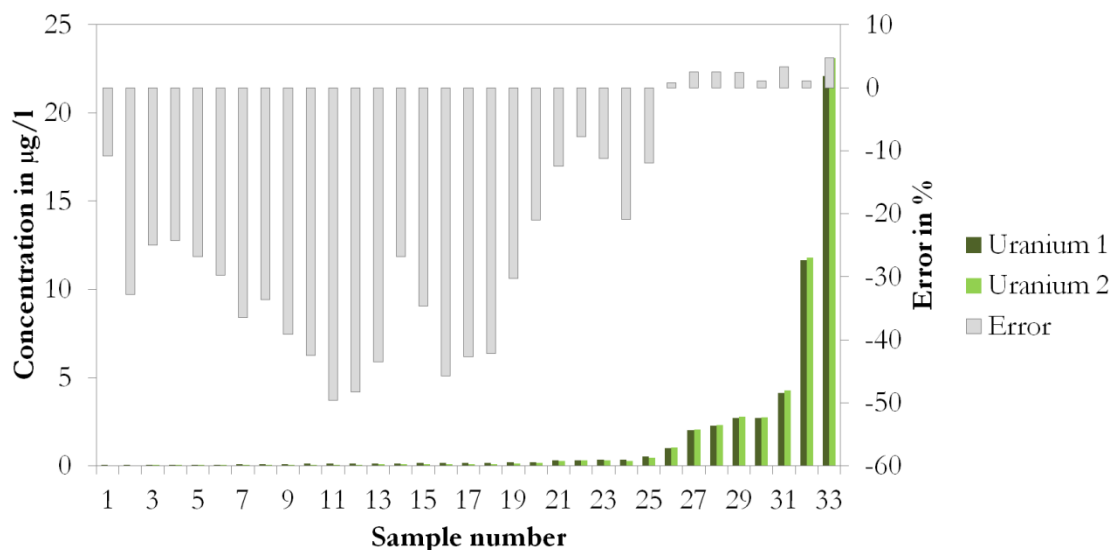


Figure 56: Experimental error of a repeated ICPMS measurement. The error is defined as the relative difference between the two measurements of the same solution: $(c_2 - c_1)/c_1$. ICP-MS using the Thermo X-Series II. Before analysis the samples were diluted 1:10.

During the experiments effects on uranium retention were stronger than expected and as a consequence the samples were of highly different concentrations. In the first run the samples were measured in the order of the experiment and therefore uranium could be carried over from uranium-rich samples to uranium-poor samples. In order to validate the measurements in a second run the samples were ordered by their uranium concentration from the first run. Figure 56 makes it apparent that in the second run the samples of low concentration had a lower concentration which proves that uranium was carried over from samples with higher concentration. Nevertheless, the samples of high concentration were measured with a higher concentration. It is thus apparent that the measurements had an error which is in the expected range. Further on, samples were carefully put in an order to avoid carrying over between the samples. The $\pm 15\%$ for ICPMS measurements appear justified.

The error of the IC measurements is validated using 4 measurements of the same sample containing bicarbonate. The relative error is between 0 and 8% and therefore the $\pm 12\%$ are also justified.

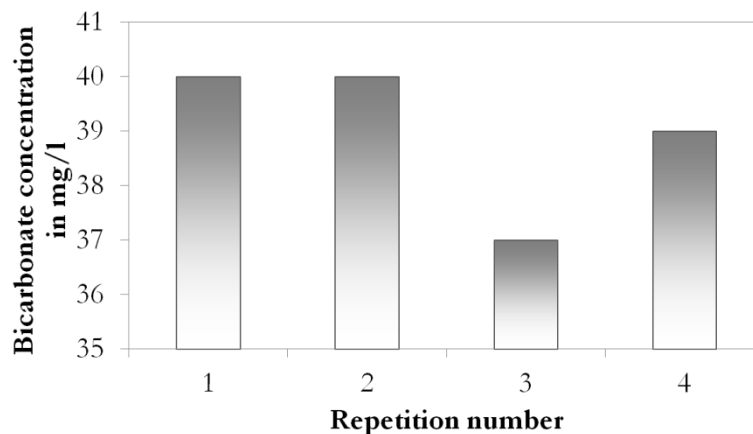


Figure 57: Experimental error of repeated IC measurement of a solution containing bicarbonate. Ion chromatography with the 850 Professional IC by Metrohm, Germany.

The error of the flux appears to be more significant than expected by $\pm 0.01\text{g}$ for the measurement of the permeate weight. An error in the range of $\pm 20\%$ is very common as shown in Figure 58. The observed flux error in the case of the ALNF membrane with a 1mM KCl solution depends most importantly on pressure and temperature. As Figure 58 shows, these parameters were stable and therefore the error is expected to arise from the balance which appears to be not suitable for dynamic weighing. However, calibration measurements have shown that the average permeate flux (determined with the balance, i.e. element 1 in Figure 25) is in good agreement with volumetric measurement using a graduated flask. The $\pm 0.3^\circ\text{K}$ for the temperature sensors are justified while the $\pm 0.16\text{ bar}$ for the trans-membrane pressure are not. This could be explained by pulsation caused by the pump.

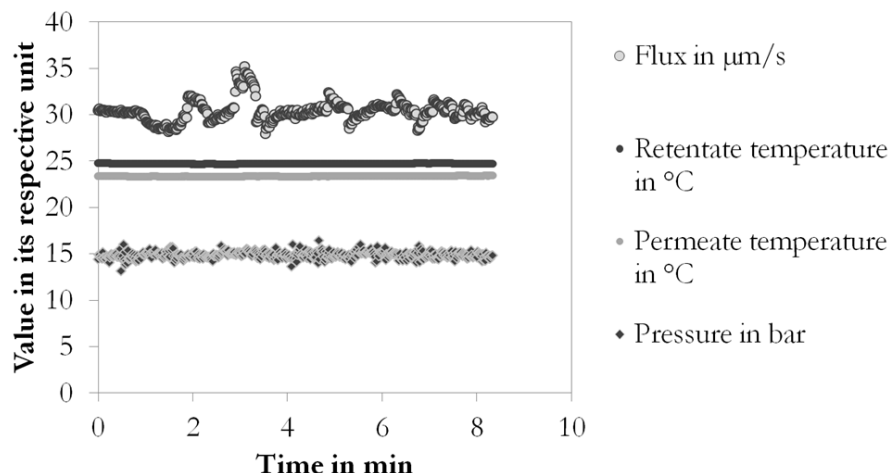


Figure 58: Observed development of flux over time in comparison with the process parameters which affect permeate flux the most. The diagram shows an 8 minute interval of the measured values of permeate flux, the process temperatures, and the trans-membrane pressure in order to illustrate the error of the membrane experiments at the example of a KCl retention experiment in Section 6.4. As in all presented measurements, the process conditions which are adjustable have been kept at a constant level (pump voltage, pressure control valve degree of opening, thermostat settings).

Process intrinsic sources of measurement error for the flux measurement are:

- Temperature of the solution which permeates through the membrane.
- Osmotic pressure difference across the membrane
- Membrane batch

The significance of these sources of error is compared in Figure 59. The most important factor, as in the determination of the thickness, is the membrane batch. Thus, in this work only membranes of the same batch have been compared this means samples of a certain membrane were ordered only once in a sufficient amount. Addition of KCl to reach a conductivity of $300\ \mu\text{S}/\text{cm}$ in order to increase the osmotic pressure proved to have only minimal influence on permeability. Hence, the conductivity of the permeability experiments of $6\ \mu\text{S}/\text{cm}$ is pure enough. Temperature strongly influences the permeability and needs to be kept at a stable level.

Figure 59 shows individual fluxes instead of permeability to visualize the experimental error. Flux vs. pressure curves are clearly linear with coefficients of determination of more than 0.95. The permeability is thus a very reliable measure of membrane properties which is easily accessible by weighing.

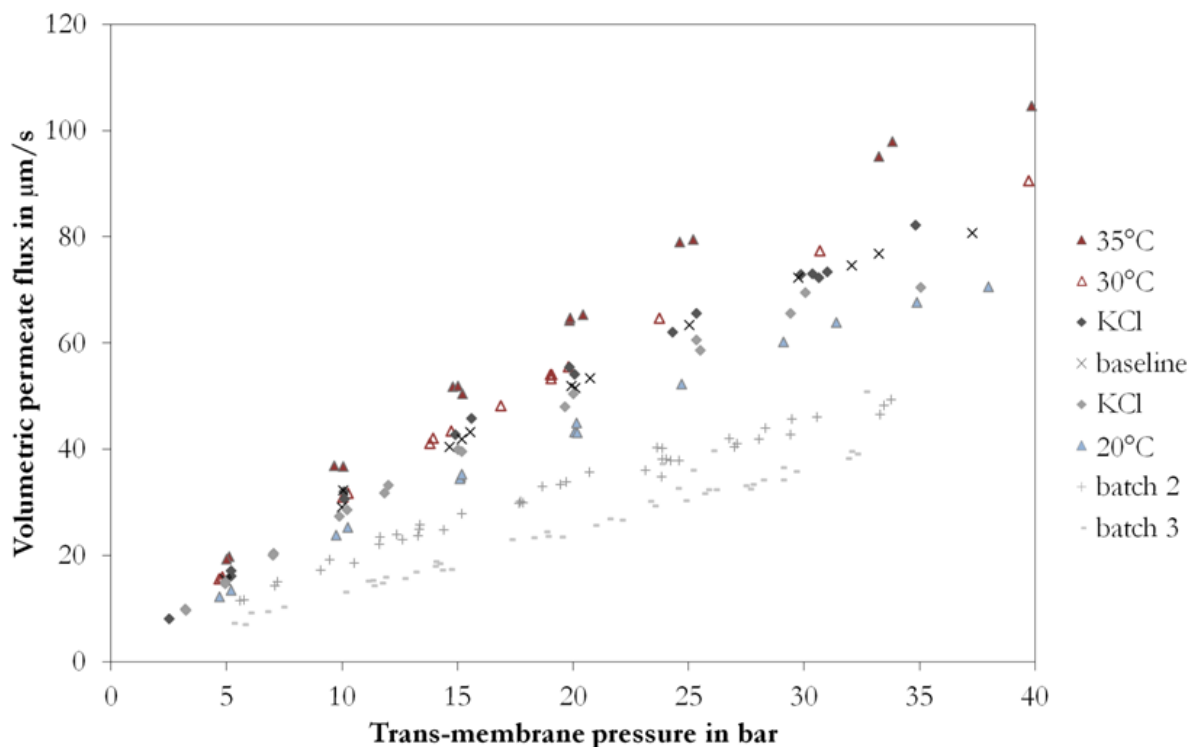


Figure 59: Risk of error analysis for a single membrane (ALNF): Experimental sensitivity of membrane permeability to variations in temperature (baseline at 25°C, variation at 20°, 30°, and 35° C), water purity (baseline deionized water at 5 μ S/cm conductivity; variation through addition of 1 mmol KCl), and membrane batch (baseline is the same batch as in the variation of temperature and purity, variation with 2 samples from a different batch). The curves clearly follow a linear trend.

Retention measurements using the conductivity electrodes proved to be very stable, as shown in Figure 60. Hence, conductivity measurement is an excellent tool to determine the point at which an experiment reached its stationary state.

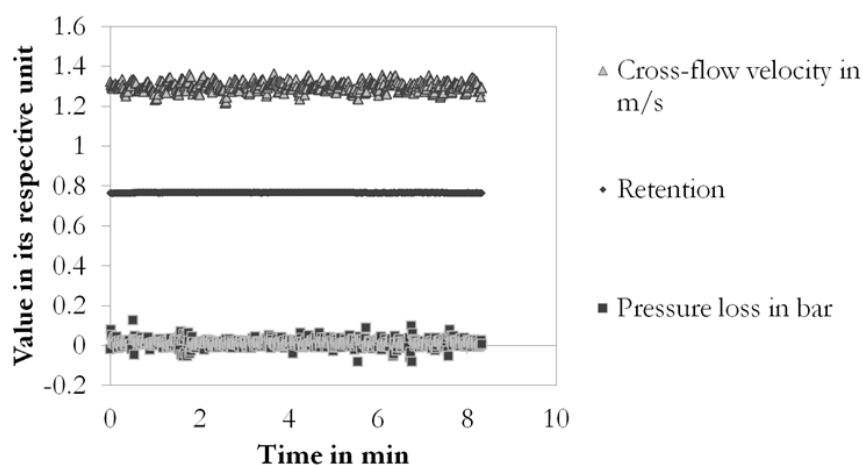


Figure 60: Development over time of the KCl retention (ALNF membrane, 25° C, 1mM), cross-flow velocity, and pressure loss along the feed channel.

The cross flow velocity is less stable than the accuracy of ± 0.05 m/s. Also here, the reason can be found in pulsation caused by the plunger pump which is also the reason for a systematic error in the trans-membrane pressure. This problem was solved by keeping a sufficiently high cross-flow velocity in order to reduce the influence of concentration polarization.

Other effects on membrane properties such as ageing, cleaning, or fouling [EMST2013 page 1028] were accounted for by keeping the same routine for all experiments performed in this work.

In light of the multitude of **sources of experimental error** the experimentally observed error is within the expected range and all effects appear to be taken into account. In any case, the inhomogeneity of the membrane is the strongest source of error which cannot be avoided.

7.2 Error analysis for Section 6.2

In Section 6.2 the Hagen-Poiseuille equation was employed in order to determine the thickness of the membrane. This approach will be further tested here in order to test its applicability which is founded on the basis of major assumptions concerning the membrane structure, i.e. containing homogeneous cylindrical pores.

The way this structural assumption is tested here is by changing the temperature of the feed solution and thereby also its viscosity. Since pure water was employed the viscosity is known and the experimental data can be fitted by the linear trend required by the Hagen-Poiseuille equation. This fitting was performed for three different nanofiltration membranes in order to increase the representativeness of this experiment.

By changing the temperature the applicability of the Hagen-Poiseuille model for the determination of the membrane parameters can be tested. According to the model the permeability needs to be inversely proportional to the viscosity of the feed solution. Figure 61 shows the comparison between the model's prediction and the measured permeability. The data suggests that the model is suitable to describe the flow through a nanofiltration membrane for aqueous systems.

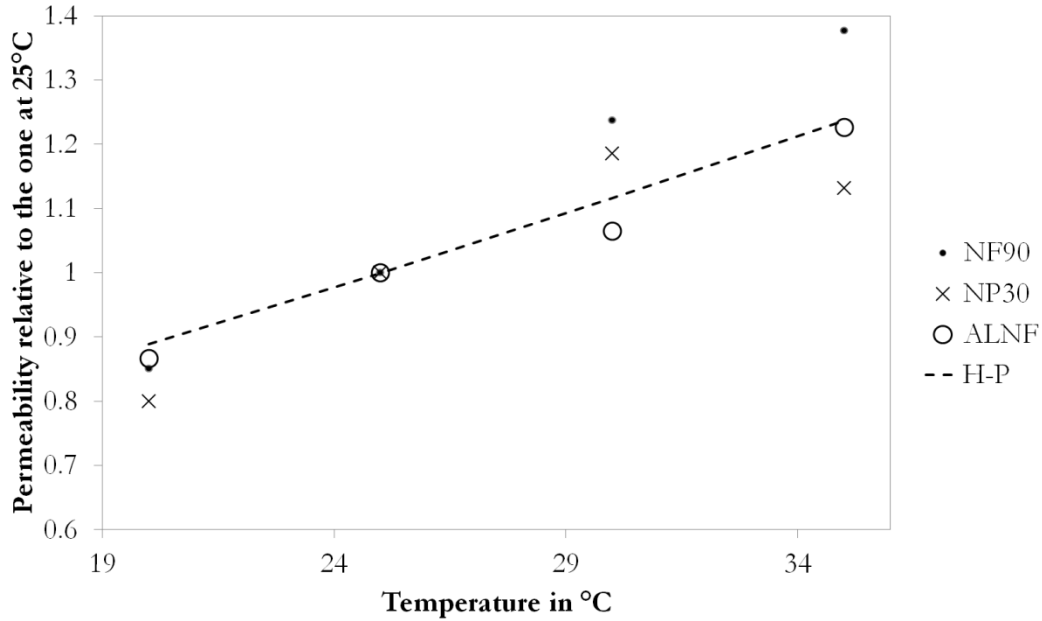


Figure 61: Influence of temperature on permeability. Experimental results for three different membranes in comparison with the theoretical prediction by the Hagen-Poiseuille model (H-P). H-P appears justified.

7.3 Error analysis for the experiments of Section 6.5

The experiments involving synthetic uranyl solutions described in Section 6.5 will be further discussed in this section by comparing them to the observed potassium and lithium rejections. These ions accompanied uranium in the solution and changes in their retention (which are rather independent of the changes in uranium retention which is present at a low concentration) can be used as markers for changes in the membrane's general retention behavior.

In case of the experiments at different pH, the pure solutions contained only uranyl nitrate and potassium chloride (ref. Section 5.4). The changes in potassium retention for the different values of pH are shown for the two membranes, DK and NP, in Figure 62.

The potassium retention of the DK membrane increases at a lower pH. As shown in Section 6.5 the uranyl retention of the DK membrane was close to 100% irrespective of pH. As a conclusion can be stated that the DK membrane's retention is generally weakly pH dependent and retention must be due to steric or dielectric effects, or even to another effect which is not considered here.

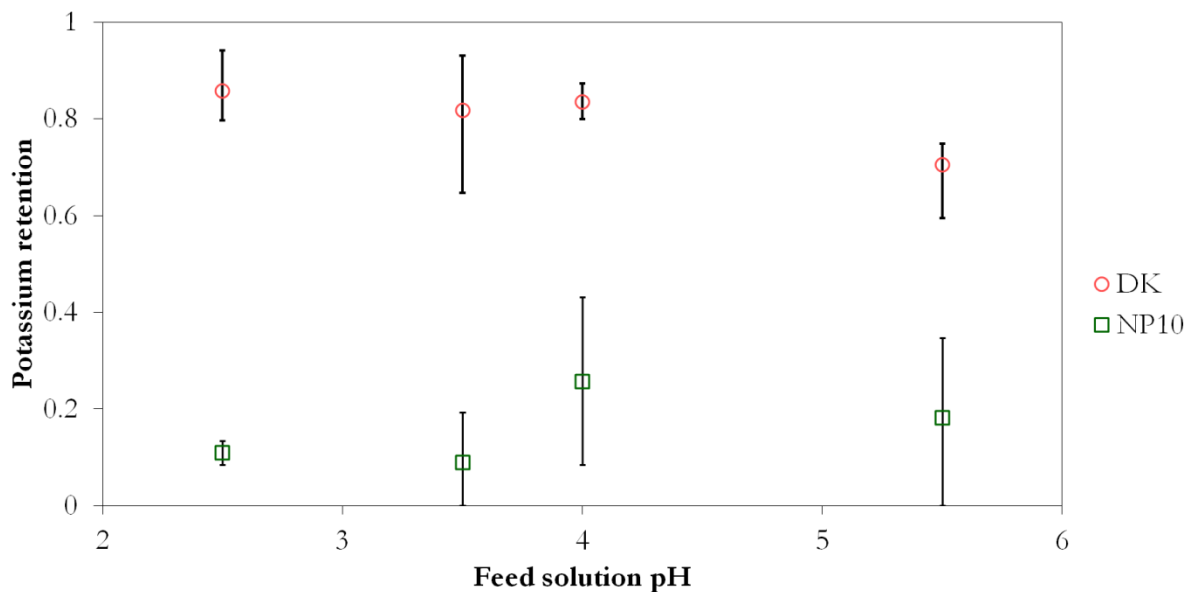


Figure 62: Variation of pH and observed effect on potassium retention for the membranes DK and NP.

In case of the NP membrane, comparison of the potassium retention to the uranyl retention shows that the effects are much stronger for uranyl than for potassium. As potassium does not form any complexes and keeps its diffusivity and size regardless of pH it varies slightly in the range of 20% retention. Uranyl, whose speciation exhibits a strong dependency on pH varies in the range of 80% retention. The much stronger effect for uranyl can be attributed to the effects of speciation.

Potassium was also present during the phosphate experiments; the result is shown in Figure 63. For the NP membrane, apart from the second retention, all values are stable regardless of phosphate concentration. Since potassium does not have a strong tendency to form complexes with phosphate, this can be seen as further evidence that the observed effects in the uranyl retention are due to changes in speciation.

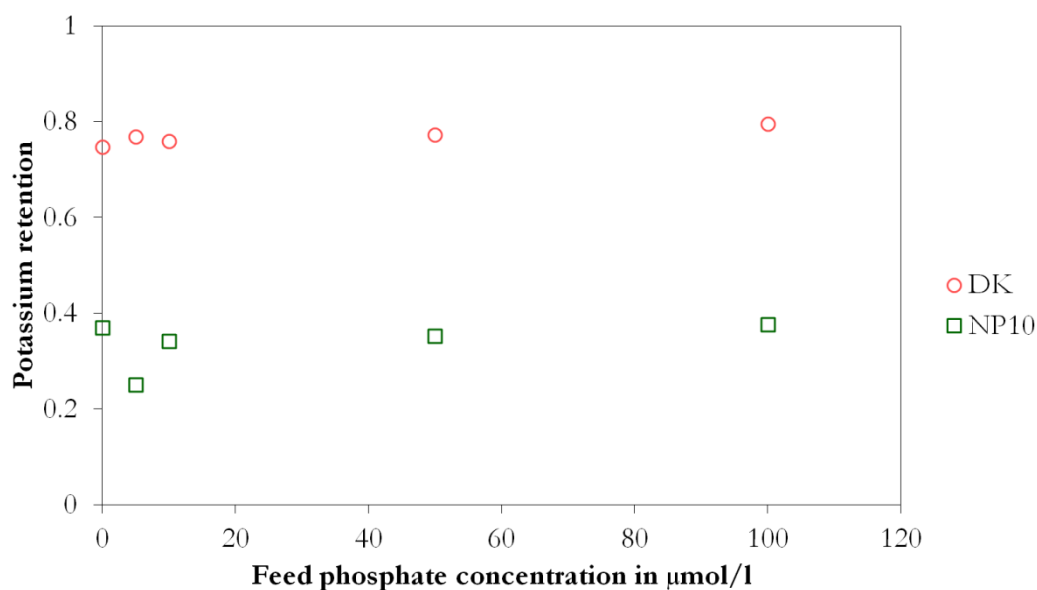


Figure 63: Development of the potassium retention during the addition of phosphate to the solution.

For the DK membrane the same reasoning applies here as to the pH experiments: Neither the potassium nor the uranium retention vary considerably and an effect of speciation cannot be observed. Addition of acid and relatively large amounts of phosphate salt is not sufficient to change the retention behavior of this membrane.

The development of the lithium retention gives further evidence to the statements made above. Furthermore the dip in retention at the second phosphate retention shows that the irregularity might be due to an error during the dilution of the samples. This dip can be seen for lithium, potassium, and also uranium.

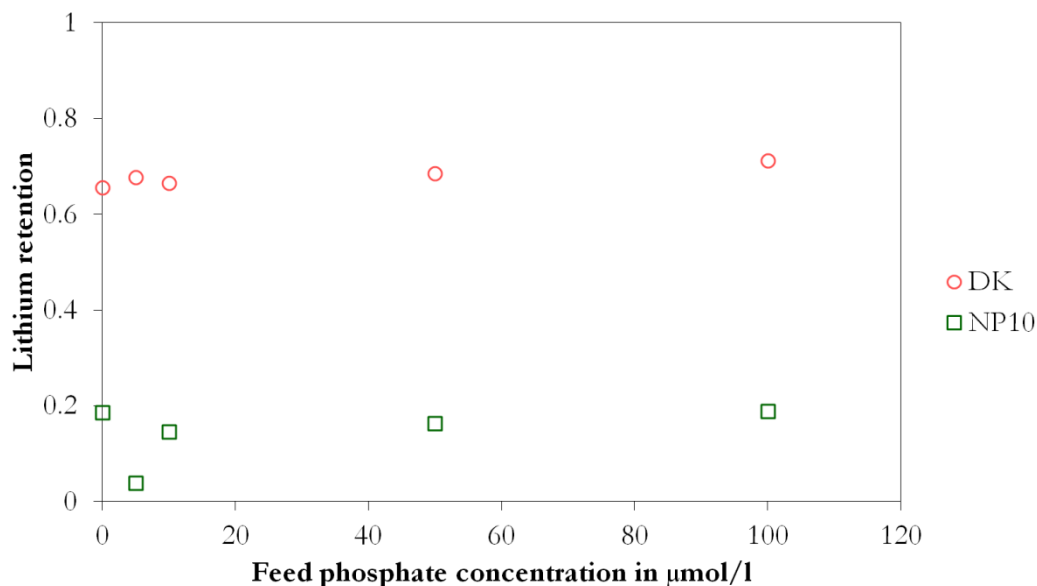


Figure 64: Development of the lithium retention during the addition of phosphate to the solution.

In conclusion, the DK membrane did not show speciation effects however, this membrane might have pores which are too small to be dependent on the uranium speciation..

The NP membrane however showed clear speciation effects which can be quantified by the changes in retention which are more significant for uranium than for potassium or lithium:

- Variation of pH: U 80 %, K 20 %
- Variation of phosphate: U 15 %, K 1 %, Li 0.5 %

Indicator elements shall be the term assigned to lithium and potassium in this section. The retention of the so called indicator elements was monitored as a point of comparison. The indicator elements were carefully chosen to not change their speciation during the course of the experiments. The changes in their retention (generally lower than those for uranium) served as a baseline for the evaluation of the uranium retention. The result gives further evidence that speciation plays a significant role in uranium retention by nanofiltration membranes.

This section concludes the critical analysis of the experimental results. The results obtained by modeling will be scrutinized in the following.

7.4 Model discretization

As shown above in Figure 12 the membrane is discretized into a certain number of nodes. Increasing the number of nodes should not change the modeled retention. Therefore, in order to choose an appropriate number of nodes, discretization needs to be analyzed. These two objectives, model convergence and necessary number of nodes, are followed up in this section.

The first set of modeling calculations involved only one component, glucose, and converged very fast after around 10 iterations. An analysis of the convergence time is not an adequate task since the consumed time depended heavily on the Matlab-Excel-Interface. Calculation time was typically in the range of a few seconds and the modeled retention as a function of the number of nodes is shown in Figure 65.

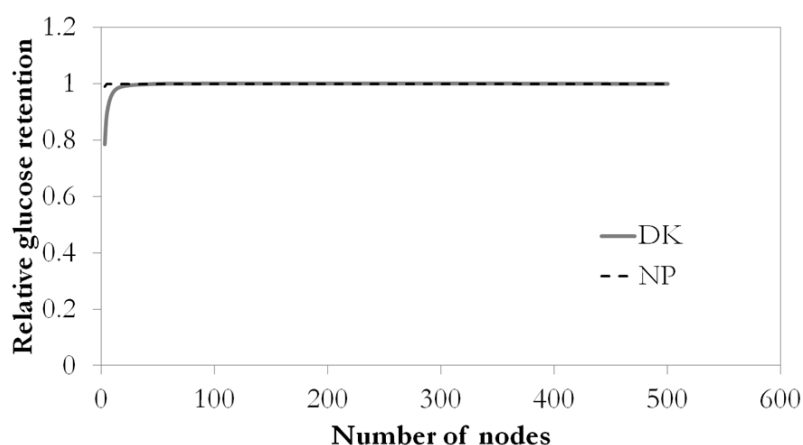


Figure 65: Model discretization for the two membranes and for the retention of glucose. Relative retention is the modeled retention at the respective node number relative to the modeled retention at the highest node number (here 500).

Glucose retention is shown relative to the retention at the highest employed node number. Hence, a satisfying convergence is indicated when the relative retention approaches 1, a condition which is well fulfilled already at 30 nodes. The node number chosen for the glucose modeling was 200 nodes simply because convergence was reached within a few minutes even for such a high node number and because the calculations necessary for the glucose experiments were not too extensive.

For the modeling of the KCl retention, a similarly rapid convergence was obtained. As shown in Figure 66 after a node number of 35, no significant deviation was found. The node number for the KCl modeling in this work is thus chosen to be 70.

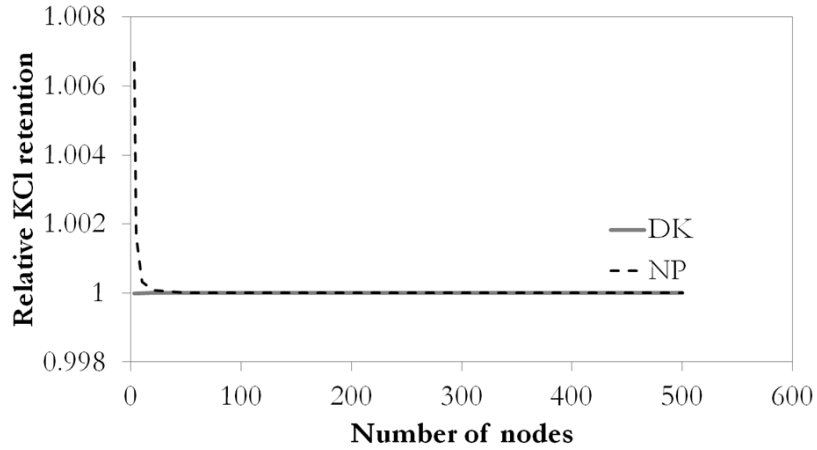


Figure 66: Model discretization for the two membranes and for the retention of KCl. Relative retention is the modeled retention at the respective node number relative to the modeled retention at the highest node number (here 500).

Surprisingly, also for the mine water, the modeled retention reached a stable value at a relatively low node number. Figure 67 shows the development of the relative retention of all 10 components over the number of nodes.

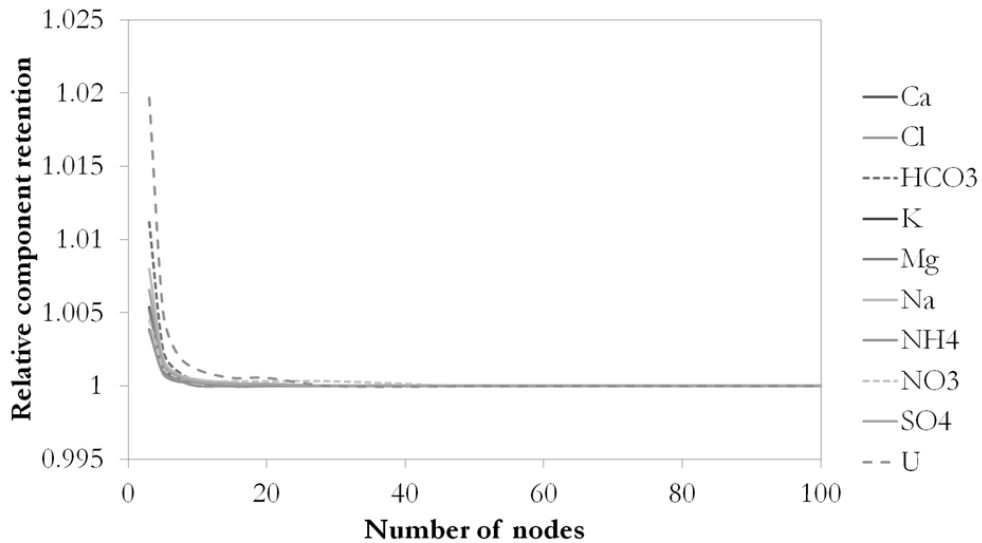


Figure 67: Model discretization for the NP membrane and for the retention of the 10 components of the complex uranium-contaminated water sample. Relative retention is the modeled retention at the respective node number relative to the modeled retention at the highest node number (here 100).

Already at 50 nodes, retention stabilized for all components. In case of modeling the retention of the complex solution a calculation time analysis is appropriate. As shown in Figure 68 calculation time increased exponentially. Hence, the number of nodes which was used in the modeling in this work was selected at 70 nodes which is a good compromise between calculation time and accuracy.

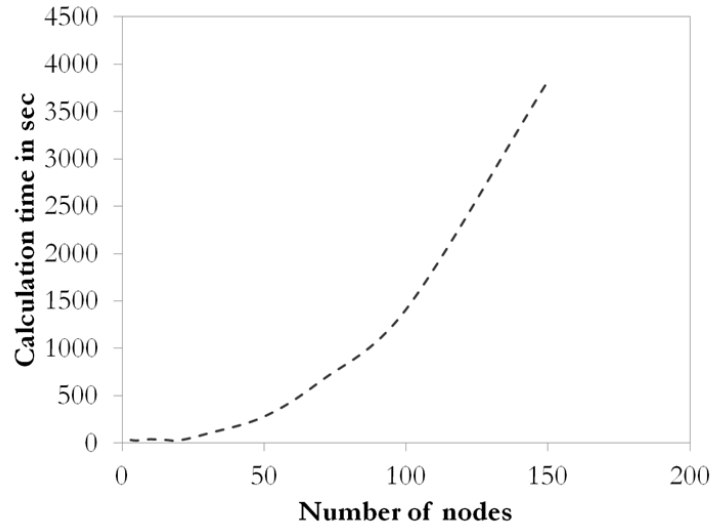


Figure 68: Calculation time for the membrane NP and the solution comprising 10 components as a function of number of nodes for the discretization of the membrane.

A solution of the model for the DK membrane was attempted, however, the solution as a function of node number continued to alternate. Already at low node numbers the solution became instable and the solver returned negative concentrations which are physically impossible.

The result of this section, the number of discretization points used in the computation of the modeling sections in this work is summarized in Table 11.

Table 22: Selected model discretization for the different modeling sections in this work.

Experiment	Node number
Glucose retention	200
KCl retention	70
Complex solution	70

Analysis of the model discretization was performed in order to determine the number of discretization nodes necessary to perform the targeted computations. For all systems in this work, the model converges towards a stable result rapidly and already at a low number of nodes, except for the 10-component system involving the finely porous membrane. For this system a stable solution cannot be found as the membrane pore size is below the size of the largest component of the solution.

7.5 Model sensitivity

In this section the model sensitivity is analyzed at the practically relevant examples of glucose, KCl, and the complex uranium-contaminated solution. The result of such a discussion will be whether the obtained result is realistic in order to validate or the model. The approach chosen for the sensitivity analysis is to keep all variables constant except for the one for which the model's sensitivity is analyzed.

GLUCOSE

In the glucose experiments the membrane dependent parameters are membrane pore size and membrane thickness. The variation by 10 % of these two parameters is shown for membrane DK, and NP in Figure 69, and Figure 70, respectively.

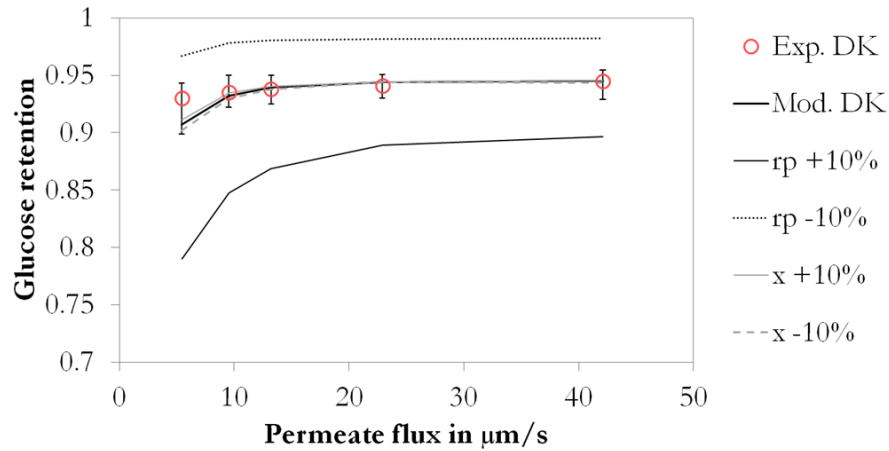


Figure 69: Glucose – Variation of pore radius r_p and membrane thickness x by $\pm 10\%$ for membrane DK. The influence of x is relatively low in the range from 0.1 to 2.5 % of retention. The initial values are: $x = 2.18 \mu\text{m}$, $r_p = 0.463 \text{ nm}$.

In both cases the observed sensitivity to changes in membrane thickness is rather low while changes in the pore radius are more significant. The resulting divergence appears in a highly realistic quantity, which gives further evidence to the validity of the model.

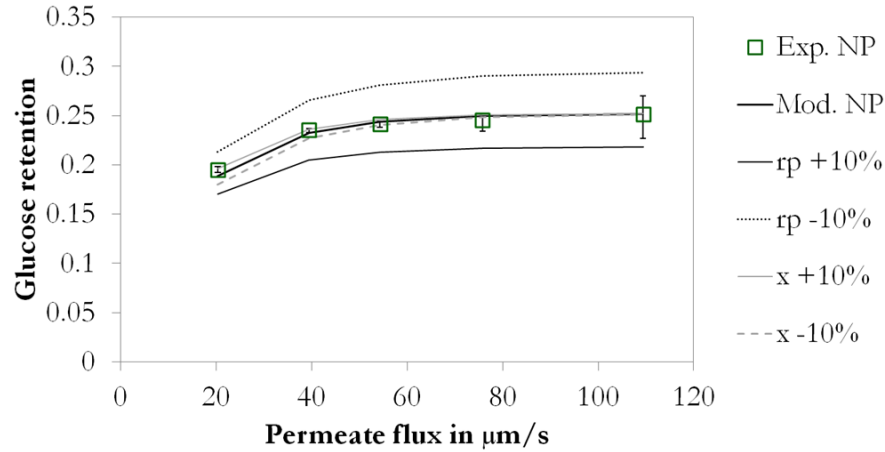


Figure 70: Glucose – Variation of pore radius and membrane thickness by $\pm 10\%$ for membrane NP. The initial values are: $x = 15.26 \mu m$, $r_p = 1.543 nm$.

POTASSIUM CHLORIDE

Analogous to the glucose experiments pore radius and membrane thickness were varied by 10% for the DK and NP membrane as shown in Figure 71, and Figure 72, respectively. The sensitivity towards the two structural membrane parameters is comparable to the one for glucose which gives further evidence to the validity of the nanofiltration model.

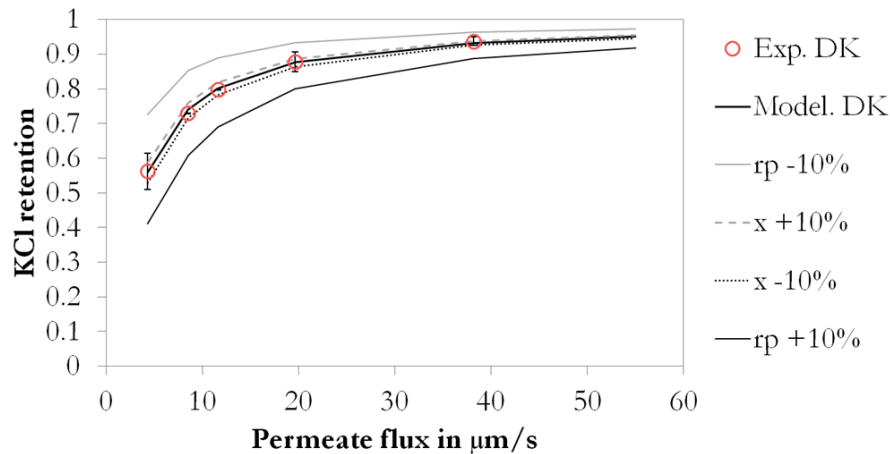


Figure 71 KCl – Variation of pore radius and membrane thickness by $\pm 10\%$ for membrane DK. The initial values are: $x = 2.18 \mu m$, $r_p = 0.463 nm$.

The difference between the sensitivity of the DK and the NP membrane appears more clearly in the potassium chloride simulation than in the glucose retention. While the DK membrane is more sensitive towards changes at low flux the flux sensitivity is reversed for the NP membrane. This might be due to the fact that the retention for the DK membrane at high flux approaches the limiting value of 1 while the NP membrane is generally in the range of lower retention.

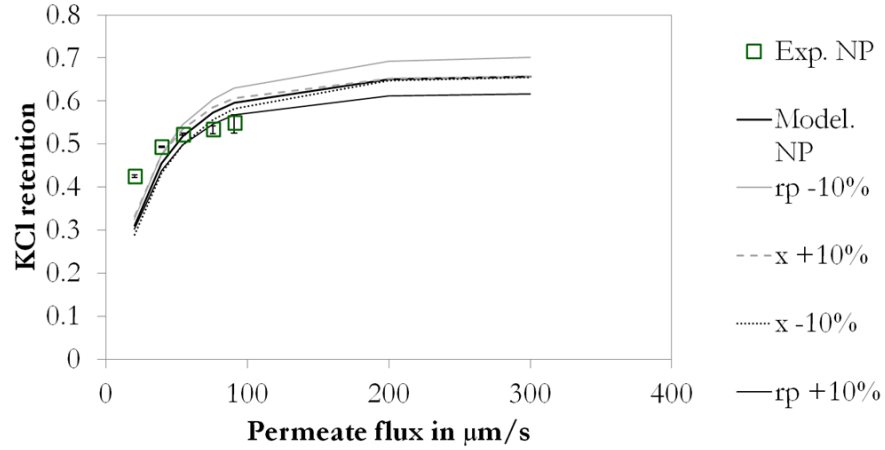


Figure 72: KCl – Variation of pore radius and membrane thickness by $\pm 10\%$ for membrane NP. The initial values are: $x = 15.26 \mu\text{m}$, $r_p = 1.543 \text{ nm}$.

In the case of the here contemplated ionic solute one more membrane parameter is of interest. Besides the pore radius and the membrane thickness also the charge density of the membrane needs to be considered. Figure 73 and Figure 74 show the charge sensitivity of membrane DK and NP, respectively.

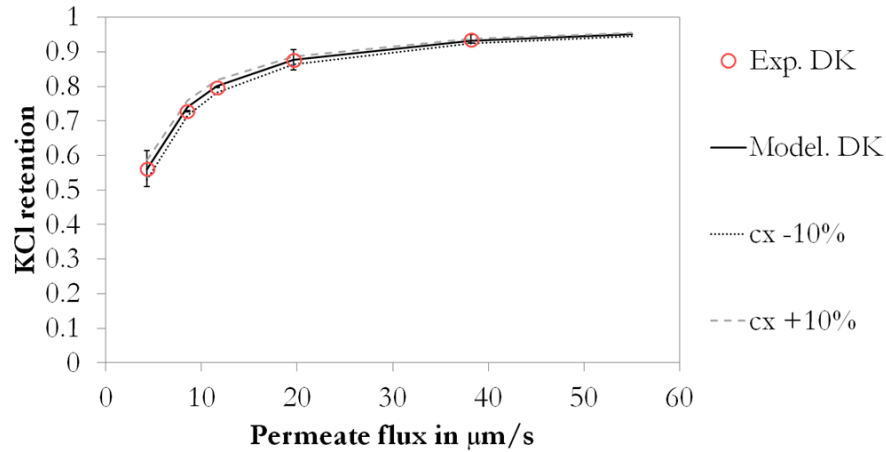


Figure 73: KCl – Variation of the membrane charge density c_x by $\pm 10\%$ for membrane DK. The initial value is: $c_x = -0.33 \text{ mol/m}^3$.

Both membranes exhibit low sensitivity towards the membrane charge density. Here again the flux sensitivity of the membrane charge is reversed for the two membranes.

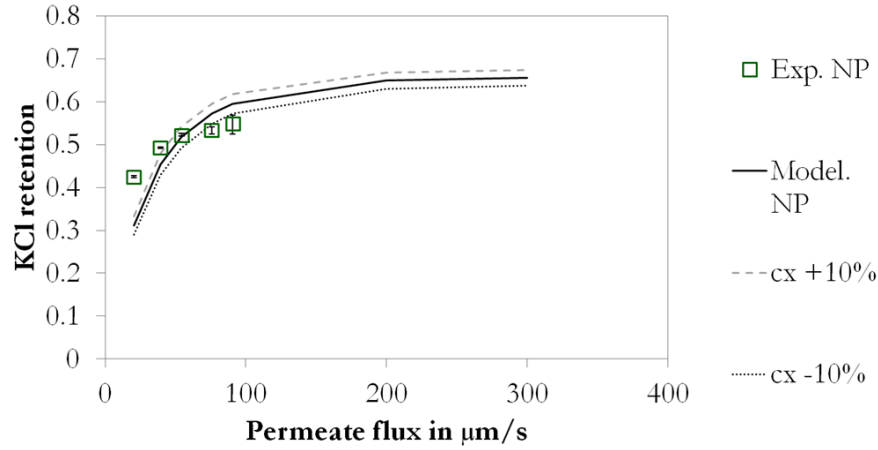


Figure 74: KCl – Variation of the membrane charge density c_x by $\pm 10\%$ for membrane NP. The initial value is: $c_x = -0.98 \text{ mol/m}^3$.

For the membrane with larger pores, the NP membrane, the charge density has a stronger influence, i.e. the open membrane is more charge sensitive.

Nevertheless, the quality of the fit for the NP membrane (up to 12% difference between modeled and experimental retention) is lower than for the DK membrane (max. 3% difference between modeled and experimental retention). This is due to the membrane thickness, as will be the subject of further analysis in Section 7.6, where a better fit will be obtained by freely fitting more than one membrane parameter.

COMPLEX SOLUTION

Figure 75 and Figure 76 show the NP membrane's sensitivity towards the structural membrane parameters pore radius and active layer thickness, respectively.

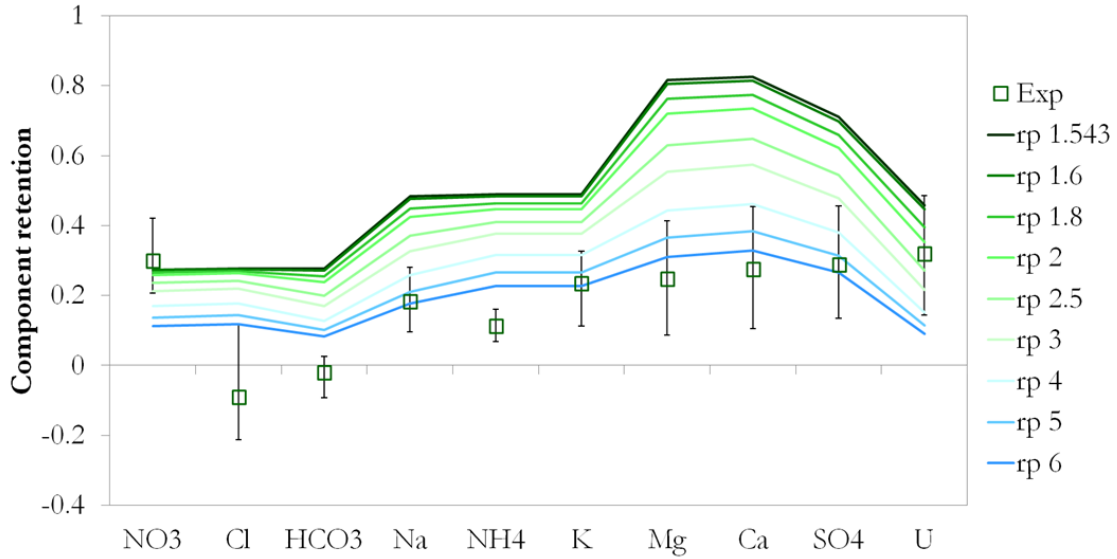


Figure 75: Complex solution – Sensitivity of modeled retentions towards membrane pore radius r_p for the NP membrane. The initial values are: $x = 15.26 \mu m$, $r_p = 1.543 nm$, $\epsilon_{rel} = 35$.

The pore radii which are necessary to reach the experimental rejection are much too large and they clearly fall in the range of ultrafiltration membranes. The membrane thickness has a strong influence for relatively thin membranes. Above a certain membrane thickness no influence can be observed at all. This appears to be realistic and could be subject to further research involving membranes of different thickness. However, concerning the here contemplated case membrane thickness has a significant influence and needs to be considered in order to reach an improved fit in Section 7.6.

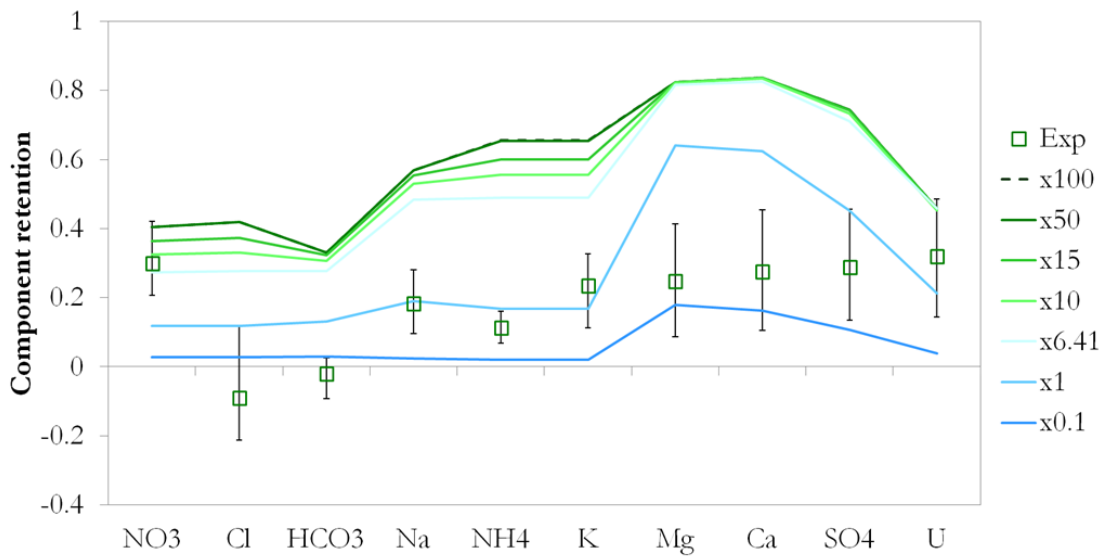


Figure 76: Complex solution – Sensitivity of modeled retentions towards membrane thickness x for the NP membrane. The initial values are: $x = 15.26 \mu m$, $r_p = 1.543 nm$, $\epsilon_{rel} = 35$.

According to Figure 76, a membrane with a thickness between 1 and 6 μm obtains the best selectivity. Increasing the membrane thickness beyond a certain point, e.g. 50 μm , will not have any significant influence on uranium retention. Electrical parameters were not capable of reaching a better fit as shown in Figure 55. However, as described in Section 4.2 the permittivity of the oriented layer of water molecules at the inner wall of the membrane's pores could be revisited. In all calculations above this parameter was kept at the value of 35. As will be shown in Section 7.6 a much better fit can be obtained when the parameter is optimized as well. The sensitivity of the modeled retention towards this parameter is significant as shown in Figure 77.

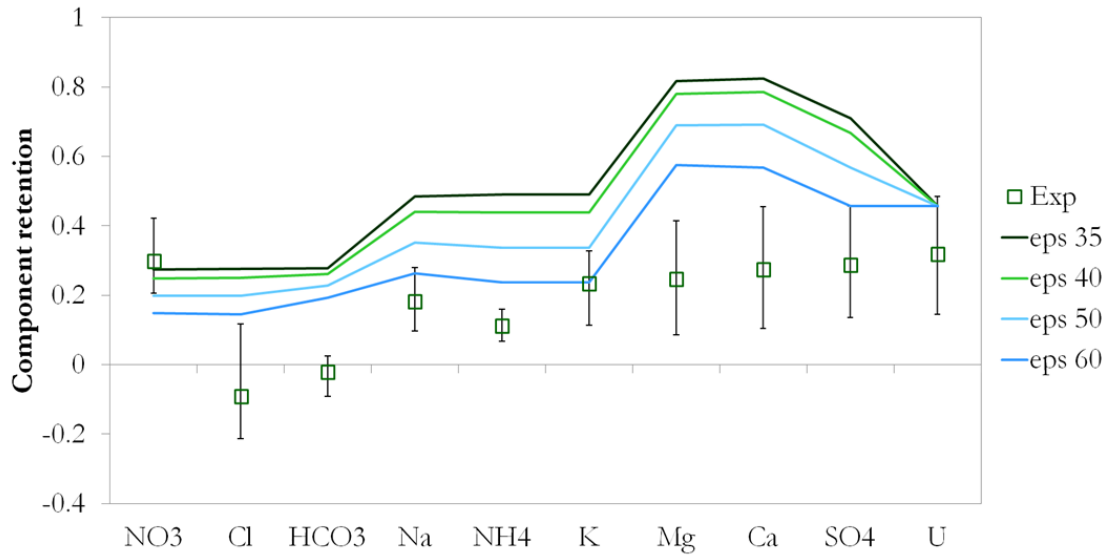


Figure 77: Complex solution – Sensitivity of modeled retentions towards the pore permittivity for the NP membrane. The initial values are: $x = 15.26 \mu\text{m}$, $r_p = 1.543 \text{ nm}$, $\epsilon_{rel} = 35$.

The quality of fit was dissatisfactory for the NP membrane and for the KCl and the complex solution. In the following section an improved fit will be developed by removing the restrictions of one parameter fitting.

The sensitivity towards the membrane's parameters was discussed in this section. Almost all sensitivities appear to be realistic, except the dependence on the pore radius for the NP membrane's retention of the 10 components. Furthermore, no single parameter can be used to reach a satisfactory quality of fit for the NP membrane and the KCl and 10 components solution. Hence a multi parameter fit will be approached in the next section.

7.6 Simultaneously fitting multiple parameters

The low quality of the fit for the NP membrane in the example shown in Figure 74 gives the incentive to approach a better agreement by fitting multiple model parameters at the same time. Fitting was performed as described in Section 4.10. The result of the improved fit is shown in Figure 78.

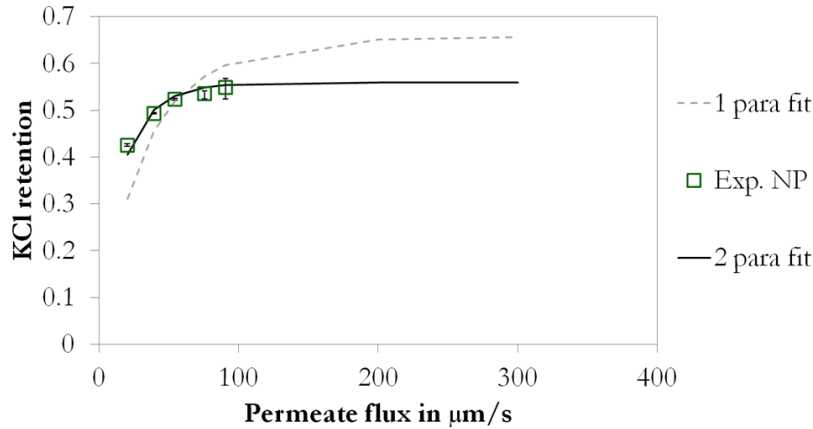


Figure 78: KCl – Improved fit for the NP membrane by keeping the membrane thickness and charge variable. The 1 parameter fit involved a variation of the membrane charge density only.

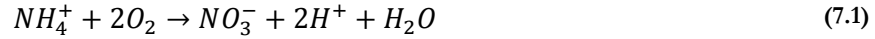
The agreement between modeled and experimental rejection is excellent. Notwithstanding this high quality of fit, the values of the fitted parameters need to be realistic as well. The values of the fitted parameters are shown in Table 23. The membrane thickness is relatively large, but still in a realistic range, as shown by membrane microscopy in Section 6.2. Furthermore, the decreased charge density results in a 50% decrease of the error relative to membrane DK as described at the end of Section 6.4. Both parameters are thus realistic and the fit can be accepted.

Table 23: KCl – Overview of membrane parameters which were used for the single and 2 parameter fit.

NP single parameter fit	Parameter	NP 2 parameter fit
$6.41 \cdot 10^{12} \cdot 1/m$	Relative Thickness $\Delta x_e / r_p^2$	$19 \cdot 10^{12} \cdot 1/m$
$15.26 \mu m$	Thickness Δx_e	$45.24 \mu m$
$-0.98 \text{ mol}/m^3$	Volume charge density c_x	$-0.5 \text{ mol}/m^3$
1.543 nm	Pore radius r_p	1.543 nm
35	Relative permittivity of the oriented water layer at the pore wall ϵ^*	35

A 4-parameter fitting of mine drainage was performed as described in Section 4.10. As shown in Figure 79 for the 10 component mine drainage the quality of fit was improved significantly. While in the 1 parameter fit only 2 modeled retentions were in some agreement with the experimental data, the picture was reversed for the 4 parameter fit.

In the 4 parameter fit the modeled retention was in disagreement only with the experimental retention of relatively unstable components: Nitrate, ammonium, and bicarbonate. Nitrification explains the large error for nitrate which can be produced by bacteria in the feed while such bacteria will be filtered out from the permeate thus creating an artificially high retention:



The bicarbonate can be formed by the dissolution of carbon dioxide which can enter the water samples since the facility is open towards the atmosphere. In the permeate the amount of dissolved substances is low and while the feed solution is in equilibrium with the atmosphere the permeate just exited the membrane and possesses a high potential to dissolve carbon dioxide from the air thus creating an artificially low retention.

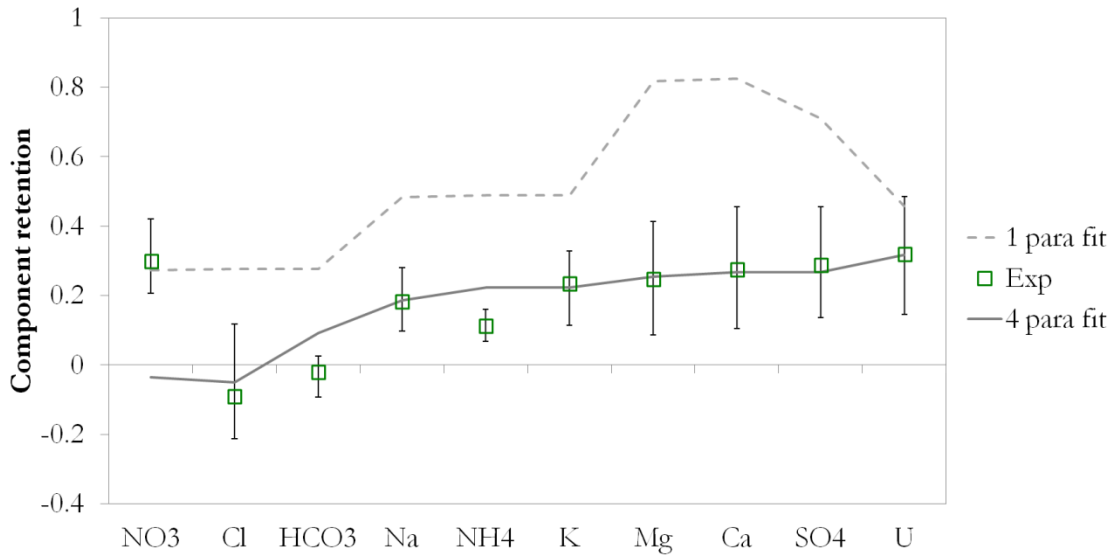


Figure 79: Multi-component solution – Improved fit by keeping the pore radius, membrane charge, membrane thickness, and pore permittivity variable. The 1 parameter fit involved a variation of the membrane charge density only.

Nevertheless, the quality of the fit is high and the values of the fitted parameters are worth inspection, as shown in Table 24. The membrane thickness is in excellent agreement with the value determined with the Hagen-Poiseuille equation. The volume charge density is in a realistic range concerning the solution's ionic strength. The pore radius is large but still realistic. The pore permittivity is below 80 thus a realistic value.

Table 24: multi-component solution – Overview of membrane parameters which were used for single and 4 parameter fit.

NP single parameter fit	Parameter	NP 4 parameter fit
$6.41 \cdot 10^{12} \cdot 1/m$	Relative Thickness $\Delta x_e / r_p^2$	$4 \cdot 10^{12} \cdot 1/m$
$15.26 \mu m$	Thickness Δx_e	$16 \mu m$
$-0.98 \text{ mol}/m^3$	Volume charge density c_x	$-60 \text{ mol}/m^3$
1.543 nm	Pore radius r_p	2 nm
35	Relative permittivity ϵ^*	71

Other authors described a relationship between the solution's composition and the permittivity. [Szymczyk2005] shows that a dielectric constant in the range between 60 and 70 is more realistic to describe observed retentions. [Oatley2012] obtains $\epsilon^* = 35$ for NaCl but $\epsilon^* = 74$ for MgSO₄. [Szymczyk2005], [Szymczyk2006], [Escoda2011], and [Silva2011] mention that even the membrane charge density can influence the value of ϵ^* .

An improved fit was obtained by fitting more than one membrane parameter. This result is not surprising, as described by [Bowen2002b] who criticized such an approach which basically converts all parameters into arbitrary fitting parameters. The approach was followed here nonetheless to show that the outcome are physically realistic values which could give a hint towards the reliability of the employed independent methods for membrane characterization. Further research is necessary in order to reconcile the conflicting approaches.

7.7 Linearity of the concentration gradient

Many authors approach the concentration gradient along the membrane as being constant. As shown in Figure 80 this assumption of a linear function is reasonable and describes the concentrations sufficiently well for most substances however a non-linear description is superior especially in case of uranium.

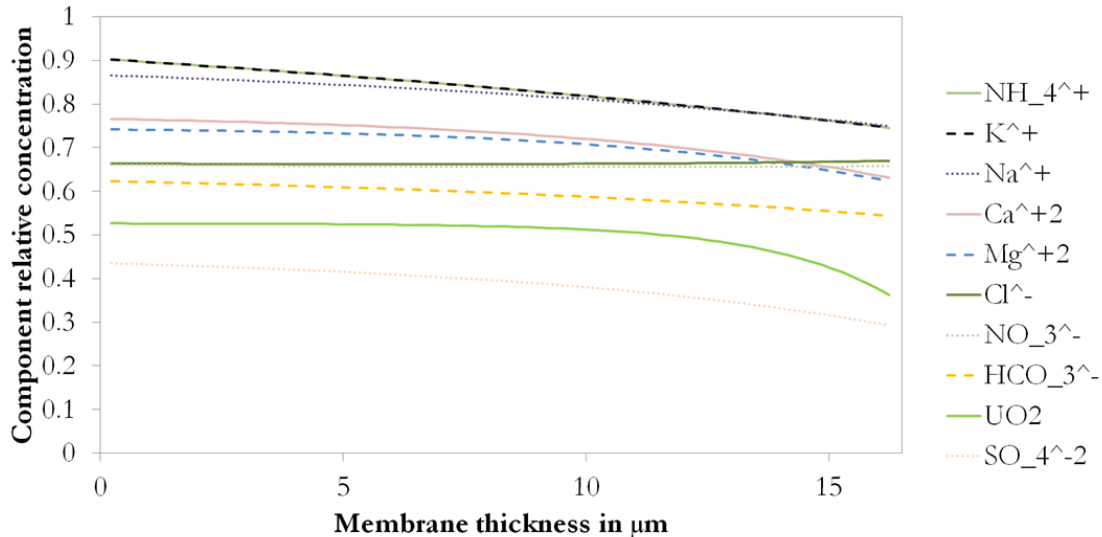


Figure 80: Concentrations of the 10 components along the membrane thickness relative to the feed concentration.

Generally, non-linearity occurs for uncharged solute and a thick membrane and thus the assumption of a linear concentration gradient does not always hold.

7.8 Discussion of separation phenomena inside the membrane

Access to the microscopic separation effects is a major advantage of the here developed mechanistic model. In this section a quantification of the separation processes, as suggested by the model, will be presented.

The separation processes inside the membrane are quantified during each simulation and will be automatically returned to the user via an Excel-output file. Here, such a quantification is presented along with the relevant equations.

PARTITIONING AT THE MEMBRANE SURFACES

Separation will occur due to effects inside the electrical double layer (EDL). This effect occurs on both sides of the membrane and is quantified by Equation (7.2).

$$\Phi_{EDL} = \frac{c_{bulk}}{c_{out}} \quad (7.2)$$

Figure 81 shows the quantified separation effect for the feed and permeate electrical double layer for each ion. A value of one, as in the case of the uncharged uranyl complex, refers to no electrostatic interaction, as would also be the case for an uncharged membrane. Since the membrane is negatively charged, all negative co-ions, e.g. chloride and sulfate, are repelled and Φ_{EDL} takes a negative sign with a magnitude depending on the charge of the membrane and the ion.

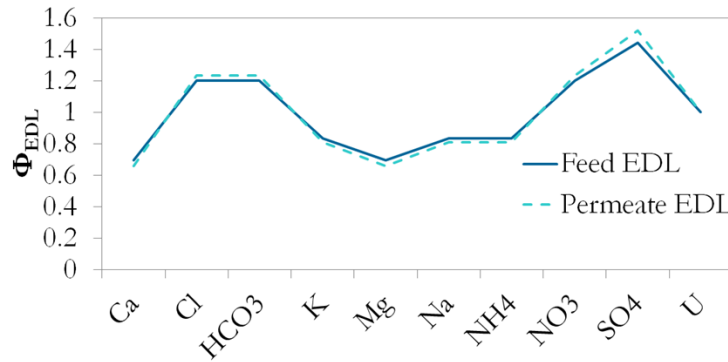


Figure 81: Partitioning due to the feed and permeate EDL for each of the 10 components of the solution.

Behind, the EDL, closer to the membrane surface, partitioning occurs due to the phase equilibrium. This type of partitioning was described in Section 4.7. Hence, the partitioning coefficients are used as described above. Their contribution to the total partitioning can be expressed by Equation (7.3).

$$\Phi_{activity} \cdot \Phi_{Donnan} \cdot \Phi_{Born} \cdot \Phi_{steric} = \frac{c_{in}}{c_{out}} \quad (7.3)$$

Figure 82 shows the resulting individual contributions of these effects for the feed solution/membrane interface in a quantified manner. As the diagram shows, steric effects limit ion passage for all ions depending on their size, with the strongest effect in case of the large uranium complex. Activity and Born effects occur nearly at the same quantity and are less important than the steric effects. Partitioning due to the Donnan effect plays a minor role in case of the feed solution/membrane interface.

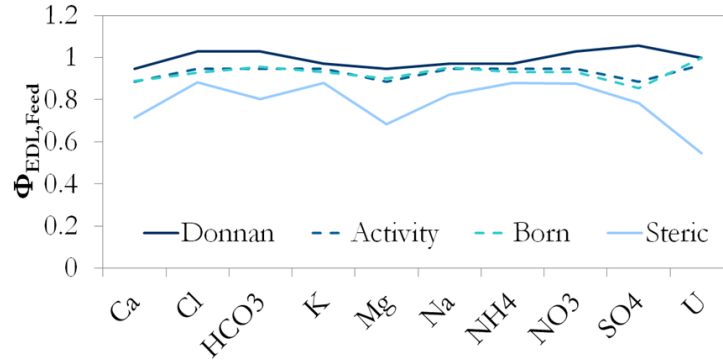


Figure 82: Quantified individual contributions to feed-side partitioning, due to Donnan, activity, Born, and steric effects.

Donnan partitioning is much more prominent for partitioning at the membrane/permeate solution interface, as shown in Figure 83. Here, the electrostatic effect dominates even over steric partitioning. The values of the other 3 contributions are close to the corresponding values on the feed side.

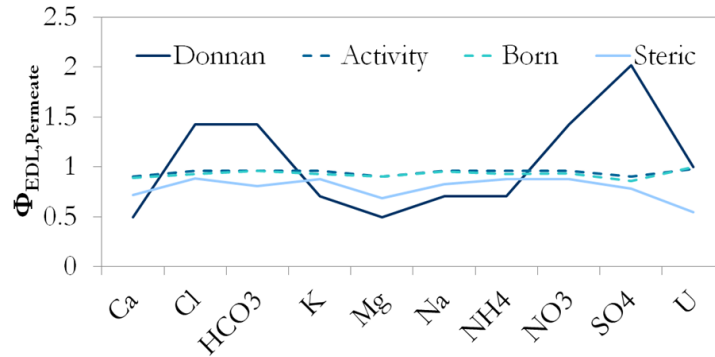


Figure 83: Quantified individual contributions to permeate-side partitioning, due to Donnan, activity, Born, and steric effects.

Quantification of separation effects can be accomplished by the here developed model. The influence increases in the following order (contributions in brackets, but ordered by the magnitude of difference from 1): electrical double layer polarization (0.99) < activity partitioning (0.94) < Born partitioning (0.93) < Donnan partitioning for positive ions (0.79) < steric partitioning (0.79) < Donnan partitioning for negative ions (1.30). Thus, for negatively charged ions the Donnan effect and for all other ions the steric effects are of highest importance. Future research can be aimed at comparison between the performances of different membranes at microscopic scale potentially in the framework of membrane modification.

8 Summary

The potential of nanofiltration modeling and simulation has been shown for uranium-contaminated mine drainage. The successful performance of a currently available and throughout the literature well-accepted model is encouraging to tackle remaining challenges such as the membrane characterization. Knowledge was extended for the complex processes during nanofiltration of uranium-contaminated real water samples.

On the one hand, nanofiltration of uranium-contaminated drainage from mine tailings represents a significant challenge to modeling and simulation since:

- The transport of a large number of components needs to be described in parallel including possible interactions of the components and including effects of chemical speciation.
- The considered specific case involves ions of strongly diverging properties such as, e.g. the extreme difference in charge and size between uranium and chloride.
- Contrary to conventional experiments with dilute synthetic solutions the mine drainage is highly concentrated and contains a plurality of trace elements.
- The multitude of components present in the solution potentially affect the membrane properties as well, e.g. by sorption to the membrane surface.

On the other hand, the studied example is of high scientific interest to explore the extent to which the currently available nanofiltration models are capable of describing the separation of real water samples, e.g. sea water or industrial waste water. Adding to this industrial relevance, the employed membranes were selected to represent a broad range of commercially available typical nanofiltration membranes.

The membranes were chosen by a membrane screening using KCl solution (ref. Figure 38) in order to cover the full range of typical nanofiltration membranes: The finely porous DK membrane and the rather open NP membrane. Membranes were characterized for their thickness, pore radius, and charge, i.e. the full set of parameters which are necessary for simulating the separation of an arbitrary solution.

In a separate experiment, the effect of speciation was successfully isolated and measured for the finely porous DK membrane and for the more open NP membrane. In case of the DK membrane the speciation effects were hidden behind the extremely high uranium retention. For the NP membrane a clear effect was observed which depended mainly on the size of the uranyl species. Hence, throughout the thesis, effects of speciation were included in the determination of size and charge of the uranium components.

The starting point of the modeling is a commonly used, well-accepted, and renowned model from the available set of models in the literature. The developed mechanistic model based on the Donnan-Steric partitioning Pore Model incorporating Dielectric Exclusion – DSPM&DE (ref. [Bowen2002b], [Bandini2003]) and the Steric, Electric, and Dielectric Exclusion model – SEDE (ref. [Szymczyk2005]) was selected since:

- This model is capable of describing multi-component transport.
- It is a mechanistic model with physically relevant parameters that can be determined in independent characterization experiments (membrane thickness – Section 6.2, pore radius – Section 6.3, membrane charge – Section 6.4)
- Further input parameters and constants required for the solution of the model are readily available from the literature (ref Table 3).

- The model is the best compromise between availability of input parameters and applicability to concentrated solutions. Strictly, only the Maxwell-Stefan approach is applicable to concentrated solutions.

The observed experimental retention for 10 components of the mine drainage was simulated in two ways:

- a) By a 1-parameter fit (fitting only the membrane charge while the remaining parameters were determined independently – ref. Section 6.6), and
- b) By a 4-parameter fit (fitting pore size, membrane thickness, and membrane charge, together with the permittivity – ref. Section 7.6)

Despite the high ionic strength of the mine drainage a good agreement between model and experiment was found by the 4-parameter fit. Furthermore, notwithstanding the free fitting, the 4 parameters do not take physically unrealistic values; a result which suggests that these parameters possess the said physical meaning and are not mere fitting parameters, thus, to some extent, justifying the models assumptions.

The 1-parameter fit did not agree as well as the 4-parameter fit, but is justified by the independent measurement of two of the parameters (membrane thickness – Section 6.2, pore radius – Section 6.3) and a literature survey for the permittivity. The 1-parameter fit can thus be seen as the state of the art.

The 1-parameter fit differed from the 4-parameter fit especially in the electric and dielectric parameters: a 60 times smaller membrane charge and half the permittivity (ref. Table 24). Thus, especially the electrical effects, which were not independently determined, seem to be not sufficiently well understood. This difference between the 1-parameter and the 4-parameter fit cannot be explained by experimental error alone, as has been shown in detail in Section 7.

In conclusion, the model was successful applied to broaden the field's knowledge on the complex phenomena during nanofiltration of uranium-contaminated real water samples. The thus developed model is a promising basis for further process design and optimization. The way is paved for modeling and experiment, e.g. for nanofiltration of other complex mine waters, waste waters, and complex aqueous industrial solutions of multi-ionic composition.

9 Outlook

In order to overcome the above mentioned limitations and to reach a better agreement between simulation and experiment the following changes are advisable.

First of all, a targeted study could resolve the question of the concentration dependency of the relative permittivity of the oriented water layer at the pore wall. The concentration as well as ionic composition of the solution inside the pores should be changed and the observed influence on the fitted relative permittivity could be analyzed in order to determine a potential dependency.

In order to arrive at a solution for membranes with a pore size smaller than any solute size a membrane with pores of different size should be implemented in the model. A pore size distribution could be included in a similar fashion as described by [Bowen2002]. In this publication the author describes clearly the advantages of a pore size distribution. Since the pore size characterization with neutral solute, e.g. glucose, is a reliable indicator, the model will return more realistic physical parameters and such contradictions as the lack of agreement between fitted charge and zeta potential measurements described in Section 6.4 can be resolved. Combination of mixtures of neutral solutes will be sufficient to determine even very complicated pore size distributions.

[Sievertsen2001 page 35] mentions that the flux at high salt concentrations decreases due to osmotic pressure and increased viscosity. This influence on viscosity was not taken into account in this work and is recommended to be investigated in further studies because it offers further insight into the mechanisms that are important for nanofiltration.

The question that was approached in Section 6.2, whether the support layer influences transport through nanofiltration membranes could be revisited by a collaboration with membrane manufacturers who could provide the unfinished membrane which is not covered with the active layer yet. Thereby this question could be conclusively resolved.

Hydration effects are critical as the diameter of the pores of nanofiltration membranes is in the range of one nanometer which is approximately the size of three water molecules [EMST2013 page 1276]. An important question is also the extent of ion hydration inside the nanopores as addressed by [Richards2013]. Experiments with other ions which exhibit different speciation and hydration properties could improve understanding of these steric effects.

Currently not included effects could be implemented, such as the dispersion forces described by [Szymczyk2005], which could lead to a lowered interaction energy barrier. However this influence has been shown to be low compared to the effect of dielectric exclusion.

As shown in this thesis, such refinements are worthwhile considering the already considerable precision of the model at its current state.

10 References

- [Afonso1998] Afonso, Maria Dina; de Pinho, Maria Norberta: Mass Transfer Modeling for Salt Transport in Amphoteric Nanofiltration Membranes. *Ind. Eng. Chem. Res.* 37, (1998) 4118-4127.
- [Anderson1974] Anderson, John L.; Quinn, John A.: Restricted transport in small pores - a model for steric exclusion and hindered particle motion. *Biophysical journal*, Vol. 14 (1974) pp. 130-150.
- [Bai2009] Bai, Jing; Liu, Chongxuan; Ball, William P.: Study of Sorption-Retarded U(VI) Diffusion in Hanford Silt/Clay Material. *Environ. Sci. Technol.*, 43 (2009) pp. 7706-7711.
- [Baker2004] Baker, Richard W. (2004): *Membrane Technology and Applications*. Chichester: John Wiley & Sons Ltd.
- [Bandini2003] Bandini, Serena; Vezzani, Daniele (2003): Nanofiltration modeling: the role of dielectric exclusion in membrane characterization. In: *Chemical Engineering Science* (58), S. 3303–3326.
- [Banks1966] Banks, W.; Sharples, A.: Studies on desalination by reverse osmosis. *J. appl.chem.* Vol.16 (1966) pp. 153-158.
- [Barthel1998] Barthel, J. M. G.; Krienke, H.; Kunz, W. (1998): *Physical Chemistry of Electrolyte Solutions*. Darmstadt: Steinkopff Verlag.
- [Bhattacharya1992] Bhattacharya D., Williams M.E.: Part VI—Reverse osmosis, Chapter 22: Theory. In: Ho WSW, Sirkar KK, (eds.): *Membrane Handbook*. New York: Van Nostrand Reinhold (1992) 269-280.
- [Bird2002] Bird R. B., Stewart W. E., Lightfoot E. N. (2002): *Transport Phenomena*. 2nd Edition. New York: Wiley.
- [Beleites1992] Beleites, Michael (1992): *Altlast Wismut. Ausnahmezustand, Umweltkatastrophe und das Sanierungsproblem im deutschen Uranbergbau*. 1. Aufl. Frankfurt am Main: Brandes und Apsel.
- [Belfort1976] Belfort, G.: A molecular friction model for transport of uncharged solutes in neutral hyperfiltration and ultrafiltration membranes containing bound water. *Desalination*, 18(3), (1976) 259-281
- [Berg1989] van den Berg, G.B.; Racz, I.G.; Smolders, C.A.: Mass transfer coefficients in cross-flow ultrafiltration. *Journal of membrane science*, 47 (1989) pp. 25-51.
- [Bernhard2005] Bernhard, Gert (2005): Speciation of uranium in environmental relevant compartments. In: *Landbauforschung Völkenrode* 55 (3), S. 139–148.
- [Bernhardt2015] Bernhardt, Claudia (2015): *Charge characterization of nanofiltration membranes*. Master's thesis at the ITUN, TU Bergakademie Freiberg.
- [Bessarabov2002] Bessarabov, Dmitri; Twardowski, Zbigniew (2002): Industrial application of nanofiltration – new perspectives. *Membrane Technology, Feature*. pp. 6-9.
- [Born1920] Born, M.: Volumen und Hydratationswärme der Ionen. *Zeitschrift für Physik*, Heft 1 (1920) pp.45-48.

- [Bosshard1992] Bosshard, E.; Zimmerli, B.; Schlatter, Ch (1992): Uranium in the Diet: Risk Assessment of its Nephro- and Radiotoxicity. In: *Chemosphere* (24), S. 309–322.
- [Boussu2006] Boussu, K.; Zhang, Y.; Cocquyt, J.; van der Meeren, P.; Volodin, A.; van Haesendonck, C. et al. (2006): Characterization of polymeric nanofiltration membranes for systematic analysis of membrane performance. In: ISSN: 0376-7388.
- [Bowen1994] Bowen, Richard W.; Sharif, Adel O.: Transport through microfiltration membranes – particle hydrodynamics and flux reduction. *Journal of Colloid and Interface Science* 168 (1994) pp. 414-421.
- [Bowen1996] Bowen, W. Richard; Mukhtar, Hilmi: Characterisation and prediction of separation performance of nanofiltration membranes. *Journal of Membrane Science* 112 (1996) 263-274
- [Bowen1997] Bowen, W. Richard; Mohammad, A. Wahab; Hilal, Nidal: Characterisation of nanofiltration membranes for predictive purposes - use of salts, uncharged solutes and atomic force microscopy. *Journal of Membrane Science* 126 (1997) 91-105.
- [Bowen1998] Bowen, W.R.; Mohammad, A.W.: Characterization and prediction of nanofiltration membrane performance - a general assessment. *Trans icheme*, Vol. 76, part A (1998) 885-893.
- [Bowen1998a] Bowen, W. Richard; Mohammad, A. Wahab: Diafiltration by nanofiltration: prediction and optimization. *AIChE journal*, vol. 44, no. 8 (1998) 1799-1812
- [Bowen1998b] Bowen, W. Richard; Mohammad, A. Wahab: Theoretical basis for specifying nanofiltration membranes - Dye/salt/water streams. *Desalination* 117 (1998) 257-264.
- [Bowen2002] Bowen, W. Richard; Welfoot, Julian S. (2002): Modelling of membrane nanofiltration—pore size distribution effects. In: *Chemical Engineering Science* (57), pp. 1393–1407.
- [Bowen2002b] Bowen, Richard W.; Welfoot, Julian S.: Modelling the performance of membrane nanofiltration—critical assessment and model development. *Chemical Engineering Science* 57 (2002) 1121 – 1137
- [Bowen2004] Bowen, W.R.; Cassey, B.; Jones, P.; Oatley, D.L.: Modelling the performance of membrane nanofiltration—application to an industrially relevant separation. *J. Membr. Sci.* 242 (2004) 211–220.
- [Bowen2009] Bowen, W. Richard; Hilal, Nidal (2009): Atomic force microscopy in process engineering. An introduction to AFM for improved processes and products. 1. Aufl. Amsterdam: Elsevier/Butterworth-Heinemann (Butterworth-Heinemann / IChemE series). Online verfügbar unter <http://site.ebrary.com/lib/alltitles/docDetail.action?docID=10329436>.
- [Brenner1977] Brenner, H.; Gaydos, L. J. (1977): The constrained brownian movement of spherical particles in cylindrical pores of comparable radius. models of the diffusive and convective transport of solute molecules in membranes and porous media. *Journal of Colloid and Interface Science*, 58(2), 312-356.
- [Bromley1973] Bromley, Leroy A.: Thermodynamic properties of strong electrolytes in aqueous solutions. *AIChE Journal*, Vol. 19, No. 2 (1973) pp. 313-320.

- [Bruggen1999] Van der Bruggen, B.; Schaep, J.; Wilms, D.; Vandecasteele, C.: Influence of molecular size, polarity and charge on the retention of organic molecules by nanofiltration. *Journal of Membrane Science* 156 (1999) 29-41.
- [Bruggen2002] van der Bruggen, B.; Vandecasteele, Carlo (2002): Modelling of the retention of uncharged molecules with nanofiltration. In: *Water Research* (36), S. 1360–1368.
- [Bungay1973] Bungay, P. M.; Brenner, H. (1973): The motion of a closely-fitting sphere in a fluid-filled tube. *Int. Jnl. Multiphase Flow*, 1(1)
- [Busby2008] Busby, C. (2008): Advanced biochemical and biophysical aspects of uranium contamination. In: Luit J. de Kok (Hg.): *Loads and fate of fertilizer derived uranium*. Leiden, Weikersheim: Backhuys; Margraf, S. 11–22.
- [Carvalho2011] Carvalho, A.; Maugeri, F.; Silva, V.; Hernández, A.; Palacio, L.; Pradanos, P.: AFM analysis of the surface of nanoporous membranes: Application to the nanofiltration of potassium clavulanate. *Journal of Materials Science* 46 (2011) pp. 3356-3369.
- [Chen1992] Chen, Yun; Chu, Min-Lin; Shieh, Mu-Chang (1992): pH Effect on the Separation of Uranium Fluoride Effluents by the Reverse Osmosis Process. In: *Separation Science and Technology* 27 (5), S. 557–571
- [Chronik]: Wismut GmbH: „Die Chronik der Wismut“ internal document 2013. Chemnitz.
- [De1997] De S.; Bhattacharya P.K.: Prediction of mass-transfer coefficient with suction in the applications of reverse osmosis and ultrafiltration. *Journal of Membrane Science* 128 (1997) 119-131.
- [Dechadilok2006] Dechadilok, Panadda; Deen, William M.: Hindrance factors for diffusion and convection in pores. *Ind. Eng. Chem. Res.*, 45 (2006) pp. 6953-6959.
- [Deen1987] Deen, W.M.: Hindered transport of large molecules in liquid-filled pores. *AIChE Journal*, Vol. 33, No. 9 (1987) pp. 1409-1425.
- [Donnan1995] Donnan, Frederick George: Theory of membrane equilibria and membrane potentials in the presence of non-dialysing electrolytes. A contribution to physical-chemical physiology. *Journal of Membrane Science* 100 (1995) pp. 45-55.
- [Dresner1972] Dresner, Lawrence: Stability of the extended Nernst-Planck equations in the description of hyperfiltration through ion-exchange membranes. *The journal of physical chemistry*, Vol.76, No 16 (1972) 2256-2267
- [Dresner1972ENP] Dresner, Lawrence: Some remarks on the integration of the extended Nernst-Planck equations in the hyperfiltration of multicomponent solutions. *Desalination* 10 (1972) 27-46.
- [Dukhin2012] Dukhin, A.S; Parlia, S. (2012): Studying homogeneity and zeta potential of membranes using electroacoustics. In: *Journal of Membrane Science* (415), S. 587–595.
- [Ekiner2006] Okan Ekiner, John Simmons (2006): Novel separation membrane made from blends of polyimide with polyamide or polyimide-amide polymers. Patent publication number US 20060156920.

- [EMST2013] Hoek, Eric M.V.; Tarabara, Volodymyr V. (2013): Encyclopedia of membrane science and technology. Hoboken, New Jersey: John Wiley & Sons.
- [Ennis1996] Ennis, J.; Zhang, H.; Stevens, G.; Perera, J.; Scales, P.; Carnie, S.: Mobility of protein through a porous membrane. *Journal of Membrane Science* 119 (1996) pp. 47-58.
- [Eriksson1988] Eriksson, Peter (1988): Nanofiltration Extends the Range of Membrane Filtration. *Environmental Progress* (Vol. 7, No. 1)
- [Escoda2011] Escoda, Aurélie; Déon, Sébastien; Fievet, Patrick: Assessment of dielectric contribution in the modeling of multi-ionic transport through nanofiltration membranes. *Journal of Membrane Science* 378 (2011) 214– 223.
- [Evans1955] Evans, Robley D. (1955): The atomic nucleus. New York, NY: McGraw-Hill (International series in pure and applied physics).
- [Fair1971] Fair, J.C.; Osterle, J.F.: Reverse electrodialysis in charged capillary membranes. *The journal of chemical physics*, vol. 54, no. 8 (1971) pp. 3307-3316.
- [Favre-Réguillon2008] Favre-Réguillon, A.; Lebusit, G.; Murat, D.; Foos, J.; Mansour, C.; Draye, M. (2008): Selective removal of dissolved uranium in drinking water by nanofiltration. In: *Water Research* 42 (4-5), S. 1160–1166.
- [Fernández1997] Fernández, D. P.; Goodwin, A. R. H.; Lemmon, Eric W.; Sengers, J. M. H. Levelt; Williams, R. C.: A Formulation for the Static Permittivity of Water and Steam at Temperatures from 238 K to 873 K at Pressures up to 1200 MPa, Including Derivatives and Debye–Hückel Coefficients. *Journal of Physical and Chemical Reference Data* 26, (1997) pp. 1125-1166
- [Fievet2002] Fievet, P.; Labbez, C.; Szymczyk, A.; Vidonne, A.; Foissy, A.; Pagetti, J.: Electrolyte transport through amphoteric nanofiltration membranes. *Chemical Engineering Science* 57 (2002) 2921 – 2931
- [Foley2013] Foley, Greg (2013): Membrane Filtration. A Problem Solving Approach with MATLAB®. Cambridge: Cambridge university press.
- [Frindrik1986] Frindrik, O. „Uran in Böden, Pflanzen und Lebensmitteln“, *Landwirtsch. Forschung* 39, 1-2, 1986
- [Garcia-Aleman2004] Garcia-Aleman, Jesus; Dickson, James M. (2004): Mathematical modeling of nanofiltration membranes with mixed electrolyte solutions. In: *Journal of Membrane Science* 2004 (235), S. 1–13.
- [Gauwbergen1997] Van Gauwbergen, D.; Baeyens, J.; Creemers, C.: Modeling osmotic pressures for aqueous solutions for 2-1 and 2-2 electrolytes. *Desalination* 109 (1997) 57-65.
- [Gekas1988] Gekas V., Olund K.: Mass transfer in the membrane concentration polarization layer under turbulent cross flow. II. Application to the characterization of ultrafiltration membranes. *Journal of Membrane Science* 37 (1988) 145-163.
- [Geraldes2006] Geraldes, Vitor; Afonso, Maria Dina: Generalized mass-transfer correction factor for nanofiltration and reverse osmosis. *AIChE journal*, Vol. 52, No. 10 (2006) pp. 3353-3362.

- [Geraldes2007] Geraldes, Vitor; Afonso, Maria Dina: Prediction of the concentration polarization in the nanofiltration/reverse osmosis of dilute multi-ionic solutions. *Journal of Membrane Science* 300 (2007) 20–27.
- [Giddings2005] Giddings, M.; Fawell, J. (2005): Uranium in Drinking-water. Background document for development of WHO Guidelines for Drinking-water Quality. World Health Organization (WHO/SDE/WSH/03.04/118).
- [Glueckauf1965] Glueckauf, E. (1967): Proceeding of the first international symposium on water desalination. Washington DC, Vol. 1, pp. 143.
- [Grathwohl1998] Grathwohl, Peter (1998): Diffusion in Natural Porous Media. Contaminant Transport, Sorption/Desorption and Dissolution Kinetics. Boston: Kluwer Academic Publishers.
- [Graziani1972] Graziani, R.; Bombieri, G.; Forsellini, E. (1972): *Journal of the Chemical Society, London. Dalton transactions*. Crystal structure of tetra-ammonium uranyl tricarbonat. London: Royal Society of Chemistry.
- [Gross1968] Gross, R.J.; Osterle, J.F.: Membrane transport characteristics of ultrafine capillaries. *The journal of chemical physics*, vol. 49, no. 1 (1968) pp. 228-234.
- [Guillaumont2003] Guillaumont, F.T.; Fuger, J.; Grenthe, I.; Neck, V.; Palmer, D.A.; Rand, M.H. (2003): Update on the Chemical Thermodynamics of Uranium, Neptunium, Plutonium, Americium and Technetium. Amsterdam: Elsevier.
- [Gupta2007] Gupta, Vineet K.; Hwang, Sun-Tak; Krantz, William B.; Greenberg, Alan R.: Characterization of nanofiltration and reverse osmosis membrane performance for aqueous salt solutions using irreversible thermodynamics. *Desalination* 208 (2007) 1–18.
- [Hagmeyer1999] Hagmeyer, G.; Gimbel, R. (1999): Modelling the rejection of nanofiltration membranes using zeta potential measurements. In: *Separation and Purification Technology* (15), S. 19–30.
- [Hassoun2011] Hassoun, Rula (2011): A statistical evaluation of the contribution of mineral and tap water to the dietary intake of As, B, Cu, Li, Mo, Ni, Pb, U and Zn by humans. Dissertation. Fakultät für Lebenswissenschaften der Technischen Universität Carolo-Wilhelmina zu Braunschweig.
- [Higdon1995] Higdon, J. J. L.; Muldowney, G. P. (1995): Resistance functions for spherical particles, droplets and bubbles in cylindrical tubes. *Journal of Fluid Mechanics*, 298, 193-210.
- [Hoffer1972] Hoffer, E.; Kedem, O.: Hyperfiltration in charged membranes - Prediction of salt rejection from equilibrium measurements. *The journal of physical chemistry*, vol. 76, no. 24 (1972) pp. 3638-3641.
- [Huber2009] Huber, M. L.; Perkins, R. A.; Laesecke, A.; Friend, D. G.; Sengers, J. V.; Assael, M. J.; Metaxa, I. N.; Vogel, E.; Mareš, R.; Miyagawa, K.: New International Formulation for the Viscosity of H₂O. *J. Phys. Chem. Ref. Data*, Vol. 38, No. 2 (2009) pp. 101-125.
- [Hussain2007] Hussain, A.A.; Abashar, M.E.E.; Al-Mutaz, I.S.: Influence of ion size on the prediction of nanofiltration membrane systems. *Desalination* 214 (2007) 150–166

- [Jacazio1972] Jacozio, G.; Probst, R.F.; Sonin, A.A.; Yung, D.: Electrokinetic salt rejection in hyperfiltration through porous materials - theory and experiment. *The journal of physical chemistry*, vol. 76, no. 26 (1972) pp. 4015-4023
- [Kedem1958] Kedem, O.; Katchalsky, A.: Thermodynamic analysis of the permeability of biological membranes to non-electrolytes. *Biochimica et biophysica acta* 27 (1958) 229-246.
- [Kerisit2010] Kerisit, Sebastien; Liu, Chongxuan: Molecular simulation of the diffusion of uranyl carbonate species in aqueous solution. *Geochimica et Cosmochimica Acta* 74 (2010) pp. 4937-4952.
- [Khedr2013] Khedr, M. Gamal (2013): Radioactive contamination of groundwater, special aspects and advantages of removal by reverse osmosis and nanofiltration. In: *Desalination* 321, S. 47–54.
- [Kirby2010] Kirby, Brian J. (2010): *Micro-and Nanoscale Fluid Mechanics. Transport in Microfluidic Devices*. Cambridge University Press: New York.
- [Knolle2009] Knolle, Friedhart (2009): *Ein Beitrag zu Vorkommen und Herkunft von Uran in deutschen Mineral- und Leitungswässern*. Zugl.: Braunschweig, Technische Universität, Diss., 2008.
- [Kortum1941] Kortüm, Gustav (1941): *Elektrolytlösungen*. Leipzig: Becker & Erler .
- [Krishna1997] Krishna, R.; Wesselingh, J.A.: The Maxwell-Stefan approach to mass transfer. *Chemical engineering science*, vol. 52, no. 6 (1997) pp. 861-911.
- [Labbez2003] Labbez, C.; Fievet, P.; Szymczyk, A.; Vidonne, A.; Foissy, A.; Pagetti, J. (2003): Retention of mineral salts by a polyamide nanofiltration membrane. In: *Separation and Purification Technology* (30), S. 47–55.
- [Lee1999] Lee, Ming; Chan, Kwong-Yu; Nicholson, David; Zara, Stephen: Deviation from electroneutrality in cylindrical pores. *Chemical Physics Letters* 307 (1999) 89–94.
- [Levenstein1996] Levenstein, R.; Hasson, D.; Semiat, R.: Utilization of the Donnan effect for improving electrolyte separation with nanofiltration membranes. *Journal of Membrane Science* 116 (1996) 77-92
- [Lewis1924] Lewis, W.K.; Whitman, W.G.: *Principles of gas absorption*. Industrial and engineering chemistry, Vol. 16, No. 12 (1924) pp. 1215-1220.
- [Lide2005] Lide, David R. (2005): *Handbook of Chemistry and Physics*. 86th Edition. Boca Raton: CRC Press.
- [Lo1998] Lo, W.Y.; Chan, K.Y.; Lee, M.; Mok, K.L.: Molecular simulation of electrolytes in nanopores. *Journal of Electroanalytical Chemistry* 450 (1998) 265–272.
- [Luckas2001] Luckas, Michael; Krissmann, Jörg (2001): *Thermodynamik der Elektrolytlösungen – Eine einheitliche Darstellung der Berechnung komplexer Gleichgewichte*. Berlin: Springer-Verlag.
- [Malone1977] Malone, Dermot M.; Anderson, John L.: Diffusional boundary-layer resistance for membranes with low porosity. *AIChE journal*, Vol. 23, No. 2 (1977) pp. 177-184.

- [Marx1976] Marx, G.; Bischoff, H.: Transport processes of actinides in electrolyte solutions. I. Determination of ionic mobilities of uranium in aqueous solution at 25°C by the radioisotope method. *Journal of Radioanalytical Chemistry*, Vol. 30 (1976) pp. 567-581.
- [Matsumoto2005] Matsumoto, Hidetoshi; Chen, Yu-Chiang; Yamamoto, Ryotaro; Konosu, Yuichi; Minagawa, Mie; Tanioka, Akihiko (2005): Membrane potentials across nanofiltration membranes: effect of nanoscaled cavity structure. In: *Journal of Molecular Structure* (739), S. 99–104.
- [Mavrovouniotis1986] Mavrovouniotis, G.M.; Brenner, H. (1986): Hindered Sedimentation and dispersion coefficients for rigid, closely fitting Brownian spheres in circular cylindrical pores containing quiescent fluids. Paper no. 85b, AIChE Ann. Meet., Miami
- [Melin2007] Melin, Thomas; Rautenbach, Robert (2007): *Membranverfahren. Grundlagen der Modul- und Anlagenauslegung*. Berlin: Springer-Verlag.
- [Merkel2002] Merkel, Broder J. (2002): Uran im Trink- und Mineralwasser. Online at http://www.cut-os.de/downloads/Vortrag_Merkel_internet.pdf, on the 28.10.2013.
- [Merkel2006] Merkel, Broder J.; Hasche-Berger, Andrea (2006): *Uranium in the Environment. Mining Impact and Consequences*. Berlin, Heidelberg: Springer-Verlag Berlin Heidelberg. Available online at unter <http://site.ebrary.com/lib/alltitles/docDetail.action?docID=10228904>.
- [Merkel2012] Merkel, Broder; Schipek, Mandy (2012): *The new uranium mining boom. Challenge and lessons learned*. Berlin: Springer (Earth sciences).
- [Merkel2013] Merkel, Broder J.; Planer-Friedrich, Britta; Wolkersdorfer, Christian (2013): *Uranium in the Aquatic Environment. Proceedings of the International Conference Uranium Mining and Hydrogeology III and the International Mine Water Association Symposium Freiberg*, Germa: Springer Verlag.
- [Metschies2013] Thomas Metschies, Jan Laubrich, Jürgen Müller, Michael Paul, Ulf Barnekow (2013): Management of water collection and treatment in the remediation process of an uranium mill tailings site. *Proceedings of the IMWA Conference 2013, At Golden, CO., USA*, pp. 1047-1053.
- [Meyer1936] Meyer, Kurt H.; Sievers, J.-F.: La perméabilité des membranes I - Théorie de la perméabilité ionique. *Helvetica Chimica. Acta*, V. 19 (1936) pp. 649-664
- [Michaels1968] Michaels, A.S.: New separation technique for the CPI. *Chemical Engineering Progress*, 64 (1968) 31-43.
- [Montana2013] Montana, M.; Camacho, A.; Serrano, I.; Devesa, R.; Matia, L.; Vallés, I. (2013): Removal of radionuclides in drinking water by membrane treatment using ultrafiltration, reverse osmosis and electrodialysis reversal. In: *Journal of Environmental Radioactivity* (125), S. 86–92.
- [Mohammad2003] Mohammad, Abdul Wahab; Takriff, Mohd Sobri: Predicting flux and rejection of multicomponent salts mixture in nanofiltration membranes. *Desalination* 157 (2003) pp. 105-111.
- [Morrison1965] Morrison, F.A.; Osterle, J.F.: Electrokinetic energy conversion in ultrafine capillaries. *The journal of chemical physics*, vol. 43 no. 6 (1965) 2111-2115.

- [Mulder1996] Mulder, M. (1996): Basic Principles of Membrane Technology. Kluwer Academic Publishers: Dordrecht.
- [Nakao1981] Nakao, Shin-ichi; Kimura, Shoji: Analysis of solutes rejection in ultrafiltration. Journal of chemical engineering of Japan Vol. 14 No. 1 (1981) 32-37
- [Nightingale1959] E.R. Nightingale Jr.: Phenomenological theory of ion solvation. Effective radii of hydrated ions. J. Phys. Chem. Vol. 63 (1959) 1381-1387.
- [NIST2011] National Institute of Standards and Technology (2011): The NIST Reference on Constants, Units, and Uncertainty. Online verfügbar unter <http://physics.nist.gov/cuu/index.html>.
- [Nitsche1994] Nitsche, Johannes M.; Balgi, Ganesh: Hindered Brownian diffusion of spherical solutes within circular cylindrical pores. Ind. Eng. Chem. Res. 33 (1994) pp. 2242-2247.
- [Noordman2002] Noordman, T.R.; Wesselingh, J.A.: Transport of large molecules through membranes with narrow pores - the Maxwell-Stefan description combined with hydrodynamic theory. Journal of Membrane Science 210 (2002) pp. 227-243.
- [Oatley2012] Oatley, Darren L.; Llenas, Laia; Pérez, Ramon; Williams, Paul M.; Martínez-Lladó, Xavier; Rovira, Miquel: Review of the dielectric properties of nanofiltration membranes and verification of the single oriented layer approximation. Advances in Colloid and Interface Science 173 (2012) 1–11.
- [Oatley2013] Oatley, Darren L.; Llenas, Laia; Aljohani, Nasser H.M; Williams, Paul M.; Martinez-Llado, Xavier; Rovira, Miquel; Pablo, Joan de (2013): Investigation of the dielectric properties of nanofiltration membranes. In: Desalination (315), S. 100–106.
- [Oatley2014] Oatley-Radcliffe, Darren L.; Williams, Steffan R.; Barrow, Matthew S.; Williams, Paul M.: Critical appraisal of current nanofiltration modelling strategies for seawater desalination and further insights on dielectric exclusion. Desalination 343 (2014) 154–161.
- [Onsager1932] Onsager, Lars; Fuoss, Raymond: Irreversible processes in electrolytes, diffusion, conductance, and viscous flow in arbitrary mixtures of strong electrolytes. Journal of physical chemistry (1932) 2689-2778
- [Parkhurst1999] Parkhurst, David L.; Appelo, C.A.J.: User's Guide to PHREEQC (Version 2)--A Computer Program for Speciation, Batch-Reaction, One-Dimensional Transport, and Inverse Geochemical Calculations. http://wwwbrr.cr.usgs.gov/projects/GWC_coupled/phreeqc/html/final.html
- [Paul2011] Paul, Michael (2011): Nachhaltigkeit und Langzeitaspekte bei der Sanierung von Uranbergbau- und Aufbereitungsstandorten. Proceedings des Internationalen Bergbausymposiums WISSYM_2011 ; Ronneburg, 25. - 27. Mai 2011. Chemnitz.
- [Persson2010] Persson, Ingmar: Hydrated metal ions in aqueous solution: How regular are their structures? Pure Appl. Chem., Vol. 82, No. 10 (2010) pp. 1901–1917.
- [Prabhakar1992] Prabhakar, S.; Panicker, Saly T.; Misra, B. M.; Ramani, M. P. S. (1992): Studies on the Reverse Osmosis Treatment of Uranyl Nitrate Solution. In: Separation Science and Technology 27 (3), S. 349–359

- [Prabhakar1996] Prabhakar, S.; Balasubramaniyan, C.; Hanra, M. S.; Misra, B. M.; Roy, S. B.; Meghal, A. M.; Mukherjee, T. K. (1996): Performance Evaluation of Reverse Osmosis (RO) and Nanofiltration (NF) Membranes for the Decontamination of Ammonium Diuranate Effluents. In: Separation Science and Technology 31 (4), S. 533–544.
- [Raff1999] Raff, Oliver; Wilken, Rolf-Dieter (1999): Removal of dissolved uranium by nanofiltration. In: Desalination 122 (2-3), S. 147–150.
- [Rashin1985] Rashin, Alexander A.; Honig, Barry: Reevaluation of the Born model of ion hydration. J. Phys. Chem. 89 (1985) pp. 5588-5593.
- [Renkin1954] Renkin, Eugene M.: Filtration, diffusion, and molecular sieving through porous cellulose membranes. The Journal of General Physiology, November 20 (1954) pp. 225-243.
- [Sastri1976] Sastri, V. S.; Ashbrook, A. W. (1976): Reverse Osmosis Performance of Cellulose Acetate Membranes in the Separation of Uranium from Dilute Solutions. In: Separation Science 11 (4), S. 361–376
- [Schaep1999] Schaep, Johan; Vandecasteele, Carlo; Mohammad, Wahab; Bowen, Richard: Analysis of the salt retention of nanofiltration membranes using the Donnan-steric partitioning pore model. Separation science and technology, 34/15 (1999) pp. 3009-3030
- [Schaep2001] Schaep, Johan; Vandecasteele, Carlo; Mohammad, Wahab; Bowen, Richard: Modelling the retention of ionic components for different nanofiltration membranes. Separation and Purification Technology 22-23 (2001) 169–179
- [Schaep2001a] Schaep, Johan; Vandecasteele, Carlo: Evaluating the charge of nanofiltration membranes. Journal of Membrane Science 188 (2001) 129–136
- [Schäfer2006] Schäfer, A.I.; Fane, A.G.; Waite, T.D. (2006): Nanofiltration: Principles and applications. Elsevier: Oxford, New York.
- [Schlögl1956] Schlögl, R.: The significance of convection in transport processes across porous membranes. Discussions of the Faraday Society, 21 (1956) pp. 46-52.
- [Schlögel1964] Schlögl, R. (1964): Stofftransport durch Membranen. Darmstadt: Steinkopff Verlag.
- [Schlogl1967] Schlögl, R. (1967): General Aspects of the transport of matter across non-semipermeable membranes. pp. 288-291. In: Frascati, June 15–18, 1965. Proceedings: Symposium on Biophysics and Physiology of Biological Transport. Book part III. Springer: Berlin Heidelberg.
- [Schnug2012] Schnug, E. (2012): Uran in Phosphor-Düngemitteln und dessen Verbleib in der Umwelt. Online at http://www.strahlentelex.de/Stx_12_612_S03-10.pdf, on 28.10.2013.
- [Seddon1984] Seddon, K.R. (1984): Gmelin handbook of inorganic chemistry, 8th Edition. U - Uranium, Supplement Volume D1: Properties of Uranium Ions in Solutions and Melts. Berlin: Springer-Verlag.
- [Sharma2008] Sharma, Ramesh R.; Chellam, Shankararaman: Solute rejection by porous thin film composite nanofiltration membranes at high feed water recoveries. Journal of Colloid and Interface Science 328 (2008) 353–366

- [Sherwood1967] Sherwood, T.K.; Brian, P.L.T.; Fisher, R.E.: Desalination by reverse osmosis. Industrial and engineering chemistry fundamentals, vol. 6 no. 1 (1967) pp. 2-12.
- [Siehl1996] Siehl, Agemar (Hg.) (1996): Umweltradioaktivität. Berlin: Ernst (Geologie und Ökologie im Kontext).
- [Siemers1998] Siemers, Andreas (1998): Multiionentransport durch geladene Nanofiltrationsmembranen – Experimentelle Ergebnisse und Berechnungsansätze. Stuttgart: Fraunhofer IRB Verlag.
- [Sievertsen2001] Sievertsen, Edvard (2001): Membrane separation of anions in concentrated electrolytes. Dissertation at the department of chemical engineering at the Norwegian university of science and technology (NTNU) in Trondheim, Norway.
- [Silva2011] Silva, V.; Geraldés, V.; Brites Alves, A.M.; Palacio, L.; Prádanos, P.; Hernández, A.: Multi-ionic nanofiltration of highly concentrated salt mixtures in the seawater range. Desalination 277 (2011) 29–39.
- [Soltanieh1981] Soltanieh, Mohammad; Gill, William: Review of reverse osmosis membranes and transport models. Chem. eng. commun. Vol 12 (1981) pp. 279-363
- [Spiegler1966] Spiegler, K. S., & Kedem, O. (1966). Thermodynamics of hyperfiltration (reverse osmosis): Criteria for efficient membranes. Desalination, 1(4), 311-326
- [Stabin2007] Stabin, Michael G. (2007): Radiation protection and dosimetry. An introduction to health physics. New York, NY: Springer. Available online at <http://www.loc.gov/catdir/enhancements/fy0825/2007930708-d.html>.
- [Starov2001] Starov, V.M.; Bowen, W.R.; Welfoot, J.S.: Flow of multicomponent electrolyte solutions through narrow pores of nanofiltration membranes. Journal of colloid and interface science 240 (2001) 509-524
- [Szymczyk2005] Szymczyk, Anthony; Fievet, Patrick: Investigating transport properties of nanofiltration membranes by means of a steric, electric and dielectric exclusion model. Journal of Membrane Science 252 (2005) 77–88.
- [Szymczyk2006] Szymczyk, Anthony; Sbai, Mohammed; Fievet, Patrick; Vidonne, Alain: Transport Properties and Electrokinetic Characterization of an Amphoteric Nanofilter. Langmuir, Vol. 22, No. 8 (2006) 3910-3919.
- [Tanaka2001] Tanaka, M.; Girard, G.; Davis, R.; Peuto, A.; Bignell, N. : Recommended table for the density of water between 0°C and 40°C based on recent experimental reports. Metrologia, 38 (2001) pp. 301-309.
- [Teorell1953] Teorell, T. (1953): Transport processes and electrical phenomena in ionic membranes. Progr. Biophys. biophys. Chem. (3), 305.
- [TVO2011] TrinkwÄndV, Bundesministerium der Justiz (2011): Verordnung über die Qualität von Wasser für den menschlichen Gebrauch - Trinkwasserverordnung 2001, geändert am 22.12.2011.

- [Vezzani2002] Vezzani, Daniele; Bandini, Serena (2002): Donnan equilibrium and dielectric exclusion for characterization of nanofiltration membranes. In: *Desalination* 2002 (149), S. 477–483.
- [Wang1995] Wang, Xiao-Lin; Tsuru, Toshinori; Nakao, Shin-ichi; Kimura, Shoji: Electrolyte transport through nanofiltration membranes by the space-charge model and the comparison with Teorell-Meyer-Sievers model. *Journal of Membrane Science* 103 (1995) 117-133.
- [Wedepohl1995] Wedepohl, K. H. (1995): The composition of the continental crust. In: *Geochimica et Cosmochimica Acta* 59.
- [Wijmans1985] Wijmans, J.G.; Nakao, S.; Van den Berg, J.W.A.; Troelstra, F.R.; Smolders, C.A.: Hydrodynamic resistance of concentration polarization boundary layers in ultrafiltration. *Journal of membrane science*, 22 (1985) 117-135.
- [Wijmans2006] Wijmans, Johannes G.; Baker, Richard W. (2006): The Solution-Diffusion Model: A Unified Approach to Membrane Permeation. In: Yuri Yampolskii (Hg.): *Materials science of membranes for gas and vapor separation*. Chichester: John Wiley.
- [Wismut2011] Wismut GmbH (2011): 20 Jahre Wismut. Online at 20jahre.wismut.de/, on 28.10.2013.
- [Wismut2012] Wismut GmbH (2012): Umweltbericht 2012. Online at <http://www.wismut.de/de/umweltberichte.php>, on 28.10.2013.
- [Wismut2014] Material directly provided by the Wismut GmbH, received during a mutual project.
- [Yaroshchuk1998] Yaroshchuk, Andriy E. (1998): Rejection mechanisms of NF membranes. *Membrane Technology* (No. 100). pp. 9-12.
- [Yaroshchuk2000] Yaroshchuk, Andriy E.: Dielectric exclusion of ions from membranes. *Advances in Colloid and Interface Science* 85 (2000) pp. 193-230.
- [Yaroshchuk2011] Yaroshchuk, Andriy; Martínez-Lladó, Xavier; Llenas, Laia; Rovira, Miquel; de Pablo, Joan: Solution-diffusion-film model for the description of pressure-driven trans-membrane transfer of electrolyte mixtures: One dominant salt and trace ions. *Journal of Membrane Science* 368 (2011) 192–201
- [Zemaitis] Zemaitis, Joseph F. Jr.; Clark, Diane M.; Rafal, Marshall, Scrivner, Noel C. (1986): *Handbook of aqueous electrolyte thermodynamics: Theory & application*. Wiley, AIChE.

Appendix A – Hagen Poiseuille for NF

[Melin2007 page 77] The Hagen Poiseuille equation describes the volume flow of an incompressible Newtonian fluid through a straight pipe at a given pressure drop between its inlet and outlet.

$$\dot{V} = \frac{\pi \cdot r^4 \cdot \Delta p}{8\mu \cdot L} \quad (\text{A.1})$$

The variables of the pipe through which the flow \dot{V} will emerge are illustrated in Figure 84.

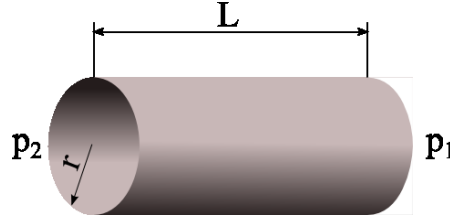


Figure 84: Model pipe for the Hagen-Poiseuille equation, equation (A.1).

The porosity of the membrane A_k is defined as its void fraction, i.e. for straight pores as the ratio of the sum of the surface of all pores to total surface.

$$A_k = \frac{\sum_{i=1}^n \pi \cdot r_i^2}{A} = \frac{n \cdot \pi \cdot r^2}{A} \quad (\text{A.2})$$

The flux will then be the sum of the volume flows through all pores divided by the effective membrane area.

$$J_v = \frac{\sum_{i=1}^n \dot{V}_i}{A} = \frac{n \cdot \dot{V}}{A} = \frac{n \cdot \dot{V} \cdot A_k}{n \cdot \pi \cdot r^2} = \frac{\dot{V} \cdot A_k}{\pi \cdot r^2} \quad (\text{A.3})$$

Equation (A.1), and (A.3), as well as the definition of the pore length by the effective membrane thickness, can be combined to yield:

$$J_v = \frac{r^2 \cdot \Delta p \cdot A_k}{8\mu \cdot \Delta x} \quad (\text{A.4})$$

The viscosity within the pores can be calculated according to Equation .

Appendix B — Friction coefficient

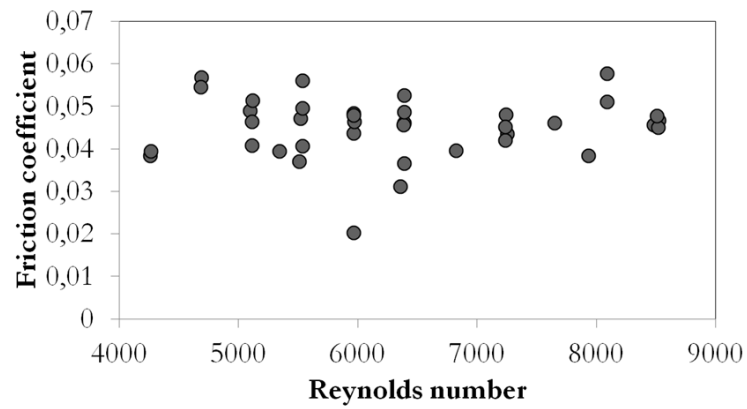


Figure 85: Friction coefficient as a function of the Reynolds number.

Appendix C – Membrane data

Literature sources are listed at the end of the data tables.

Table 25: Properties of membranes from Microdyn-Nadir.

Membrane name	NP030	NP010	MP005
Material	Polyethersulfone [MN2014]	Polyethersulfone [MN2014]	Polyethersulfone [MN2014]
Type	NF [MN2014] (semi-porous [Darvishmanesh2009])	NF [MN2014] (porous [Darvishmanesh2009])	MF [MN2014]
Pore radius	0.74 nm [Wang2005b] and [Carvalho2011b] Volume fraction of small pores 53.7 % and large pores 8.3 % [Conidi2014]	1.33 nm [Wang2005b] but 0.743 [Carvalho2011b]	25 nm [MN2014]
Thickness	REM images in [Wang2005b]	REM images in [Wang2005b]	
Performance	@ 40 bar, 20°C, stirred cell 700 min ⁻¹ $J_{H_2O} > 40$ l/m ² h [MN2014] $J_{H_2O} = 40...70$ l/m ² h [Wang2005b] $R_{Na_2SO_4} = 80...95$ % [Wang2005b] $R_{NaCl} = 25...35$ % [Wang2005b] $R_{Na_2SO_4} = 100$ % @0.2 g/l, 18 bar, pH 8, 25°C, Re=890 [Afonso2012] $R_{NaCl} = 99$ % @0.2 g/l, 18 bar, pH 8, 25°C, Re=890 [Afonso2012] $R_{Glucose} = 28$ % @0.2 g/l, 18 bar, pH 8, 25°C, Re=890 [Afonso2012] $R_{Xylose} = 16$ % @0.2 g/l, 18 bar, pH 8, 25°C, Re=890 [Afonso2012]	@ 40 bar, 20°C, stirred cell 700 min ⁻¹ $J_{H_2O} > 200$ l/m ² h [MN2014] $J_{H_2O} = 200...400$ l/m ² h [Wang2005b] $R_{Na_2SO_4} = 35...75$ % [Wang2005b] $R_{NaCl} = 10...20$ % [Wang2005b] $R_{Na_2SO_4} = 99$ % @0.2 g/l, 18 bar, pH 8, 25°C, Re=890 [Afonso2012] $R_{NaCl} = 97$ % @0.2 g/l, 18 bar, pH 8, 25°C, Re=890 [Afonso2012] $R_{Glucose} = 6$ % @0.2 g/l, 18 bar, pH 8, 25°C, Re=890 [Afonso2012] $R_{Xylose} = 8$ % @0.2 g/l, 18 bar, pH 8, 25°C, Re=890 [Afonso2012]	@ 0.7 bar, 20°C, stirred cell 700 min ⁻¹ $J_{H_2O} > 200$ l/m ² h [MN2014]
Contact angle	Hydrophilic [MN2014]	Hydrophilic [MN2014]	

	[Wang2005b] 31° [Gönder2011] 82° [Conidi2014]	[Wang2005b]
MWCO	400 Da [MN2014] [Conidi2014]	1000 Da [MN2014]
pH range	0...14 [MN2014]	0...14 [MN2014]
T_{max}	95°C [MN2014]	95°C [MN2014]
p_{max}	40 [Carvalho2011b]	40 [Carvalho2011b]
Permeability L_p	4.36 10-11 m/Pa s [Carvalho2011b] 16 L/m ² /h/bar [Arkell2013] 1.3 L/m ² /h/bar @20°C [Koschuh2005] 2...6 L/m ² /h/bar @25°C [Afonso2012] 2...6 kg/h/m ² /bar [Restolho2009]	6.47 10-11 m/Pa s [Carvalho2011b] 50 L/m ² /h/bar [Arkell2013] 9.5 L/m ² /h/bar @20°C [Koschuh2005] 11...30 L/m ² /h/bar @25°C [Afonso2012] 11...30 kg/h/m ² /bar [Restolho2009]
$A_k/\Delta x$	300,058 m ⁻¹ [Wang2005b]	35,757 m ⁻¹ [Wang2005b]
Charge characteristics		IEP pH 4 [Hepsen2012]

Table 26: Properties of membranes from Dow Filmtec.

Membrane name	NF 270	NF 90
Material	Polyamide [DOW2014] Semi-aromatic piperazine composite [Kim2007] Active groups: COO-	Polyamide [DOW2014]
Type	NF [DOW2014]	NF [DOW2014]
Pore radius	0.38 nm [Richards2013] 0.42 nm [Semiao2013]	0.494 nm [Carvalho2011b] 0.34 nm [Richards2013] 0.34 nm [Nghiem2008] 0.476 nm [Santa2008]
Thickness	21 nm [Semiao2013]	REM images in [Brito2013]
Permeability L_p	0.2232 L/m ² bar h [Richards2013] 4.7 L/m ² bar h [Narbaitz2013] 0.6 L/m ² bar h [Brito2013] 20...31 L/m ² /h/bar @25°C [Afonso2012] 3.88 µm/s/bar @15°C [Cancino2011] 20...31 kg/h/m ² /bar [Restolho2009] 29.1 m/d/bar [Kim2007] 14.86 L/m ² /h/bar [Yüksel2013]	5.5 L/m ² bar h [Carvalho2011b] 12.5 L/m ² bar h [Sotto2013] 0.1998 L/m ² bar h [Richards2013] 11.1 L/m ² bar h [Richards2013] 5.03 L/m ² bar h [Heff2013] 0.85 L/m ² bar h [Brito2013] 10.4 L/m ² bar h [Xu2006] 1.54 µm/s/bar @15°C [Cancino2011] 6.05 L/m ² /h/bar [Yüksel2013] 8.1 L/m ² /h/bar [Zirehpour2012]

		17 L/h/m ² /bar [Semiao2013] 14.6 L/h/m ² /bar [Zirehpour2012]	
MWCO		200...300 Da [Brito2013] [Kim2007] [Bunani2013] 150...200 Da [Cancino2011] 180 Da [Semiao2013]	180 Da [Carvalho2011b] or 200 Da [Sotto2013] [Cancino2011] [Bunani2013]
	T_{max}	45°C [DOW2014]	45°C [DOW2014]
	p_{max}	41 bar [DOW2014]	41 bar [DOW2014]
pH		3...10 [DOW2014]	3...10 [DOW2014] 2...11 [Carvalho2011b] 4...11 [Sotto2013] 3...10
Performance		@ 0.48 MPa, 25°C $R_{MgSO_4} = 97\%$ @2000ppm [DOW2014] $R_{CaCl} = 40...60\%$ @500ppm [DOW2014] $R_{Na_2SO_4} = 96\%$ @0.2 g/l, 18 bar, pH 8, 25°C, Re=890 [Afonso2012] $R_{NaCl} = 96\%$ @0.2 g/l, 18 bar, pH 8, 25°C, Re=890 [Afonso2012] $R_{NaCl} = 52\%$ @0.1 M, 10 bar [Semiao2013] $R_{NaCl} = 35\%$ [Zirehpour2012] $R_{Glucose} = 52\%$ @0.2 g/l, 18 bar, pH 8, 25°C, Re=890 [Afonso2012] $R_{Xylose} = 34\%$ @0.2 g/l, 18 bar, pH 8, 25°C, Re=890 [Afonso2012] $R_{CaCl_2} = 40...60\%$ [Kim2007]	@ 0.48 MPa, 25°C, 2000 ppm $R_{NaCl} = 85...95\%$ [DOW2014] $R_{MgSO_4} > 97\%$ [DOW2014] $R_{CaCl} = 40...60\%$ (@500ppm CaCl) [DOW2014] $R_{NaCl} = 95\%$ @10mM, 13.8 bar, pH 7 [Cancino2011] $R_{NaCl} = 84\%$ [Zirehpour2012]
	$A_k/\Delta x$	990,099 m ⁻¹ [Richards2013] 1.1 µm [Semiao2013]	684,932 m ⁻¹ [Richards2013] 0.2 µm [Santa2008]
Zeta potential		-10 mV @ pH 6.2 [Richards2013] -41.3 mV @pH 9 [Cancino2011] -6.8 mV @pH 7 stream-through potential [Cancino2011] -15 mV @pH 7 stream-across potential [Cancino2011] Isoelectric point at 3.3 [Cancino2011] $\zeta = -51.6$ mV @ 10mM NaCl, pH 7 [Kim2007] IEP pH 3.3 [Hepsen2012] $\zeta = -55$ mV @ 1mM NaCl, pH 7, 30°C [Kaufman2014] $\zeta = -25$ mV @ 150mM NaCl, pH 7, 30°C [Kaufman2014] IEP at pH 3.6 [Semiao2013] $\zeta = -80$ mV [Dukhin2012] $\zeta = -54$ mV @ pH 8	-18 mV @ pH 6.2 [Richards2013] -10 mV @ pH 7 [Heff2013] -37 mV @pH 9 [Cancino2011] Isoelectric point at 3.6 [Cancino2011] IEP pH 3.5 [Hepsen2012] $\zeta = -27$ mV @ pH 8 [Zirehpour2012]

	[Zirehpour2012]	
Contact angle	Hydrophilic [Brito2013] 30° [Cancino2011] 29.1° [Zirehpour2012]	Hydrophilic [Brito2013] 44.7° or 63.2° [Cancino2011] 65.6° [Zirehpour2012]

Table 27: Properties of membranes from Koch Membrane Systems.

Membrane name	SelRO MPF34	SelRO MPF36	SW	SR100
Material	Proprietary [Koch2012] Polysulphone active- and sublayer and cellulose acetate support [Matsumoto2005] or Polydimethylsiloxane [Othman2010] or Polysulfone on Polypropylene [Ramadan2010]	Proprietary [Koch2012]	Proprietary [Koch2012] Polyamide	Proprietary [Koch2012] Polyamide
Type	NF [Koch2012] (dense [Darvishmanesh2009])	NF [Koch2012]	RO [Koch2012]	NF [Koch2012]
Pore radius				
Thickness	REM image in [Matsumoto2005]			
T_{max}	50°C [Koch2012] 70°C [Sungpet2004]	50°C [Koch2012] 70°C [Sungpet2004]	45°C [Koch2012]	50°C [Koch2012]
p_{max}	35 bar [Koch2012] [Arkell2013]	35 bar [Koch2012] [Arkell2013]	82,75 bar [Koch2012]	41.4 bar [Koch2012]
pH	0...14 [Koch2012] [Guastalli2009]	1...13 [Koch2012] 0...14 [Guastalli2009]	4...11 [Koch2012]	4...10 [Koch2012]
MWCO	200 Da [Koch2012] [Arkell2013] [Sungpet2004] 325 Da [Matsumoto2005] or 200 Da [Darvishmanesh2009] 300 Da [Guastalli2009]	1000 Da [Koch2012] [Arkell2013] [Sungpet2004] [Koschuh2005] [Guastalli2009]		200 Da [Koch2012]
Permeability L_p	2 L/m ² bar h [Koch2012] or 667 m/bar/s	6 L/m ² bar h [Koch2012] 6.7 L/h/m ² /bar	1 L/m ² bar h [Koch2012]	0.9 L/m ² bar h [Koch2012]

	[Matsumoto2005] 0.6072µm/s/bar [Othman2010] 2 L/h/m ² /bar [Guastalli2009] 1.75 L/m ² /h/bar [Arkel2013] 2.79 L/m ² /bar/h @60°C [Sungpet2004]	[Guastalli2009] 25 L/m ² /h/bar [Arkel2013] 21.24 L/m ² /bar/h @60°C [Sungpet2004] 6 L/m ² /h/bar @20°C [Koschuh2005]		
Performance	@ 30 bar, 30°C $R_{NaCl} = 35 \% @5\%$ [Koch2012] [Guastalli2009] [Arkel2013] $R_{Glucose} = 95 \% @3\%$ [Koch2012] $R_{Sucrose} = 97 \% @3\%$ [Koch2012]	@ 30 bar, 30°C $R_{MgSO_4} = 92 \% @5000ppm$ $R_{NaCl} = 10 \% @5\%$ [Koch2012] [Guastalli2009] [Arkel2013] $R_{Glucose} = 30 \% @3\%$ [Koch2012] $R_{Sucrose} = 50 \% @3\%$ [Koch2012]	@ 55.2 bar, 25°C, 32.8 g/L NaCl, pH 7.5 $R_{Cl^-} = 99.75 \%$ [Koch2012]	@ 6.55 bar, 25°C, pH 7.5, 5 g/L $R_{MgSO_4} > 99 \%$ [Koch2012]
Contact angle	Hydrophilic [Darvishmanesh2009]			

Table 28: Properties of membranes from Alfa Laval.

Membrane	NF (NF99)	RO90	RO99	NF99 HF
Material	Polyamide thin film composite on Polyester [AL2013]	Proprietary thin film composite on polyester support [AL2013]	Proprietary thin film composite on polyester support [AL2013]	Polyamide thin film composite on Polyester [AL2013]
Type	NF	RO		NF [AL2013]
Pore radius				
Thickness				
Performance	$R_{Na_2SO_4} > 98 \% @2 \text{ g/l, } 9 \text{ bar, pH } 8, 25^\circ\text{C}$ [AL2013] [Catarino2011]	$R_{NaCl} > 90 \% @2 \text{ g/l, } 9 \text{ bar, pH } 8, 25^\circ\text{C}$ [AL2013]	$R_{Na_2SO_4} = 98 \% @0.2 \text{ g/l, } 18 \text{ bar, pH } 8, 25^\circ\text{C, Re}=890$ [Afonso2012] $R_{NaCl} = 97 \% @0.2 \text{ g/l, } 18 \text{ bar, pH } 8, 25^\circ\text{C, Re}=890$ [Afonso2012] $R_{Glucose} = 96 \% @0.2 \text{ g/l, } 18 \text{ bar, pH } 8, 25^\circ\text{C, Re}=890$	$R_{MgSO_4} > 98 \% @2000ppm, 9 \text{ bar, pH } 8, 25^\circ\text{C}$ [AL2013] [Catarino2011] $R_{Na_2SO_4} = 97 \% @0.2 \text{ g/l, } 18 \text{ bar, pH } 8, 25^\circ\text{C, Re}=890$ [Afonso2012] $R_{NaCl} = 72 \% @0.2 \text{ g/l, } 18 \text{ bar, pH } 8, 25^\circ\text{C, Re}=890$

				[Afonso2012] $R_{Xylose} = 93\%$ @0.2 g/l, 18 bar, pH 8, 25°C, Re=890	[Afonso2012] $R_{Glucose} = 75\%$ @0.2 g/l, 18 bar, pH 8, 25°C, Re=890
				[Afonso2012] $R_{NaCl} > 98\%$ @2 g/l, 16 bar, pH 8, 25°C [AL2013]	[Afonso2012] $R_{Xylose} = 59\%$ @0.2 g/l, 18 bar, pH 8, 25°C, Re=890 [Afonso2012]
T_{max}	50°C @max. 33 bar [AL2013]	50°C [AL2013]		50°C [AL2013]	50°C [AL2013]
p_{max}	55 bar @30°C [AL2013]	55 bar [AL2013]		55 bar [AL2013]	55 bar @30°C [AL2013]
pH	3...10 @25°C [AL2013]	3...10 @25°C [AL2013]		3...10 @25°C [AL2013]	3...10 @25°C [AL2013]
Permeability L_p	10 kg/h/m ² /bar [Restolho2009] 5.4118 l/m ² /h/bar [Li2010]			2...3 L/m ² /h/bar @25°C [Afonso2012] 2...3 kg/h/m ² /bar [Restolho2009] 2.5 l/m ² /h/bar [Li2010]	13 l/m ² /h/bar [Li2010] 1.12 L/m ² bar h @23°C, pure ethanol [Fornasero2013] 1.57 L/m ² bar h @35°C, pure ethanol [Fornasero2013] 9...18 L/m ² /h/bar @25°C [Afonso2012] 9...18 kg/h/m ² /bar [Restolho2009]
MWCO	200 Da [Catarino2011]				200 Da [Catarino2011]

Table 29: Properties of membranes from GE Desal Osmonics.

Membrane	SG	DK	DL	HL	CK
Material	Proprietary [GE2013]	Proprietary [GE2013] Polysulphone active- and sublayer and cellulose acetate support [Matsumoto2005] or Polyamide [Othman2010]	Proprietary [GE2013] Polyamide [Othman2010]	Proprietary [GE2013]	Cellulose acetate [GE2013]
Type	RO [GE2013]	NF [GE2013] (dense	NF [GE2013]	NF [GE2013]	NF [GE2013]

		[Darvishmanesh2009])			
Pore radius		0.45 nm [Oatley2013]	0.73 nm [Sharma2008] Volume fraction of small pores 18.8 % and large pores 1.7 % [Conidi2014]		
Thickness		REM image in [Matsumoto2005]			
Performance	$J_{H_2O} \approx 22 \text{ l/m}^2\text{h}$ [GE2013] $R_{NaCl} \approx 98.2 \%$ [GE2013]	$J_{H_2O} \approx 22 \text{ l/m}^2\text{h}$ [GE2013] $R_{MgSO_4} \approx 98 \%$ [GE2013] $R_{NaCl} < 50 \%$ @5%, 30bar, 30°C [Guastalli2009] [GE2013]	$J_{H_2O} \approx 31 \text{ l/m}^2\text{h}$ [GE2013] $R_{MgSO_4} \approx 96 \%$ [GE2013] $R_{NaCl} < 40 \%$ @5%, 30bar, 30°C [Guastalli2009] [GE2013]	$J_{H_2O} \approx 39 \text{ l/m}^2\text{h}$ [GE2013] $R_{MgSO_4} \approx 95 \%$ [GE2013]	$J_{H_2O} \approx 28 \text{ l/m}^2\text{h}$ [GE2013] $R_{Na_2SO_4} \approx 92 \%$ [GE2013]
Contact angle		Hydrophilic [Darvishmanesh2009]	46° [Conidi2014]		
pH	1...11 [GE2013]	2...10 [GE2013] 1...11 [Guastalli2009]	2...10 [GE2013] 1...11 [Guastalli2009]	3...9 [GE2013]	2...8 at 25°C [GE2013]
T_{max}	80°C [GE2013]	80°C [GE2013] 90°C [Guastalli2009]	80°C [GE2013] 90°C [Guastalli2009]	50°C [GE2013]	30°C [GE2013]
p_{max}	40 bar [GE2013]	40 bar [GE2013]	40°C [GE2013]	40 bar [GE2013]	15 bar [GE2013]
MWCO		285 Da [Matsumoto2005] 150-300 Da [Darvishmanesh2009] 150-300 Da [Guastalli2009]	150-300 Da [Guastalli2009] 268 Da [Sharma2008]		200 Da [GE2013] 150 Da [Bunani2013]
Permeability L_p		1278 $\mu\text{m}/\text{bar h}$ [Matsumoto2005] 1.1395 $\mu\text{m}/\text{s}/\text{bar}$ [Othman2010] 2.4 $\text{L}/\text{h}/\text{m}^2/\text{bar}$ [Guastalli2009]	1.3665 $\mu\text{m}/\text{s}/\text{bar}$ [Othman2010] or 10 $\text{L}/\text{h}/\text{m}^2/\text{bar}$ [Guastalli2009]		
Charge characteristics		-4 mV for KCl, -6 mV for MgSO_4 , -14 mV for Na_2SO_4 , IEP at pH 3.5...4	Effective charge density of -2.02 meq/L [Sharma2008] IEP pH 3.2		

	[Oatley2013]	[Hepsen2012]
Thickness to porosity ratio		144 μm [Sharma2008]

Table 30: Properties of membranes from Toray.

Membrane	UTC 60	UTC 70	UTC 70 HF
Material	Polyamide separation layer [Tsuru1994] Polypiperazine polyamide composite [Kim2007]	Polypiperazine-amide [Ahmed2010] Polypiperazine polyamide composite [Kim2007]	
Type	NF [Kim2007]	tight NF [Ahmed2010] Low pressure RO [Kim2007]	
Pore radius			
Thickness			
Permeability L_p	10 L/m ² /h/bar @25°C [Bruggen2001] 2.5 μm /s/bar [Tsuru1994] 14.9 m/d/bar [Kim2007]	13.2 m/d/bar [Kim2007]	
pH	3...9 [Bruggen2001] 3...8 [Tsuru1994]		
T_{max}	35°C [Bruggen2001] 45°C [Tsuru1994]		
p_{max}	15 bar [Bruggen2001] 28 bar [Tsuru1994]		
Charge characteristics	Positive Negative @pH 7 [Tsuru1994] $\zeta = -34.7 \text{ mV @ } 10 \text{ mM NaCl, pH 7 [Kim2007]}$	$\zeta = -51.1 \text{ mV @ } 10 \text{ mM NaCl, pH 7 [Kim2007]}$	
MWCO	$\approx 200 \text{ Da}$ 150 Da [Kim2007]	65 Da [Kim2007]	
Performance	@30 mol/m ³ , 5 bar, 25°C $R_{NaCl} = 58 \%$ $R_{Na_2SO_4} = 97 \%$ $R_{MgCl_2} = 65 \%$ $R_{NaCl} = 45...55 \%$ [Kim2007]	$R_{NaCl} = 99.52 \%$ @1.5 g/L, 7.5 bar [Ahmed2010] $R_{NaCl} = 99.5 \%$ [Kim2007]	
Contact angle	51.6° [Kim2007]	54.4° [Kim2007]	

Literature for the membrane's data:

- [Afonso2012] Afonso, Maria Diná (2012): Assessment of NF and RO for the potential concentration of acetic acid and furfural from the condensate of eucalyptus spent sulphite liquor. In: Separation and Purification Technology (99), S. 86–90.
- [Ahmed2010] Ahmed, Saber; Rasul, M.G; Hasib, M.A; Watanabe, Y. (2010): Performance of nanofiltration membrane in a vibrating module (VSEP-NF) for arsenic removal. In: Desalination (252), S. 127–134.
- [AL2013] Alfa Laval (Hg.) (2013): Product data sheet. Alfa Laval NF Series.
- [Arkell2013] Arkell, A.; Krawczyk, H.; Thuvander, J.; Jönsson, A.-S (2013): Evaluation of membrane performance and cost estimates during recovery of sodium hydroxide in a hemicellulose extraction process by nanofiltration. In: Separation and Purification Technology (118), S. 387–393.
- [Brito2013] Brito Martínez, M.; Jullok, N.; Rodriguez Negrin, Z.; van der Bruggen, B.; Luis, P. (2013): Effect of impurities in the recovery of 1-(5-bromo-fur-2-il)-2-bromo-2-nitroethane using nanofiltration. In: Chemical Engineering and Processing: Process Intensification (70), S. 241–249.
- [Bruggen2001] van der Bruggen, Bart; Vandecasteele, Carlo (2001): Flux Decline during Nanofiltration of Organic Components in Aqueous Solution. In: Environ. Sci. Technol. (35), S. 3535–3540.
- [Bunani2013] Bunani, Samuel; Yörükoğlu, Eren; Sert, Gökhan; Yüksel, Ümran; Yüksel, Mithat; Kabay, Nalan (2013): Application of nanofiltration for reuse of municipal wastewater and quality analysis of product water. In: Desalination (33-36), S. 33–36.
- [Cancino2011] Cancino-Madariaga, Beatriz; Hurtado, Carlos Felipe; Ruby, Rene (2011): Effect of pressure and pH in ammonium retention for nanofiltration and reverse osmosis membranes to be used in recirculation aquaculture systems (RAS). In: Aquacultural Engineering (45), S. 103–108.
- [Carvalho2011b] Carvalho, A.L; Maugeri, F.; Prádanos, P.; Silva, V.; Hernández, A. (2011): Separation of potassium clavulanate and potassium chloride by nanofiltration. Transport and evaluation of membranes. In: Separation and Purification Technology (83), S. 23–30.
- [Catarino2011] Catarino, Margarida; Mendes, Adélio (2011): Dealcoholizing wine by membrane separation processes. In: Innovative Food Science and Emerging Technologies (12), S. 330–337.
- [Conidi2014] Conidi, C.; Cassano, A.; Garcia-Castello, E. (2014): Valorization of artichoke wastewaters by integrated membrane process. In: Water Research (48), S. 363–374.
- [Darvishmanesh2009] Darvishmanesh, Siavash; Degreè, Jan; van der Bruggen, Bart (2009): Comparison of pressure driven transport of ethanol/n-hexane mixtures through dense and microporous membranes. In: Chemical Engineering Science (3914-3927).
- [DOW2014] DOW (Hg.) (2014): Filmtec™ Membranes. Form No. 609-00345-0312 and Form No. 609-50107-0613. DOW Filmtec.
- [Dukhin2012] Dukhin, A.S; Parlia, S. (2012): Studying homogeneity and zeta potential of membranes using electroacoustics. In: Journal of Membrane Science (415), S. 587–595.

- [Fornasero2013] Fornasero, M. L.; Marenchino, R. N.; Pagliero, C. L. (2013): Deacidification of Soybean Oil Combining Solvent Extraction and Membrane Technology. In: *Advances in Materials Science and Engineering*.
- [GE2013] GE Power & Water (2013): Flat Sheet Membrane Chart. Online verfügbar unter <https://knowledgecentral.gewater.com/.../TB1152EN>.
- [Gönder2011] Gönder, Z. Beril; Arayici, Semiha; Barlas, Hulusi (2011): Advanced treatment of pulp and paper mill wastewater by nanofiltration process: Effects of operating conditions on membrane fouling. In: *Separation and Purification Technology* (76), S. 292–302.
- [Guastalli2009] Guastalli, Andrea R.; Labanda, Jordi; Llorens, Joan (2009): Separation of phosphoric acid from an industrial rinsing water by means of nanofiltration. In: *Desalination* (243), S. 218–228.
- [Heff2013] Heffernan, R.; Semião, A.J.C; Desmond, P.; Cao, H.; Safari, A.; Habimana, O.; Casey, E. (2013): Disinfection of a polyamide nanofiltration membrane using ethanol. In: *Journal of Membrane Science* (448), S. 170–179.
- [Hepsen2012] Hepsen, R.; Kaya Y. (2012): Optimization of membrane fouling using experimental design: An example from dairy wastewater treatment. In: *Industrial and Engineering Chemistry Research* (49), S. 16074–16084.
- [Kaufman2014] Kaufman, Y.; Grinberg, S.; Linder, C.; Heldman, E.; Gilron, J.; Shen, Yue-xiao et al. (2014): Towards supported bolaamphiphile membranes for water filtration: Roles of lipid and substrate. In: *Journal of Membrane Science* (457), S. 50–61.
- [Kim2007] Kim, Hyun-Ah; Choi, Jae-Hoon; Takizawa, Satoshi (2007): Comparison of initial filtration resistance by pretreatment processes in the nanofiltration for drinking water treatment. In: *Separation and Purification Technology* (56), S. 354–362.
- [Koch2012] Koch MS (Pub.) (2012): Datasheet. For spiral wound modules.
- [Koschuh2005] Koschuh, Werner; Thang, Vu Hong; Krasteva, Stanimira; Novalin, Senad; Kulbe, Klaus D. (2005): Flux and retention behaviour of nanofiltration and fine ultrafiltration membranes in filtrating juice from a green biorefinery: A membrane screening. In: *Journal of Membrane Science* (261), S. 121–128.
- [Matsumoto2005] Matsumoto, Hidetoshi; Chen, Yu-Chiang; Yamamoto, Ryotaro; Konosu, Yuichi; Minagawa, Mie; Tanioka, Akihiko (2005): Membrane potentials across nanofiltration membranes: effect of nanoscaled cavity structure. In: *Journal of Molecular Structure* (739), S. 99–104.
- [MN2014] Microdyn-Nadir (Hg.) (2014): Produkte. Online at <http://www.microdyn-nadir.com/de/Produkte/NADIR%C2%AE/>.
- [Narbaitz2013] Narbaitz, Roberto M.; Rana, Dipak; Dang, Huyen T.; Morrisette, Jordan; Matsuura, Takeshi; Jasim, Saad Y. et al. (2013): Pharmaceutical and personal care products removal from drinking water by modified cellulose acetate membrane: Field testing. In: *Chemical Engineering Journal* (225), S. 848–856.

- [Nghiem2008] Nghiem, Long D.; Vogel, Dirk; Khan, Stuart (2008): Characterising humic acid fouling of nanofiltration membranes using bisphenol A as a molecular indicator. In: *Water Research* (42), S. 4049–4058.
- [Oatley2013] Oatley, Darren L.; Llenas, Laia; Aljohani, Nasser H.M; Williams, Paul M.; Martinez-Llado, Xavier; Rovira, Miquel; Pablo, Joan de (2013): Investigation of the dielectric properties of nanofiltration membranes. In: *Desalination* (315), S. 100–106.
- [Othman2010] Othman, Rahimah; Mohammad, Abdul Wahab; Ismail, Manal; Salimon, Jumat (2010): Application of polymeric solvent resistant nanofiltration membranes for biodiesel production. In: *Journal of Membrane Science* (348), S. 287–297.
- [Ramadan2010] Ramadan, Y.; Pátzay, G.; Szabó, G.T (2010): Effect of quaternary ammonium salts on the separation efficiency of nanofiltration membranes. In: *Desalination* (256), S. 54–57.
- [Restolho2009] Restolho, Jose Augusto; Prates, Antonio; Pinho, Maria Norberta de; Afonso, Maria Dina (2009): Sugars and lignosulphonates recovery from eucalyptus spent sulphite liquor by membrane processes (33), S. 1558–1566.
- [Richards2013] Richards, Laura A.; Richards, Bryce S.; Corry, Ben; Schäfer, Andrea I. (2013): Experimental Energy Barriers to Anions Transporting through Nanofiltration Membranes. In: *Environmental Science & Technology* (47), S. 1968–1976.
- [Santa2008] Santafé-Moros, A.; Gozávez-Zafrilla, J.M; Lora-García, J. (2008): Applicability of the DSPM with dielectric exclusion to a high rejection nanofiltration membrane in the separation of nitrate solutions. In: *Desalination* (221), S. 268–276.
- [Semiao2013] Semiao, Andrea J.C; Foucher, Matthieu; Schäfer, Andrea I. (2013): Removal of adsorbing estrogenic micropollutants by nanofiltration membranes: Part B — Model development. In: *Journal of Membrane Science* (431), S. 257–266.
- [Sharma2008] Sharma, Ramesh R.; Chellam, Shankararaman (2008): Solute rejection by porous thin film composite nanofiltration membranes at high feed water recoveries. In: *Journal of Colloid and Interface Science* (328), S. 353–366.
- [Sotto2013] Sotto, Arcadio; Arsuaga, Jesús M.; van der Bruggen, Bart (2013): Sorption of phenolic compounds on NF/RO membrane surfaces: Influence on membrane performance. In: *Desalination* (309), S. 64–73.
- [Sungpet2004] Sungpet, Anawat; Jiraratananon, Ratana; Luangsowan, Piyanoot (2004): Treatment of effluents from textile-rinsing operations by thermally stable nanofiltration membranes. In: *Desalination* (160), S. 75–81.
- [Tsuru1994] Tsuru, Toshinori; Shutou, Takatoshi; Nakao, Shin-Ichi; Kimura, Shoji (1994): Peptide and Amino Acid Separation with Nanofiltration Membranes. In: *Separation Science and Technology* (29), S. 971–984.
- [Wang2005b] Wang, Kai Yu; Chung, Tai-Shung (2005): The characterization of flat composite nanofiltration membranes and their applications in the separation of Cephalexin. In: *Journal of Membrane Science* (247), S. 37–50.

[Xu2006] Xu, Pei; Drewes, Jörg E. (2006): Viability of nanofiltration and ultra-low pressure reverse osmosis membranes for multi-beneficial use of methane produced water. In: *Separation and Purification Technology* (52), S. 67–76.

[Yüksel2013] Yüksel, Suna; Kabay, Nalan; Yüksel, Mithat (2013): Removal of bisphenol A (BPA) from water by various nanofiltration(NF) and reverse osmosis (RO) membranes. In: *Journal of Hazardous Materials* (263), S. 307–310.

[Zirehpour2012] Zirehpour, Alireza; Jahanshahi, Mohsen; Rahimpour, Ahmad (2012): Unique membrane process integration for olive oil mill wastewater purification. In: *Separation and Purification Technology* (96), S. 124–131.

Appendix D – Model input data and testing

Besides parameters that are specific of the membrane (Section 6.1) and the feed solution (Section 6.5 and 6.6) the model requires a number of physical constants and system parameters that should be listed here in order to be clear about their values used in the computations.

- Molar gas constant 8.3144621 J/mol/K
- Feed side characteristic length of the channel L is 0.17 m
- Avogadro constant $6.02214129 \cdot 10^{23}$ in 1/mol
- Constants for Sherwood: $a = 0.002$ $b = 0.04$

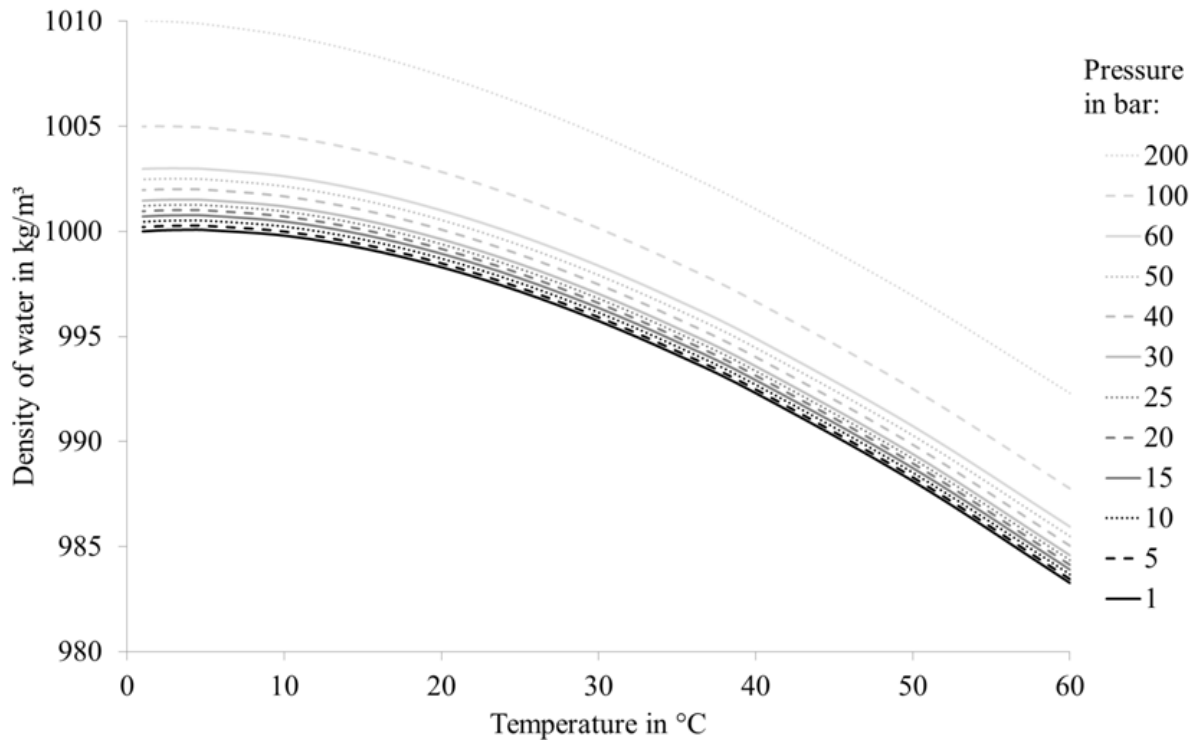


Figure 86: Density of water as a function of temperature for different pressures in bar. Calculated using the formulation proposed by [Tanaka2001].

Program code for the pure water density formulation:

```
function [waterdensity] = Density( temp, TMP )
% water density formulation
% from Tanaka-M._2001_Metrologia.pdf
temcelsius = temp - 273.15; %conversion from K to °C
TMPPa = (TMP+1)*10^(5); %conversion from bar to Pa
aa1 = -3.983035; %in °C
aa2 = 301.797; %in °C
aa3 = 522528.9; %in °C
aa4 = 69.34881; %in °C
aa5 = 999.97495; %in °C
kk0 = 50.74*10^(-11); %in 1/Pa
kk1 = -0.326*10^(-11); %in 1/Pa/°C
```

```

kk2 = 0.00416*10^(-11); %in 1/Pa/°C²
waterdensity = aa5*(1-
((temcelsius+aa1)^2*(temcelsius+aa2))/(aa3*(temcelsius+aa4)))*(1+(kk0+kk1*temc
elsius+kk2*temcelsius^2)*TMPPa);
end

```

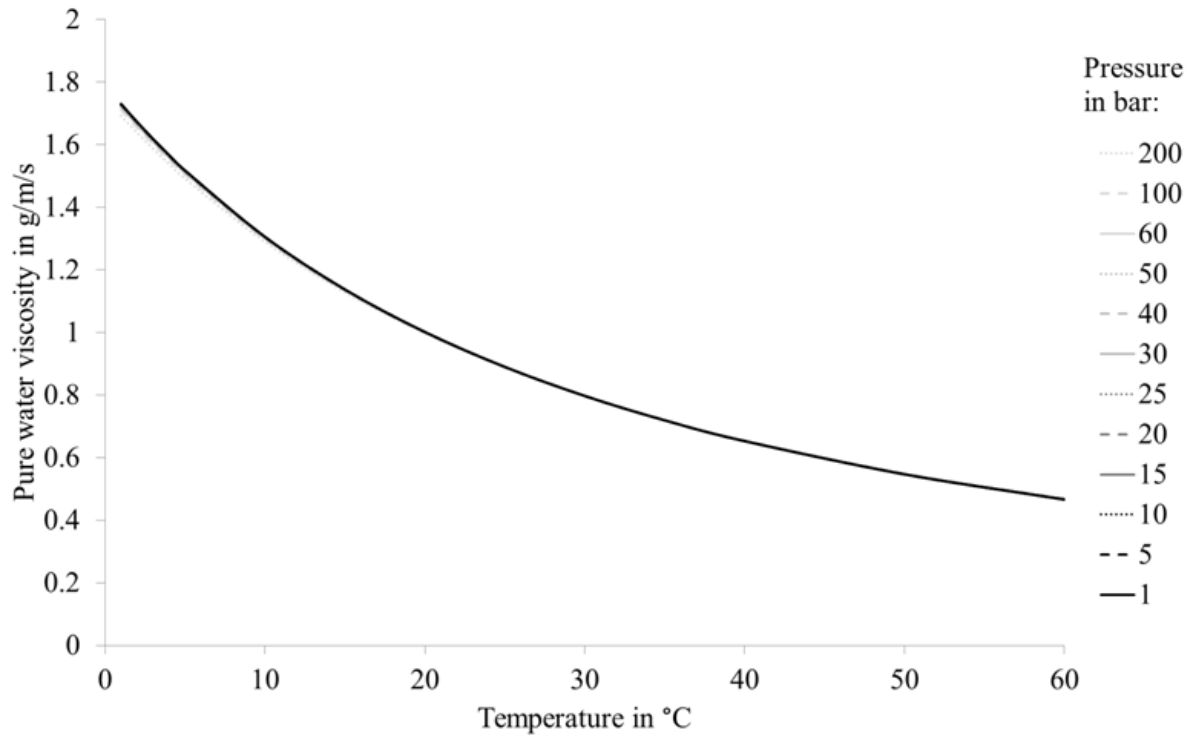


Figure 87: Viscosity of water as a function of temperature for different densities (expressed as pressures by the relationship in Figure 86) calculated using the formulation proposed by [Huber2009].

Program code for the pure water viscosity formulation:

```

function [waterviscos] = Viscosity( temp, waterdensity )
%From Huber-M.L._2009_J.-Phys.-Chem.-Ref.-Data.pdf
%dimensionless formulation
t_quer = temp/647.096; %relative to critical temperature in K
rho_quer = waterdensity/322; %relative to critical density in kg/m³
%p_quer = TMP/220.64; %relative to critical pressure in bar
%0. zero density term
H_0 = 1.67752;
H_1 = 2.20462;
H_2 = 0.6366564;
H_3 = -0.241605;
mu_0 = 100*(t_quer)^(0.5)/(H_0 + H_1/(t_quer) + H_2/(t_quer^2) +
H_3/(t_quer^3));
%1. residual density term
H_00 = 5.20094*10^(-1) ;
H_10 = 8.50895*10^(-2) ;
H_20 = -1.08374 ;
H_30 = -0.289555 ;
H_01 = 2.22531*10^(-1) ;
H_11 = 9.99115*10^(-1) ;

```

```
H_21 = 1.88797 ;
H_31 = 1.26613 ;
H_51 = 1.20573*10^(-1) ;
H_02 = -0.281378 ;
H_12 = -0.906851 ;
H_22 = -0.772479 ;
H_32 = -0.489837 ;
H_42 = -0.25704 ;
H_03 = 1.61913*10^(-1) ;
H_13 = 2.57399*10^(-1) ;
H_04 = -0.0325372 ;
H_34 = 6.98452*10^(-2) ;
H_45 = 8.72102*10^(-3) ;
H_36 = -0.00435673 ;
H_56 = -0.000593264 ;
mu_li0 = (1/t_quer - 1)^(0) * (H_00*(rho_quer-1)^(0)+H_01*(rho_quer-1)^(1)+H_02*(rho_quer-1)^(2)+H_04*(rho_quer-1)^(4)+H_03*(rho_quer-1)^(3));
mu_li1 = (1/t_quer - 1)^(1) * (H_10*(rho_quer-1)^(0)+H_11*(rho_quer-1)^(1)+H_12*(rho_quer-1)^(2)+H_13*(rho_quer-1)^(3));
mu_li2 = (1/t_quer - 1)^(2) * (H_20*(rho_quer-1)^(0)+H_21*(rho_quer-1)^(1)+H_22*(rho_quer-1)^(2));
mu_li3 = (1/t_quer - 1)^(3) * (H_30*(rho_quer-1)^(0)+H_31*(rho_quer-1)^(1)+H_32*(rho_quer-1)^(2)+H_34*(rho_quer-1)^(4)+H_36*(rho_quer-1)^(6));
mu_li4 = (1/t_quer - 1)^(4) * (H_42*(rho_quer-1)^(2)+H_45*(rho_quer-1)^(5));
mu_li5 = (1/t_quer - 1)^(5) * (H_51*(rho_quer-1)^(1)+H_56*(rho_quer-1)^(6));
mu_1 = exp(rho_quer * (mu_li0+mu_li1+mu_li2+mu_li3+mu_li4+mu_li5));
%2. nearcritical term - not considered here
mu_2 = 1;
% Combination of the three terms
mu_quer = mu_0 * mu_1 * mu_2;
waterviscos = mu_quer * 10^(-6); %water viscosity in Pa*s
end
```

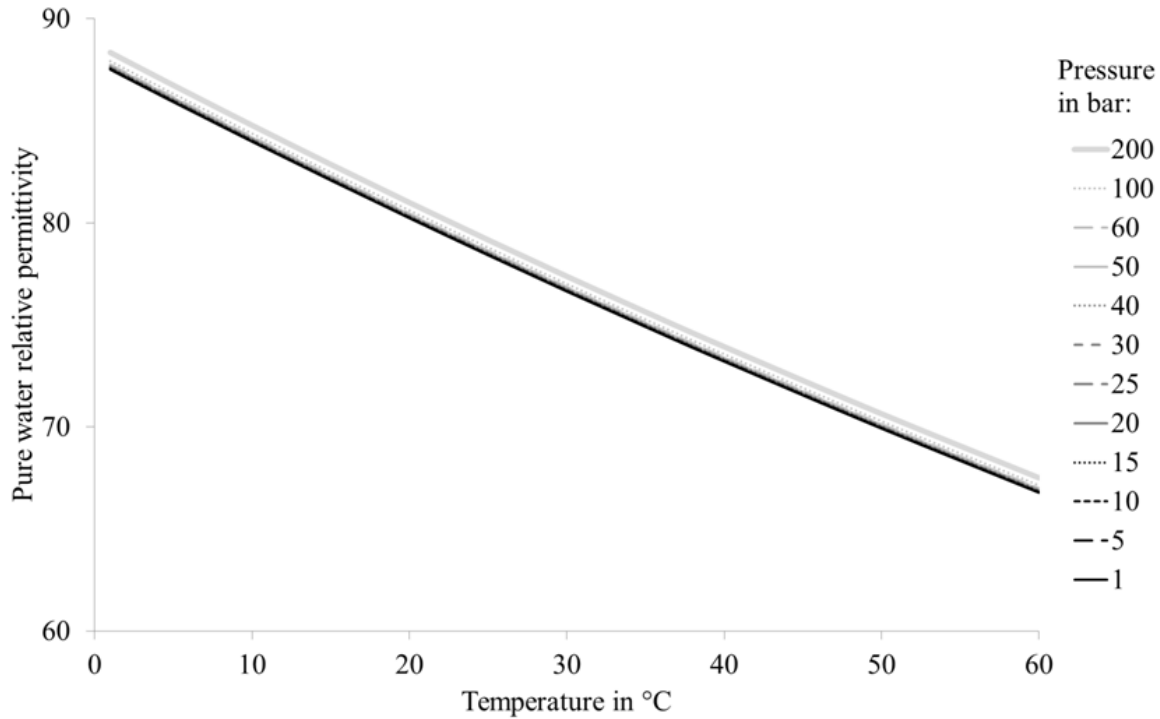



Figure 88: Relative permittivity of water as a function of temperature for different densities (expressed as pressures by the relationship in Figure 86) calculated using the formulation proposed by [Fernandez1997].

Program code for the pure water permittivity formulation:

```
function [eps_b] = Permittivity( avogadro, boltzmann, temp, eps_0,
waterdensity )
% Water relative permittivity from Fernandez-D.P._1997_J.-Phys.-Chem.-Ref.-
Data.pdf
%parameters from Fernandez-D.P._1997_J.-Phys.-Chem.-Ref.-Data.pdf
Nk(1)=0.978224486826;
Nk(2)=-0.957771379375;
Nk(3)=0.237511794148;
Nk(4)=0.714692244396;
Nk(5)=-0.298217036956;
Nk(6)=-0.108863472196;
Nk(7)=0.949327488264*10^-1;
Nk(8)=-0.980469816509*10^-2;
Nk(9)=0.165167634970*10^-4;
Nk(10)=0.937359795772*10^-4;
Nk(11)=-0.123179218720*10^-9;
Nk(12)=0.196096504426*10^-2;

jayk(1)=0.25;
jayk(2)=1;
jayk(3)=2.5;
jayk(4)=1.5;
jayk(5)=1.5;
jayk(6)=2.5;
jayk(7)=2;
jayk(8)=2;
jayk(9)=5;
```

```

jayk(10)=0.5;
jayk(11)=10;

eyek(1)=1;
eyek(2)=1;
eyek(3)=1;
eyek(4)=2;
eyek(5)=3;
eyek(6)=3;
eyek(7)=4;
eyek(8)=5;
eyek(9)=6;
eyek(10)=7;
eyek(11)=10;

geesum=0;
for i=1:11
    geesum=geesum+Nk(i)*(waterdensity/322)^(eyek(i))*(647.096/temp)^(jayk(i));
end

gee=1+geesum+Nk(12)*(waterdensity/322)*(temp/228-1)^(-1.2);

waterpolarizability = 1.636*10^(-40); %unit: C2/J/m2
waterdipolemoment = 6.138*10^(-30); %unit: C*m
watermolarmass = 0.018015268; %unit: kg/mol
asubden=waterdensity/watermolarmass; %water amount of substance density in
mol/m3
afern = (avogadro * waterdipolemoment^2 * asubden*gee)/(eps_0 * boltzmann *
temp);
bfern = (avogadro * waterpolarizability * asubden)/(3* eps_0);
eps_b_counter = (1 + afern + 5 * bfern + (9 + 2 * afern + 18 * bfern + afern^2
+ 10 * afern * bfern + 9 * bfern^2)^(0.5));
eps_b_denom = (4 - 4 * bfern);
eps_b = eps_b_counter/eps_b_denom;
end

```

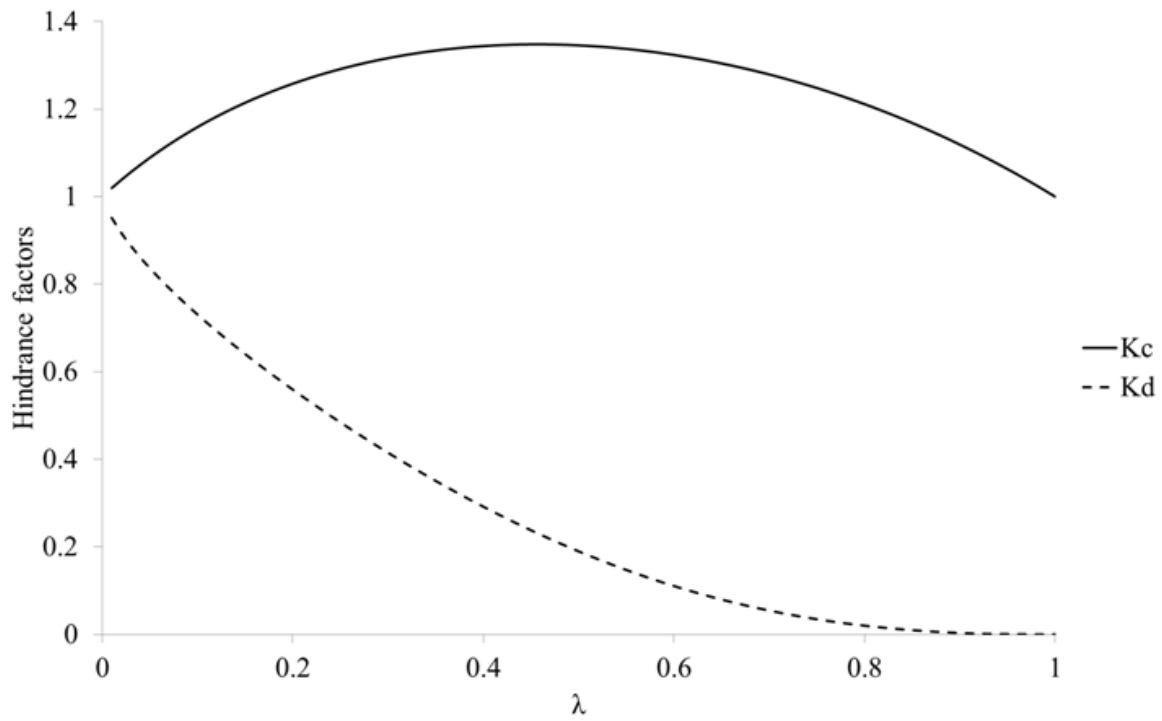


Figure 89: Testing the model: Calculation of hindrance factors for different values of pore radius. The results differed only in the range of 10^{-14} and can thus be seen as an accurate representation of the equations used.

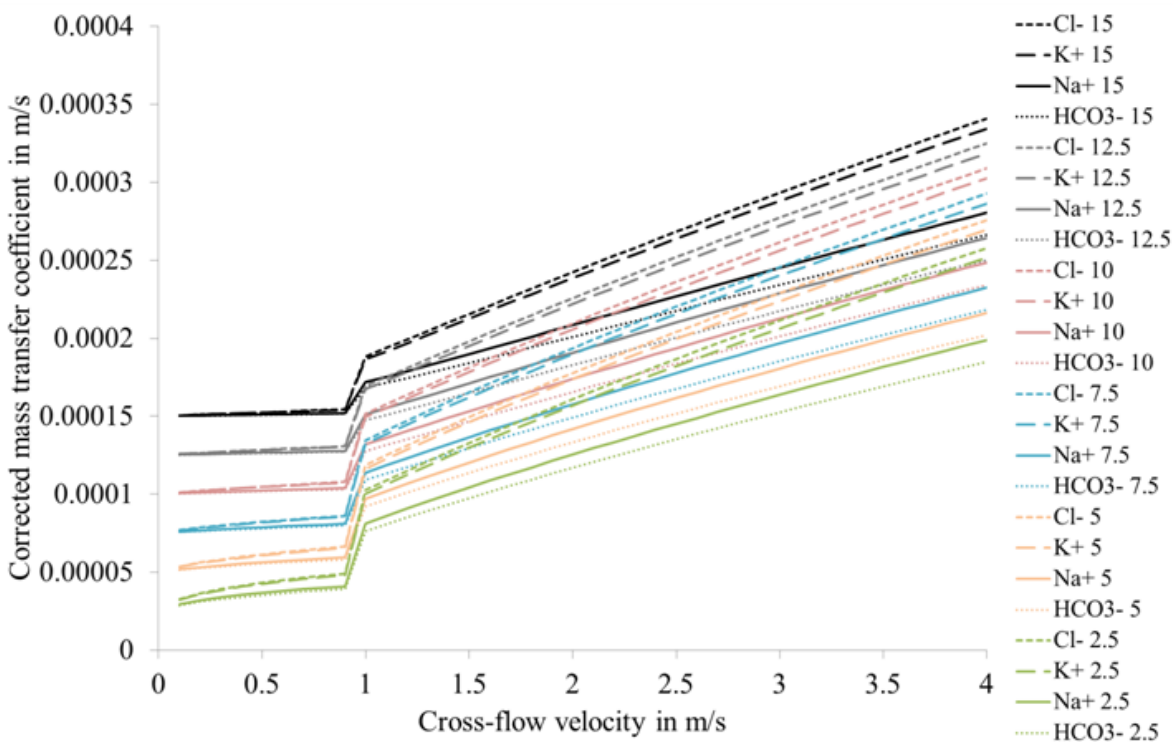


Figure 90: Corrected mass transfer coefficient at different hydrodynamic conditions, i.e. versus cross-flow velocity and for different volumetric permeate flux values (the value is indicated in the legend behind the ions name, where e.g. “Cl- 5” means for a flux of $5 \cdot 10^{-5}$ m/s). Conditions used for the calculation: NaHCO₃ and KCl both at 10mM, 25°C, 15bar. Test cell geometry as specified in Section 4.

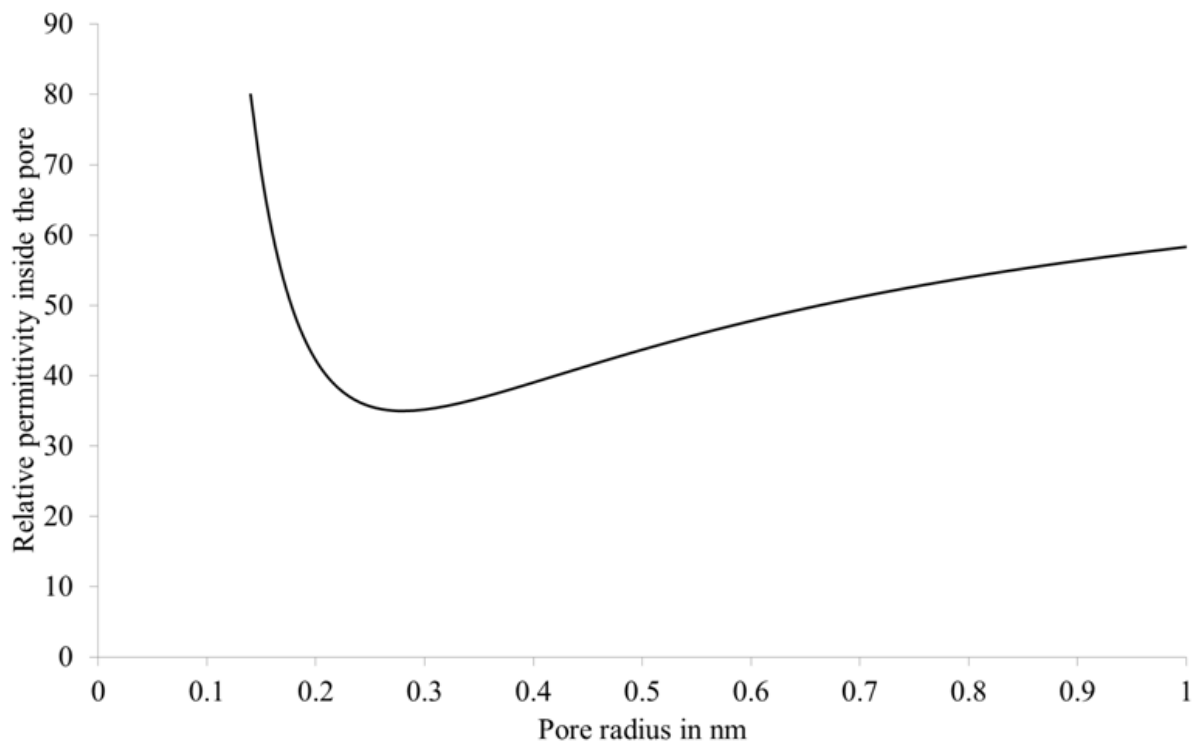


Figure 91: Pore dielectric constant calculated according to Equation (4.2).

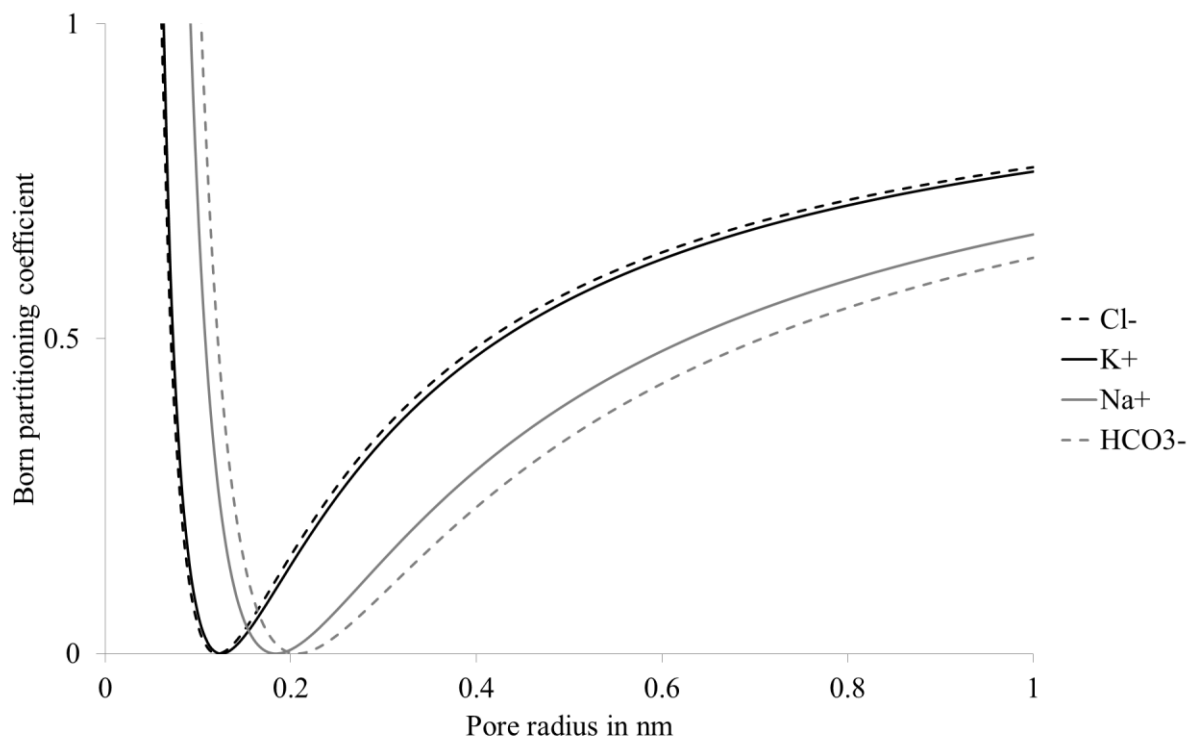


Figure 92: Born partitioning coefficient versus pore radius at the example given in the caption of Figure 90.

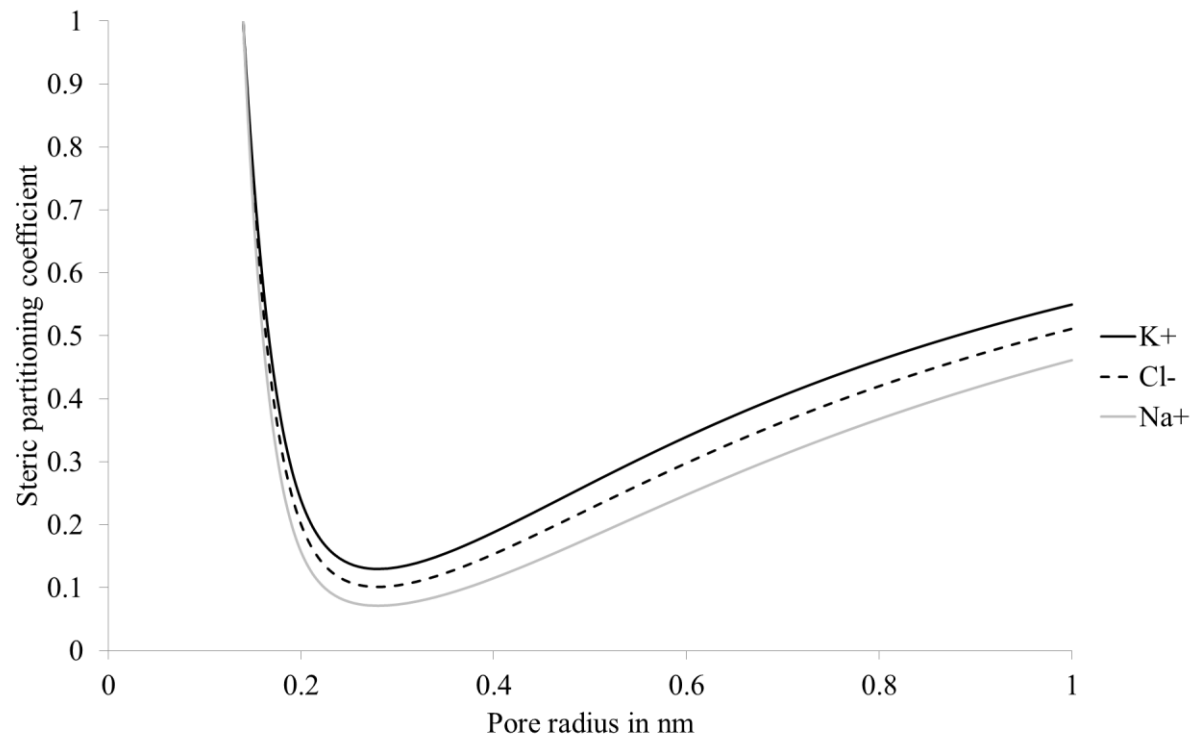


Figure 93: Steric partitioning coefficient versus pore radius at the example given in the caption of Figure 90.

Appendix E – Publications, conferences, and supervised theses

M. Hoyer, D. Zabelt, R. Steudtner, V. Brendler, R. Haseneder, J.-U. Repke: **Influence of speciation during membrane treatment of uranium contaminated water**, *Separation and Purification Technology* (2014), pp. 413-421

M. Hoyer, R. Haseneder, J.-U. Repke: **Membrane filtration of uranium contaminated water – focus on speciation**, *Wissenschaftliche Mitteilungen Inst. Geol. TU Bergakademie Freiberg*, 44 (2013), pp. 37–41

07/2014	oral presentation	at ICOM in Suzhou, China
05/2014	oral presentation	at Melpro in Prague, Czech Republic
09/2013	oral presentation	at Mine water symposium in Freiberg, Germany
09/2013	oral presentation	at Permea in Warsaw, Poland
08/2013	poster presentation	at WCCE&APCCChE in Seoul, South Korea
09/2012	poster presentation	at IWA world water congress in Busan, South Korea
08/2011	oral presentation	at Waste water reuse Asia conference in Bangkok, Thailand

Supervised theses

2012:

- Studienarbeit - Anja Schmuck: "Untersuchung zur Wasserreinigungstechnik an Haldensickerwässern"
- Studienarbeit - Martin Quegwer: "Gewinnung seltener Erden"

2013:

- Projektarbeit - Sabrina Kruse, Janina Haase: "Untersuchungen zur Membrandestillation salzhaltiger Lösungen"
- Diplomarbeit - Christopher Schwarz: "Aufbau und Erprobung einer Membranfiltrationsanlage"
- Projektarbeit - Patrizia Hunger, Elisabeth Clauß: "Untersuchung zur Nanofiltration von metallsalzhaltigen Lösungen"
- Bachelorarbeit - Denise Zabelt: "Untersuchung zur Abtrennung von Uranverbindungen aus Grubenwässern"
- Studienarbeit - Benjamin Mede: "Optimierung des Betriebsverhaltens einer Membranfiltrationsanlage"

2014

- Masterarbeit - Marcel Knoblich: "Modellierung der Nanofiltration von wässrigen Mehrsalzlösungen und experimentelle Validierung"
- Projektarbeit - Shahnaz Mansour: "Characterization of nanofiltration membranes"

2015

- Masterarbeit - Claudia Bernhardt: "Bestimmung der Ladungseigenschaften von Nanofiltrationsmembranen"
- Masterarbeit - Denny Göbel: "Ermittlung des Diffusionskoeffizienten von Uranspezies in Nanofiltrationsmembranen"
- Projektarbeit - Meiqiang Wang, Dominik Schäfer: "Laboruntersuchungen zur Nanofiltration realer Bergbauabwässer"